

**Design of a Radiation Hard
Silicon Pixel Sensor
for X-ray Science**

Dissertation

zur Erlangung des Doktorgrades

des Department Physik

der Universität Hamburg

vorgelegt von

JÖRN SCHWANDT

aus Bremen

Hamburg
2014

Gutachter der Dissertation: Prof. Dr. ROBERT KLANNER
Prof. Dr. ECKHARD ELSSEN
Prof. Dr. SOL M. GRUNER

Gutachter der Disputation: Prof. Dr. ERIKA GARUTTI
Prof. Dr. HEINZ GRAAFSMA

Datum der Disputation: 19.06.2014

Vorsitzender des Prüfungsausschusses: DR. GEORG STEINBRÜCK

Vorsitzender des Promotionsausschusses: Prof. Dr. DANIELA PFANNKUCHE

Dekan der MIN Fakultät: Prof. Dr. HEINRICH GRAENER

Leiter des Department Physik: Prof. Dr. PETER HAUSCHILDT



Für meine Eltern

Abstract

At DESY Hamburg the European X-ray Free-Electron Laser (EuXFEL) is presently under construction. The EuXFEL has unique properties with respect to X-ray energy, instantaneous intensity, pulse length, coherence and number of pulses/sec. These properties of the EuXFEL pose very demanding requirements for imaging detectors. One of the detector systems which is currently under development to meet these challenges is the Adaptive Gain Integrating Pixel Detector, AGIPD. It is a hybrid pixel-detector system with 1024×1024 p^+ pixels of dimensions $200 \mu\text{m} \times 200 \mu\text{m}$, made of $16 p^+nn^+$ - silicon sensors, each with $10.52 \text{ cm} \times 2.56 \text{ cm}$ sensitive area and $500 \mu\text{m}$ thickness. The particular requirements for the AGIPD are a separation between noise and single photons down to energies of 5 keV, more than 10^4 photons per pixel for a pulse duration of less than 100 fs, negligible pile-up at the EuXFEL repetition rate of 4.5 MHz, operation for X-ray doses up to 1 GGy, good efficiency for X-rays with energies between 5 and 20 keV, and minimal inactive regions at the edges. The main challenge in the sensor design is the required radiation tolerance and high operational voltage, which is required to reduce the so-called plasma effect. This requires a specially optimized sensor. The X-ray radiation damage results in a build-up of oxide charges and interface traps which lead to a reduction of the breakdown voltage, increased leakage current, increased interpixel capacitances and charge losses. Extensive TCAD simulations have been performed to understand the impact of X-ray radiation damage on the detector performance and optimize the sensor design. To take radiation damage into account in the simulation, radiation damage parameters have been determined on MOS capacitors and gate-controlled diodes as function of dose. The optimized sensor design was fabricated by SINTEF. Irradiation tests on test structures and sensors show that the sensor design is radiation hard and performs as predicted by the TCAD simulations. In addition, detailed TCAD simulations have been performed which have led to a qualitative understanding of the charge losses observed in p^+-n silicon sensors at the Si-SiO₂ interface under different environmental conditions.

Kurzfassung

Derzeit befindet sich der European X-ray Free-Electron Laser (EuXFEL) am DESY in Hamburg im Bau. Der EuXFEL wird einzigartige Eigenschaften bezüglich der Röntgenstrahlungsenergie, instantanen Intensität, Kohärenz und Anzahl der Pulse pro Sekunde aufweisen. Diese Eigenschaften des EuXFEL stellen sehr hohe Anforderungen an bildgebende Detektoren. Eines der Detektorsysteme, das sich derzeit in Entwicklung befindet, um diesen Anforderungen zu genügen, ist der Adaptive Gain Integrating Pixel Detector (AGIPD). Beim AGIPD handelt es sich um ein hybrides Pixeldetektorsystem bestehend aus 1024×1024 p^+ Pixel mit den Abmessungen von $200 \mu\text{m} \times 200 \mu\text{m}$, hergestellt aus $16 p^+nn^+$ -Siliziumsensoren wobei jeder eine sensitive Fläche von $10.52 \text{ cm} \times 2.56 \text{ cm}$ hat und eine Dicke von $500 \mu\text{m}$. Die speziellen Anforderungen an den AGIPD sind die Unterscheidung von Rauschen und einzelnen Photonen bis zu Energien von 5 keV , mehr als 10^4 Photonen pro Pixel innerhalb einer Pulsdauer von 100 fs , vernachlässigbarer "pile-up" für die EuXFEL Wiederholungsrate von 4.5 MHz , Röntgenstrahlungshärte bis zu einer Dosis von 1 GGy , hohe Quanteneffizienz für Energien im Bereich von 5 and 20 keV und minimale nicht-sensitive Bereiche. Die größte Herausforderung für das Sensordesign ist die geforderte Strahlentoleranz bei gleichzeitig hoher Betriebsspannung, die notwendig ist um Plasmaeffekte zu minimieren. Um diese Anforderungen zu erfüllen, ist ein speziell optimierter Sensor notwendig. Die Röntgenstrahlungsschäden führen zum Aufbau von Oxidladungen und Grenzflächenhaftstellen die zu einer Reduzierung der Durchbruchspannung, einem erhöhten Dunkelstrom, einer erhöhter Interpixelkapazität und Ladungsverlusten führen. Umfangreiche TCAD Simulationen wurden durchgeführt, um den Einfluss der Röntgenstrahlungsschäden auf die Detektoreigenschaften zu verstehen und den Sensor zu optimieren. Um die Strahlenschäden in den Simulationen zu berücksichtigen, wurden Parameter, die die Strahlenschädigung beschreiben, aus Messungen an MOS Kondensatoren und "gate-controlled" Dioden als Funktion der Dosis bestimmt. Der optimierte Sensor wurde von SINTEF hergestellt und Bestrahlungstests an Teststrukturen und Sensoren zeigen, dass er strahlenhart ist und sich so verhält, wie es von den TCAD Simulationen beschrieben wurde. Zusätzlich wurden genaue TCAD Simulationen durchgeführt, die es ermöglichen beobachtete Ladungsverluste in p^+-n Siliziumsensoren nahe an der Si-SiO_2 Grenzfläche unter verschiedenen Umgebungseinflüssen zu verstehen.

Contents

Abstracts in english and german	IV
1. Introduction	1
2. Basics of silicon detectors	5
2.1. The working principle of silicon sensors	5
2.2. Electrical properties of silicon	6
2.2.1. Crystal structure and energy bands	6
2.2.2. Carrier concentration in intrinsic silicon	8
2.2.3. Extrinsic silicon	10
2.2.4. Carrier transport	12
2.2.5. Recombination and generation	14
2.2.5.1. Shockley-Read-Hall Recombination	15
2.2.5.2. Auger Recombination	17
2.2.5.3. Avalanche Generation	18
2.2.5.4. Generation by X-ray interaction	20
2.3. The diode	23
2.3.1. The p^+-n junction	23
2.3.2. The $n-n^+$ junction	29
2.4. Metal-Oxide-Semiconductor structures	30
2.4.1. MOS capacitor	30
2.4.2. Gate-controlled diode	37
3. Effects of X-ray radiation on the Si-SiO₂ system	41
3.1. Properties of SiO ₂ and the Si-SiO ₂ interface	41
3.1.1. Silicon dioxide	41
3.1.2. Si-SiO ₂ interface	43
3.1.3. Nomenclature of oxide charges associated with thermally oxidized silicon	45
3.2. Basic mechanisms of the build up of radiation-induced surface damage	47
3.3. Effects on MOS	51
3.3.1. Radiation damage parameters	51
3.3.2. MOS capacitor with oxide charges and interface traps	52
3.3.3. Determination and summary of X-ray radiation-damage parameters	55

4. Optimization of the AGIPD sensor	63
4.1. Sensor requirements and specifications	63
4.2. Impact of X-ray radiation damage on p^+-n sensors	68
4.3. Doping profile calculations	69
4.3.1. Ion implantation	71
4.3.2. Diffusion	73
4.3.3. Simulated profiles	77
4.4. Device simulations	80
4.5. Sensor optimization strategy	81
4.6. Guard ring optimization	82
4.6.1. Guard ring fundamentals	83
4.6.2. Zero guard ring	86
4.6.3. Optimization of the guard-ring structure	99
4.6.4. Summary and conclusions	105
4.7. Pixel optimization	107
4.7.1. Introduction	107
4.7.2. 2D-Simulation results	107
4.7.3. 3D-Simulation results	115
4.8. AGIPD-sensor layout	118
4.9. Summary	121
5. Measurement results of optimized AGIPD test structures	123
5.1. AGIPD sensor processing and overview on the test structures	123
5.2. Electrical characteristics of the non-irradiated test structures	130
5.3. High dose X-ray irradiation at PETRA III	135
5.4. Measurement results after irradiation	137
5.4.1. Dose dependence of damage-related parameters from the test structures	137
5.4.2. Dose dependence of the electrical characteristics of test sensors	139
5.5. Humidity related effects	144
5.6. Summary	146
6. Charge losses and boundary conditions in segmented p^+-n silicon sensors	147
6.1. Sensor under investigation	147
6.2. Electrostatic potential and weighting potential	149
6.3. Summary of measurements and discussion of the results	154
6.4. Summary	162
7. Summary and conclusions	163
Literature	i

A. Appendix	xiii
A.1. Simulated doping profiles	xiii
List of Publications	xiv
Acknowledgements	xv

1. Introduction

With the commissioning and operation of the Linac Coherent Light Source (LCLS) [1] in 2009, more than 30 years after the invention of the Free-electron laser (FEL) by John Madey [2], FELs entered the stage as the fourth-generation of hard X-ray sources. The X-ray pulses delivered by a FEL have an approximately nine magnitude higher peak brightness compared to synchrotron sources of the third-generation (see Figure 1.0.1), duration in the femtosecond range and a high degree of spatial coherence. These features will greatly impact many scientific disciplines by

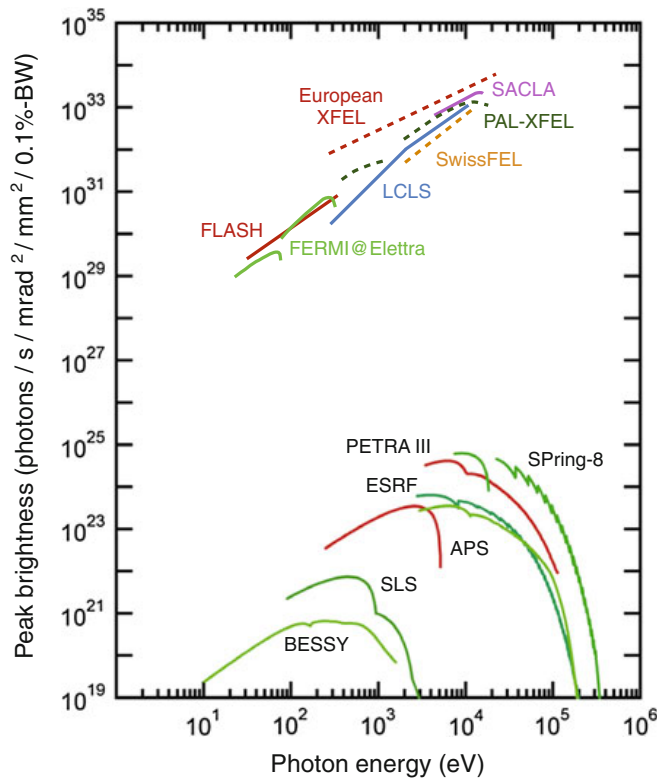


Figure 1.0.1.: Peak brightness (photons/(s·mm²·mrad²·0.1%BW)) as function of photon energy for planned and existing FELs compared to synchrotron sources [3].

enabling studies of materials at the length of interatomic distances and at time scales of atomic motions [4]. In condensed matter science, for example, material properties can be drastically altered by inducing transient structures using ultrafast light pulses. Similarly, matter at extreme

1. Introduction

limits of temperature and pressure, similar to conditions in the cores of stars and planets, can be created transiently in the laboratory using intense optical pulses. With X-ray pulses of a FEL the direct imaging of processes in these systems will be possible. In the biological sciences, time-resolved X-ray crystallography will experience a dramatic increase using FEL sources. The extreme instantaneous brightness of the pulses will allow to shrink the crystal sizes all the way down possibly to single molecules, giving three-dimensional movies of conformational dynamics and chemical reactions, and allowing the imaging of macromolecules that cannot be crystallized.

The European X-ray Free-Electron Laser (EuXFEL) [5], which is currently under construction in Hamburg, Germany, and which will enter user operation in 2016, will go one step further compared to LCLS or SACLA (SPring-8 Ångstrom Compact free electron laser) [6] by using superconducting RF cavities. This will result in an unique bunch time pattern in contrast to the 120 evenly spaced pulses produced at the LCLS. The EuXFEL pulses will be delivered in trains (see Figure 1.0.2) of typically 2700 pulses with more than 10^{12} photons/pulse at 4.5 MHz followed by a gap of 99.4 ms. The high instantaneous intensity, short pulse duration

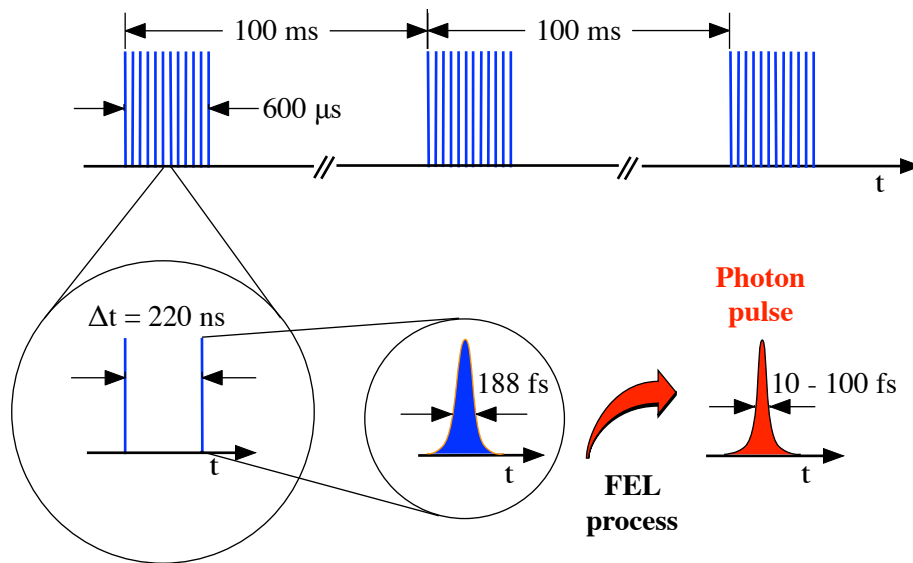


Figure 1.0.2.: European XFEL bunch time pattern.

and high repetition rate will pose very demanding requirements for imaging detectors. The European XFEL initiated therefore three independent detector development projects to meet the requirements for the different instruments which will be installed at initially 6 beamlines.

The Adaptive Gain Integrating Pixel Detector (AGIPD) [7, 8], which is one of these projects, is currently under development for the usage in the SPB (Diffraction of Single Particles and Biomolecules [9]) and MID (Materials Imaging and Dynamics [10]) instruments. It is a hybrid-pixel detector system with 1024×1024 p^+ -pixels of dimensions $(200 \mu\text{m})^2$, built of 16 p^+-n

silicon sensors, each with a sensitive area of $10.52 \text{ cm} \times 2.56 \text{ cm}$ and a thickness of $500 \text{ }\mu\text{m}$. The particular requirements (see Figure 1.0.3) are a dynamic range of 0, 1 to more than 10^4 photons of 12.4 keV per pixel for a pulse duration of less than 100 fs, negligible pile-up at the XFEL repetition rate of 4.5 MHz, and operation for X-ray doses up to 1 GGy in 3 years [11]. In addition, the sensors should have a good detection efficiency for X-rays with energies between 5 and 20 keV, and minimal inactive regions at their edges. At the Detector Lab of the Institute

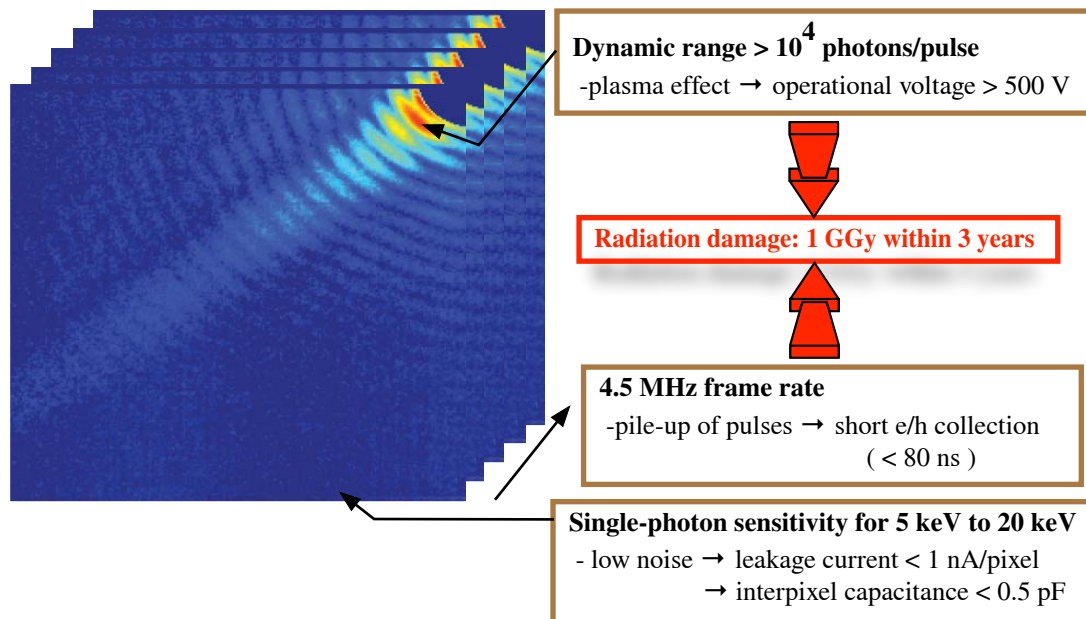


Figure 1.0.3.: Challenges of silicon detectors used at the European XFEL for imaging experiments. Diffraction pattern taken from [12].

of Experimental Physics Hamburg University in a systematic way the consequences of these requirements on the sensor have been studied in a number of Phd theses. The implication of the high number of photons per pixels, which cause the so-called plasma effect, was studied by Becker [13] with the main result for the AGIPD that an operation voltage of well above 500 V is required. The radiation damage was studied by Zhang [14] on test structures to extract radiation damage parameters, and charge losses have been studied by Poehlsen [15]. The impact of the radiation damage on the sensor can be summarize in the following way:

1. Reduction of the breakdown voltage.
2. Increase of the leakage current.
3. Increase of the depletion voltage and interpixel capacitance.
4. Occurrence of charge losses close to the Si-SiO₂ interface.

These studies results in valuable information and constraints for the sensor. Taking these into account, the sensor was optimized in a way as will be described in this thesis to fulfill all the requirements which are according to our understanding are necessary for a successful operation at the EuXFEL.

The Phd thesis is organized as follows. It begins with a chapter about silicon detectors explaining the basics of semiconductor and device physics which are required for the understanding of the later chapters. Then the Si-SiO₂ system is explained and the X-ray radiation damage in this system discussed. Furthermore the method is describe how the radiation-damage parameter are extracted which are needed for the sensor optimization. This is followed by the main chapter of the thesis which describes in detail the specifications the sensor should meet and how the optimization of the guard-ring structure and the pixel have been performed to meet these specifications. The chapter ends with the optimized sensor layout of the AGIPD. Sensors with this design have been ordered and with test structures the radiation hardness and therefore the optimization has been verified. The last chapter summarizes simulations which have been done for explaining the charge losses in silicon sensors at the Si-SiO₂ interface. The thesis ends with a short summary and conclusions are given.

The presented work is part of a larger project and therefore this thesis includes also some work done by others. All simulations were done by the author of this thesis. Irradiations, measurements and the analysis of test structures for the extraction of radiation-damage parameters were done by J. Zhang, I. Kopsalis and the author of this thesis. The drawing of the GDS files for the AGIPD wafer was done by J. Zhang. The measurements of charges losses in silicon sensors at the Si-SiO₂ interface was done by T. Poehlsen.

2. Basics of silicon detectors

This chapter contains the canonical material on silicon sensors and is based on standard textbooks about semiconductor physics, semiconductor device physics and radiation detectors [16–25].

2.1. The working principle of silicon sensors

The basic operating principle of a semiconductor detector is analogous to a gas ionizing chamber. In the simplest configuration the semiconductor replaces the gas as an absorbing medium and is covered by a pair of electrodes with an applied voltage. In a more complex design the electrodes on one side are segmented into strips or pixels as shown in Figure 2.1.1. The individual segments are diodes which are reverse biased to fully deplete the silicon bulk from free charge carriers and thereby form the sensitive volume. Ionizing radiation creates electron-hole (e/h) pairs in the depleted volume, which drift under the influence of the applied field to the electrodes and induce an electrical current in the external circuit. The integrated measured current is proportional to the number of created e/h-pairs in the depleted volume and the number of created e/h-pairs is on the other hand proportional to the absorbed energy.

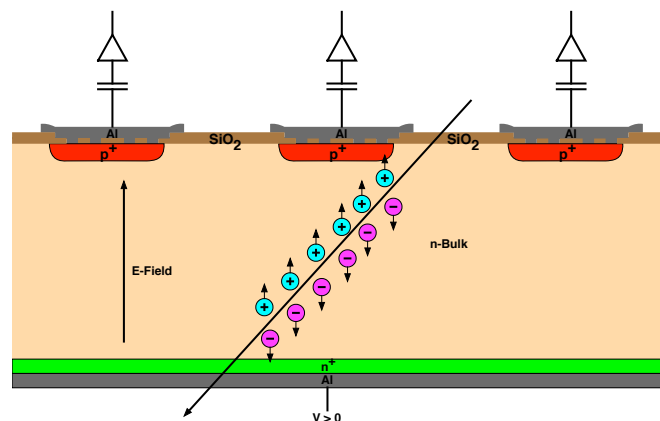


Figure 2.1.1.: Schematic of the working principles of a silicon sensor.

2.2. Electrical properties of silicon

2.2.1. Crystal structure and energy bands

Silicon (Si) has the atomic number 14 and belongs to the IVth main group of the periodic table. It has four covalent-bound electrons and crystallizes in the diamond lattice structure shown in Figure 2.2.1. This structure can be seen as two interpenetrating face-centered cubic (fcc) sublattices displaced from each other by one-quarter of the distance along the body diagonal structure.

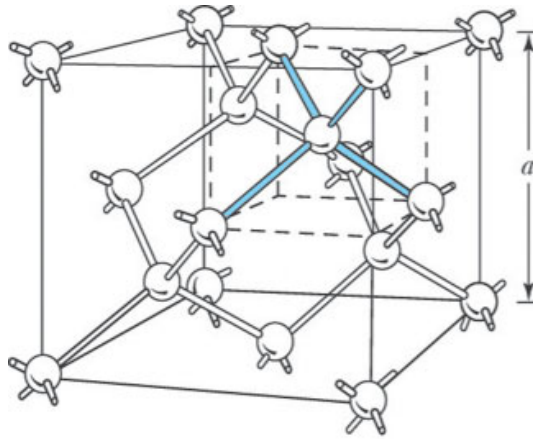


Figure 2.2.1.: Diamond cubic crystal structure of silicon with four valence electrons. The distance a is the lattice constant which is for silicon 5.431 \AA [17].

The electrons of an isolated Si atom have discrete energy levels. If one brings N isolated Si atoms close together to form a crystal, with decreasing interatomic distance the electrons in the outer subshell of the atoms interact and overlap to form bands as shown in Figure 2.2.2. Decreasing the distance further until the equilibrium is reached, which is given by the condition of minimum energy, results in a splitting of the bands into a lower band (valence band) and an upper band (conduction band). The top of the valence band is called E_V and the bottom of the conduction band E_C . The energy of the bandgap, E_g , is given by

$$E_g = E_C - E_V. \quad (2.2.1)$$

For silicon at 300 K the bandgap is $E_g = 1.12 \text{ eV}$ and the temperature dependence is given by the empirical relation

$$E_g(T) = E_g(0K) - \frac{\alpha T^2}{T + \beta} \quad (2.2.2)$$

with $E_g(0K) = 1.1696 \text{ eV}$, $\alpha = 4.73 \cdot 10^{-4} \text{ eV/K}$ and $\beta = 636 \text{ K}$.

Si is a semiconductor, meaning that at a temperature approaching 0 K the electrons occupy

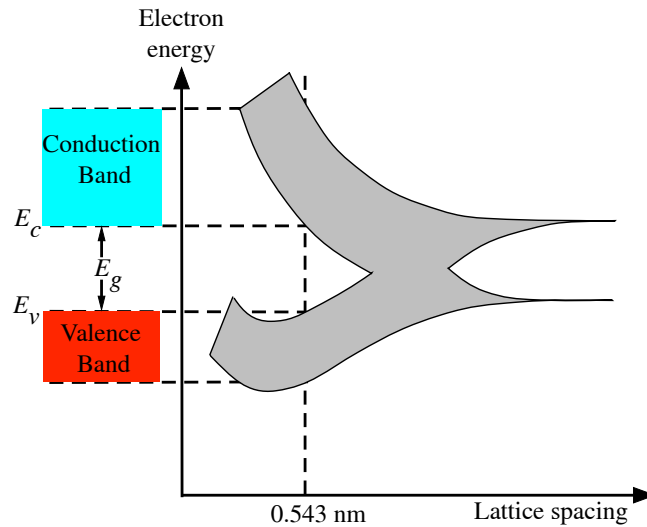


Figure 2.2.2.: The formation of energy bands as the diamond lattice crystal is formed by bringing isolated silicon atoms together. Adapted after [17].

the lowest energy states, so that all states in the valence band are filled and the states in the conduction band are empty and no current can flow. At higher temperatures the thermal energy is high enough to break bonds and lift electrons from the valence band to the conduction band, thus creating a weak conductivity due to free electrons and holes (unoccupied electron states in the valence band). An insulator has a similar structure as a semiconductor, except that the bandgap is much larger (typically > 5 eV) resulting in zero occupation probability of the states in the conduction band at room temperature. Metals may either have overlapping valence and conduction bands or a partially filled conduction band.

To calculate the energy band structure a quantum mechanical treatment is inevitable. In principle one has to solve a many-particle Schrödinger equation. Because this is too complicated a large number of simplifications¹ have to be made to end up with an one-electron Schrödinger equation in a periodic potential which has solutions that can be expressed as Bloch functions. The detailed calculations are too sophisticated to be present here, so that only a few results are mentioned. 1.) Si is an indirect semiconductor, which means that the valence-band maximum and the conduction-band minimum are not at the same position in the momentum space. The generation of an electron-hole pair by an indirect transition from the valence-band maximum to the conduction-band minimum must be accompanied by a gain of momentum. Similarly, the electron-hole recombination must involve some momentum loss. Candidates for the momentum exchange are phonons. The direct bandgap of silicon is 3.4 eV, so that photons with a larger

¹ First the electrons have to be separated into valence and core electrons. Then due to the large mass of the ions compared to the electrons the Born-Oppenheimer or adiabatic approximation can be made and at the end the mean-field approximation assuming that every electron experiences the same average potential $V(r)$.

energy can make a direct transition from the valence-band maximum into the conduction-band. 2.) In Si there are six conduction band valleys, two along each of the $\langle 100 \rangle$ directions. Near the minima, the surface of the six valleys can be approximated by a ellipsoids. 3.) The electrons and holes in the crystal can be treated as free particles as long as the effect of the lattice is taken into account by introducing an effective mass m_n for electrons and m_p for holes, respectively.

2.2.2. Carrier concentration in intrinsic silicon

The calculation of the free electron concentration n under thermal equilibrium conditions in intrinsic silicon (no impurities) requires the integration of the density of states $N(E)$ multiplied by the occupation probability $F(E)$ over the conduction band (see Figure 2.2.3)

$$n = \int_{E_C}^{\infty} N(E)F(E) dE. \quad (2.2.3)$$

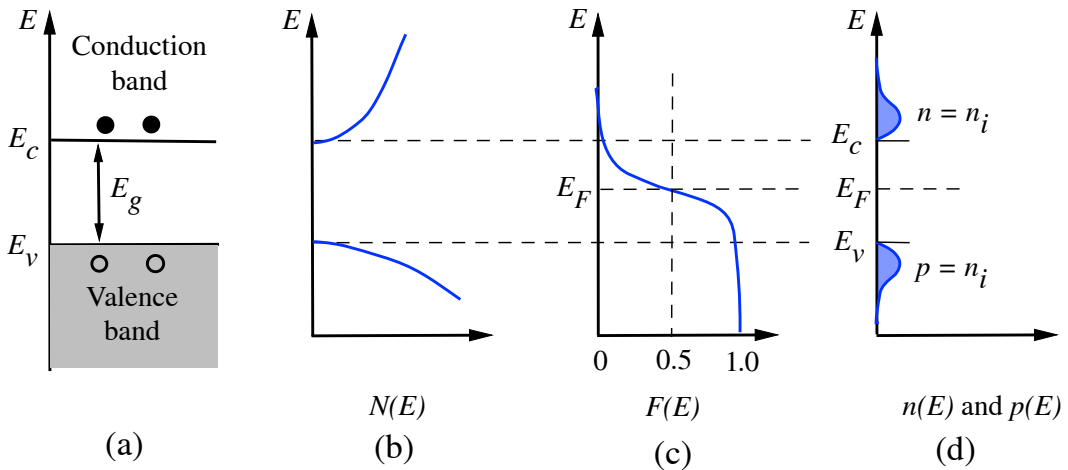


Figure 2.2.3.: Intrinsic silicon. (a) Schematic band diagram. (b) Density of states. (c) Fermi-dirac distribution (d) Carrier concentration. After [17].

The occupation probability for electronic states is given by the Fermi-Dirac function

$$F(E) = \frac{1}{1 + \exp\left(\frac{E-E_F}{k_B T}\right)} \quad (2.2.4)$$

where k_B is the Boltzmann constant, T the temperature in Kelvin and E_F is the Fermi energy. The Fermi energy is the energy at which the occupancy probability of a state is one half. For $|E - E_F| > 3k_B T$ the Fermi-Dirac distribution for electrons F_n and hole F_p can be

approximated by the Boltzmann distribution

$$F_n(E) \approx \exp\left(-\frac{E - E_F}{k_B T}\right) \quad (2.2.5)$$

$$F_p(E) = 1 - F_n(E) \approx \exp\left(-\frac{E_F - E}{k_B T}\right). \quad (2.2.6)$$

For low enough carrier densities and temperatures the density of states can be approximated by the density near the bottom of the conduction band and with the assumption of a parabolic band edge and no valley degeneration the result is:

$$N(E) = \frac{\sqrt{2} m_n^{3/2} (E - E_C)^{1/2}}{\pi^2 \hbar^3} \quad (2.2.7)$$

In the case of the Boltzmann distribution using (2.2.5) and (2.2.7) the integral in (2.2.3) can be evaluated resulting in:

$$n = 2 \left(\frac{2\pi m_n k_B T}{h}\right)^{\frac{3}{2}} \exp\left(-\frac{E_C - E_F}{k_B T}\right) = N_C \exp\left(-\frac{E_C - E_F}{k_B T}\right) \quad (2.2.8)$$

For holes a similar calculation gives:

$$p = 2 \left(\frac{2\pi m_p k_B T}{h}\right)^{\frac{3}{2}} \exp\left(-\frac{E_F - E_V}{k_B T}\right) = N_V \exp\left(-\frac{E_F - E_V}{k_B T}\right) \quad (2.2.9)$$

N_C and N_V are the effective densities of states in the conduction and valence band respectively. For an intrinsic semiconductor under thermal equilibrium conditions, the concentrations of electrons and holes are the same

$$n_i = n = p. \quad (2.2.10)$$

Therefore

$$n_i = \sqrt{np} = \sqrt{N_C N_V} \exp\left(-\frac{E_g}{2k_B T}\right). \quad (2.2.11)$$

For the intrinsic-carrier concentration in silicon the expression [26]

$$n_i = 1.64 \cdot 10^{15} T^{1.706} \exp\left(-\frac{E_g}{2k_B T}\right) \quad (2.2.12)$$

can be used in the temperature range 77 K to 400 K. At 300 K one finds $n_i = 9.97 \cdot 10^9 \text{ cm}^{-3}$.

Using the neutrality condition for the intrinsic semiconductor the Fermi level can be determined as

$$E_i = \frac{E_C + E_V}{2} + \frac{3k_B T}{4} \ln\left(\frac{m_p}{m_n}\right), \quad (2.2.13)$$

which is located close to the middle between valence and conduction band and where the deviation from the middle is due to the different effective masses of electrons and holes.

2.2.3. Extrinsic silicon

For many applications the conductivity of intrinsic silicon is too low. By intentional incorporating impurities (dopants) on a lattice site of Si new levels in the bandgap are introduced and the conductivity can be altered in a controlled manner. In general one distinguishes between donor and acceptor levels. A donor is neutral if filled by an electron and positive if empty. An acceptor on the other hand is negative if filled by an electron, and neutral if empty.

The standard example for a donor in silicon is P which introduces an energy level E_D at $E_C - E_D = 0.045$ eV. P has five electrons in its outer shell, from which four are required to satisfying the tetrahedral bonds to the neighboring electrons of the Si atoms (see Figure 2.2.4). The extra electron is bound to the P^+ ion via Coulomb interaction at sufficient low temperatures, but can be easily thermally excited into the conduction band at higher temperatures and is then not anymore bound to the P atom. Silicon doped with P is called *n*-type silicon.

An example for an acceptor in silicon is B which introduces an energy level E_A at $E_A - E_V = 0.045$ eV. Boron contains three electron in its outer shell and therefore lacks one electron needed to form electron pair bonds with the four nearest neighbor Si atoms. The missing electron of the B atom can be regarded as a hole (see Figure 2.2.4). At low temperatures the hole is bond to the B atom, but at higher temperatures an electron from the electron gas (in the valence band) can be transferred to the B atom to form the fourth bond to the Si neighbors. The hole is thereby transferred to an other bond. Silicon doped with B is called *p*-type silicon.

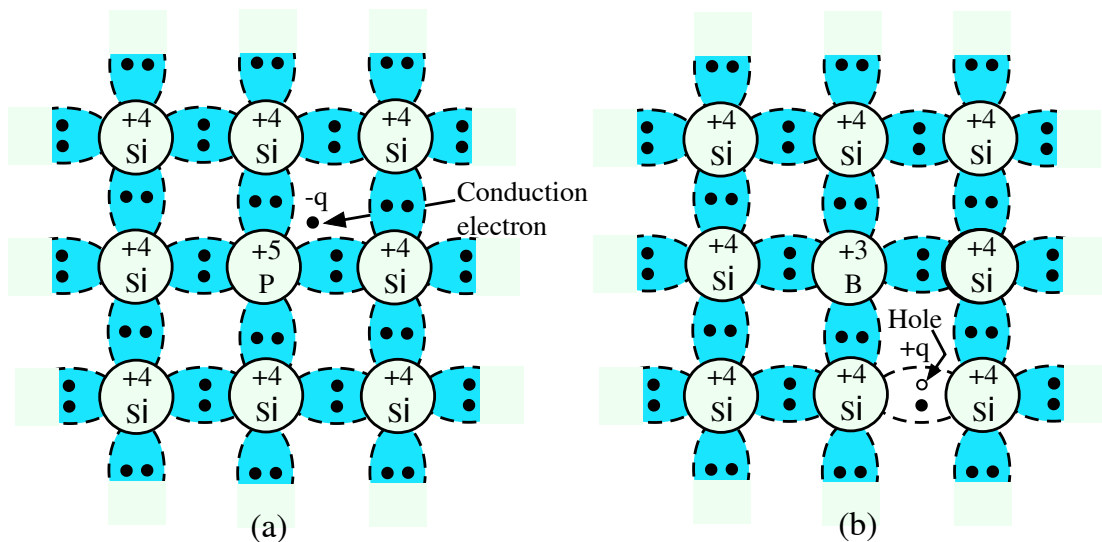


Figure 2.2.4.: (a) *n*-type Si with donor (phosphorus). (b) *p*-type Si with acceptor (Boron). After [17].

The introduction of dopants results in a change of the position of Fermi level. If the donor concentration is N_D and all donors are completely ionized the electron density is $n = N_D$ and the Fermi level given by

$$E_C - E_F = k_B T \ln \left(\frac{N_C}{N_D} \right). \quad (2.2.14)$$

Similarly, for an acceptor concentration N_A one gets $p = N_A$ and

$$E_F - E_V = k_B T \ln \left(\frac{N_V}{N_A} \right). \quad (2.2.15)$$

In Figure 2.2.5 the Fermi level in silicon as function of temperature for different doping levels (n -type and p -type) is shown. With increasing temperature the Fermi level shifts from close to the band edge toward the band center. This shifts begin at a higher temperature for a higher doping.

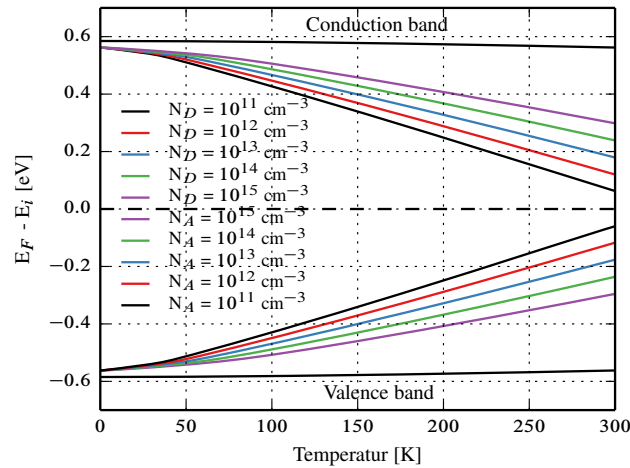


Figure 2.2.5.: Fermi level in silicon as function of temperature for different doping levels (n -type and p -type). The intrinsic Fermi level is chosen as zero energy.

The carrier concentration can be expressed in terms of the Fermi level as

$$n = n_i \exp \left(\frac{E_F - E_i}{k_B T} \right) \quad (2.2.16)$$

$$p = n_i \exp \left(\frac{E_i - E_F}{k_B T} \right) \quad (2.2.17)$$

where both concentration are connected via the mass-action law $n \cdot p = n_i^2$. This law is only valid in thermodynamic equilibrium. In nonequilibrium situations the electron and hole densities

each can take arbitrary values, in principle. Furthermore there is no constant Fermi level any more. In such a situation one defines quasi-Fermi levels E_{Fn} and E_{Fp} for electrons and holes, respectively, as

$$n = N_C \exp\left(\frac{E_{Fn} - E_C}{k_B T}\right) = n_i \exp\left(\frac{E_{Fn} - E_i}{k_B T}\right) \quad (2.2.18)$$

and

$$p = N_V \exp\left(\frac{E_V - E_{Fp}}{k_B T}\right) = n_i \exp\left(\frac{E_i - E_{Fp}}{k_B T}\right). \quad (2.2.19)$$

In highly doped regions additional effects have to be considered. At a concentration of $\approx 3 \cdot 10^{18} \text{ cm}^{-3}$, the impurity sites can no longer be considered as discrete because their electron wave functions overlap. This increases the probability for electrons to be shared between dopant sites and their levels split into a set of allowed energy levels. At even higher concentration the energy levels broaden into bands resulting in a decrease of the ionization energy until it vanishes at $\approx 3 \cdot 10^{19} \text{ cm}^{-3}$. A further increase results in a merging of the impurity band with the conduction band. An important consequence of this high doping is the bandgap narrowing, ΔE_g , which is attributed to the lowering of the energy gap as impurity concentrations are increased and results in an increased intrinsic carrier concentration.

2.2.4. Carrier transport

The derivation of the carrier transport equations is a lengthy task and it typically starts with the Boltzmann transport equation. Depending on the approximation one makes equations can be derived, which describe the transport on different length scales. For silicon detector the active regions are in general large enough to utilize the drift-diffusion model which will be here described on a phenomenological basis.

The main sources of carrier flow in a semiconductor device are:

- Drift of electrons and holes caused by an electrical field as driving force with a resulting drift current density J_n^{drift} and J_p^{drift} .
- Diffusion of the electron and hole ensembles with resulting diffusion current densities J_n^{diff} and J_p^{diff} .

For the total current densities the assumption is made that the electron and hole current flows are determined by linearly superimposing the diffusion and the drift processes, i. e.:

$$J_n = J_n^{\text{drift}} + J_n^{\text{diff}}, \quad J_p = J_p^{\text{drift}} + J_p^{\text{diff}} \quad (2.2.20)$$

The drift current densities are defined as the products of particle charge, carrier concentration and drift velocity

$$J_n = q n v_n, \quad J_p = q p v_p. \quad (2.2.21)$$

In the field-free case the carriers perform a random motion resulting from collisions with impurities, phonons or other perturbations. The mean velocity is the thermal velocity $v_{th} = \sqrt{3k_B T/m_n}$, which is for silicon $\approx 10^7$ cm/s. The typical mean free path is 10^{-5} cm and the mean free time $\tau_C \approx 10^{-12}$ s. In the presence of an electric field, \mathbf{E} , the charge carriers will be accelerated between the collisions in a direction determined by the electric field and a net average drift velocity will be obtained, which is proportional to the electric field at moderate field strengths and are given by

$$\mathbf{v}_n = -\mu_n \mathbf{E}, \quad \mathbf{v}_p = \mu_p \mathbf{E}, \quad (2.2.22)$$

where μ_n and μ_p are the mobilities of electrons and holes, respectively. The carrier mobilities are physically related to the electron and hole relaxation times τ_n^r and τ_p^r via

$$\mu_n = \frac{q \cdot \tau_n^r}{m_n} \quad (2.2.23)$$

$$\mu_p = \frac{q \cdot \tau_p^r}{m_p}. \quad (2.2.24)$$

The relaxation times represent the average times between two consecutive scattering events of carriers. Modeling the mobilities accurately requires the determination of the different scattering mechanisms (ionized impurity scattering, carrier-carrier scattering etc.) and their temperature dependence. The different scattering mechanisms are typically assumed to be independent and the combined effect is assessed using the Matthiessen rule, i. e., $1/\mu = \sum_i 1/\mu_i$, where μ_i is the mobility due to the scattering mechanisms of type "i".

For high electrical fields strong deviation from linearity in the relation between drift velocity and field are observed with a final saturation of the velocity. The field dependence of the mobility is often parameterized using the Caughey–Thomas formula [27]

$$\mu_{n,p}(E) = \frac{\mu_{n,p}^0}{\left(1 + \left(\frac{\mu_{n,p}^0 E}{v_{n,p}^{sat}}\right)^{\beta_{n,p}}\right)^{1/\beta_{n,p}}}, \quad (2.2.25)$$

where $\mu_{n,p}^0$ is the low field mobility, $v_{n,p}^{sat}$ the saturation velocity and $\beta_{n,p}$ a parameter. All parameters are temperature dependent.

Differences in the electron and hole concentration lead to a diffusion of electron and holes from regions of high concentration into regions of low concentration. Diffusion is governed by Fick's law, which states that the diffusion flux, which is the number of carriers crossing an unit area perpendicular to their direction of motion in unit time, is proportional to the concentration gradient. The diffusion current densities are obtained by multiplying the diffusion fluxes with

the charge per particle, which is $-q$ for electrons and $+q$ for holes leading to

$$\begin{aligned} \mathbf{J}_n^{\text{diff}} &= qD_n \nabla n \\ \mathbf{J}_p^{\text{diff}} &= -qD_p \nabla p \end{aligned} \quad (2.2.26)$$

where D_n and D_p are the diffusion constants for electrons and holes, respectively. Mobility and diffusion constants are related in equilibrium to each other by the Einstein equation

$$D_n = \frac{k_B T}{q} \mu_n, \quad D_p = \frac{k_B T}{q} \mu_p. \quad (2.2.27)$$

Combing the drift (2.2.21) and the diffusion (2.2.26) current contributions, one obtains the current densities:

$$\begin{aligned} \mathbf{J}_n &= q\mu_n n \mathbf{E} + qD_n \nabla n \\ \mathbf{J}_p &= q\mu_p p \mathbf{E} - qD_p \nabla p. \end{aligned} \quad (2.2.28)$$

The current equations have to be completed by the continuity and the Poisson equations. The continuity equations are given by

$$\begin{aligned} \frac{\partial n}{\partial t} &= \frac{1}{q} \nabla \cdot \mathbf{J}_n - R \\ \frac{\partial p}{\partial t} &= -\frac{1}{q} \nabla \cdot \mathbf{J}_p - R, \end{aligned} \quad (2.2.29)$$

where R can physically be interpreted as the difference of the rate at which electron-hole carrier pairs recombine and the rate at which they are generated in the semiconductor. Therefore R is called the recombination-generation rate. Generation prevails in those region in which $R < 0$ holds and recombination prevails if $R > 0$.

The Poisson equation is given by

$$\nabla^2 \phi = -\frac{\rho}{\epsilon_{Si} \epsilon_0} \quad (2.2.30)$$

where ϕ is the electrostatic potential, ϵ_{Si} the relative permittivity of silicon, ϵ_0 the vacuum permittivity and $\rho = q(p - n + N_D^+ - N_A^-)$ the charge density in the semiconductor with N_D^+ and N_A^- the concentration of electrically active donor and acceptor atoms, respectively.

2.2.5. Recombination and generation

Here only the most important recombination and generation mechanisms will be discussed. In silicon these are the recombination via defects (Shockley-Read-Hall (SRH) mechanism), the Auger mechanism which is a direct band-to-band recombination and the avalanche generation.

2.2.5.1. Shockley-Read-Hall Recombination

Traps with density N_t and energy level E_t (see Figure 2.2.6) can capture electrons from the

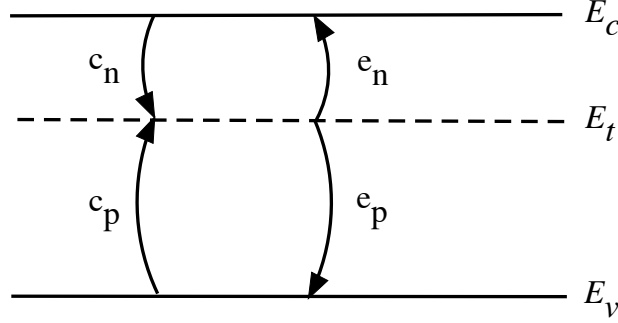


Figure 2.2.6.: Capture and emission of a trap in the bandgap at a energy level E_t .

conduction band and emit electrons to the conduction band. Also holes can be captured from the valence band and be emitted to the valence band. With n_t the concentration of trapped electrons the capture rate is proportional to the electron density n and $(N_t - n_t)$, whereas the emission rate is proportional to n_t . The net capture rate of conduction band electrons, R_n , and of valence band holes, R_p , can be written as

$$R_n = -\frac{\partial n}{\partial t} = c_n n (N_t - n_t) - e_n n_t \quad (2.2.31)$$

$$R_p = -\frac{\partial p}{\partial t} = c_p p n_t - e_p (N_t - n_t) \quad (2.2.32)$$

with c_n and e_n the constants of capture and emission for the interaction with the conductance band. c_p and e_p are the corresponding constants of capture and emission for the interaction with the valence band. In the case of equilibrium the distribution function for trapped electrons is

$$f_t^0 = \frac{n_t}{N_t} = \frac{1}{1 + \exp\left(\frac{E_t - E_F}{k_B T}\right)}, \quad (2.2.33)$$

where it is assumed that the spin degeneracy factor of the trap is one. The application of the detailed balance condition, i. e. $R_n = R_p = 0$, results in

$$e_n = c_n n \frac{1 - f_t^0}{f_t^0} \quad (2.2.34)$$

$$e_p = c_p p \frac{f_t^0}{1 - f_t^0}. \quad (2.2.35)$$

Under the assumption of the Boltzmann distribution n and p are given by (2.2.8) and (2.2.9), respectively. If the capture cross sections σ_n and σ_p are introduced to express the capture constant as $c_{n,p} = \sigma_{n,p} v_{th}$, where v_{th} is the thermal velocity, one obtains for the emission rates

$$e_n = \sigma_n v_{th} n_1 \quad (2.2.36)$$

$$e_p = \sigma_p v_{th} p_1 \quad (2.2.37)$$

with $n_1 = N_C \exp\left(\frac{E_t - E_C}{k_B T}\right)$ and $p_1 = N_V \exp\left(-\frac{E_t - E_V}{k_B T}\right)$ for which $n_1 p_1 = n_i^2$ holds.

In non-equilibrium steady-state charge conservation requires $R_n = R_p = R \neq 0$ resulting in the distribution function

$$f_t = \frac{c_n n + e_p}{c_n n + c_p p + e_n + e_p}. \quad (2.2.38)$$

from which one finally gets for the net recombination rate

$$R = \frac{np - n_i^2}{\tau_{p0}(n + n_1) + \tau_{n0}(p + p_1)} \quad (2.2.39)$$

where the capture time constants $\tau_{n0} = (\sigma_n v_{th} N_t)^{-1}$ and $\tau_{p0} = (\sigma_p v_{th} N_t)^{-1}$ have been introduced. From (2.2.39) it can be seen that depending on the term $(np - n_i^2)$ recombination or generation will take place.

In the case of $np \ll n_i^2$ and $\tau_r = \tau_{n0} = \tau_{p0}$ the expression (2.2.39) can be simplified to

$$R = -\frac{n_i}{2\tau_r \cosh\left(\frac{E_t - E_i}{k_B T}\right)} \equiv -\frac{n_i}{\tau_g} \quad (2.2.40)$$

showing that under this circumstances the maximal generation rate is reached if the energy level of the trap is at the intrinsic level and that the generation lifetime is $\tau_g = 2\tau_r$.

If in (2.2.39) the non-equilibrium carrier densities are replaced by $n = n_0 + \Delta n$ and $p = p_0 + \Delta p$ with n_0 and p_0 the equilibrium carrier densities and makes the assumption of no trapping, i.e. $\Delta n = \Delta p$, the recombination rate can be written as $R = \Delta n / \tau_{SRH}$ with

$$\tau_{SRH} = \frac{\tau_{p0}(n_0 + n_1 + \Delta n) + \tau_{n0}(p_0 + p_1 + \Delta n)}{n_0 + p_0 + \Delta n} \quad (2.2.41)$$

the SRH lifetime. For n -type silicon and low-level injection ($\Delta n \ll n_0 + p_0$) this reduces to $\tau_{SRH} \approx \tau_{p0}$ indicating that the minority carrier capture essentially determines the recombination lifetime.

The function of a trap or more precisely of a deep center in the bandgap can be classified into recombination center, electron trap, hole trap and generation center. A simple consideration shows that the function depends on the capture and emission rates in the following way:

- Recombination center if $c_n \gg e_p$ and $c_p \gg e_n$.

- Electron trap if $c_n \gg e_p$ and $c_p \ll e_n$.
- Hole trap if $c_p \gg e_n$ and $c_n \ll e_p$.
- Generation center if $c_p \ll e_n$ and $c_n \ll e_p$.

For multiple traps the SRH recombination (2.2.39) has to be extended. In the case of noninteracting traps the total SRH recombination is given by the sum of the individual contribution of the different traps. In the case of interacting or coupled traps additional interference terms have to be taken into account. An example for two traps can be found in [28] where the steady-state recombination rate for two coupled defect levels is calculated.

The surface (interface) recombination may be described in the same manner as in the bulk case. Interface traps are typically described by an continuous distribution of noninteracting states. Let $D_{it}(E_{it})$ be the density of interface traps (traps per $\text{cm}^2 \text{eV}$) at the energy E_{it} , then the surface recombination rate, R_{surf} , is given by the integral

$$R_{surf} = \int_{E_V}^{E_C} \frac{n_s p_s - n_i^2}{(n_s + n_1)/c_{ps} + (p_s + p_1)/c_{ns}} D_{it}(E_{it}) dE_{it}, \quad (2.2.42)$$

where n_s and p_s are the electron and hole density at the surface and c_{ns} and c_{ps} the capture constants which are given by a similar expression as for the bulk case. Assuming that $D_{it}(E_{it})$ is constant throughout the bandgap and that the cross sections are given by the same value σ_s the integral can be expressed in the form [29]

$$R_{surf} = \sigma_s v_{th} D_{it} \left[\int_{E_V}^{E_C} \frac{dE_{it}}{n_s + p_s + 2n_i \cosh\left(\frac{E_{it} - E_i}{k_B T}\right)} \right] (n_s p_s - n_i^2). \quad (2.2.43)$$

In the case of a depleted surface $n_s + p_s \ll 2n_i$ and $n_s p_s \ll n_i^2$ the integral in (2.2.43) can be evaluated to be $\pi k_B T / (2n_i)$, so that the surface recombination is

$$R_{surf} = -\frac{\pi}{2} \sigma_s v_{th} D_{it} k_B T n_i = -s_0 n_i, \quad (2.2.44)$$

where

$$s_0 = \frac{\pi}{2} \sigma_s v_{th} D_{it} k_B T \quad (2.2.45)$$

is the surface recombination velocity.

2.2.5.2. Auger Recombination

In indirect semiconductors like silicon the Auger recombination is an important nonradiative mechanism. In the Auger recombination the energy released during the recombination of an electron and hole is not emitted by a photon but, instead, transferred to a third particle which can

be an electron or hole. This particle will then be a hot carrier and transfer its energy nonradiatively via phonon emission to the lattice. As a three-particle process the Auger recombination becomes likely in heavy doped region of $\approx 5 \cdot 10^{19} \text{ cm}^{-3}$ or under forward bias. This recombination rate is given by

$$R_{Au} = (C_n n + C_p p)(np - n_i^2) \quad (2.2.46)$$

with C_n and C_p are constants that vary slightly with temperature. At 300 K the values are $C_n = 2.8 \cdot 10^{-31} \text{ cm}^6 \text{ s}^{-1}$ and $C_p = 9.9 \cdot 10^{-32} \text{ cm}^6 \text{ s}^{-1}$ [27].

2.2.5.3. Avalanche Generation

Impact ionization is the inverse of the Auger recombination. If the electrical field strength in the semiconductor is above a certain threshold, the carriers gain enough kinetic energy to generate electron-hole pairs by impact ionization as shown in Figure 2.2.7. Consider the electron (designated by 1) in the conduction band which is accelerated in the high electrical field before it collides with a valence band electron. This electron can transfer some of its kinetic energy to the valence band electron to make an upward transition to the conduction band. An electron-hole pair (designated by 2 and 2') is generated. Now also the generated pair is accelerated in the electrical field and collides with other valence band electrons to generate new electron-hole pairs as indicated in the figure by 3 and 3' and so on. This processes leads to an avalanche.

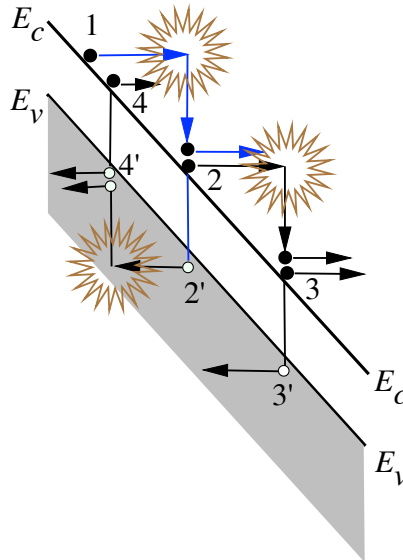


Figure 2.2.7.: Energy band diagram for the avalanche process. After [17].

The electron-hole pair generation rate G is given by

$$G = \alpha_n \frac{J_n}{q} + \alpha_p \frac{J_p}{q}, \quad (2.2.47)$$

where α_n and α_p are the ionization coefficients for electrons and holes, respectively. α_n gives the number of generated electron-hole pairs by an electron per unit distance traveled and similar for α_p . The ionization coefficients are strongly depended on the magnitude of the electrical field E and are often expressed by the semi-empirical formula of Chynoweth [30]

$$\alpha_{n,p} = a_{n,p} \exp\left(-\frac{b_{n,p}}{E}\right). \quad (2.2.48)$$

Based on this formula different impact ionization models can be formulated which will be discussed later.

The calculation of the total generated avalanche current, I_{av} , assumes that an initial current, $I_n(0)$, of electrons enters at $x = 0$ as shown in Figure 2.2.8 a region of high electrical field where impact ionization takes place. This current at $x = W$ has increased to $I_n(W) = I = M_n I_n(0)$,

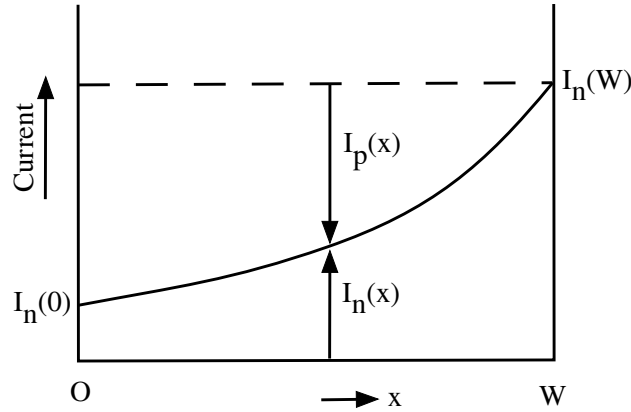


Figure 2.2.8.: Avalanche multiplication of an initial electron current $I_n(0)$ to the value $I_n(W)$

where M_n is the multiplication factor of electrons. A hole current is also generated, in such a way that everywhere $I = I_n(x) + I_p(x) = I_n(W) = \text{const}$ holds. Using (2.2.47) one gets

$$dI = \alpha_n I_n dx + \alpha_p I_p dx = (\alpha_n - \alpha_p) I_n dx + \alpha_p I dx \quad (2.2.49)$$

or

$$\frac{dI_n}{dx} = (\alpha_n - \alpha_p) I_n + \alpha_p I. \quad (2.2.50)$$

The avalanche current is $I_{av} = I - I_n(0) = [1 - (1/M_n)] I$. Solving the differential equation (2.2.50) leads to

$$\frac{1}{1 - M_n} = \int_0^W \alpha_n(x) \exp\left[-\int_x^W (\alpha_n(x') - \alpha_p(x')) dx'\right] dx. \quad (2.2.51)$$

The integral on the right side is the ionization integral, which is also abbreviated as I_n . Similarly, for holes

$$\frac{1}{1 - M_p} = \int_0^W \alpha_p(x) \exp \left[- \int_0^x (\alpha_p(x') - \alpha_n(x')) dx' \right] dx, \quad (2.2.52)$$

where the ionization integral is also designated by I_p . In the case of an avalanche $M_{n,p} \rightarrow \infty$ resulting in $I_n = I_p = 1$ for the ionization integrals. The ionization integrals are often used for an approximate breakdown analysis. As can be seen from (2.2.51) the current does not enter so that for the calculation it is sufficient to use the Poisson equation and to assume a constant quasi Fermi level within the depletion region. This method is a simplification because in deriving the ionization integrals the existence of a threshold energy is not taken into account and changes of the field due to movable carriers are neglected.

2.2.5.4. Generation by X-ray interaction

The main interaction mechanisms of photons with matter are the photoelectric effect, coherent (Rayleigh) scattering, incoherent (Compton) scattering and pair production. As shown schematically in the Figure 2.2.9 in the photoelectric effect the photon can be completely absorbed during

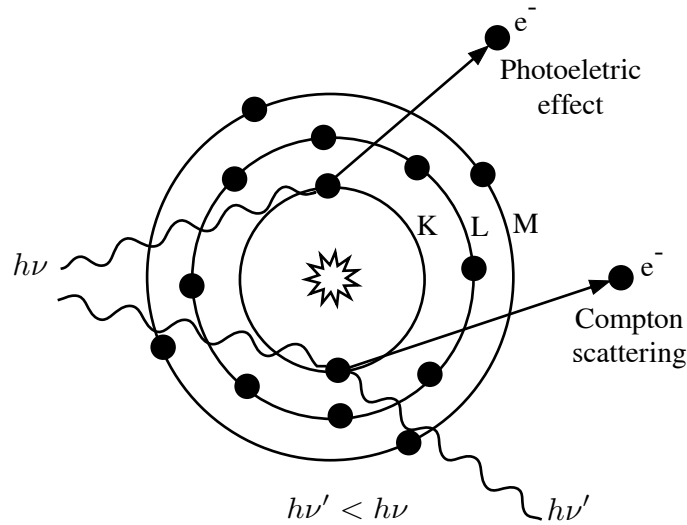


Figure 2.2.9.: Schematics of photoelectric effect and Compton scattering.

the interaction with an atom which, in turn, emits an electron. The absorption probability is higher for tightly bound electrons because a free electron can not absorb a photon. To preserve the momentum and the energy the atom as a whole has to take up the extra energy and momentum carried by the photon; however, because of the relatively large nuclear mass, the atom recoil energy can be neglected. So, if E_{ph} is the photon energy and E_b the binding energy of the

electron the kinetic energy of the emitted electron is

$$E_k = E_{ph} - E_b. \quad (2.2.53)$$

Because the emission of an electron from a certain shell requires that the photon energy is larger than the binding energy of this shell the absorption curves exhibit characteristic absorption edges which coincide with the ionization energies of electrons for the different shells.

In the Compton effect an incoming photon is scattered on an individual atomic electron (see Figure 2.2.9). The change of photon energy during the scattering event is given by the Compton wavelength shift formula

$$\Delta\lambda = \lambda_c(1 - \cos \theta_\nu) \quad (2.2.54)$$

where $\Delta\lambda$ is the Compton shift, $\lambda_c = h/(m_e c) = 2.43 \cdot 10^{-12}$ m the Compton wavelength of the electron and θ_ν the angle between the incoming and the outgoing photon. The maximum Compton shift occurs for backward scattered photons, where $\theta_\nu \rightarrow 180^\circ$, and is twice the Compton wavelength. The recoiling electron is emitted at $\theta_e \rightarrow 0^\circ$ with an maximum kinetic energy of

$$E_{e,max} = \frac{2E_{ph}^2}{m_e c^2 + 2E_{ph}}. \quad (2.2.55)$$

The Rayleigh scattering is a process by which photons interact with atom-bound electrons, leaving the target atom neither excited nor ionized. The atom as a whole absorbs the transferred momentum but its recoil energy is very small and the incident photon scattered under some angle has essentially the same energy as the original photon. Therefore Rayleigh scattering does not deposit energy in the matter but it has to be taken into account in the attenuation of a photon beam.

The pair production requires a minimum photon energy of 1.022 MeV, which is far beyond the energy range of the experiments at the European XFEL and its discussion will be omitted.

When a beam of X-rays tranverses matter the individual photons are absorberd or scattered resulting in an attenuation of the beam. If the initial photon intensity of the beam is I_0 after the beam passage through the material a distance x the intensity is given by the Lambert-Beer law:

$$I(x) = I_0 e^{-\mu_m \rho x} \quad (2.2.56)$$

where μ_m is the mass attenuation coefficient and ρ is the density of the material. The mass attenuation coefficient is related to the cross-section σ by

$$\mu_m = \frac{N_A}{A} \sigma \quad (2.2.57)$$

where N_A is the Avogadro constant and A the atomic weight of the material. For silicon the mass attenuation coefficient as function of photon energy is shown for the different processes in

Figure 2.2.10. As can be seen the photoelectric effect dominates up to an energy of 50 keV.

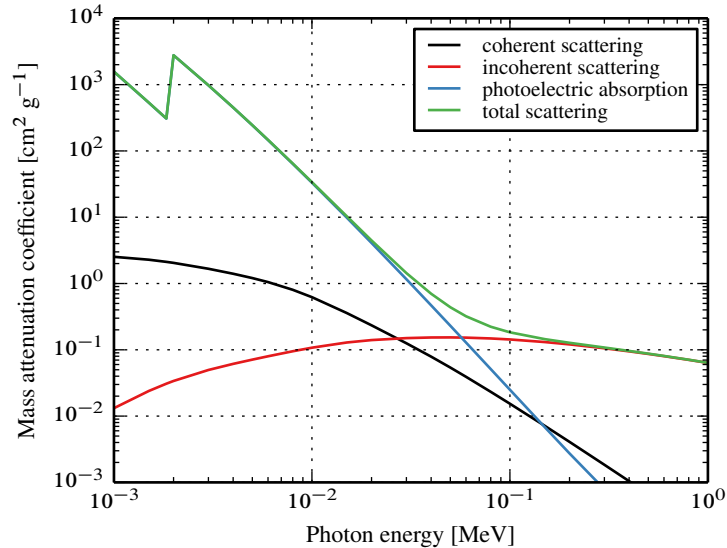


Figure 2.2.10.: Mass attenuation coefficient in silicon in units of cm^2/g as a function of the photon energy (in units of MeV) from 1 keV up to 1 MeV. The Compton and Rayleigh scattering is denoted as incoherent and coherent scattering. Data from [31].

After the interaction of the photon by the photoelectric effect or Compton scattering, the atom is in an excited state due to the vacant electron in one of the inner shells. The atomic relaxation to the ground state proceeds by transition of an electron from a higher atomic shell to fill the shell vacancy whereby the energy difference in the binding energy between the initial and the final shell or sub-shell is emitted from the atom in form of fluorescence photons, Auger electrons, Coster-Kronig electrons or shake-off emission² [32]. For silicon the K shell (binding energy 1.84 keV) fluorescence yield is only 4.4%. The atomic relaxation proceeds until all vacancies, except those due to shake-off emission, are transferred to the valence band (M shell). The electron which is emitted by the photoelectric effect or Compton scattering together with the vacancy after the following relaxation process yields the primary e/h pairs. The primary and secondary electrons lose their kinetic energy in processes like electron-phonon interaction, valence band ionization, excitation of plasmons, core L-shell ionization and core K-shell ionization producing secondary e/h pairs. The mean energy, W , to create an e/h pair is (3.66 ± 0.03) eV for photons with energies between 50 eV and 1500 eV [33]. The mean number N of generated e/h pairs for

² Shake-off emission arises from the sudden change of the atomic potential resulting from the fast removal of the primary electron.

a photon with energy E_{ph} is therefore given by

$$N = \frac{E_{ph}}{W} \quad (2.2.58)$$

resulting in 3388 e/h pairs for a 12.4 keV photon.

2.3. The diode

Silicon sensors are basically diodes with a reverse biased $p^+ - n$ or $n^+ - p$ junctions to build up a depletion region where the density of free charge carriers is so low that signals of $O(10^3)$ e/h pairs can be detected. In practice a sensor on n -type silicon has the structure $p^+ - n - n^+$ where the $n - n^+$ junction is formed to have a good ohmic contact and to reduce minority carrier injection from the backside into the depletion region. Therefore, the most important properties of this junctions will be discussed.

2.3.1. The $p^+ - n$ junction

A $p - n$ junction is formed by bringing a p -type region and a n -type region into contact. Consider two separated uniformly doped p and n regions with concentrations N_A and N_D . The carrier concentrations in the p -region are $p_p = N_A$ and $n_p = n_i^2/N_A$ and in the n -region $n_n = N_D$ and $p_n = n_i^2/N_D$. A band diagram is shown in the left of Figure 2.3.1. Since the regions are uniformly doped, the electrical fields inside each region is zero. If both region are brought into contact they form an abrupt junction with a band diagram as shown in the right of Figure 2.3.1. Initially the system will be in non-equilibrium. The concentration gradients of electron and

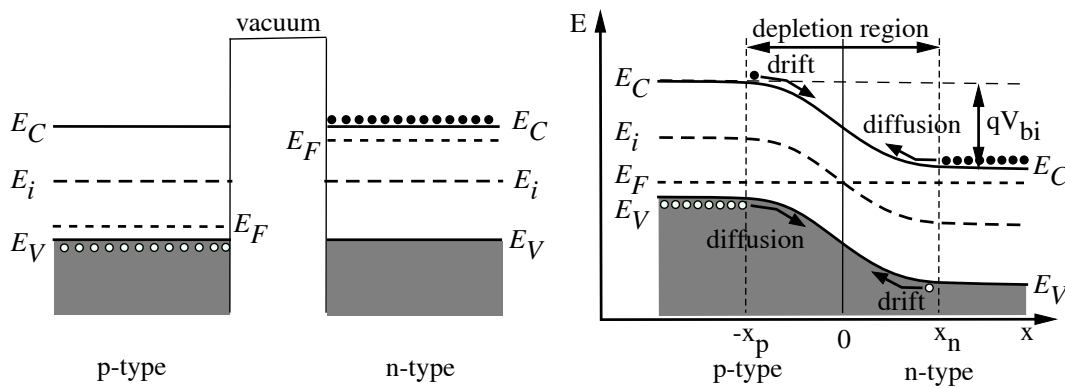


Figure 2.3.1.: Band diagram of a $p - n$ junction before and after equilibrium.

holes between the p -region and n -region at the boundary $x = 0$ will lead to diffusion currents. Electrons will diffuse from the n into the p -region, and holes will diffuse from the p into the n -region. The diffusion of electrons leaves behind a space charge of positively charged, fixed

donor ions in the n -region. Similarly, the diffusion of holes leaves a negative space charge of fixed acceptor ions in the p -region. The fixed charges build up an electrical field which creates a drift current in opposite direction to the diffusion current. At equilibrium, i.e. constant Fermi energy, drift and diffusion current components cancel each other for each carrier type. The concentrations of the carrier which diffuse from one region where they are majority carriers into a region where they are minority carriers leads to recombination so that in the space charge region (depletion region) the free charge carrier density is strongly reduced.

The electrostatic potential difference between the neutral n -region and the neutral p -region is called built-in or diffusion voltage V_{bi} . In the neutral n -region the electrostatic potential relative to the intrinsic Fermi level is

$$\phi_n = \frac{E_F^n - E_i}{q} = \frac{k_B T}{q} \ln \left(\frac{N_D}{n_i} \right) \quad (2.3.1)$$

and in the neutral p -region

$$\phi_p = \frac{E_i - E_F^p}{q} = \frac{k_B T}{q} \ln \left(\frac{N_A}{n_i} \right) \quad (2.3.2)$$

therefore the built-in voltage is given by

$$V_{bi} = \phi_n + \phi_p = \frac{k_B T}{q} \ln \left(\frac{N_A N_D}{n_i^2} \right), \quad (2.3.3)$$

which is depending on the dopant concentration and temperature, and can reach values between 0 and approximately 1 V.

To calculate the width of the depletion region W and the electrical field E as shown in Figure 2.3.2, the Poisson equation has to be solved. In the depletion approximation the Poisson equation for the four regions is:

$$\frac{d^2\phi}{dx^2} = -\frac{dE}{dx} = \begin{cases} 0 & x \leq -x_p \text{ and } x \geq x_n \\ -q \frac{N_D}{\epsilon_{Si} \epsilon_0} & 0 < x < x_n \\ q \frac{N_A}{\epsilon_{Si} \epsilon_0} & -x_p < x < 0 \end{cases} \quad (2.3.4)$$

Using the boundary condition of 1) vanishing field at $x = x_d$ and $x = -x_p$ and 2) $\phi(x_n) - \phi(-x_p) = V_{bi}$ together with the charge neutrality condition $N_D x_d = N_A x_p$ the equation (2.3.4) can be integrated to yield

$$W = x_n + x_p = \sqrt{\frac{2\epsilon_{Si} \epsilon_0 V_{bi}}{q} \left[\frac{1}{N_A} + \frac{1}{N_D} \right]}. \quad (2.3.5)$$

In the case of an one-sided abrupt $p^+ - n$ junction, where $N_A \gg N_D$, the depletion layer width

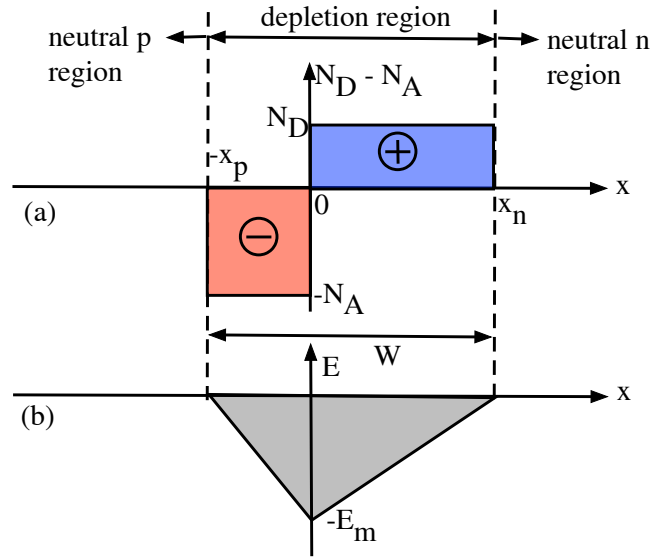


Figure 2.3.2.: (a) Space charge distribution in the depletion region in thermal equilibrium. (b) Electric-field distribution.

of the p -region is much smaller and the expression for W can be simplified to

$$W = \sqrt{\frac{2\epsilon_{Si}\epsilon_0 V_{bi}}{qN_D}} \quad (2.3.6)$$

and the electrical field is given for $0 < x < W$ by

$$E(x) = -E_m \left(1 - \frac{x}{W}\right) \quad (2.3.7)$$

with the maximum field

$$E_m = \frac{qN_D W}{\epsilon_{Si}\epsilon_0}. \quad (2.3.8)$$

If a positive voltage V is applied to the n -side the $p^+ - n$ junction is reversed biased and the total electrostatic potential across the junction is increased by V . Replacing in (2.3.6) V_{bi} by $V_{bi} + V$ yields the voltage dependence of the depletion region

$$W(V) = \sqrt{\frac{2\epsilon_{Si}\epsilon_0 (V_{bi} + V)}{qN_D}}, \quad (2.3.9)$$

which is valid as long as $W \leq d$ with d the distance between the $p^+ - n$ junction and the rear contact.

The junction depletion-layer capacitance is defined by

$$C(V) = \frac{dQ}{dV} = \frac{dQ}{dW} \frac{dW}{dV}, \quad (2.3.10)$$

where dQ is the incremental change in the depletion-layer charge for an incremental change in applied voltage V . Using the derivative of (2.3.9) with respect to V for an one-sided abrupt $p^+ - n$ junction and $dQ = qN_D A dW$, where A is the junction area, one obtains the expression

$$C(V) = \epsilon_{Si} \epsilon_0 \frac{A}{W(V)} = A \sqrt{\frac{\epsilon_{Si} \epsilon_0 q N_D}{2(V + V_{bi})}} \quad \text{for } W \leq d \quad (2.3.11)$$

or

$$\frac{1}{C^2(V)} = \frac{2(V + V_{bi})}{\epsilon_{Si} \epsilon_0 q A^2 N_D} \quad \text{for } W \leq d \quad (2.3.12)$$

which gives a straight line in the plot of $1/C^2$ versus V for a uniform doping. The slope gives the doping concentration N_D of the substrate, and the intercept ($1/C^2 = 0$) gives V_{bi} . At the full depletion voltage V_{dep} the depletion region reaches the backside ($W = d$) resulting in

$$C_{end} = \epsilon_{Si} \epsilon_0 \frac{A}{d} \quad (2.3.13)$$

which is called the geometrical end capacitance because it depends only on the area and thickness. It should be mentioned that the capacitance measurement on a real diode includes also edge, corner and parasitic effects for which one has to correct before the above analysis can be applied.

The current-voltage characteristic of an ideal $p - n$ diode was first derived by Shockley. The assumptions which were made are: abrupt junction, Boltzmann approximation, low carrier injection, i.e. the injected minority-carrier density is small compared to the majority-carrier density, and zero generation current in the depletion region, i.e. the electron and hole currents are constant throughout the depletion region. Using the quasi-Fermi levels E_{Fn} and E_{Fp} defined in (2.2.18) and (2.2.19) or equivalent the quasi-Fermi potentials defined by $-q\phi_{Fn} = E_{Fn}$ and $-q\phi_{Fp} = E_{Fp}$ the np product is

$$np = n_i^2 \exp \left[\frac{q}{k_B T} (\phi_{Fp} - \phi_{Fn}) \right] = n_i^2 \exp \left[\frac{qV}{k_B T} \right] \quad (2.3.14)$$

with $V = \phi_{Fp} - \phi_{Fn}$ the voltage drop across the depletion region.

If the electron density and hole density on the p -side are denominated n_p and p_p , and on the n -side by n_n and p_n the electron density at the boundary of the depletion layer on the p -side ($x = -x_p$) is given by

$$n_p = \frac{n_i^2}{p_p} \exp \left(\frac{qV}{k_B T} \right) = n_{p0} \exp \left(\frac{qV}{k_B T} \right). \quad (2.3.15)$$

Similarly, the hole density on the n -side ($x = x_n$) is

$$p_n = p_{n0} \exp\left(\frac{qV}{k_B T}\right). \quad (2.3.16)$$

Solving the continuity equation under the boundary condition that far away from the depletion layer the hole density is p_{n0} , the hole density on the n -side is

$$p_n(x) - p_{n0} = p_{n0} \left[\exp\left(\frac{qV}{k_B T}\right) - 1 \right] \exp\left(-\frac{x - x_n}{L_p}\right) \quad (2.3.17)$$

where $L_p = \sqrt{D_p \tau_p}$ is the hole diffusion length. From this the hole current density at the boundary of the depletion layer on the n -side can be calculated with the result

$$J_p(x_n) = -qD_p \frac{\partial p_n}{\partial x} = \frac{qD_p p_{n0}}{L_p} \left[\exp\left(\frac{qV}{k_B T}\right) - 1 \right]. \quad (2.3.18)$$

Similar calculations for the electron current in the depletion layer gives

$$J_n(-x_p) = \frac{qD_n n_{p0}}{L_n} \left[\exp\left(\frac{qV}{k_B T}\right) - 1 \right]. \quad (2.3.19)$$

The total current is

$$J = J_p(x_n) + J_n(-x_p) = J_s \left[\exp\left(\frac{qV}{k_B T}\right) - 1 \right] \quad (2.3.20)$$

with the saturation current

$$J_s = \frac{qD_p p_{n0}}{L_p} + \frac{qD_n n_{p0}}{L_n} \approx q \sqrt{\frac{D_p}{\tau_p}} \frac{n_i^2}{N_D} + q \sqrt{\frac{D_n}{\tau_n}} \frac{n_i^2}{N_A}. \quad (2.3.21)$$

For the description of a real Si p - n junction additional effects have to be taken into account. These are recombination-generation in the depletion region, high-carrier injection, i.e. $p_n \ll n_n$ is not anymore valid, series resistance R_s , junction breakdown at high reverse voltage and surface effects. Here the discussion will be limited to the recombination-generation and series resistance.

Under reverse voltage the current flow, which is called leakage current J_{leak} , is the sum of the saturation diffusion current J_s and the generation current J_{gen} . The current due to generation is given by

$$J_{gen} = \frac{qn_i W}{\tau_g}. \quad (2.3.22)$$

The generation current depends on depletion region width, which depends on the voltage

$$J_{gen} \propto W \propto \sqrt{V + V_{bi}} \quad \text{for } V \leq V_{dep}. \quad (2.3.23)$$

For one-sided abrupt p^+-n junctions the leakage current density can be written as

$$J_{leak} = q \sqrt{\frac{D_p}{\tau_p} \frac{n_i^2}{N_D}} + \frac{q n_i W}{\tau_g}. \quad (2.3.24)$$

The question whether the diffusion current or the generation current dominates the leakage current depends on the temperature and on the lifetimes. In older devices the behavior was so that for $T < 40^\circ\text{C}$ the generation was dominant while for $T > 125^\circ\text{C}$ diffusion current dominated and the breakpoint temperature where the two were equal was 85°C . Due to process improvements the breakpoint temperature was close to room temperature in device from the 1980' [34]. On today's high purity silicon the lifetimes can be so long that even at room temperature a dominating diffusion current can occur.

Under forward bias the concentrations of both electrons and holes exceed their equilibrium values and recombination processes will take place. The total forward current can be approximated for a p^+-n junction and $V \gg k_B T/q$

$$J_F = q \sqrt{\frac{D_p}{\tau_p} \frac{n_i^2}{N_D}} \exp\left(\frac{qV}{k_B T}\right) + \sqrt{\frac{\pi}{2}} \frac{k_B T n_i}{\tau_p E_m} \exp\left(\frac{qV}{2k_B T}\right) \quad (2.3.25)$$

where E_m is the electric field at the location of maximum recombination. The experimental results are often represented by the empirical form

$$J_F \propto \exp\left(\frac{qV}{\eta k_B T}\right) \quad (2.3.26)$$

where the ideality factor η equals 1 if the diffusion current dominates and η equals 2 if the recombination current dominates. In case of comparable contributions of both currents the current can be described with η in the range of 1 and 2.

The series resistance also affects the current voltage characteristics by reducing the voltage drop across the junction by $R_s \cdot I$. This effect is small at low injection but has to be taken into account at high injection by replacing V with $V - R_s \cdot I$ resulting in

$$I = I_s \exp\left(\frac{q(V - R_s \cdot I)}{\eta k_B T}\right). \quad (2.3.27)$$

This is an implicit equation which can be solved only numerically.

The above mentioned effects on the current-voltage characteristic of a real silicon diode are shown in Figure 2.3.3 together with the ideal curves.

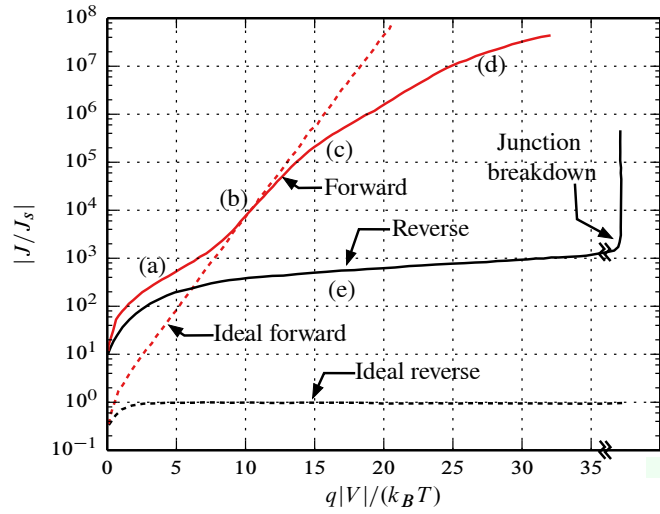


Figure 2.3.3.: Current-voltage characteristic of a real silicon diode. (a) Generation-recombination current region. (b) Diffusion-current region. (c) High-injection region. (d) Series-resistance effect. (e) Reverse leakage current due to generation and surface effects. Diagram adapted from [16].

2.3.2. The $n-n^+$ junction

On the backside of a silicon sensors typically a highly doped silicon layer is introduced to reduce the contact resistance between silicon and the metal contact, and the minority carrier injection. On n -type silicon this results in an $n-n^+$ junction which is also called high-low junction. Assuming a doping concentration in the n^+ region of N_{D^+} and in the n region of N_D then electrons will diffuse from the high concentration region into the region of lower concentration. This diffusion of electrons creates a positive space charge in the n^+ region and a negative charge due to the excess of electron in the n region. Therefore an electrical field builds up which pushes back the diffusing electrons. In equilibrium the diffusion voltage is

$$V_{bi} = \frac{k_B T}{q} \ln \left(\frac{N_{D^+}}{N_D} \right). \quad (2.3.28)$$

Different to a p^+-n junction the space charge region of a $n-n^+$ junction is not a depletion layer³ because the electrons are on both sides of the junction majority carriers. In a p^+-n-n^+ structure the electrical field direction of the p^+-n and $n-n^+$ junction is the same. This results in a vanishing total hole current flow at the $n-n^+$ junction.

³In a p^+-n-n^+ sensor this is only true as long as the sensor is not fully depleted.

2.4. Metal-Oxide-Semiconductor structures

Beside the p - n diodes the properties of the metal-oxide-semiconductor (MOS) structure have to be understood for understanding of semiconductor sensors. For example CCDs are based on MOS structures and silicon strip sensors often use an AC readout where a MOS capacitor structure is integrated in the sensor. The MOS structures are also important test structures for the investigation of surface effects. In the following only the ideal behavior will be discussed, whereas the changes due to oxide charges and interface traps will be discussed in the next chapter.

2.4.1. MOS capacitor

A MOS capacitor (MOS-C) is a semiconductor covered by an insulator on which a metal layer, called gate, is deposited. On the backside a second electrode is deposited as ohmic contact. A sketch is shown in Figure 2.4.1(a) where t_{ox} is the thickness of the oxide. In an ideal MOS-C there is no current flowing through the oxide under DC biasing, no oxide charges or interface traps are present, and the semiconductor is uniformly doped. One further condition is that the work function difference, Φ_{MS} , between metal and semiconductor is zero, so that one obtains at $V_G = 0$ an energy-band diagram for a n -type semiconductor as shown in Figure 2.4.1(b) where the Fermi levels in the metal and in the semiconductor are aligned. The work function

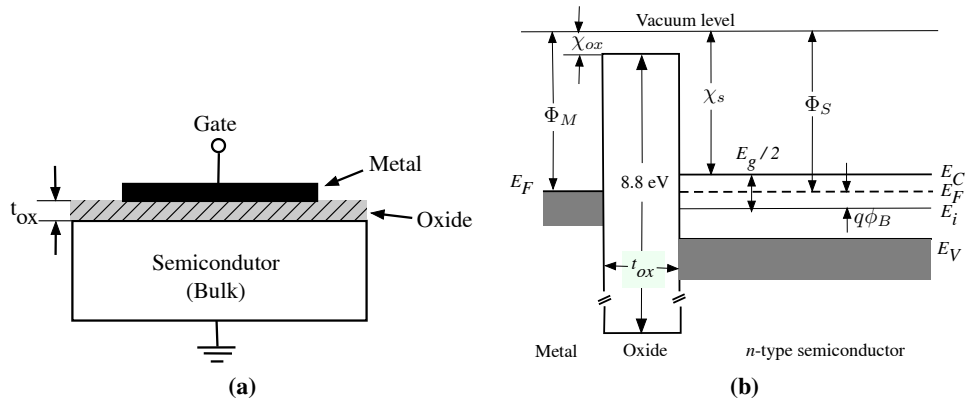


Figure 2.4.1.: (a) Sketch of a MOS capacitor (b) Energy-band diagram for a n -type semiconductor MOS structure.

for the metal, Φ_M , and for the semiconductor, Φ_S , is the energy difference between the Fermi level and the vacuum level. The energy difference between the conduction band and the vacuum level is the electron affinity, which is $\chi_s = 4.05$ eV for silicon and $\chi_{ox} = 0.95$ eV for SiO_2 . The bandgap of SiO_2 is 8.8 eV. $q\phi_B$ is the energy difference between E_F and E_i and given for n -type silicon in (2.3.1). From Figure 2.4.1(b) it follows that the work function difference is

given by

$$\Phi_{MS} = \Phi_M - \Phi_S = \Phi_M - \left(\chi_s + \frac{E_g}{2} - q\phi_B \right). \quad (2.4.1)$$

For Al the work function is $\Phi_M = 4.10$ eV resulting for n -type in

$$\Phi_{MS} \approx -0.51 + \phi_B \quad (V) \quad (2.4.2)$$

for an Al-SiO₂-Si system.

For the discussion of the conditions near the Si-SiO₂ interface it is customary to define the potentials as shown in Figure 2.4.2. The band bending, $\psi(x)$, within the depletion layer is

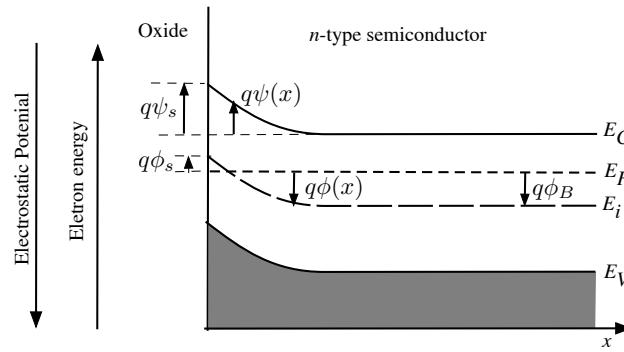


Figure 2.4.2.: Band diagram at the surface of a n -type semiconductor MOS structure.

defined as

$$\psi(x) = \phi(x) - \phi_B \quad (2.4.3)$$

and at the surface $\psi_s = \phi_s - \phi_B$, where ϕ_s is the surface potential which is given by the difference of the Fermi level and the intrinsic Fermi level at the surface. For n -type silicon $\phi_B > 0$ and ψ_s is negative if the bands bend upward, and positive when the bands bend downward. With the help of the potentials the electron and hole densities at the silicon surface n_s and p_s , respectively, are given by

$$n_s = n_i \exp\left(\frac{q\phi_s}{k_B T}\right) = N_D \exp\left(\frac{q\psi_s}{k_B T}\right) \quad (2.4.4)$$

$$p_s = n_i \exp\left(-\frac{q\phi_s}{k_B T}\right) = \frac{n_i^2}{N_D} \exp\left(-\frac{q\psi_s}{k_B T}\right) \quad (2.4.5)$$

When a voltage is applied to the gate with respect to the silicon, charge flows to the metal-oxide interface which has to be balanced by a charge of opposite polarity in the silicon. For the case of $V_G > 0$, as shown in Figure 2.4.3(a), the positive bias on the gate attracts electrons on the silicon surface. The bands will bend down so that $\phi_s > 0$ and $\psi_s > 0$. From (2.4.5) one obtains $n_s > N_D$ so that the surface charge consist of an electron accumulation layer.

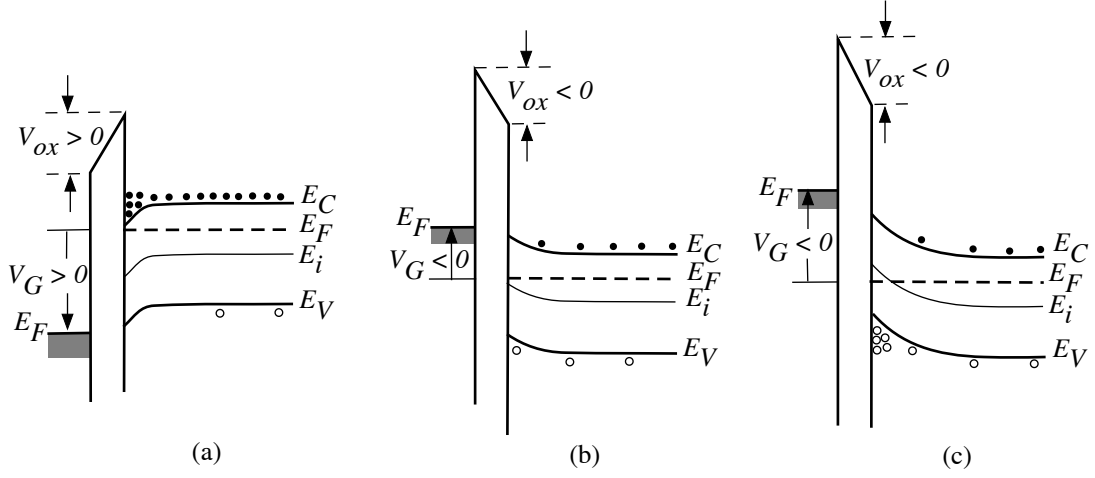


Figure 2.4.3.: Energy band diagram for n -type MOS-C (a) Accumulation (b) Depletion (c) Inversion

When $V_G = 0$, $\phi_s = \phi_B$ and $\psi_s = 0$. The band will be flat throughout the silicon. The charge-carrier densities at the surface are now $n_s = N_D$ and $p_s = n_i^2/N_D$, the same as in the bulk. This condition is called flatband.

When $V_G < 0$ the electrons are repelled from the silicon surface and holes are attracted, so that the bands bend up as shown in Figure 2.4.3(b). As long as $-\phi_B < \psi_s < 0$ the surface potential is $\phi_s > 0$ and the electron density at the surface is $n_i < n_s < N_D$. This mode is called depletion. At midgap $\psi_s = -\phi_B$ the surface is intrinsic with $n_s = p_s = n_i$. A further increase of $-\psi_s$ results in $p_s > n_s$ and an inversion layer of holes begins to form as shown in Figure 2.4.3(c). In the range of $-2\phi_B < \psi_s < -\phi_B$ this mode is called weak inversion. At $\psi_s = -2\phi_B$ the hole density is $p_s = N_D$ and a further increase of $-\psi_s$ results in an inversion layer.

For the calculation of the surface charge the Poisson equation for $\psi(x)$ has to be solved. The integration gives a relation between ψ and the electrical field

$$E = -\frac{\partial\psi}{\partial x} = \pm\sqrt{2}\frac{k_B T}{qL_D}F(\psi, N_D) \quad (2.4.6)$$

with the positive sign for $\psi \geq 0$ and the negative sign for $\psi < 0$. The extrinsic Debye length L_D , which is a characteristic length of a doped semiconductors, and $F(\psi, N_D)$ are defined as

$$L_D = \sqrt{\frac{\epsilon_0\epsilon_{Si}k_B T}{q^2 N_D}} \quad (2.4.7)$$

and

$$F(\psi, N_D) = \sqrt{\left[\exp\left(\frac{q\psi}{k_B T}\right) - \frac{q\psi}{k_B T} - 1 \right] + \left(\frac{n_i}{N_D}\right)^2 \left[\exp\left(-\frac{q\psi}{k_B T}\right) + \frac{q\psi}{k_B T} - 1 \right]}. \quad (2.4.8)$$

The surface electrical field E_s is given by substituting ψ_s for ψ into (2.4.8). Using Gauss's law the total surface charge Q_s per unit area in the silicon required to produce E_s is

$$Q_s(\psi_s) \equiv -\epsilon_0 \epsilon_{Si} E_s = \mp \frac{\sqrt{2} \epsilon_0 \epsilon_{Si} k_B T}{q L_D} F(\psi_s, N_D) \quad (2.4.9)$$

with negative sign for $\psi_s \geq 0$ and positive sign for $\psi_s < 0$.

In Figure 2.4.4 the variation of the surface charge density $|Q_s|$ as a function of band bending ψ_s for n -type silicon doped with $N_D = 1 \cdot 10^{12} \text{ cm}^{-3}$ ($\phi_B = 0.13 \text{ V}$) is shown. In the plot also the surface potential is shown on the top axis and on the right axis the oxide electrical field $|E_{ox}|$ which is calculated using the relation $|Q_s| = \epsilon_0 \epsilon_{ox} |E_{ox}|$. For $\psi_s > 0$ the surface charge is

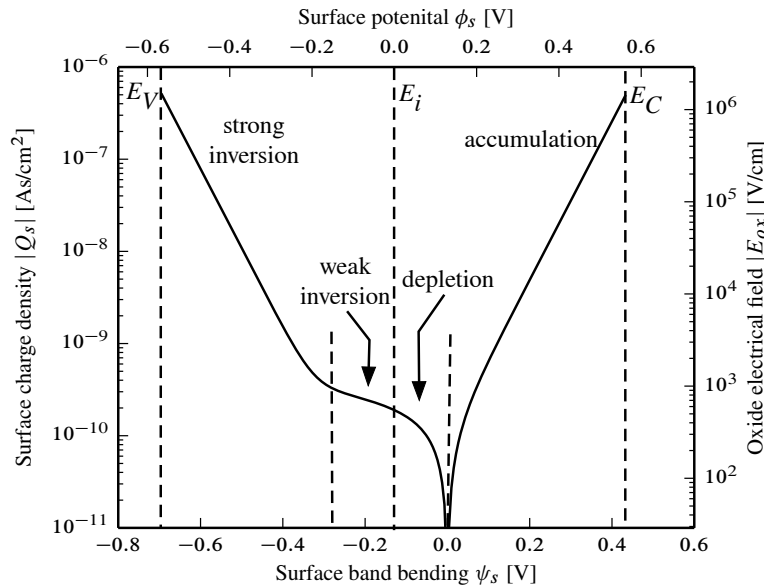


Figure 2.4.4.: Variation of the semiconductor charge density $|Q_s|$ as a function of band bending ψ_s for n -type silicon doped with $N_D = 1 \cdot 10^{12} \text{ cm}^{-3}$ ($\phi_B = 0.13 \text{ V}$) at 293 K.

negative (accumulation) and proportional to $Q_s \propto -\exp(q\psi_s/(2k_B T))$. For $-\phi_B < \psi_s < 0$ the charge is positive (depletion) and proportional to $Q_s \propto \sqrt{-\psi_s}$. For $\psi_s \ll -\phi_B$ (inversion) the charge is $Q_s \propto \exp(-q\psi_s/(2k_B T))$.

For the ideal MOS-C the gate voltage is the sum of the voltage across the oxide, V_{ox} , and the

voltage between the surface and the bulk of silicon

$$V_G = V_{ox} + \psi_s. \quad (2.4.10)$$

The voltage drop across the oxide is given by

$$V_{ox} = E_{ox}t_{ox} = -\frac{Q_s t_{ox}}{\epsilon_0 \epsilon_{ox}} = -\frac{Q_s(\psi_s)}{C_{ox}} \quad (2.4.11)$$

with the oxide capacitance per unit area

$$C_{ox} = \frac{\epsilon_0 \epsilon_{ox}}{t_{ox}}. \quad (2.4.12)$$

Therefore, (2.4.10) can be rewritten as

$$V_G(\psi_s) = \psi_s - \frac{Q_s(\psi_s)}{C_{ox}}. \quad (2.4.13)$$

When the Q_s and V_G are expressed as function of ψ_s the capacitance of the MOS-C can be obtained. The capacitance C is defined as the ratio of the charge increment dQ_m on the gate to the increment dV_G of the applied bias

$$C = \frac{dQ_m}{dV_G} = -\frac{dQ_s}{dV_G}. \quad (2.4.14)$$

From (2.4.13) it follows that the voltage increment dV_G is

$$dV_G = d\psi_s - \frac{dQ_s}{C_{ox}} \quad (2.4.15)$$

which leads in combination with (2.4.14) to

$$\frac{1}{C} = \frac{1}{C_{ox}} + \frac{1}{-dQ_s/d\psi_s} = \frac{1}{C_{ox}} + \frac{1}{C_s} \quad (2.4.16)$$

where

$$C_s = -\frac{dQ_s}{d\psi_s} \quad (2.4.17)$$

is the depletion layer capacitance. C_s can be calculated by the following expression

$$C_s(\psi_s) = \frac{\epsilon_0 \epsilon_{Si}}{\sqrt{2}L_D} \left| \frac{\exp\left(\frac{q\psi_s}{k_B T}\right) - 1 + \left(\frac{n_i}{N_D}\right)^2 \left(1 - \exp\left(-\frac{q\psi_s}{k_B T}\right)\right)}{F(\psi_s, N_D)} \right|. \quad (2.4.18)$$

From (2.4.16) it is clear that the ideal MOS-C is the series combination of the oxide capacitance

and the depletion layer capacitance. Using the equations (2.4.18), (2.4.16), (2.4.9) and (2.4.13) the ideal capacitance-voltage (C - V) curve can be calculated in the following way. For each value of ψ_s calculate

1. C_s , the depletion region capacitance, using (2.4.18),
2. C , the total capacitance, using (2.4.16),
3. Q_s , the surface charge, using (2.4.9),
4. finally the gate voltage V_G using (2.4.13).

This gives for every chosen ψ_s the point (V_G, C) which can then be drawn.

The behavior of the ideal C - V in the different biasing region can be describes as follows: In accumulation $\psi_s > 0$ and $C_s \propto \exp(q\psi_s/(k_B T))$, which means that C_s becomes very large. Thus, in accumulation

$$C \approx C_{ox} \quad (\text{accumulation}). \quad (2.4.19)$$

Decreasing the gate voltage from accumulation toward depletion decreases the charge at the interface and thus C_s . To calculate the flatband capacitance C_{FB} of the MOS-C the depletion layer capacitance C_s has to be evaluated for $\psi_s \rightarrow 0$ which gives

$$C_{s,FB} = \frac{\epsilon_0 \epsilon_{Si}}{L_D} \quad (2.4.20)$$

resulting in

$$C_{FB} = \left(\frac{1}{C_{ox}} + \frac{L_D}{\epsilon_0 \epsilon_{Si}} \right)^{-1}. \quad (2.4.21)$$

In accumulation and depletion mode the capacitance is practically frequency independent. In inversion the capacitance is frequency dependent due to the response of the minority carriers which form the inversion layer. The concentration of minority carriers can change only as fast as carriers can be generated within the depletion region near the surface. For sufficiently low frequencies the minority carries can follow the AC signal resulting in the low frequency (lf) or DC curve. However, when the AC signal frequency is too high so that the minority carries cannot follow, it results in the high frequency (hf) curve. The expression for C_s in (2.4.18) was derived under equilibrium conditions and is therefore the lf depletion layer capacitance. From the behavior for large $-\psi_s$ one sees that the C_s is increasing so that the lf capacitance in inversion is just that associated with the charge layer on either side of the oxide

$$C \approx C_{ox} \quad (\text{inversion lf}). \quad (2.4.22)$$

The expression for C_s in the hf case can be derived by ignoring the minority carrier terms in

(2.4.18) and is given by

$$C_s^{hf}(\psi_s) = \frac{\epsilon_0 \epsilon_{Si}}{\sqrt{2} L_D} \frac{\left| \exp\left(\frac{q\psi_s}{k_B T}\right) - 1 \right|}{\sqrt{\exp\left(\frac{q\psi_s}{k_B T}\right) - \frac{q\psi_s}{k_B T} - 1}}. \quad (2.4.23)$$

At inversion the inversion layer charge can be assumed to be constant for a given DC bias and the AC-voltage of the capacitance bridge will result in an oscillation of the maximum steady-state depletion layer width. Changing the DC bias will increase the inversion layer charge but will not change the steady-state width and thus the capacitance. So the capacitance will be constant. Assuming that the maximum depletion layer width is reached at the onset of strong inversion $\psi_s \approx -2\phi_B$ results in the depletion layer capacitance

$$C_s^{hf} = \sqrt{\frac{\epsilon_0 \epsilon_{Si} q N_d}{4\phi_B}} \quad (\text{inversion hf}). \quad (2.4.24)$$

A more accurate approximation uses the optimal match point, v_m , which is for n -type silicon

$$v_m = -2.098\phi_B - \frac{k_B T}{q}(2.08 - 0.75) \quad (2.4.25)$$

and uses (2.4.23) with $C_s^{hf}(v_m)$ for $\psi_s \leq v_m$.

A different C - V curve is obtained if the MOS-C is swept from accumulation to the inversion region at a sufficiently fast rate so that there is not enough time for the thermal generation of the inversion charge carriers (minority carriers). This is a non-equilibrium situation in which the depletion width increases with gate bias until avalanche breakdown occurs. In this case the capacitance will continue to drop following the depletion curve and become fixed for gate biases beyond avalanche breakdown because then minority carriers are produced rapidly. The resulting C - V curve is called deep depletion (dd) curve. Thus the kind of curve (lf,hf,dd) depends on the AC frequency and the DC sweep rate.

To give an example of ideal C - V curves on a high-ohmic silicon bulk in Figure 2.4.5 1-D model calculations for different frequencies for a MOS-C with $t_{ox} = 380$ nm, doping concentration of $N_D = 1 \cdot 10^{12} \text{ cm}^{-3}$ and a silicon thickness of $285 \mu\text{m}$ are shown. The model implements the equivalent circuit presented in [35] which includes also the generation in the depletion layer and the resistance of the quasi-neutral silicon bulk R_s . Shown is the parallel capacitance. For frequencies ≤ 1 kHz the capacitances in accumulation are practical independent of frequency. The decrease of the capacitance in accumulation for increasing frequency is due to the series resistance R_s of the quasi-neutral silicon bulk. The condition for the series resistance to be negligible in the capacitance measurement is $\omega R_s C \ll 1$ which is not satisfied for high frequencies. With the exception of the 1 MHz curve the same capacitances are expected in the depletion region. As mention above the behavior in inversion depends on how fast minority

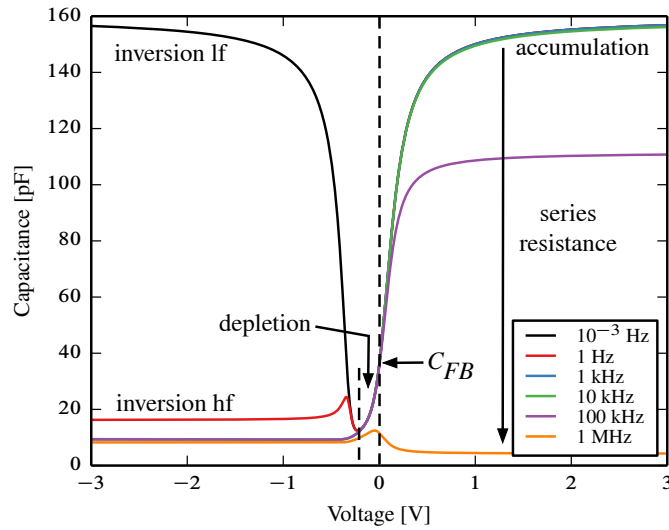


Figure 2.4.5.: Ideal C - V curves of a MOS-C with $t_{ox} = 380$ nm on a high-ohmic silicon bulk with a doping concentration of $N_D = 1 \cdot 10^{12} \text{ cm}^{-3}$. The equivalent circuit consists of the series combination of C_{ox} , C_s and R_s , which is the resistance of the quasi-neutral silicon bulk. Shown are the parallel capacitances.

carrier can be generated in the depletion layer. Using a life time of 0.75 ms in the model calculation shows that only the 10^{-3} Hz curve is a low frequency curve. In such a case a quasi-static measurement has to be performed.

2.4.2. Gate-controlled diode

A gate-controlled diode (GCD) is a three-terminal device used mainly for the characterization of surface effects, especially of the surface current due to interface traps. As shown schematically in Figure 2.4.6 the GCD consists of a diode in combination with a MOS capacitor. On n -doped silicon the diode is formed by a p^+ region and usually the gate slightly overlaps the p^+ region to prevent potential barriers. But also designs with a gap between the p^+ region and the gate are used. Common designs of GCDs are with a circular diode surrounded by a circular gate ring or finger structure.

The measurement of the surface current, I_{surf} , is usually done in the following way. A reverse bias voltage, V_D , is applied to the diode to partially deplete the silicon bulk and the gate voltage, V_G , is changed to change the field in the silicon region below the Si-SiO₂ interface under the gate from accumulation to depletion toward inversion. The current is measured on the backside.

In accumulation ($V_G > V_{FB}$), as shown Figure 2.4.6(a), the electrons accumulate below the Si-SiO₂ interface. In this case the measured current is the sum of the generation current in the depletion region around the p^+ - n junction, I_{scr} , and the diffusion current from the quasi-neutral

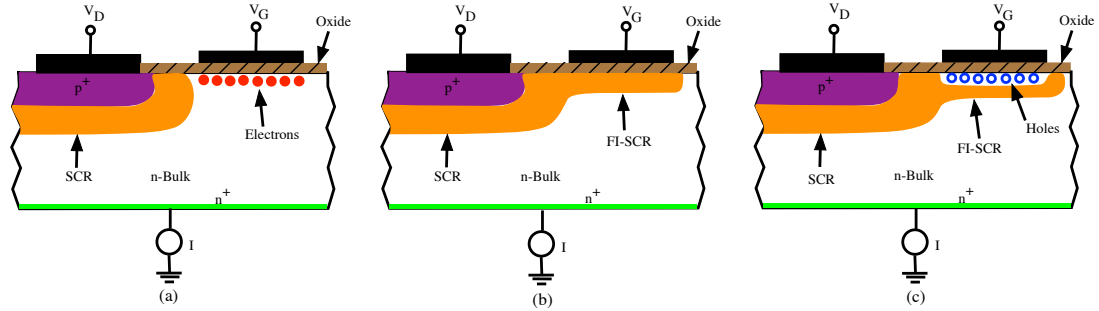


Figure 2.4.6.: Cross section and operation principle of a gate-controlled diode. (a) Accumulation (b) Depletion (c) Inversion

silicon region, I_{diff} , thus $I_{scr} + I_{diff}$.

With decreasing voltage at $V_G < V_{FB}$ the silicon region below the gate starts to deplete as shown in Figure 2.4.6(b). Thereby a field induced space charge region is formed which gives an additional current contribution, I_{fi-scr} . Because the interface traps are exposed to an electrical field they generate the surface current I_{surf} . The measured current in depletion is thus given by $I_{surf} + I_{scr} + I_{fi-scr} + I_{diff}$.

A further decrease toward inversion leads to the formation of the inversion layer below the interface, which shields the interface traps and suppresses the contribution of the surface current. The current measured in inversion is hence $I_{scr} + I_{fi-scr} + I_{diff}$. From the current contribution in the different bias region the surface current can be extracted by the difference of the peak current in depletion and the current in inversion.

In Figure 2.4.7 a nearly ideal I - V curve of a gate-controlled diode on n -type silicon with $V_{diode} = -6$ V is shown. The dashed line in depletion indicates the current without the surface contribution. This current is slightly increasing from accumulation to inversion due to the increase of the field induced depletion layer. For a gate-controlled diode the condition of the strong inversion is different compared to the condition for MOS capacitor which is $\psi_s = -2\phi_B$. In the case of the gate-controlled diode the condition is $\psi_s = -2\phi_B + V_D$. The reason is that the p^+ region close to the gate extracts holes from the interface which modifies the electrical field and the potential, and creates a non-equilibrium situation.

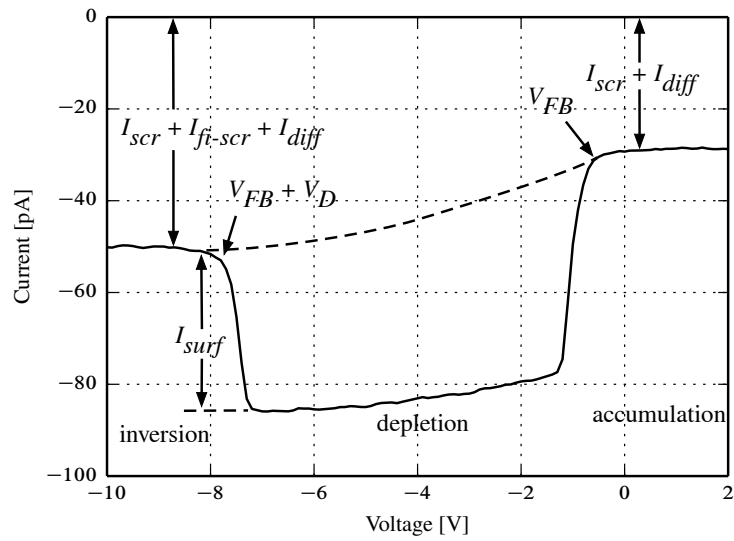


Figure 2.4.7.: Measured I - V curve of a gate-controlled diode on n -type silicon with $V_{diode} = -6$ V.

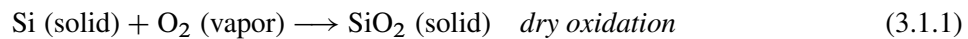
3. Effects of X-ray radiation on the Si-SiO₂ system

For the understanding of the X-ray radiation damage on the Si-SiO₂ system in the first section of this chapter the properties and defects of the as-processed SiO₂ and Si-SiO₂ interface are presented. Then the basic mechanisms of the build up of the radiation induced surface damage are described. In the last section of this chapter the effects on a MOS capacitor and the extraction of the radiation damage parameters are described.

3.1. Properties of SiO₂ and the Si-SiO₂ interface

3.1.1. Silicon dioxide

The success of silicon devices using the planar processes relies strongly on the possibility to passivate the surface with an oxide layer. A SiO₂ layer is easily grown thermally on silicon or deposited by different methods. Most often the thermal growth is used in which the silicon is exposed to an oxidizing ambient at elevated temperatures (typically 900°C to 1200°C). Two basic reaction schemes are used [36]: dry and wet oxidation



The oxidation reaction occurs at the Si-SiO₂ interface. Thus, as the oxide grows, silicon is consumed and the interface moves into the silicon. The amount of consumed silicon is $\approx 44\%$ of the final oxide thickness. The wet oxidation is much faster than the dry one. The oxidation rate depends on the crystal orientation, temperature, pressure, dopants and gas mixture (e.g. addition of HCl).

Thermal SiO₂, grown under conventional conditions are vitreous (glassy), that is, it exhibits a short-range order [37]. Often the distinction between vitreous and amorphous is not made and one says amorphous oxide. The short-range order is centered around the structural formula of a material which is SiO₄⁴⁻. So, the structure is based on a tetrahedron consisting of a silicon atom at the center and four oxygen atoms at the corners (Figure 3.1.1(a)). This tetrahedra is characterized by the distance between the atoms Si-O and O-O, as well the bond angle Si-O-Si. In the case of crystalline SiO₂ two neighboring tetrahedra share an O atom which is called bridging oxygen

3. Effects of X-ray radiation on the Si-SiO₂ system

and the bond angle is fixed. In the vitreous state, however, a continuous random network of linked Si-O-Si bonds is formed where the bond angle varies from 110 to 180° with a mean value around 144°. Furthermore some of the tetrahedra will have non-bridging ions. As only 43% of the space is occupied, diffusion of foreign atoms through the network will be easy. A schematic representation of the network of vitreous SiO₂ is shown in Figure 3.1.1(b) including network formers (P⁵⁺, B³⁺), bridging and non-bridging oxygen, and network modifiers (Na⁺, K⁺).

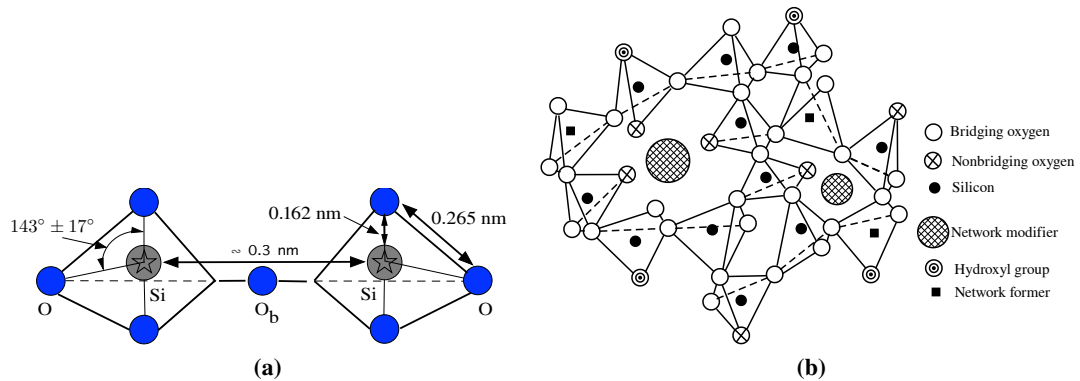


Figure 3.1.1.: (a) Typical dimensions of the SiO₄ tetrahedra of amorphous SiO₂. Picture adapted from [37] (b) Structure of vitreous SiO₂. Picture adapted from [36].

The defects in vitreous silicon oxide are classified into three categories: microheterogeneities, point defects and complex defects [37]. Microheterogeneities corresponds to variations of the bond angle or the distance of the Si-O leading to a change in the network structure without causing its rupture. Point defects in the vitreous SiO₂ are defined in a similar way as in a monocrystal by an imperfection that disturbs the short-range order. They can be intrinsic (vacancies, interstitials) if they are only related to atoms of the original network (Si or O) or extrinsic if they are due to foreign atoms. Complex defects are combinations of several point defects. For a detailed overview see [37].

Using Electronic Paramagnetic Resonance (EPR) spectroscopy the microscopic structure of a number of intrinsic defects could be identified. From all these defects it was found that for radiation damage the most important are the so called E' centers which are linked to an oxygen vacancy [38, 39]. The oxygen vacancy which can be represented by O₃ ≡ Si-Si ≡ O₃ is diamagnetic and electrically neutral [40]. Thus it cannot be detected by EPR or by electrical methods. However, a hole can get trapped on the vacancy and modifies the defects structure. After hole trapping, one of the silicon atoms possesses an unpaired electron, located on a sp³ dangling orbital and remains in a tetrahedral configuration. The other silicon atoms carry the trapped positive charge (the trapped hole) and relax in the plane of its three remaining oxygen neighbors, as shown in Figure 3.1.2. The asymmetrical relaxation is possible thanks to the flexibility of the Si-O-Si bond. Due to the unpaired electron the defect is paramagnetic and

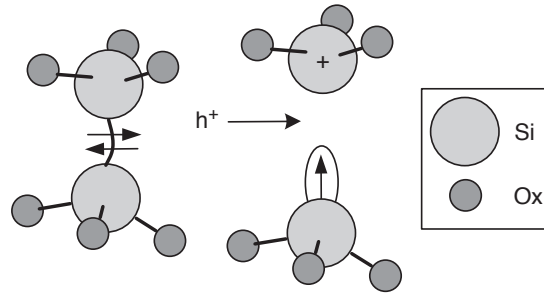


Figure 3.1.2.: Model for hole trapping and E' center formation in SiO₂. Picture taken from [41].

detectable by EPR. The defects build on an asymmetric relaxed oxygen vacancy are called E' centers. Depending on the immediate environment of the two silicon atoms, different types of defects are created. A commonly in irradiated thermal oxide identified variant is the E'_γ center which is obtained by the sole trapping of a hole on an oxygen vacancy. The creation can be written as:



where "•" represents the unpaired electron. As in thermal oxide the precursor (the neutral oxygen vacancy) exists prior to irradiation, they occur usually in greatest density close to the Si-SiO₂ interface. This is due to the lattice mismatch between the silicon bulk and the oxide, or due to out-diffusion during high-temperature inert anneal of oxygen from the oxide into interstitial sites in the Si substrate [42]. For detailed discussions about the E' centers in irradiated MOS device see [41].

3.1.2. Si-SiO₂ interface

At the Si-SiO₂ interface is a 0.5 nm to 3 nm thick transition region between the silicon crystal and the stoichiometric silicon dioxide network [43]. The composition of the transition region is largely controlled by details of the process chemistry. Interface states are the result of the structural imperfection at the silicon surface due to the termination of the silicon crystal periodicity and the discontinuity of the potential. As silicon is in the bulk tetrahedrally bonded with each Si atom to four Si atoms in a freshly-cleaved crystal one bond will be cut leaving an "dangling" bond. The density of silicon atoms at the surface is $\approx 10^{15} \text{ cm}^{-2}$ resulting in the same amount of dangling bonds. This will be reduced when the silicon is oxidized since most of the Si atoms will be bond to oxygen at the surface, some will bond to hydrogen but as shown in Figure 3.1.3 some will remain unbonded.

Under the term interface trap or P_b center one usually understands an interface trivalent Si atom with an unsaturated (unpaired) valence electron denoted by Si₃ ≡ Si[•]. The P_b center was identified by ESR as a paramagnetic dangling bond [44]. As shown in Figure 3.1.3(a) in the case of (111)-oriented silicon the unbounded central atom orbital of the P_b center is perpendicular to

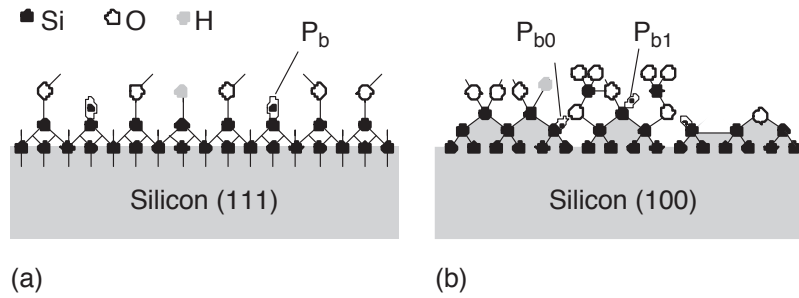


Figure 3.1.3.: Structural model of (a) (100) Si surface (b) (111) Si surface. Picture taken from [41].

the Si-SiO₂ interface. In (100)-oriented silicon two defects, P_{b0} and P_{b1}, shown in Figure 3.1.3(b) where identified. Both defects are chemical identical to the P_b.

The interface traps are electrically active acting as generation and recombination centers. Their energy is distributed throughout the Si bandgap. A schematic illustration of the P_{b0} and P_{b1} densities of states, D_{it} [1/(eV · cm²)], is shown in Figure 3.1.4. The distribution of P_b is nearly identical to the distribution of P_{b0}. The P_b centers are amphoteric defects having two

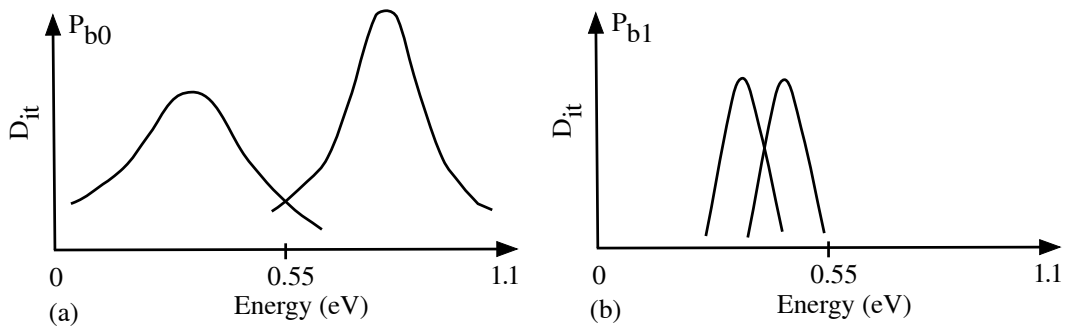


Figure 3.1.4.: A schematic illustration of the (a) P_{b0} and (b) P_{b1} densities of states. Sketch adapted from [41].

levels in the silicon bandgap [41]. The P_b and P_{b0} defects levels are centered approximately around midgap with the acceptor (0/-) level about 0.3 eV above midgap, the donor (+/0) level about 0.3 eV below midgap and an electron correlation energy of $\approx 0.6-0.7$ eV. The distribution is relatively wide and can be in principle explained by bond-angle variations. For the P_{b1} the electron correlation energy is roughly 0.3 eV, the distribution is narrower and slightly shifted (by several tenths of an electron volt) below midgap.

As the dominant interface traps are the P_b centers it is commonly assumed that interface traps are acceptor-like in the upper half and donor-like in the lower half of the band gap [41, 45]. As shown in Figure 3.1.5(a) for an *n*-type MOS at flatband the electrons occupy states below the Fermi energy. Therefore the states in the lower half of the bandgap are neutral (occupied donors). The states between midgap and the Fermi energy are negatively charged (occupied

acceptors) and the states above the Fermi energy are neutral (unoccupied acceptors). Biasing in accumulation bends the bands down and thus increases the number of occupied acceptors. In inversion, Figure 3.1.5(b), the fraction of interface traps between midgap and the Fermi level consists now of unoccupied donors, leading to a positively charged interface.

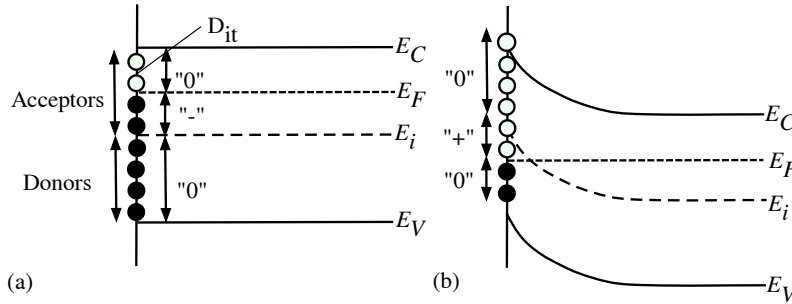


Figure 3.1.5.: Band diagrams of the *n*-type MOS with acceptor-like in the upper half and donor-like in the lower half of the band gap. (a) Flatband (b) Inversion. Picture adapted from [41].

It should be mentioned that after the thermal growth of the oxide the interface trap density is still too high for the practical usage of MOS devices. To reduce the interface trap density the MOS device is often subject to a post metallization anneal or to a forming gas anneal, for which the reaction models



and



have been suggested [46, 47].

3.1.3. Nomenclature of oxide charges associated with thermally oxidized silicon

The different types of the charges in the oxide were classified in 1979 and a standard terminology was proposed [48]. These charges are as shown in Figure 3.1.6: 1) Mobile ionic charge, 2) Fixed oxide charge, 3) Oxide trapped charge, and 4) Interface traps. Later Fleetwood [49] suggested to add the term border traps as shown at the left boundary of Figure 3.1.6. In each case, Q denotes the net effective charge per unit area at the Si-SiO₂ interface (C/cm²). Further N the net effective number of charges per unit area (1/cm²) and D_{it} are given in 1/(eV · cm²) are used.

Mobile ionic charge (Q_m, N_m): Primarily due to ionic impurities such as Na⁺, K⁺, Li⁺, and possibly H⁺. Negative ions and heavy metals may contribute to this charge. Sodium is the dominant contaminant and was a problem for MOSFETs in the 1960s. The ionic charge is relatively mobile in the oxide and can lead to gate bias instabilities.

Fixed oxide charge (Q_f, N_f): This is a positive charge in the transition region of the Si-SiO₂ interface, which does not change their charge state by exchange of mobile carriers with the

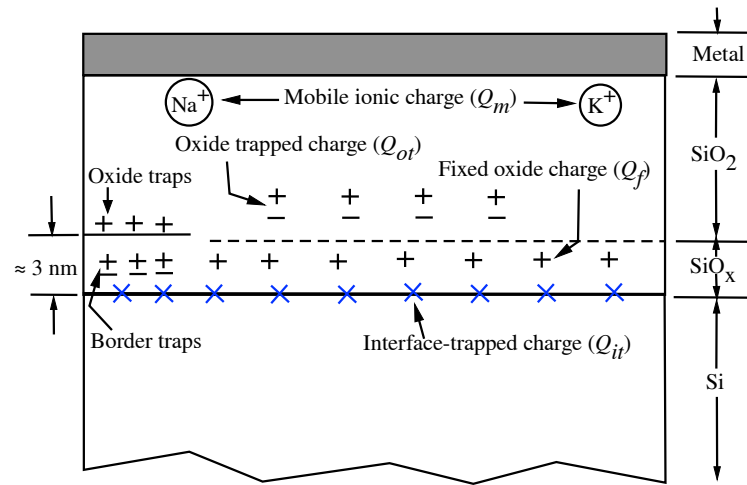


Figure 3.1.6.: Terminology for the charges associated with thermally oxidized silicon.

silicon. The charge density is process related and depends on the oxidation ambient, temperature and cooling rate as well as the crystal orientation. The dependence of the fixed charge on the temperature, oxidation and annealing in nitrogen or argon is known as the "Deal-triangle" [50]. For a recent quantitative model relating the formation of the fixed charge in silicon dioxide to generation of silicon interstitials during thermal oxidation see [51].

Oxide-trapped charge (Q_{ot}, N_{ot}): This charge may be positive or negative due to holes or electrons trapped in the bulk of the oxide. Trapping may result from ionizing radiation, avalanche injection or similar processes. Different to fixed oxide charges, oxide trapped charges can be sometimes annealed by low-temperature (< 500°C) treatment, although neutral traps may remain.

Interface-trapped charge (Q_{it}, N_{it}, D_{it}): These are positive or negative charges, due to structural defects, oxidation-induced defects, metal impurities, or other defects caused by radiation or similar bond-breaking processes. The interface-trapped charges are located at the Si-SiO₂ interface. Unlike fixed charges or trapped charges, interface-trapped charges are in electrical communication with the underlying silicon and can thus be charged or discharged, depending on the surface potential.

Border traps (Q_{bt}, N_{bt}): These traps have been also designated as slow states, near-interface oxide traps, switching oxide traps, and by other names. The border traps are those near-interfacial oxide traps located within approximately 3 nm of Si-SiO₂ interface. There is no distinct depth limit, however, border traps are considered to be those traps that can communicate with the semiconductor through capture and emission of electrons and/or holes on the time scale of interest of measurement. The switching time of slower border traps are ~ 1 s, whereas fast border traps can have switching times between ~ 10⁻⁶s and ~ 1 s [52] and can be confused with interface traps (P_b centers) in C-V measurements.

3.2. Basic mechanisms of the build up of radiation-induced surface damage

The basic mechanisms of the build up of radiation-induced surface damage are depicted in Figure 3.2.1 and are well described in [45, 53–58]. Figure 3.2.1 shows the bandgap diagram of a MOS capacitor with positive bias applied on the gate. The ionizing radiation, in our case X-rays, create electron-hole pairs in the SiO_2 . Immediately after the electron-hole pairs are created, most of the electrons will rapidly drift toward the gate and the hole will drift toward the Si-SiO₂ interface. However, even before the electrons can leave the oxide some of them will recombine with holes. Those holes which escape the initial recombination will be transported through the oxide toward the Si-SiO₂ interface by hopping through localized states in the oxide. As the holes approach the interface some will be trapped forming positive oxide-trap charge. It is believed that holes during hopping or as they are trapped can release hydrogen ions (protons) which will also drift to the Si-SiO₂ interface where they may react to form interface traps. In the rest of this section some more details of the above processes are summarized.

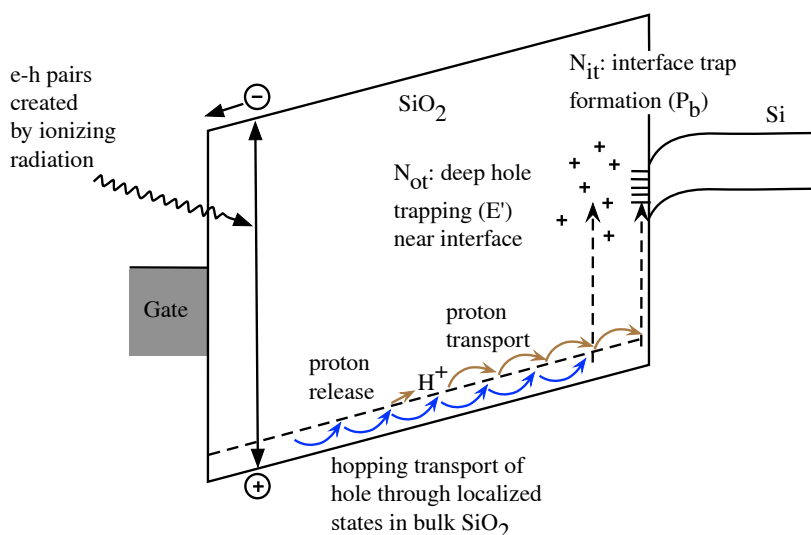


Figure 3.2.1.: Band diagram of an MOS capacitor with a positive gate bias. Illustrated are the main processes for radiation-induced charge generation. Pictures adapted from [58].

Generated electron-hole pairs: The number of generated electron-hole pairs by the ionizing particles depends on the average energy required for creating an electron-hole pair, E_p . For silicon dioxide this value is $E_p = 17 \text{ eV}$ with a uncertainty of 1 eV, so that some authors also use the older value 18 eV [53]. From this value the initial electron-hole pair density per unit dose, g_0 , is easily determined to be $8.2 \cdot 10^{14} \text{ cm}^{-3} \text{ Gy}^{-1}$.

One mechanism which affects the total number of generated electron-hole pairs in the SiO_2 is the dose enhancement. In a MOS capacitor this problem arises due to the adjacent Al and Si

which are materials with a different atomic mass and cross sections than SiO₂. The effect is largest for low-energy photons, because most of the energy deposition is actually by secondary electrons. The point is that the charged particle equilibrium (CPE), which means that the number of secondary electrons scattering into any increment of volume is equal to the number of electrons scattering out, is not maintained because more secondary electrons cross an interface from the high-Z side than from the low-Z side [56]. For oxide thicknesses of less than 100 nm the doses enhancement for 10-keV X-rays can be relatively large (≈ 1.7), whereas for thick oxides of 500 nm it is ≈ 1.2 .

Charge yield: The fraction of holes escaping recombination, $f_y(E_{ox})$, is a function of the magnitude of the electrical field in the SiO₂, acting to separate the electron and holes, and the initial density of electron-hole pairs created by the incident radiation. The pair line density is determined by the linear energy transfer (LET), and is, therefore, a function of the incident particle type and energy. The line density is also inversely proportional to the average separation distance between electron-hole pairs. Therefore the higher the line density the smaller the separation and thus more recombination at a given electrical field. This effect can be seen in Figure 3.2.2 where the fraction of unrecombined holes (charge yield) is shown for different particles as function of electrical field. As in general, strongly ionizing particles form dense charge columns the recombination is higher than for the weakly ionizing particles which forms relatively isolated charge pairs.

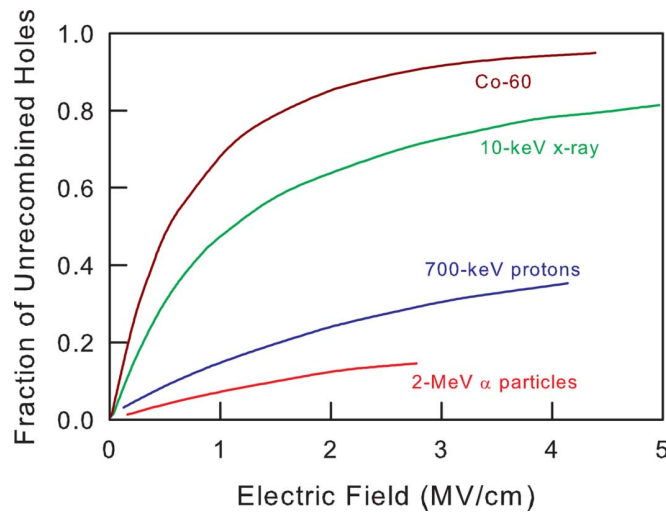


Figure 3.2.2.: The fraction of holes that escape initial recombination for different particle. Picture taken from [58].

For 10 keV X-rays the charge yield can be approximated by

$$f_y(E_{ox}) = \left[1 + \frac{E_c}{E_{ox}} \right]^{-m} \quad (3.2.1)$$

where $m = 0.9$ and $E_c = 1.35 \text{ MV/cm}$ [54] and the number of holes escaping the initial recombination, N_h , for a given dose, D , and a given oxide thickness, t_{ox} , is

$$N_h = f_y(E_{ox})g_0Dt_{ox} \quad (3.2.2)$$

where the dose enhancement is neglected.

Hole transport: The electron mobility in SiO_2 at room temperature is about $20 \text{ cm}^2\text{V}^{-1}\text{s}^{-1}$, so that not recombined electrons can easily leave the oxide. The mobility of holes is typically 10^{-4} – $10^{-11} \text{ cm}^2\text{V}^{-1}\text{s}^{-1}$ and the transport is very slow. Depending on the field direction the hole can move to the Si-SiO₂ interface or to the gate. The hole transport is dispersive and temperature and oxide thickness dependent. The transport is explained by polaron hopping [58]. Due to its charge the moving hole will polarize its local environment forming a polaron. The polaron increases the effective mass and decrease the mobility.

Oxide traps: From etchback measurements it is found that close to the Si-SiO₂ interface a large number of oxygen vacancies exist [42]. As shown in section 3.1.1 the oxygen vacancies acts as a trapping center. Therefore, as holes approach the Si-SiO₂ interface a fraction of them will be trapped. The fraction of trapped holes depends on the capture cross-section, which is field and process dependent. In radiation-hard oxide only a few percent will be trapped, whereas in soft oxide 50 to 100% can be trapped [58]. Oxide trapped holes are relatively stable but they undergo a long-term annealing. In general the annealing can be due the tunneling of electrons from the silicon into either oxide traps or electron traps associated with trapped holes, and/or the thermal emission of electrons from the oxide valence band into oxide traps [56].

As mentioned in the previous section border traps are those traps close to the interface which can communicate with the silicon. One kind of border traps associated with the oxygen vacancy was suggested by Lelis [59, 60] after switch bias annealing studies and is shown in Figure 3.2.3. In this model the trapping of a hole results in an E'_y center. Instead of that an electron during annealing tunnels to the positively charged Si and neutralizes it to reform the Si-Si bond, it tunnels to the neutral Si forming a dipole structure, where the electron can tunnel back and forth to the substrate in response to bias change. This defect model is today important in the modeling of bias temperature instability in MOS devices [61].

Interface traps: The build-up of interface traps is a relatively slow process compared to the build-up of oxide-trapped charges. For the build-up of interface traps several different mechanisms have been proposed which break the Si-H bond of a passivated dangling bond. In Figure 3.2.4 a relative complete picture of suggested electrical and chemical radiation-induced processes is shown. The mechanisms are based on the liberation of species linked to hydrogen, such as H^0 or H^+ . The different mechanisms can explain observed field dependences in the build-up of the interface traps. For a detailed discussion see [53].

High-dose effects: If the dose is high enough the accumulated oxide traps results in a space charge which alters the oxide electrical field. Under positive gate bias the accumulation of positive charge in the oxide enhance the electrical field between the space-charge region and

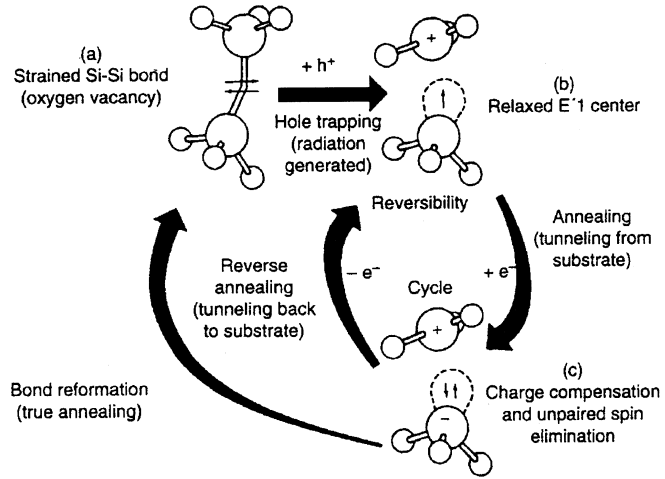


Figure 3.2.3.: Model of hole trapping, permanent annealing, and compensation processes. Picture taken from [56].

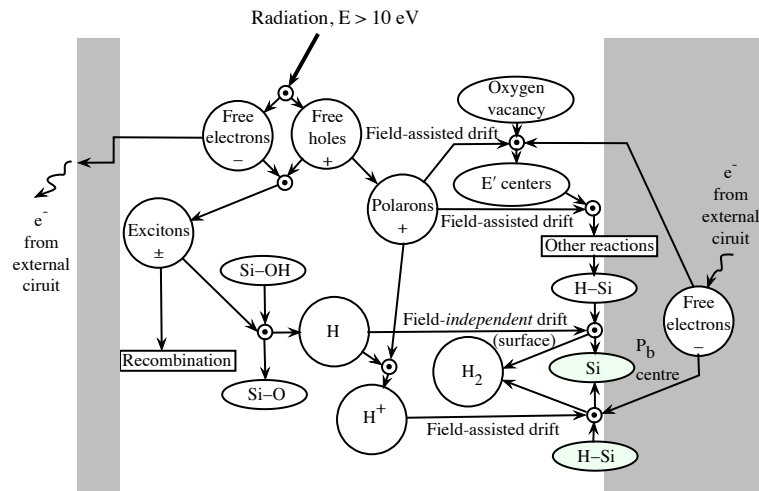


Figure 3.2.4.: Diagram of electronic and chemical processes induced by irradiation in MOS structures of SiO₂ and its interface with silicon. Picture adapted from [62].

the silicon and even reduces the electrical field between the space-charge and the gate to almost zero. The altered local oxide field will, in turn, alter the local charge yield and lead to enhanced recombination of electrons and trapped holes. For simulations of this effects see [54].

Dose-rate effects: Similar, simulations in [63] for an oxide thickness of 600 nm and a low applied field show that at high dose rates an electric field reversal and a resultant low field region in the oxide bulk occurs which results in a space charge limited transport. This can lead to a reduced built up of interface traps [64].

3.3. Effects on MOS

3.3.1. Radiation damage parameters

As seen in section 3.1.3 in the oxide and at the interface different type of charges exists. Instead of referring to the individual charge contributions it is convenient to define an equivalent sheet of charge center density N_{ox} located at the Si-SiO₂ interface by

$$N_{ox} = N_f + N_m + N_{ot} \quad (3.3.1)$$

and which is called oxide charge density. For the fixed oxide charge one can assume that it is located directly at the interface, whereas the oxide-trapped charge and mobile ionic charge are distributed in the oxide bulk, so that

$$N_{ot} = \frac{1}{t_{ox}} \int_0^{t_{ox}} x \rho_{ot}(x) dx \quad (3.3.2)$$

and

$$N_m = \frac{1}{t_{ox}} \int_0^{t_{ox}} x \rho_m(x) dx \quad (3.3.3)$$

where ρ_{ot} and ρ_m are the volume densities of the oxide-trapped charge and mobile ionic charge, respectively and where the zero point of the integration is at the gate and t_{ox} the oxide thickness.

The interface traps are characterized by the interface-state density $D_{it}(E_t)$, the cross sections $\sigma_n(E_t)$ and $\sigma_p(E_t)$, and the type (acceptor, donor or amphoteric). The interface-trap density N_{it} is the integral of $D_{it}(E_t)$ over the bandgap:

$$N_{it} = \int_{E_V}^{E_G} D_{it}(E_{it}) dE_{it}. \quad (3.3.4)$$

As described in section 2.2.5 interface traps generate surface current. From (2.2.44) one finds the surface-current density, J_{surf} , is related to the surface generation velocity s_0 by

$$J_{surf} = q n_i s_0. \quad (3.3.5)$$

Thus measuring the surface current I_{surf} with a gate-controlled diode and knowing the gate area the surface generation velocity can be determined. That this so determined surface generation velocity is gate length dependent and typically less than the true surface-generation velocity is shown in [65, 66]. The main reason is that the assumption of a constant quasi Fermi level of the minority carriers beneath the gate is not valid.

3.3.2. MOS capacitor with oxide charges and interface traps

Due to the presence of oxide charges, interface traps and other effects like lateral nonuniformities or a polysilicon gate, the measured C - V curves of a real MOS capacitor deviate from the ideal curves. In the case of oxide charges and interface traps the charge conservation requires that the charge on the gate Q_G has to be balanced by the total space charge below the interface Q_s given by (2.4.9), the oxide charges Q_{ox} and the charge stored in the interface traps Q_{it} so that

$$Q_G = -(Q_s + Q_{ox} + Q_{it}). \quad (3.3.6)$$

Using this the relation between the gate voltage and the band bending can be written as

$$V_G(\psi_s) = \psi_s + \Phi_{MS} + V_{ox}(\psi_s) \quad (3.3.7)$$

$$= \psi_s + \Phi_{MS} - \frac{Q_{ox}}{C_{ox}} - \frac{Q_s(\psi_s)}{C_{ox}} - \frac{Q_{it}(\psi_s)}{C_{ox}} \quad (3.3.8)$$

where here also the work function difference Φ_{MS} is taken into account. The charge stored in the interface traps depends on the band bending and the type of the interface traps, and can be written according to [20] as

$$Q_{it}(\psi_s) = \begin{cases} -q \int_{E_G}^{E_C} D_{it}(E_{it}) f_{it}^0(E_{it}, \psi_s) dE_{it} & \text{for acceptors} \\ q \int_{E_V}^{E_G} D_{it}(E_{it}) (1 - f_{it}^0(E_{it}, \psi_s)) dE_{it} & \text{for donors} \end{cases} \quad (3.3.9)$$

where $f_{it}^0(E_{it}, \psi_s)$ is the occupation probability of a trap at the energy E_{it} and at a band bending ψ_s which is:

$$f_{it}^0(E_{it}, \psi_s) = \frac{1}{1 + \exp \frac{E_{it} - q\psi_s - E_F}{k_B T}} \quad (3.3.10)$$

From the arguments in (3.3.10) one finds that $f_{it}^0(E_{it}, \psi_s) = 1/2$ for $E_{it} = q\psi_s + E_F$ which is the energy level at the interface which is opposed to the Fermi level.

The interface traps can interact with the conduction band by capture or emission of electrons and with the valence band by capture or emission of holes. The relevant equivalent circuit for an n -type MOS capacitor with single-energy level interface traps is shown in Figure 3.3.1. C_D

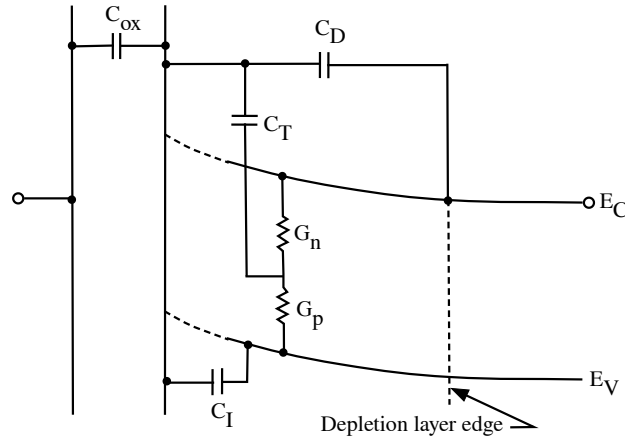


Figure 3.3.1.: Equivalent circuit of a n -type MOS capacitor with single-energy level interface traps. Picture adapted from [20].

represents the depletion layer capacitance and C_I the inversion layer capacitance. The traps are characterized by the trap capacitance

$$C_T = \frac{q^2}{k_B T} N_T f_{it}^0 (1 - f_{it}^0) \quad (3.3.11)$$

and the capture conductances

$$G_n = \frac{q^2}{k_B T} N_T c_n n_s (1 - f_{it}^0) \quad (3.3.12)$$

$$G_p = \frac{q^2}{k_B T} N_T c_p p_s f_{it}^0 \quad (3.3.13)$$

where N_T is the density of interface traps per unit area, n_s and p_s are the electron and hole densities per unit volume at the interface given in (2.4.5), f_{it}^0 is given by (3.3.8), and c_n and c_p the capture rates.

A continuous distribution in energy of interface traps can be modeled by a set of discrete interface trap energies. The circuit of the discrete traps are Y-circuits which are connected in series and have to be converted into Δ -circuits¹ for the admittance calculation. The details are given in [20]. To show the impact of the oxide charges and an interface trap distribution the model used in section 2.4.1 for the calculation of the ideal C - V curves was extended and cross checked with 1D TCAD simulations. In Figure 3.3.2(a) the parallel capacitances and in Figure 3.3.2(b) the parallel conductances for different frequencies are shown for the MOS capacitor simulated in section 2.4.1. In the calculation the oxide-charge density is $N_{ox} = 5 \cdot 10^{11} \text{ cm}^{-2}$ and the

¹The Y- Δ transformation is often used for the analysis of three-phase electric power circuits.

3. Effects of X-ray radiation on the Si-SiO₂ system

interface trap distribution consists of two Gaussians. The first Gaussian is a distribution of acceptors with a peak of $1 \cdot 10^{12} \text{ eV}^{-1} \text{ cm}^{-2}$, mean energy $E_{it}^0 = 0.35 \text{ eV}$, sigma of 0.15 eV , cross sections $\sigma_n^0 = 10^{-15} \text{ cm}^2$ and $\sigma_p^0 = 10^{-16} \text{ cm}^2$. The second Gaussian is a distribution of donors with a peak of $1 \cdot 10^{12} \text{ eV}^{-1} \text{ cm}^{-2}$, mean energy $E_{it}^1 = 0.75 \text{ eV}$, sigma of 0.15 eV , cross sections $\sigma_n^1 = 10^{-16} \text{ cm}^2$ and $\sigma_p^1 = 10^{-15} \text{ cm}^2$.

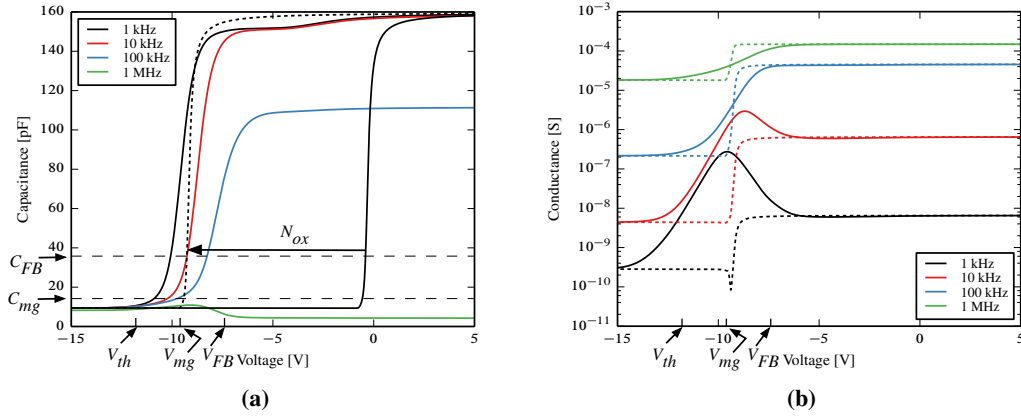


Figure 3.3.2.: Simulations of (a) the parallel capacitance and (b) parallel conductance of a MOS-C with oxide charges and interface traps on high ohmic silicon.

For comparison in the capacitance plot (Figure 3.3.2(a)) are shown also the ideal 1 kHz curve shown located around 0 V and the 1 kHz curve (dashed) for the case with oxide charges and without interface traps. In addition the horizontal dashed lines indicate the flatband capacitance of $C_{FB} = 35.8 \text{ pF}$ and the capacitance at midgap which is $C_{mg} = 14.2 \text{ pF}$. From the relationship between gate voltage and band bending (3.3.8) it is evident, that in the presence of oxide charges without interface traps the ideal curves are shifted parallel along the voltage axis to negative values. Thus, in this case the oxide charge could be determined by simply measuring the flatband voltage shift. If the frequency is so high that the interface trap charge occupancy cannot follow the AC voltage the interface traps will not contribute to the total capacitance, but they will respond to the slow DC bias change. Again, from the relation (3.3.8) it can be seen that the curves will be stretched out depending on the type of traps. Since acceptors are negatively charged when they are below the Fermi level they will produce, depending on the band bending, a positive voltage shift of the C - V curve, while donors will produce a negative shift. The Terman method [67] uses the high frequency curve for the determination of the interface-trap distribution by comparing the measured curve with an ideal curve. But as shown in [68], it is not possible to determine from the C - V curve either the type of the interface traps nor the quantity of oxide charges.

The frequency above which one typically assumes that the traps do not respond is 1 MHz. For high-ohmic silicon at this frequency the series resistance of the bulk is too high. To show the

stretch out in Figure 3.3.2(a) the flatband voltage $V_{FB} = -7.4 V$, the midgap voltage $V_{mg} = -9.6 V$ and the threshold voltage $V_{th} = -11.8 V$ are marked². Because in the simulation the trap distribution was chosen so that at midgap the interface traps are neutral the midgap voltage shift corresponds to the oxide charge.

As can be seen from Figure 3.3.2(a) the contribution to the capacitance increases with decreasing frequency, if one neglects the drop of the 100 kHz and 1 MHz curve in accumulation due to series resistance, which will result in a full contribution when the frequencies are so low that the interface traps can change the occupancy immediately in response to the AC voltage.

3.3.3. Determination and summary of X-ray radiation-damage parameters

For a detailed simulation of silicon sensors the knowledge of the radiation-damage parameters is required. As there is little information on X-ray radiation damage for high-ohmic silicon sensors, test structures fabricated by different vendors have been irradiated and the radiation-damage parameters have been extracted. The irradiations have been performed in the "white" X-ray beam F4 at DORIS III up to a dose of 1 GGy with a mean energy of ~ 12 keV and dose rates between 1 and 200 kGy/s [14]. Further irradiation of AGIPD test structures have been performed at PETRA III and will be presented in chapter 5. The test structures were fabricated by Canberra [69], CiS [70], Hamamatsu [71] and Sintef [72] on *n*-type silicon with a resistivity between 3 and 14 k Ω -cm and with crystal orientations $\langle 111 \rangle$ and $\langle 100 \rangle$. The SiO₂ thickness was between 250 and 775 nm, and some structures had a Si₃N₄ layer on top of the oxide. The MOS capacitors (MOS-C) of Canberra, CiS, and Hamamatsu were circular, with a diameter of 1.5 mm. The Sintef MOS-C was a rectangle of 1 mm \times 3.5 mm. The Gate-Controlled Diodes (GCD) of CiS and Hamamatsu were circular with 1 mm diameter and 5 Al-gate rings of 50 μ m width on top of the insulator, each separated by 5 μ m. The GCD of Sintef was circular with a central diode of 400 μ m diameter surrounded by a 210 μ m wide gate. The Canberra GCD was a finger structure with 100 μ m wide gates and 100 μ m wide diodes.

Directly after irradiation, within 30 minutes, a Capacitance/Conductance-Voltage (*C/G-V*) measurement of the MOS-C for different frequencies and a Current-Voltage (*I-V*) measurement of the GCD have been performed at room temperature. After an annealing for 10 minutes at 80°C the same measurements have been performed and the Thermal Dielectric Relaxation Current (TDRC) technique [73, 74] was applied to the MOS-C: The capacitor is first biased in accumulation at room temperature to fill the traps at the Si-SiO₂ interface. The device is then cooled down to ~ 30 K and biased into the deep-depletion in which state the traps remain filled because the temperature is too low to allow the electrons to be thermally excited out of the traps in the Si-band gap. The temperature of the device is then raised at a constant rate, and the current due to the release of electrons from the traps is recorded. The shape of the *I-T* characteristic is a direct image of the interface-trap distribution.

²The midgap voltage is defined by a band bending of $\psi_s = -\phi_B$ and the threshold voltage by $\psi_s = -2\phi_B$.

A typical $C-V-f$ measurement of a MOS-C produced by Sintef for the AGIPD (250 nm SiO₂, crystal orientation $\langle 100 \rangle$, resistivity 7.9 k Ω ·cm) irradiated to 10 kGy (contacts floating) after annealing for 10 minutes at 80°C is shown in Figure 3.3.3. The measurement was performed with a sweep rate of 0.11 V/s from accumulation to inversion (solid lines) and back (dashed lines), and an AC voltage of 50 mV. The pronounced hysteresis effects are a clear sign for the

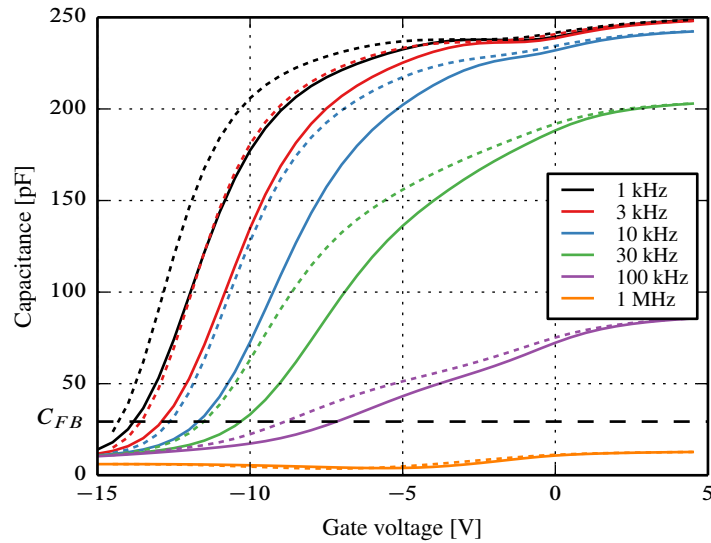


Figure 3.3.3.: $C-V$ measurement in parallel mode of a MOS-C produced by Sintef for the AGIPD (250 nm SiO₂, crystal orientation $\langle 100 \rangle$, resistivity 7.9 k Ω ·cm) irradiated to 10 kGy after annealing for 10 minutes at 80°C. The flatband capacitance is 29.3 pF. Solid: From accumulation to inversion. Dashed: From inversion to accumulation.

presence of border traps.

Because of the high series resistance of the silicon bulk and the strong frequency dependence due to the interface traps, methods based on the high-frequency $C-V$ measurements or the conductance method cannot be used to extract the oxide-charge density, N_{ox} , and the interface-trap density, D_{it} . Therefore, for the determination of N_{ox} and D_{it} in [14, 75] an attempt was made to measure the TDRC spectra, the $C/G-V$ curves and use the equivalent RC model as shown in Figure 3.3.4 with the spectra as input and fit the $C/G-V$ curves which were measured by sweeping from accumulation to inversion at room temperature.

The circuit takes the silicon bulk into account (C_{bulk}, G_{bulk}), the recombination/generation resistance R_f in the depletion layer for the supply of minority carriers and 3 interface traps. By comparison with the circuit for interface traps of Figure 3.3.1 it is clear that this circuit lacks the connections to the valence band and is therefore only an approximation in weak and not valid in strong inversion. Furthermore it is not possible to determine the hole cross sections of the

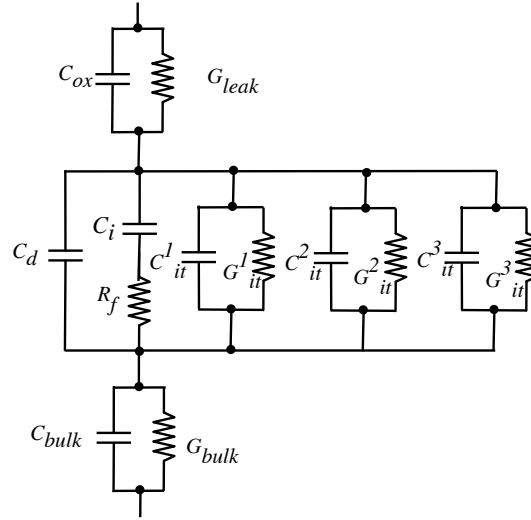


Figure 3.3.4.: Equivalent circuit model of the MOS capacitor with 3 interface traps includes.

interface traps.

The TDRC measurements were done typically by applying a bias voltage of $V_{ch} = 0$ V at room temperature and cooling slowly down to a temperature of ≤ 30 K. During cooling down a charge of $N_{acc} = C_{ox}(V_{ch} - V_{FB})/q$, where V_{FB} is the flatband voltage at room temperature, will be stored in interface traps. At the low temperature the voltage is changed to V_{sw} which was chosen as the voltage where the 1 kHz and 10 kHz $C-V$ starts to merge. In the example for the AGIPD MOS-C in Figure 3.3.3 the temperature was 10 K and $V_{sw} = -15$ V. After a waiting time of ≈ 30 s during which the electrons from the silicon bulk and from traps close to the conductance band are released, the MOS-C is heated up with a constant heating rate β which was usually 0.183 K/s and the TDRC signal recorded. For the AGIPD MOS-C irradiated to 10 kGy the spectrum is shown in Figure 3.3.5 as the red curve. The signal shows the typical characteristics for $\langle 100 \rangle$ crystal orientation observed in [14]. The current starts to rise at a certain temperature, in this case around 80 K, linearly increases with temperature around 200 K, showing a pronounced peak at around 230 K and then drops at 250–260 K. The number of electrons per unit area which have been release during heating up is

$$N_t = \frac{1}{q\beta A_g} \int_{T_0}^{T_1} I_{TDRC}(T) dT \quad (3.3.14)$$

where A_g is the gate area and T_0 , T_1 the start and end temperature. In Figure 3.3.5 also shown is the case with $V_{ch} = 5$ V where a signal below 100 K can be seen, which means that using $V_{ch} = 0$ V did not fill all available interface traps.

The drop to zero of the signal at ≈ 260 K is related to the bias voltage used during heating up. As the sample is heated up the energy level from which electrons are emitted is moving down

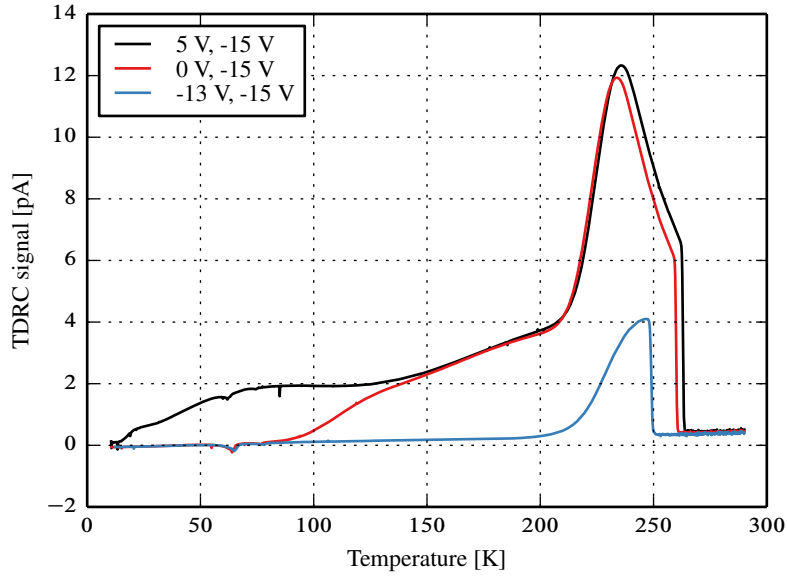


Figure 3.3.5.: TDRC spectra of a AGIPD MOS-C irradiated to 10 kGy for different charging voltages and a heating rate of 0.183 K/s.

in the bandgap. As this level approaches, and passes below the midgap energy the probability of generation of electron-hole pairs through empty interface traps will dominate the emission process. In addition bulk-generation will take place. With increasing temperature the non-steady state will approach the steady-state and the generation processes will build up the inversion layer charge which depends on the applied reverse bias voltage. To avoid these problems the bias voltage was chosen as described above. But this limits the energy range up to which one can determine the interface trap distribution. A further problem is that the analysis of the TDRC spectra assumes separated peaks which are either only due to emission or due to generation. As the measurement with $V_{ch} = -13$ V and $V_{sw} = -15$ V show the peak around 230 K also includes surface generation.

In [14, 75] similar spectra were fitted with 3 Gaussian distributions and the assumption was made that the measured spectrum is due to emission only. This is clearly not a unique parametrization and also assumes that all traps are filled. The transformation from I - T to D_{it} - E_{it} is based on the following relationships [74]

$$E_C - E_{it} = 10^{-4} T \cdot [1.92 \cdot \log_{10}(v/\beta) + 3.2] \text{ eV/K} - 0.0155 \text{ eV} \quad (3.3.15)$$

and

$$D_{it}(E_{it}) = \frac{I_{TDRC}(T)}{q\beta A_g 10^{-4} \cdot [1.92 \cdot \log_{10}(v/\beta) + 3.2] \text{ eV/K}} \quad (3.3.16)$$

with the attempt-to-escape frequency $\nu = \sigma_n v_{th} N_C$ and where for the temperature dependence of the capture cross section the assumption $\sigma_n \propto T^{-2}$ is made. These formulas are linearizations and are based on a series of approximations of the non-steady state problem. The energy transformation is derived under the assumption that for the emission rates $e_n \gg e_p$. Approaching midgap this assumption can not be made and errors in the energy transformation will increase [73]. A similar transformation exists for the surface generation which is valid in the lower part of the bandgap.

For the $C/G-V$ simulations the type of the interface traps has to be assumed. In [14, 75] the assumption was made that all traps within the measured spectrum are acceptors. Further it is assumed that the cross sections within one Gaussian is energy independent. With these assumptions the spectrum can be transformed from $I-T$ into $D_{it}-E_{it}$ and the $C/G-V$ curves can be approximately described up to weak inversion and values for the oxide charge density, interface trap distribution and electron cross sections determined. But one has to point out some problems with this procedure:

1. As mentioned above the hole cross sections are not determined. These are essential for the surface generation process. Using the extracted results in TCAD simulations of GCDs or sensors will not correctly reproduce the surface current and using TCAD to adjust these parameters is difficult and time consuming.
2. Assuming only emission, that all measured interface traps are acceptor (actually parts of the traps are below midgap) and the way how the TDRC is measured (0 V for charging, V_{sw} cuts the spectrum) implies the implicit assumption $N_{ox} = N_{it}$. This one can see by looking at the $C-V$ curves in Figure 3.3.3. The TDRC measured interface traps have to appear in the $C-V$ measurement in the voltage range between $V_{sw} = -15$ V and 0 V. At room temperature all traps below the Fermi level, which means $V_{sw} \leq V_G \leq V_{FB}$, are filled with electrons and applying 0 V during cooling down fills all traps between V_{FB} and 0 V. As the acceptors shift the $C-V$ curve to positive voltages it follows from the relation between band bending and gate voltage (3.3.8) that the thus determined oxide charge must be of the same amount as the interface traps to shift the curves back in the negative direction to describe the $C-V$ curves. Therefore N_{ox} is not independently determined.
3. Assuming that the deep peak is a donor or is due to surface generation will result in a lower value for N_{ox} .

To have at least an estimate of N_{ox} the flatband-voltage shift of the 1 kHz $C-V$ curves was used. This is an overestimation and can be assumed as an upper limit. The results measured directly after irradiation as function of dose are shown in Figure 3.3.6(a). For comparison the results after annealing for 10 minutes at 80°C using the same method are shown in Figure 3.3.6(b). Directly after irradiation the maximum of N_{ox} is $4.5 \cdot 10^{12} \text{ cm}^{-2}$ and for some oxides N_{ox} decreases by a factor of 2 after annealing. For the results after annealing it is observed that, in spite of the different fabrication processes, oxide thicknesses and crystal orientations, the trends

3. Effects of X-ray radiation on the Si-SiO₂ system

of N_{ox} as function of X-ray dose are similar: N_{ox} increases up to dose values of 10 to 100 MGy and then saturates, with saturation values between 2 and $3.6 \cdot 10^{12} \text{ cm}^{-2}$.

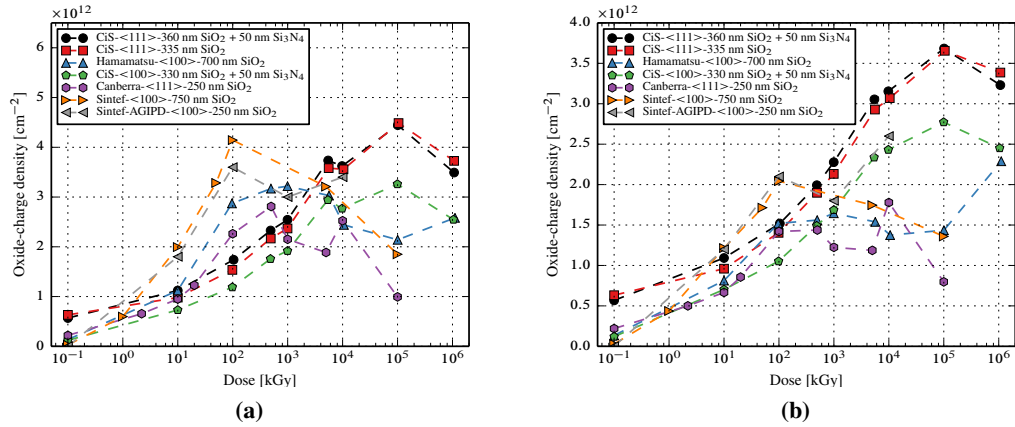


Figure 3.3.6.: Dose dependence of N_{ox} for MOS-Cs irradiated with floating contacts. The value of N_{ox} before irradiation is plotted at a dose of 10^{-1} kGy. N_{ox} is determined measuring the flatband shift of the 1 kHz $C-V$ curve. (a) As irradiated. (b) After annealing at 80°C for 10 minutes.

The surface-current density was extracted from the $I-V$ measurements on GCDs. For these measurements the diodes were biased to -12 V and the diode current as function of voltage on the first gate close to the diode was measured. The surface current I_{surf} is obtained from the difference of the current when the gate is in depletion and when it is in accumulation, and the surface current density J_{surf} by dividing I_{surf} by the gate area. Since the investigated GCDs had different gate areas, one has to mention, that the underlying assumption for the calculation of J_{surf} is that the gate area is fully depleted. As mentioned in section 3.3.1, part of the gate could be weakly inverted, so that, for the longer gates (Canberra and Sintef) the surface-current densities may be underestimated by up to 50%. The results of J_{surf} as function of dose directly after irradiation and after annealing are shown in Figure 3.3.7. After irradiation the maximum measured J_{surf} is $9 \mu\text{A}/\text{cm}^2$, which reduces to $6 \mu\text{A}/\text{cm}^2$ after annealing. As function of dose J_{surf} increases with maxima in the range of 1 to 10 MGy. The following decrease for higher doses is not yet fully understood.

As mention above for a detailed comparison between TCAD simulations and measurements the radiation-damage parameter in form of the oxide charge density, interface trap distribution and their cross section for electrons and holes are required. Whereas for the optimization of the sensor with respect to breakdown and surface current it is better to assume a worst case and then it is sufficient to use the oxide charge density and the surface generation velocity calculated from the surface current density.

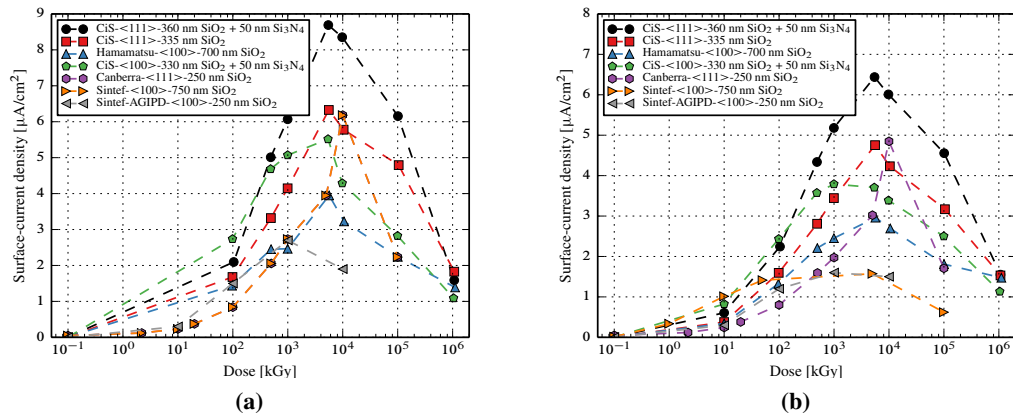


Figure 3.3.7.: Dose dependence of J_{surf} for GCDs irradiated with contacts floating contacts. The value of J_{surf} before irradiation is plotted at a dose of 10^{-1} kGy (a) As irradiated. (b) After annealing at 80°C for 10 minutes

4. Optimization of the AGIPD sensor

In this chapter the optimization of the AGIPD sensor will be discussed. It starts with the discussion of the requirements and the specifications of the sensor. Next the impact of X-ray radiation damage on p^+ - n sensors is summarized and shown that a precise knowledge of the doping profile is essential for accurate simulations. The calculation of these doping profiles with the help of a process simulation will be described next. Then the details of the used models in the device simulations and how the surface damage was incorporated in the simulations will be presented. The next topics are then the general optimization strategy used as well as the optimization of the guard-ring and the pixel structure, which leads to the sensor layout, as is shown at the end of the chapter.

4.1. Sensor requirements and specifications

To be able to provide specifications for the sensor, studies were carried out in the framework of the AGIPD collaboration that investigated the various aspects of the challenging requirements of the EuXFEL. Here, only a summary of the main considerations is given which led to the sensor specifications as listed in Table 4.1.1.

The decision to use a pixel size of $200\ \mu\text{m} \times 200\ \mu\text{m}$ was taken after studying the requirements of the scientific applications in more depth with the system simulation tool HORUS [76] to estimate the impact of various technology choices on the system performance. It was realized [77, 78], that $200\ \mu\text{m}$ pixels are acceptable for most CXDI (Coherent X-ray Diffractive Imaging) applications but will be too large for many XPCS (X-ray Photon Correlation Spectroscopy) applications, where a pixel size of less than $50\ \mu\text{m}$ is often required. With the used technology for the ASICs, only a very severe reduction of the maximum number of recorded images per pulse train and dynamic range would have allowed a significantly smaller pixel size; this solution was ruled out very early by the European XFEL management. In addition, the studies in [79] shows that certain XPCS experiments should be possible with the AGIPD detector employing a logarithmic sampling or a pixel aperturing¹.

Another critical geometrical parameter is the sensor thickness. The thickness determines the quantum efficiency (QE) and the absorbed dose on the ASIC. In [77] the difference between a sensor thickness of $500\ \mu\text{m}$ and $700\ \mu\text{m}$ was investigated with respect to the modulation transfer

¹Recently, for a PILATUS detector with a pixel size of $172\ \mu\text{m} \times 172\ \mu\text{m}$ XPCS experiments have been successfully performed using a grid mask resolution enhancer with holes of about $45\ \mu\text{m}$ in diameter bored in a tantalum foil and placed in front of the pixels [80].

4. Optimization of the AGIPD sensor

Parameter	Value
<i>Geometry parameters</i>	
Sensitive area	10.52 cm × 2.56 cm
Thickness	500 ± 20 μm
Pixel dimensions	200 μm × 200 μm
Deviation from flatness	< 20 μm
Distance pixel to cut edge	1200 ± 5 μm
<i>Electrical parameters before irradiation</i>	
Coupling	DC
n doping of Si crystal	3 – 8 kΩ·cm
n doping non-uniformity	< 10%
Dead layer n^+ -side	≤ 2.5 μm
Breakdown voltage	> 900 V
Dark current of all pixels@500V	< 200 nA
Dark current of single pixel@500V	< 20 nA
Dark current of CCR@500V	< 200 nA
<i>Electrical parameters for 0 Gy to 1 GGy</i>	
Breakdown voltage	> 900 V
Dark current of all pixels@500V	< 50 μA
Dark current of single pixel@500V	< 50 nA
Dark current of CCR@500V	20 μA
Interpixel capacitance	500 fF

Table 4.1.1.: Specifications for the AGIPD sensor. Dark currents and interpixel capacitance are specified at a temperature of 20°C.

function (MTF) and the expected noise. The conclusion was that the increased sensor thickness does not translate into notably worse MTF, nor noise, while it enables an appreciable gain in stopping power resulting in a QE of 96% vs. 90% for 12.4 keV photons. This increased stopping power would reduce the integrated dose on the ASIC by 60% compared to the thinner sensor. On the other hand there are also technical issues like increased depletion voltage, which scales with the square of the sensor thickness for material with the same resistivity and the need for a increased inactive area between the outer pixels and the sensor edge. Due to this issues for the first version of the AGIPD a sensor thickness of 500 μm was chosen, which gives a QE of more than 90% for 12.4 keV photons

For an n -type silicon substrate the basic configuration is $p^+ - n - n^+$ and the read out i. e. the segmented electrode could be on the p^+ or on the n^+ -side. Both choices have advantages and drawbacks. In the $p^+ - n$ sensor approach the ohmic side (n^+ -side) is completely unstructured and the p^+ -pixels are electrically isolated without additional technological steps which lead

to a relative simple and low cost processing of the sensor. In addition, most sensors for X-ray science are of this type and hence there is more experience in the ASIC design for $p^+ - n$ sensors. A drawback of this approach is that the sensor edges on the p^+ -side are on high voltage whereas the read-out chip is on ground potential. The distance between the sensor and the chip is given by the height of the bump bonds which is of the order of 15 μm . The high voltage difference over this small distance can lead to sparking and limit the maximum operational voltage. The details depends at the end on the arrangement of the chip and the sensor, where especially the distance between the wire-bonds and the cut-edge of the sensor is important and the environmental conditions. A spark protection can be realized by using a low- κ dielectric² as an additional passivation layer. Examples are benzocyclobutene (BCB) or Parylene-C. In [81] a layer of 3 μm BCB was spin-on, prior to the under bump metallization (UBM). Since the process has been performed at wafer level the cutting lines and the vertical sides of the sensors are not protected in this approach. In the case of Parylene-C, a conformal coating may be conducted after the wire bonding which also protect the cutting lines and the vertical sides of the sensor. Vacuum operation of the detector will strongly reduce the sparking probability. In vacuum better than 10^{-4} Torr, less than $3 \cdot 10^{12}$ molecules per cm^3 are estimated to be present. The length of the mean free path of an electron in this condition is in the order of meters making the formation of an electron avalanche on the scale of interest for sensors unlikely. However, if a gas cloud is able to form in the vacuum by outgassing or literally pulling charge carriers out from the electrodes and dielectric materials due to high electric fields, the usual kind of breakdown process takes place [82].

The sparking problem could be avoided by the use of an $n^+ - n$ sensor approach because in this case, on the otherwise unstructured p^+ -side guard-rings are required in order to reduce the applied high voltage to ground potential at the cut-edge. Otherwise the $p^+ - n$ junction would be shorted by a conductive layer which is present at the cut edge and is a result of the defects from sawing the crystal. In addition in an $n^+ - n$ sensor an electrical isolation of the n^+ -pixels using p-spray and/or p-stops is needed and has to be carefully adjusted. The double side process and the steps for the isolation makes the $n^+ - n$ sensor approach more cost expensive and complicated. Therefore for the AGIPD it was decided to use a DC coupled $p^+ - n$ sensor design.

This choice implies that the entrance window for the X-rays is the ohmic side of the sensor, which consists typically of an Al layer and a highly doped n^+ layer. The thicknesses of these layers, called dead layer, determine the lower energy limit of the detectable photons. In [83] the approximate quantum efficiency of the AGIPD for a standard window (0.5 μm Al, 1.2 μm n^+) and for a thin window (0.1 μm Al, 0.1 μm n^+) was computed. As one can see in Figure 4.1.1 the thin window significantly improves the QE for energies below approximately 5 keV. But this thin window carries the risk of impairing the high voltage operation and was therefore disregarded for the first version of the AGIPD.

One of the major challenges [84] of the EuXFEL is the high instantaneous X-ray intensity

²Low- κ dielectrics are materials with a small dielectric constant relative to SiO_2 .

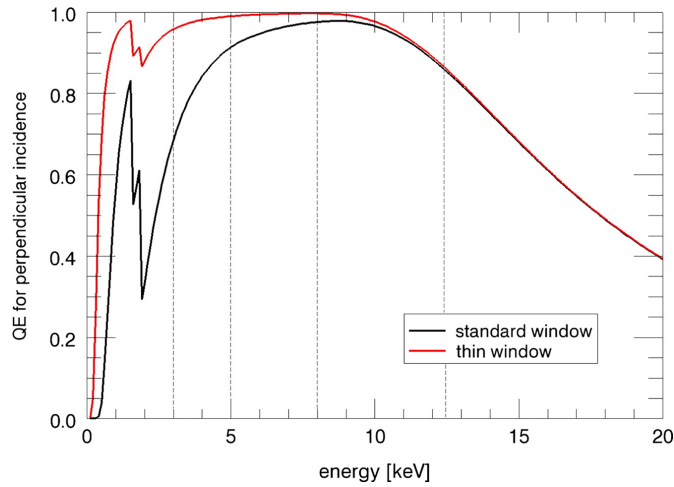


Figure 4.1.1.: Approximate quantum efficiency as a function of energy for the two different window designs. The thin window significantly improves the QE for energies below approximately 5 keV. Picture taken from [83].

which cause the so-called plasma effect. The plasma effect occurs when the density of electron-hole (eh) pairs produced by the radiation is large, typically of the order or larger than the doping of the silicon bulk. For 10^5 photons of 12.4 keV in a pixel of $200 \mu\text{m} \times 200 \mu\text{m}$ the density of eh pairs is a few times 10^{13}cm^{-3} , compared to the typical doping of 10^{12}cm^{-3} . On a time scale of picoseconds after their generation, holes and electrons move in opposite directions in the electric field and form a neutral eh plasma with a field-free region in the plasma, surrounded by high-field regions. The plasma erodes by ambipolar diffusion, resulting in a delayed charge collection and a spreading of the charges by diffusion and electrostatic repulsion.

This effect has been studied using a p^+n strip sensor read out by a multi-TCT system (Transient Current Technique) [13] for charge carriers generated by sub-nanosecond focused light with absorption lengths between $3.5 \mu\text{m}$ and 1mm (660-1060 nm wavelengths). From the analysis of the current transients of a $450 \mu\text{m}$ thick sensors as function of the applied voltage the conclusion was drawn that the plasma effect is relevant for the operation of silicon sensors at the EuXFEL, and that operating voltages of about 500 V are required for $450 \mu\text{m}$ thick sensors to assure a complete charge collection in-between EuXFEL pulses. Furthermore, as for a number of experiments at the EuXFEL the precise measurement of the shape of high-intensity diffraction peaks is important the point-spread function was investigated and with the conclusion in that an operating voltage well above 500 V should be possible for AGIPD. Thus a breakdown voltage of more than 900 V should be reached.

The other major challenge of the EuXFEL is the required radiation hardness, especially for the harder X-rays of 12.4 keV. Estimation of the expected dose are very difficult, because of its dependence on the kind of experiment which will be performed. In [11] a worst case scenario was considered which results in a maximal absorbed dose of 1 GGy over 3 years. This estimation

is based on the assumption that in a small angle scattering experiment a maximum of $5 \cdot 10^4$ photons per pixel are expected, all the time the same pixel is hit and a detector operational time of 1250 hours per year. Even if this dose might be much too high, it was decided that the detector should be designed to withstand the maximum possible dose. A problem which also has to be taken into account is that the irradiation will be highly nonuniform. Pixels that are located near the central hole of the detector will absorb orders of magnitude higher dose values than those which are far away from the hole.

In the following optimization it will become evident that the real challenge for the sensor design is the combination of the required high voltage and the radiation hardness. One of the results will be that, if one used standard technology, a relative large guard ring structure of $1200 \mu\text{m}$, which corresponds to 6 pixels, is required.

The deviation from the flatness is specified to be $< 20 \mu\text{m}$. This value is important for the bump-bond process to be able to apply a uniform pressure on all the bumps simultaneously. The parallelism between the sensor and chip, the planarity, and the bump uniformity must all together give “out of plane” effects below $1 \mu\text{m}$ to avoid excessive bump squashing and consequent risk of short circuits or high cross talk. The most critical parameter is the parallelism of the flip-chip machine that must always be kept below 0.1 mrad [85]. To achieve the required flatness some vendors use an additional thin film of deposited Si_3N_4 on the front or on the back side of the sensor to control the residual stress left in these devices after fabrication processing and thus the bow of the sensor. The solution with Si_3N_4 on the back side, which is for the AGIPD sensor the entrance window, should be avoided, since this additional layer will reduce the QE for the lower energy photons.

Dark currents of the pixels and current collection ring (CCR) are specified at a voltage of 500 V and a temperature of 20°C before and after irradiation. The values before irradiation are used for the quality control to distinguish between good and bad sensors. For the pixels after irradiation the dark current of all pixels at 500 V should be less than $50 \mu\text{A}$ which corresponds to a current of 0.76 nA per pixel. Assuming an integration time of 100 ns this current results in 475 electrons or 0.14 photons per pixel for 12.4 keV X-rays. In comparison to the other noise sources the noise contribution of the dark current of ≈ 20 electrons rms is in general negligible for the AGIPD [86]. To take also bad pixel into account the maximum dark current of a single pixel is specified to $< 50 \text{ nA}$. The dark current from the CCR should not exceed $20 \mu\text{A}$ to limit the power consumption of the sensor.

By far the largest contribution to the total capacitance is given by the interpixel capacitance, which is the capacitance to the neighbor pixels. To avoid cross talk between pixels and to limit the noise the interpixel capacitance should be low. For the AGIPD sensor the interpixel capacitance should be less than 500 fF .

A last point which one must also take into account in the sensor optimization are the environmental condition of the AGIPD detector operation. In particular, the humidity conditions are important because they determine the boundary conditions at the surface of the sensor and these conditions must be properly considered in the simulations. The full AGIPD detector will

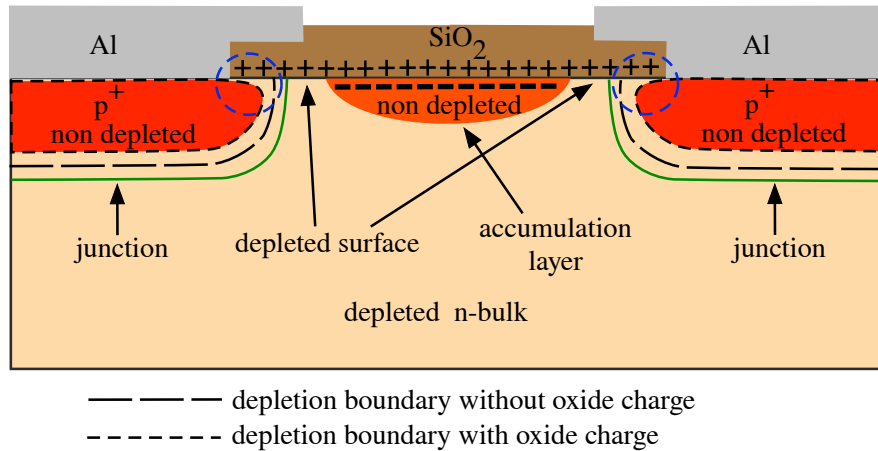


Figure 4.2.1.: Effects of the oxide charge on a p^+-n sensor. A positive oxide charge bends the depletion boundary and increases the width of the accumulation layer. Thus the width of the depleted region at the Si-SiO₂ interface decreases.

be operated in a vacuum chamber and in a temperature range from -25°C to 25°C . However, for calibrations, laboratory test and other applications operation in typical laboratory condition ($< 60\%$ relative humidity) should be possible.

4.2. Impact of X-ray radiation damage on p^+-n sensors

In this section the main effects of X-ray radiation damage on a segmented p^+-n sensor are summarized, where the main concern is to highlight the importance of the doping profile for an accurate simulation. The details will be discussed later in this chapter

As discussed in chapter 3 the X-ray irradiation results in the build-up of a net positive oxide charge and interface traps. Depending on the type (donor or acceptor), energy level and quasi Fermi energy the interface traps can be positively or negatively charged and thus contribute to the effective oxide charge, which is typical also positive. To illustrate the impact of the surface damage on a segmented p^+-n sensor a sketch of two half strips for a sensor under reversed bias is schematically shown in Figure 4.2.1 for the case with and without positive oxide charges. For the discussion the reverse bias is applied at the n^+ -side and the strips are grounded.

In the case without oxide charges the space charge region in the p^+ -implant at the Si-SiO₂ interface grows along the Si-SiO₂ interface with a boundary approximately normal to the interface. In the case with positive oxide charges the holes in the p^+ -implant will also be pushed away from the interface due to the Coulomb repulsion and attract electrons, which results in a strong bending of the depletion boundary close to the interface and thus a region of high electric field. Furthermore, if the p^+ -implant concentration at the interface is too low, the attracted electrons can form an inversion layer and if this inversion layer reaches the negatively biased Al

electrode, an electron current may flow directly from the metal electrode through the inverted n -type region to the positively biased electrode, by passing the p^+ - n junction and enormously increasing the leakage current. Since the electron concentration of the inverted region may be much larger than that of the n -bulk, the breakdown of the p^+ - n junction formed by the p^+ -implant and the n channel may be much lower than what is expected from the resistivity of the n -material used.

In addition, as a result of the positive charges in the oxide and at the Si-SiO₂ interface, an electron-accumulation layer forms at the interface, or, if already present for the non-irradiated sensor, its width increases. The electron-accumulation layer prevents the full depletion of the sensor at the surface and is therefore on a higher potential compared to the case without positive charges. The potential difference between the electron-accumulation layer and the p^+ -implant results in a high electric field at the corner of the p^+ -implant and a breakdown path will be formed from the accumulation layer along the interface through the point of the smallest curvature radius of the depletion boundary into the p^+ -implant. The appearance of the high electric field is demonstrated in Figure 4.2.2, where a simulation of the electric field 10 nm below the Si-SiO₂ interface for a sensor at 500 V is shown for values of N_{ox} of 10^{11} and $2 \cdot 10^{12} \text{ cm}^{-2}$. The corresponding values of the maximal fields are 50 and 450 kV/cm. In the contour plots of Figure 4.2.2 the depletion boundary are indicated as white lines.

Another effect of the electron-accumulation layer is that the interpixel capacitance will increase and that charge losses close to the Si-SiO₂ interface can occur. Both effects will be discussed later.

More important is, that the interface traps can cause an increase of the dark current by several orders of magnitude. The current is given by the product of the surface-current density J_{surf} and the area of the depleted Si-SiO₂ interface as shown in Figure 4.2.1. The depleted area depends in first approximation on the difference of the distance between the p^+ implants minus the width of the electron-accumulation layer. As the accumulation layer shrinks with increasing bias voltage, the dark current does not saturate when the sensor is depleted as expected from the bulk generation current, but continues to rise approximately linear with voltage.

The details of the formation of the electron-accumulation layer and its effects strongly depends on the sensor geometry, doping profile and the boundary conditions on top of the SiO₂ or the passivation layer.

4.3. Doping profile calculations

From the discussion in the preceding section it is clear that the doping profiles, in particular the one of the p^+ -implant are essential for a realistic device simulation. The problem with which one is confronted here is that the doping profile depends on the process details and vendors seldom provide these profiles. And if so, then these are 1D depth profile, which gives only a limited hint on how the lateral extension looks like. Due to the lack of this information often

4. Optimization of the AGIPD sensor

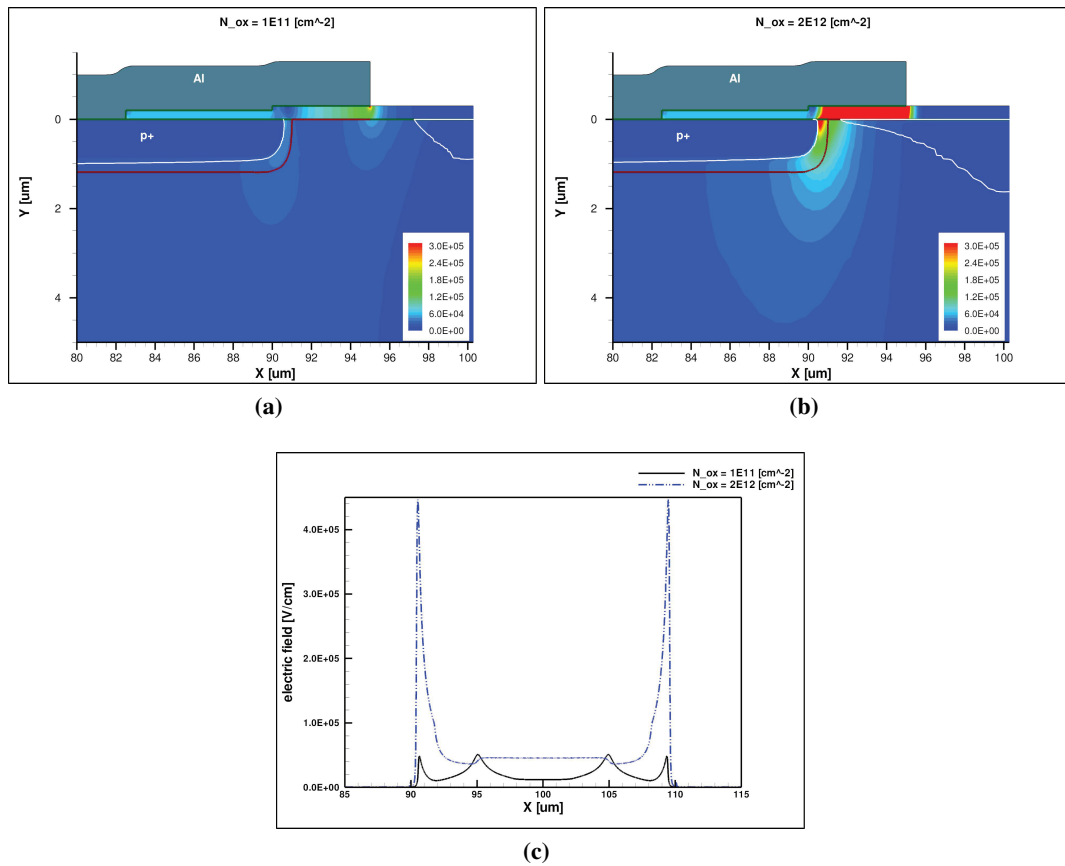


Figure 4.2.2.: Influence of the oxide-charge density N_{ox} on the electric field close to the Si-SiO₂ interface. (a) 2D field distribution for $N_{ox} = 10^{11} \text{ cm}^{-2}$. (b) 2D field distribution for $N_{ox} = 2 \cdot 10^{12} \text{ cm}^{-2}$. (c) Electric field in the silicon 10 nm from the Si-SiO₂ interface for the two values of N_{ox} .

simple Gaussian profiles are used in simulations, but this can also lead to optimizing the sensor with a profile which no vendor will ever produce. Therefore, the approach which was taken here to get realistic profiles was to perform 2D process simulations with process parameters which were used for sensor production and which were then varied within reasonable limits.

Today, for the formation of a $p^+ - n$ junction during silicon sensor processing, most vendors use the ion implantation with boron (B^+) and a subsequent “drive-in” or annealing step instead of a thermal doping, which means dopant diffusion out of a gaseous, liquid or solid phase. Ion implantation is the introduction of energetic charged particles into a substrate. The main advantage of this process is the precise control of implanted dopant atoms in the substrate, reproducibility of impurity doping, the possibility to implant through a thin surface layer (e. g. SiO₂) and that it is a low temperature step, which allows the usage of a photoresist for

masking [36].

The process which was used for the calibration of the simulation is a boron implantation through a 200 nm SiO₂ layer under a tilt angle of 0° with an energy of 70 keV and a dose of 10¹⁵ cm⁻² into a wafer with a phosphorous doping of 10¹² cm⁻³ and <111> crystal orientation. The drive-in was done at a temperature of 975°C for 4 hours. The distributions after each of these steps have to be calculated.

4.3.1. Ion implantation

During ion implantation the energetic ions lose their energies through collision with electrons and nuclei in the substrate and finally come to rest at some depth within the crystal. In these collisions the incident particle loses energy at a rate of dE/dx of a few 100 eVnm⁻¹ depending on the energy, mass, and atomic number of the ion as well as on the mass, atomic number, and density of the substrate material. The total distance that an ion travels in the target before coming to rest is called its range R (see Figure 4.3.1(a) and is determined by the rate of energy-loss along the path of the ion

$$R = \int_{E_0}^0 \frac{1}{dE/dx} dE, \quad (4.3.1)$$

where E_0 is the incident energy of the ion as it penetrates the substrate. The projection of this distance along the axis of incidence is called the projected range R_p . Because the number of collisions per unit distance and the energy lost per collision are randomly distributed, there will be a spatial distribution of ions having the same mass and the same initial energy. The statistical fluctuation along the direction of the projected range is called projected straggle ΔR_p , and in the direction perpendicular, projected lateral straggle ΔR_{\perp} .

In a first approximation the range parameter can be calculated with the classical LSS theory [87] which then results for a uniform flux along the axis of incidence in a symmetrical Gaussian distribution for the ion concentration C (see Figure 4.3.1(b)):

$$C(x) = \frac{\phi_i}{\sqrt{2\pi} \Delta R_p} \exp \left[-\frac{(x - R_p)^2}{2\Delta R_p^2} \right], \quad (4.3.2)$$

where ϕ_i is the ion dose per unit area.

From experiments it is found that this simple description of implanted profiles is not adequate for most ions in silicon and higher moments have to be taken into account for the construction of the range distribution. Other problems are the appropriate description of the implantation through layers and the accurate prediction of the lateral shape of the implanted dopant profile. With the process simulator Sentaurus Process of Synopsys TCAD [88] analytic functions can be used to compute the distribution of implanted ions and the implantation damage which take these problems into account. A problem here is that the analytical functions use look up tables for different implantation parameters and tables for implantation through SiO₂ are only available

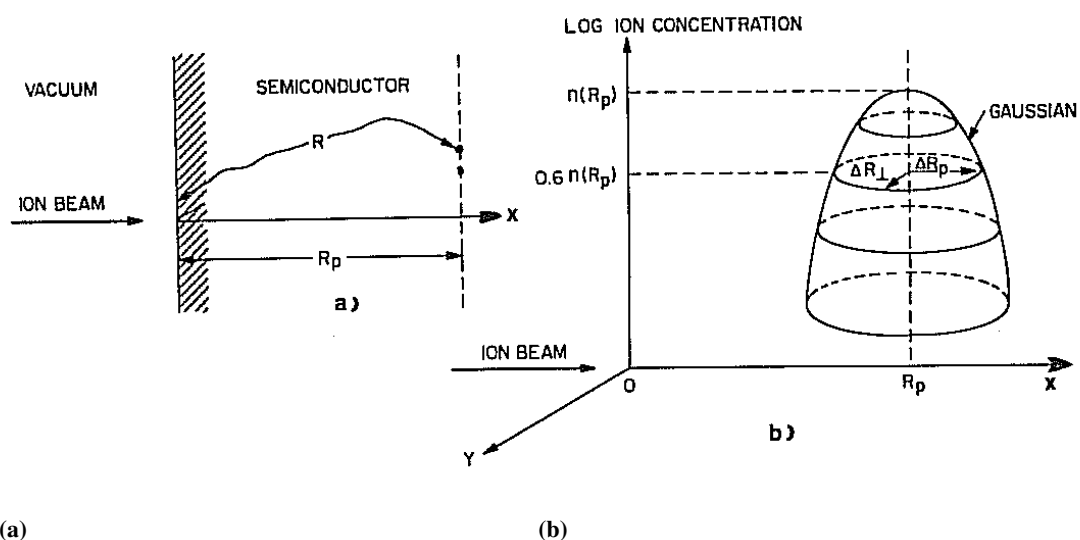


Figure 4.3.1.: (a) Schematic of the ion range R and projected range R_p (b) Two-dimensional distribution of the implanted ions. Picture taken from [36].

up to 100 nm. Therefore, a Monte Carlo (MC) method has been used.

Sentaurus MC simulates ion implantation into single-crystalline materials or into amorphous materials of arbitrary composition. The calculation assumes that ions lose energy through nuclear scattering, where the nucleus of the ion elastically scatters off the nucleus of an atom in the target. The interactions with the electrons of the target atoms is an inelastic process and does not alter the direction of the motion of the ion. Basic assumption are that the nuclear and electronic energy losses are independent and that during nuclear collision an ion interacts with only one target atom at a time, which enables the use of the binary scattering theory from classical mechanics. For details see [88] and [89].

Here we only mention how the damage accumulation was calculated. As the ions travel through a crystalline target, they collide with the target atoms and displace many of them from their lattice sites. In the binary collision approximation (BCA) code, it is assumed that, if the transferred energy exceeds a certain threshold, the target atom is displaced and, at this lattice site, a vacancy is generated. When the displaced atom comes to rest, it is identified as an interstitial. This defect production rate can be evaluated either by the modified Kinchin–Pease [90] formula or by simulating the full cascade, which was used in the following simulations. In the full cascade mode, Sentaurus traces all of the generated secondary recoils. After each collision, a calculation is performed to determine the trajectories of the silicon atoms that are knocked from their sites in the lattice by collisions with implanted ions. A silicon atom is assumed to be knocked from its site when it absorbs an energy greater than a damage threshold from a collision. The silicon atoms freed from the lattice can, in turn, knock other atoms from their sites so that

cascades of damage result. The trajectories of these knock-off ions are calculated with the same detail as the implanted ions. A vacancy (V) is assumed to have formed whenever a lattice atom is knocked from its site. An interstitial (I) is assumed to have formed whenever a silicon lattice atom that has been knocked from its site comes to rest. Since not all of the defects will survive, Sentaurus uses a statistical approach to calculate the final defect distribution, which takes into account the interstitial–vacancy recombination in both intracascades and intercascades.

For the simulation the following structure was used (see Figure 4.3.2). A silicon bulk which was 10 μm wide and 5 μm thick. The implant window was 5 μm wide with a 200 nm SiO_2 layer on top and the other part was also 5 μm wide with 300 nm of SiO_2 and a 1 μm thick photoresist on top. The coordinate system is so that the x-axis is parallel to the Si- SiO_2 interface and the positive y-axis points into the Si bulk with the zero point at Si- SiO_2 interface.

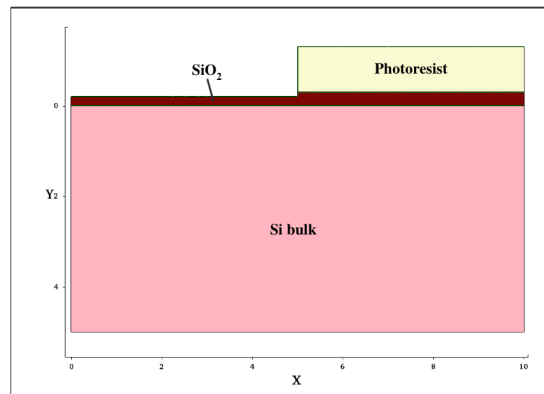


Figure 4.3.2.: Structure used for the calculation of the doping profiles. The silicon bulk is 10 μm wide and 5 μm thick. The implant window is 5 μm wide with 200 nm SiO_2 on top and the other part is also 5 μm wide with 300 nm SiO_2 and 1 μm photoresist on top.

The Figure 4.3.3(b) shows the 2D distribution of the boron concentration around the edge of the implant window for the implantation with an energy of 70 keV and a dose of 10^{15} cm^{-2} , and the Figure 4.3.3(a) a depth profile at $x = 2 \mu\text{m}$. The peak concentration is $6.3 \cdot 10^{19} \text{ cm}^{-3}$ at a depth of 76 nm measured from the Si- SiO_2 interface and the dose in the silicon is $8.3 \cdot 10^{14} \text{ cm}^{-2}$. The 2D distributions shows clearly the lateral straggling in the silicon with a maximum concentration at the implant window edge of $3 \cdot 10^{19} \text{ cm}^{-3}$. This value is half of the peak concentrations in the inner of the implant window and consistent with theoretical considerations [91].

4.3.2. Diffusion

After ion implantation the silicon crystal is damaged and most dopant atoms are electrically inactive, because they do not occupy lattice sites in the crystal. By means of diffusion processes the crystal is repaired, the dopants are activated and the final shape of the distribution of dopants is obtained. In the continuum and purely phenomenological approach to diffusion the

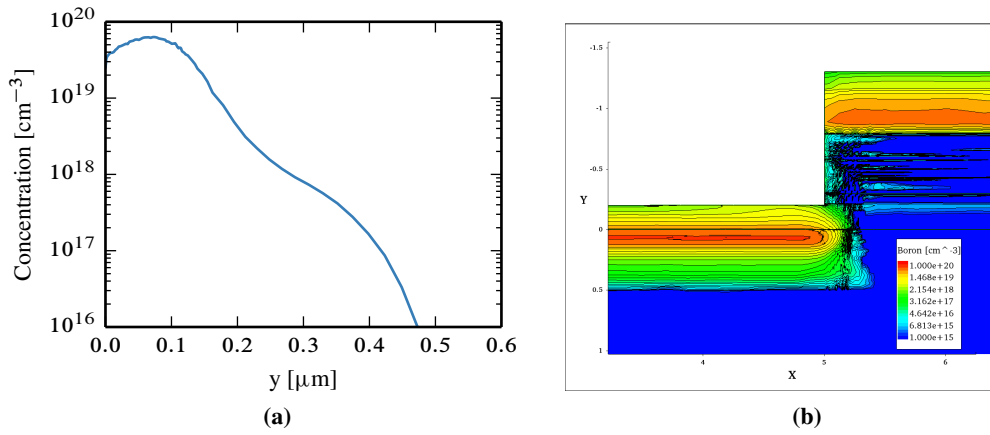


Figure 4.3.3.: Boron concentration for implantation with an energy of 70 keV and a dose of 10^{15} cm^{-2} .
 (a) Depth profile at $x = 2 \mu\text{m}$. (b) 2D distribution around the edge of the implant window.

governing equations are Fick's laws. The flux or diffusion current, \vec{J} , is defined as the number of atoms passing a unit area within a unit time interval. It can be related to the gradient of their concentration C by

$$\vec{J} = -D\nabla C. \quad (4.3.3)$$

Equation (4.3.3) is generally referred to as Fick's first law of diffusion and represents a macroscopic definition for the diffusion coefficient D . Combining this equation with the continuity equation

$$\frac{\partial C}{\partial t} = -\nabla \cdot \vec{J} \quad (4.3.4)$$

leads to the so-called Fick's second law of diffusion:

$$\frac{\partial C}{\partial t} = \nabla \cdot (D\nabla C) \quad (4.3.5)$$

In the case of a position independent diffusion coefficient D this equation reduces in 1D to

$$\frac{\partial}{\partial t} C(y, t) = D \frac{\partial^2}{\partial y^2} C(y, t) \quad (4.3.6)$$

which can easily be solved analytically under the assumption that the silicon ranges from $-\infty$ to ∞ . With the boundary condition $\partial C(y, t)/\partial y|_{y=0} = 0$, i. e. no outdiffusion at the surface, the general solution is

$$C(y, t) = \frac{1}{\sqrt{4\pi Dt}} \int_0^{\infty} f(y') \left\{ \exp\left[-\frac{(y' - y)^2}{4Dt}\right] + \exp\left[-\frac{(y' + y)^2}{4Dt}\right] \right\} dy' \quad (4.3.7)$$

with the dopant distribution $f(y)$ at time $t = 0$.

The temperature dependence of diffusion coefficients determined from empirical measurements shows that the data usually obey an Arrhenius relation

$$D = D_0 \exp\left(-\frac{E_a}{k_B T}\right) \quad (4.3.8)$$

characterized by the coefficient D_0 and the activation energy E_a . k_B and T are the Boltzmann constant and absolute temperature, respectively.

In Figure 4.3.4 the boron distribution after a diffusion at 975°C for 4 hours is plotted using equation (4.3.7) with the implanted distribution from the previous section as initial distribution and values $D_0 = 0.76 \text{ cm}^2/\text{s}$ and $E_a = 3.46 \text{ eV}$, which were taken from [36]. In addition the result of the process simulation with a constant diffusion model and the SIMS (Secondary Ion Mass Spectrometry) measurement of this process are given.

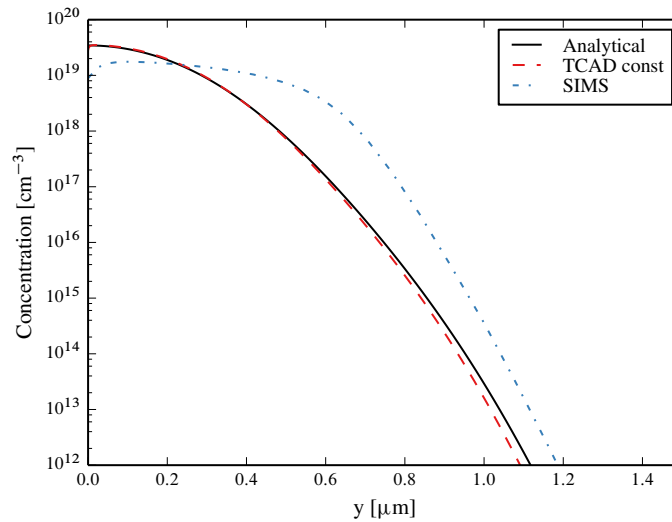


Figure 4.3.4.: Boron distribution after a diffusion at 975°C for 4 hours with the implanted distribution from the previous section as initial distribution. The analytical curve is calculated with equation 4.3.7 and the TCAD curve with a constant diffusion model.

The difference between the SIMS measurements and the calculated profiles indicates that the assumption of a constant diffusion coefficient is inadequate and additional effects have to be taken into account. The assumption of a constant diffusion coefficient is only valid as long as the doping concentration is lower than the intrinsic carrier density $n_i(T)$ at the diffusion temperature and the diffusion is then called intrinsic diffusion [17]. For the case that the doping concentration is larger than n_i the silicon becomes extrinsic and the diffusion is called extrinsic diffusion.

This is the case for the above process, since $n_i(975^\circ\text{C})$ is about $9 \cdot 10^{18} \text{ cm}^{-3}$, whereas the peak concentration of the initial distribution is $6.3 \cdot 10^{19} \text{ cm}^{-3}$. For a detailed discussion on the impurity diffusion in silicon one has to refer to the book of Pichler [92]. Here only two effects should be mentioned which were considered in the process simulation to reproduce the SIMS measurement.

In the case of extrinsic diffusion one effect is due to the electric field which exerts additional forces on the dopants and which is a drift effect. In a first-order estimation, the charge-neutrality condition can be used to describe the electric field and to express the gradient of the electrostatic potential in terms of the dopant concentrations. For systems with only one dopant being present in the system this leads to a modified version of Fick's second law

$$\frac{\partial C}{\partial t} = \nabla \cdot (D f_f \nabla C) \quad (4.3.9)$$

with the field enhancement factor f_f given by

$$f_f = 1 + \frac{C}{\sqrt{C^2 + 4 \cdot n_i^2}}. \quad (4.3.10)$$

Another effect of extrinsic diffusion is that the diffusivity varies with concentration, with higher-concentrations diffusing faster and smoothing the concentration gradient. One can still use Fick's second law 4.3.5 but a numerical integration is required. For the determination of the diffusivity one has to consider the atomistic mechanisms (interstitial, vacancy or interstitialcy³) which are relevant for the diffusion of the dopant. In case of the vacancy mechanism the diffusion coefficient D is assumed to be the sum of several diffusivities, where each accounts for the impurity interactions with different charge states of lattice vacancies [93].

$$D = D^0 + D^- \left(\frac{n}{n_i} \right) + D^\ominus \left(\frac{n}{n_i} \right)^2 + D^+ \left(\frac{p}{n_i} \right) \quad (4.3.11)$$

D^0 is the diffusion coefficient for diffusing with neutral vacancies, D^- for diffusing with single-negatively charged vacancies, D^\ominus for diffusing with double-negatively charged vacancies, and D^+ for diffusing with single-positive charged vacancies. The given concentrations of the charged vacancies are valid under Boltzmann statistics and normalized to the concentration of neutral vacancies. The dependencies of individual diffusion coefficients are usually given by Arrhenius relations.

If in the process simulation these effects are considered and one assumes that due to the long diffusion time all dopants are electrical active, the SIMS measurements can be matched as can be seen in the Figure 4.3.5(a). From the depth profile a junction depth of $1.2 \mu\text{m}$ can be extracted and from the 2D distribution a lateral extension of $1.0 \mu\text{m}$, measured from the edge of

³A interstitialcy is a configuration in which two silicon atoms share a site. Is is also called split interstitial [92].

the implant.

Even if there is no possibility to compare the 2D distribution (see Figure 4.3.5(b)) with a measurement it is assumed that the lateral distribution is calculated with sufficient accuracy using the physics models which are included in the process simulator.

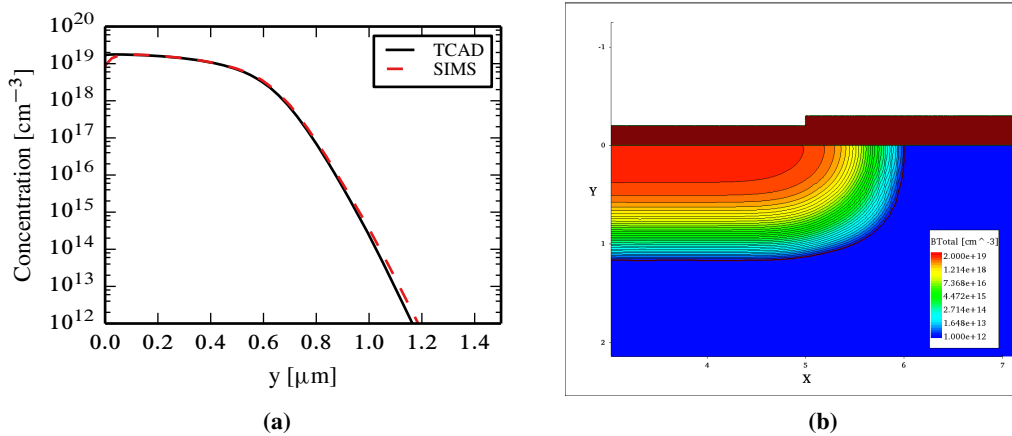


Figure 4.3.5.: (a) Comparison of the simulated boron profile with a parameterization of the SIMS measurement. (b): Simulated 2D boron profile.

4.3.3. Simulated profiles

For silicon sensors junction depths of the order of 1 μm are common [94, 95], but to optimize the sensor for high surface damage it is expected that a deeper junction as commonly used is needed. Therefore additional process simulations were performed to get doping profiles with deeper junctions by variation of the process parameter. For the energy values of 70 keV, 150 keV and 200 keV were used, and for the implanted dose values of $1 \cdot 10^{15} \text{ cm}^{-2}$, $5 \cdot 10^{15} \text{ cm}^{-2}$, $1 \cdot 10^{16} \text{ cm}^{-2}$. These values are in the range of currently used high current implanter. The implantation was again through an oxide layer of 200 nm, which should reduce channeling effect if one wants to use a <100> crystal orientation instead of <111>. For the drive-in temperatures of 975°C and 1025°C were used with a duration of 4 hours.

From the results which are summarized in the Appendix A.1 it is found, that the maximum junction depth which can be achieved is 3 μm, but only with a dose of $1 \cdot 10^{16} \text{ cm}^{-2}$ and an energy of 200 keV. These parameters are relatively extreme for sensor production. Therefore and also to reduce the parameter space in the optimization only the doping profiles with the 1.2 μm junction depth, from a process with an energy of 70 keV, dose of $5 \cdot 10^{15} \text{ cm}^{-2}$ annealed at 1025°C for 4 hours, which is shown in Figure 4.3.6 and results in a junction depth of 2.4 μm with a lateral extension of 1.95 μm was used.

Because of the used tilt angle of 0° for the implantation the 2D profiles are symmetrical

4. Optimization of the AGIPD sensor

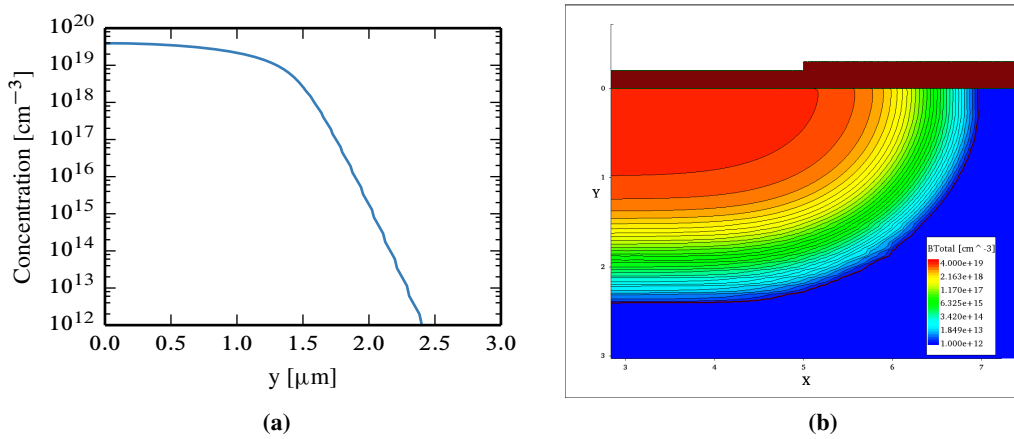


Figure 4.3.6.: Simulated boron profile for an energy of 70 keV, dose of $5 \cdot 10^{15} \text{ cm}^{-2}$ annealed at 1025°C for 4 hours. The junction depth is 2.4 μm and the lateral extension is 1.95 μm.

around the vertical axis at $x = 0 \text{ μm}$ and can be used in the device simulation for both edges of the implant window if one performs a mirror transformation. For implant windows which are larger than 10.0 μm the depth profile at $x = 0 \text{ μm}$ is continued to fill the lacking range. As shown in the three-dimensional view in Figure 4.3.7 the mask for the implantation of a pixel has corners which are spherical or spherical shell like depending on the radius at the corners. In principle a full 3D simulation of the implantation and diffusion should be performed for the corner region. But this requires a large amount of main memory and runtime. One possibility to use the 2D simulated profiles, and this was done in this work, is to sweep the 2D profiles along the ring segment which defines the rounding at the corner. For large enough radii the difference between the 3D and the 2D simulated profiles with an following sweeping should be negligible.

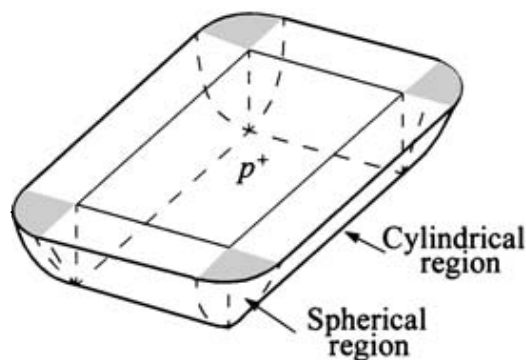


Figure 4.3.7.: Three-dimensional view of a planar diffusion or implantation process. At the edges of the mask the junction is cylindrical and at the corners spherical. Picture taken from [16].

For good ohmic contact typically a $n^+ - n$ junction on the backside of the sensor is formed.

Often the n^+ -region is also used for extrinsic gettering with POCl_3 or phosphorus-doped polysilicon [96] resulting in depths which can reach $10.0 \mu\text{m}$ and more. But, as mentioned in Section 4.1 the backside of the sensor is the entrance window for the X-rays and therefore the n^+ -implant should be as thin as possible to have a high quantum efficiency. On the other hand the n^+ -implant can impact the high voltage operation due to minority carrier injection. Therefore the doping profile must be chosen in such a way that the minority carriers generated at the backside do not enter the depletion region. Since the minority carrier recombination lifetime decreases with increasing doping concentration, a high doping concentration and a certain depth is required. For the optimization of the sensor with respect to X-ray radiation damage the backside implant is not important and different vendors will use different doping profiles to guarantee the high voltage operation before irradiation. But for completeness in Figure 4.3.8 the n^+ doping profile is shown which was used in the simulations. The simulated process is a phosphorus implantation through an oxide of 100 nm with an energy of 180 keV and a dose of $1 \cdot 10^{15} \text{ cm}^{-2}$.

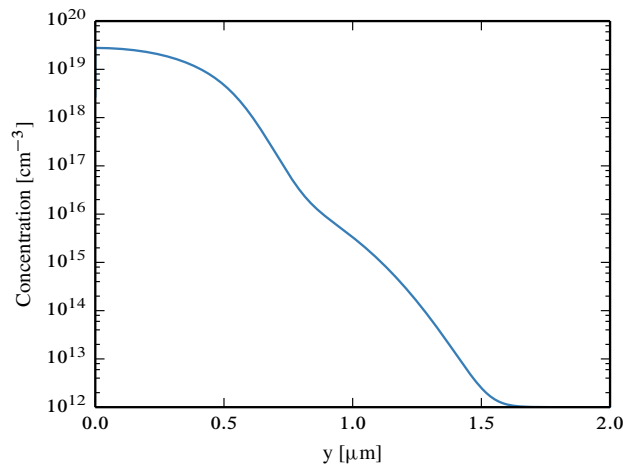


Figure 4.3.8.: Backside phosphorus profile used in the simulations.

4.4. Device simulations

For the optimization of the sensor device simulations have been performed using the doping profiles calculated in the previous section. The simulations were performed for a temperature of 293 K using the drift-diffusion model. The carrier lifetime in the bulk was assumed to be 1 ms, the mobility was modeled doping dependent with a degradation at the interface, and for the avalanche process the van Overstraeten – de Man model with the default parameters [88] was used. To take into account possible tunneling effects in very high field regions the band-to-band tunneling model of Hurkx [97] was also switched on.

The X-ray-radiation damage was implemented in the following way: The oxide charge density, N_{ox} , was simulated as a charge-sheet located at the Si-SiO₂ interface with a uniform distribution along the interface. For the simulation of the surface-current density, J_{surf} , it was assumed, that the surface current is generated via a trap at mid-gap with the same surface recombination velocity, s_r , for electrons and holes. In Table 4.4.1 the values, which were used in the simulations, for N_{ox} , J_{surf} and s_r are given. The corresponding dose values were estimated from measurements on X-ray-irradiated MOS capacitors and gate-controlled diodes after annealing at 80°C for 10 minutes [98]. As it has been found, that N_{ox} and J_{surf} saturate or even decrease for dose values above approximately 10 MGy, the maximum values given in Table 4.4.1 are considered valid for the entire dose range between 10 MGy and 1 GGy, the highest values expected at the European XFEL.

Dose [MGy]	N_{ox} [cm ⁻²]	J_{surf} [μA/cm ²]	s_r [cm/s]
0	$1 \cdot 10^{11}$	0.005	8
0.01	$1 \cdot 10^{12}$	2.3	3580
1	$2 \cdot 10^{12}$	5	7500
10 – 1000	$3 \cdot 10^{12}$	8	12040

Table 4.4.1.: X-ray radiation damage parameters used in the simulations, and the corresponding dose values.

On top of the SiO₂ Neumann boundary conditions (zero normal component of the electric field) were used. The results from references [15, 99, 100] imply, that the boundary conditions on top of the oxide separating p^+ implants at the same potential change with time from Neumann to Dirichlet (constant potential). The corresponding time constants vary between minutes and days, depending on environmental conditions like relative humidity. It was decided to use Neumann boundary conditions (NBC), as simulations have shown, that they result in a lower breakdown voltage after X-ray irradiation. They are also considered to be valid for the sensor operation in vacuum or in a very dry ambient [101]. No additional passivation layer on top of the SiO₂ has been simulated.

For the simulations we typically used 16 threads of Intel Xeon E5520 2.5 GHz PCs. For the 2-

D pixel simulations the minimum mesh size close to the Si-SiO₂ interface and at the edge of the p^+ implantation required to obtain reliable results, was 3 nm transverse and 6 nm perpendicular to the interface. The total number of vertices was 135 000, and the number of elements 255 000. An $I-V$ scan from 0 to 1000 V in 10 V steps took 30 minutes for an oxide-charge density of 10^{11} cm^{-2} and 70 minutes for $3 \cdot 10^{12} \text{ cm}^{-2}$. For the 3-D simulation of a quarter of a pixel, the minimal mesh size used was $30 \times 90 \times 90 \text{ nm}^3$, resulting in 900 000 vertices and 5 000 000 elements. A voltage scan took between 30 and 200 hours, and the iterative solver required approximately 80 GB of main memory.

4.5. Sensor optimization strategy

A sensor consists of a sensitive and a non-sensitive area. The sensitive area includes the individual pixels and the non-sensitive area the edge termination. The edge termination is required in order to obtain a smooth decrease of the applied bias voltage to the potential of the pixels and to ensure that the depletion area does not touch the cut edge. Both the pixels and the edge termination need to be optimized for radiation hardness. The optimizations are not independent from each other since process integrations, design rules, and cost factors must be considered. This is particularly true for the edge termination, where a variety of different technologies are possible. The most frequently used edge termination and also used in this work consists out of a current-collection ring (CCR), which serves to keep the leakage current from the non-sensitive part away from the sensitive part, together with a number of floating guard rings (GR). This structure has the big advantage that no additional photolithographic steps in the production are necessary but on the other hand the disadvantage that a relative large surface area is required to reach high voltages. A useful rule of thumb is to foresee a distance of roughly three times the wafer thickness between the cut edge and the sensitive region [85]. Another consequence is that the oxide thickness and the doping profile of the pixels and the guard rings have to be the same, if one does not want additional mask steps.

The geometrical parameters of a pixel which can be optimized are shown in Figure 4.5.1. Because the pixel size and thickness are fixed one has the pixel gap, the aluminum (Al) overhang, radius of implant and radius of Al layer at the corners as free parameter. For the guard-ring structure the parameters are the number of rings, implantation widths, spacings and Al overhangs. In addition, one has the depth of the p^+-n junction and the oxide thickness as process parameters.

The performance parameters which have to be optimized for doses between 0 and 1 GGy are the breakdown voltage, the leakage current and interpixel capacitance for the pixels, and the breakdown voltage and the voltage drop between the individual guard rings for the guard-ring structure. Moreover, it has to be ensured that the depletion boundary does not touch the cut edge. The strategy followed for the optimization can be summarized as follows:

- Guard ring (GR) optimization (2D simulations in (x,y) for the straight edges and in (r,z)

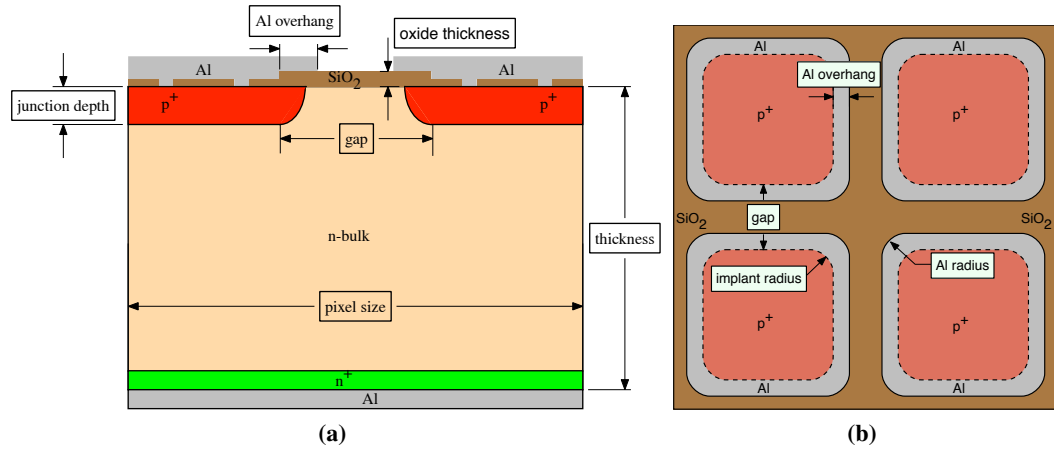


Figure 4.5.1.: Layout of the sensor region simulated for the pixel optimization.

for the corners):

1. Optimize the breakdown voltage V_{bd} without guard ring (0 GR - only CCR) for different values of N_{ox} and J_{surf} as function of oxide thickness, junction depth and Al overhang.
 2. Estimate the number of floating GRs required for $V_{bd} = 1000$ V.
 3. Vary the spacings between GRs, junction widths and Al overhangs, to achieve the maximum V_{bd} for a minimum width of the GR structure. This was achieved when the maximum electric fields in the gaps between the guard rings just below the breakdown voltage are approximately the same.
- Pixel optimization (2D simulations in (x,y)):
 1. Optimize the oxide thickness, Al overhang, gap and junction depth with respect to breakdown voltage, dark current and interpixel capacitance.
 2. Extrapolate the dark current and interpixel capacitances to 3D values.
 3. Check the breakdown voltage and dark current as function of voltage by a 3D simulation (only 1/4 pixel simulated).

In the following two sections the optimization will be described in this order even if the actual optimization was done in a more iterative way to find a common oxide thickness and junction depth for the pixels and guard rings.

4.6. Guard ring optimization

This section starts with the description of the working principle of guard rings, different design choices and shows the need for a special design for X-ray radiation hardness. The remainder of

this section will then follow the sequence of the optimization for the guard rings as stated in 4.5.

4.6.1. Guard ring fundamentals

As shown in Section 4.3 a planar p - n junction consists of a plane (or flat) region with approximately cylindrical edges and in addition if the mask contains sharp corners, the metallurgical junction near the corner will be roughly spherical in shape. Even without oxide charges the breakdown voltage of the planar p - n junction is strongly reduced compared to a plane junction due to avalanche breakdown in the high electric field regions at the edges and corners [102].

In order to reduce the field at the surface and to prevent surface breakdown, in the late 1960s field-limiting rings have been devised by Kao and Woolley [103] (see Figure 4.6.1 for the case of one ring). The field-limiting ring is floating electrically and the spacing from the main junction has to be in such a way that if one starts to increase the applied reverse main junction potential the depletion region punch through to the ring junction at a voltage which is considerably less than the breakdown of the bulk or the flat part of the junction. After the punch-through, any increase in voltage will be taken up by the ring junction as the carriers are depleted on the outside of the ring junction as shown in Figure 4.6.1. The maximum electric field across the depletion region of the main junction at the surface is determined by the punch-through voltage, and this can be controlled by properly adjusting the spacing so that the critical field⁴ is not reached. The ring junction acts like a voltage divider, and the voltage between the main junction and the first ring is essentially determined by their spacing. After the punch-through to the ring junction occurs, the field intensity at the main junction edge is appreciably reduced since the radius of curvature becomes now much larger.

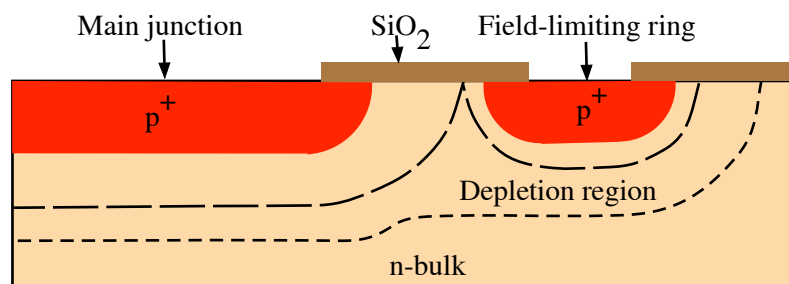


Figure 4.6.1.: p - n junction with field-limiting ring which has no metal contact. (After Kao and Woolley [103])

A detailed analysis of the floating field-ring termination was first performed by Adler et al. [104] using two-dimensional numerical solution of Poisson's equation. Because the potential of the floating rings is not known an iterative procedure based on the fact that once the fields have

⁴The critical field is defined as the field at which the multiplication factors owing to impact ionization approach infinity.

reached steady-state conditions, there must be zero net current into each field ring, was used. In order to satisfy this criterion, the field ring junction cannot be completely reverse biased or heavily forward biased. Therefore, the potential of the ring must be equal to the lowest potential along the ring junction minus a built-in potential. A potential higher than this by even a fraction of a volt would mean that the junction is heavily forward biased. A lower potential would mean the junction is reverse biased along its entire length with a net current entering the ring. Either of these conditions is obviously not consistent with the floating ring remaining at a constant potential.

It was also numerically shown by the same authors and in [105] analytically that an optimal spacing exists for one ring at which the breakdown voltage reaches its maximum value. If the floating field ring spacing is too small, almost all the applied voltage is transferred to the floating field ring resulting in a high electric field at the floating field ring and a reduced breakdown voltage. If the floating field ring spacing is too large, almost no voltage is transferred from the main junction to the floating field ring and the high electric field occurs at the main junction leading to a low breakdown voltage. If the floating ring is at the optimal position the electric field at both junctions is equal and the breakdown occurs simultaneously.

The optimum position depends not only on the junction depth, spacing and bulk doping but also on the surface charges and the ring width. A negative surface charge leads to an extension of the depletion layer at the interface which reduces the punch-through voltage. For positive surface charge the accumulation between the main junction and the ring tends to retard the depletion layer at the Si-SiO₂ interface. The point of punch-through at the ring has to move from the interface into the bulk which increases the punch-through voltage and disturbs the potential acquired by the floating ring. In both cases the electric field distribution for an optimally spaced floating ring designed without taking surface charges into account changes when surface charges are considered resulting in a lower breakdown voltage. For multiple floating rings in [106] it is shown that a wide field ring improves the decrease of the maximum field in the preceding region and that the ring spacings of an optimal designed structure increases in the direction from the inner to the outer rings.

In a guard-ring design for silicon sensors the floating rings are commonly equipped with metal overlaps (field plates, metal overhang) as shown in Figure 4.6.2 for a *n*-type sensor with *p*⁺ floating rings. The metal overlap changes the surface potential where the effect depends on whether they are directed inwards or outwards relative to the sensitive area and on the details of the underlying MOS structure [107]. Because the metal is on the same potential as the *p*⁺ implant an outward directed metal overlap will be on a lower potential than the silicon surface below it. Therefore the silicon surface can be in the state of accumulation, depletion or inversion. If the positive oxide charge is sufficiently high to cause an accumulation layer, the negative potential of the metal overlap will compensate it, which reduces the electric field at the implant edge. If the oxide charge is low the surface under the metal overlap can be in inversion which reduces the gap between the rings resulting in a lower punch-through voltage. To reduce this effect the overlaps have to be kept relative small. If the metal overlap is directed inwards the

silicon surface below will be always in accumulation, unless the oxide charge is very small, which suppresses the punch-through hole current and increases the punch-through voltage. Following [85, p. 93] this can be understood by interpreting the outer ring in Figure 4.6.2 as source, the inner ring as drain and the metal overlap of the outer ring as gate of a p-MOSFET. Because the gate is at the same potential as the source the transistor will always be in the switched-off state independent of the state of irradiation. Such a geometry is easier to predict compared to a structure with only outwards field plate and therefore preferred [107].

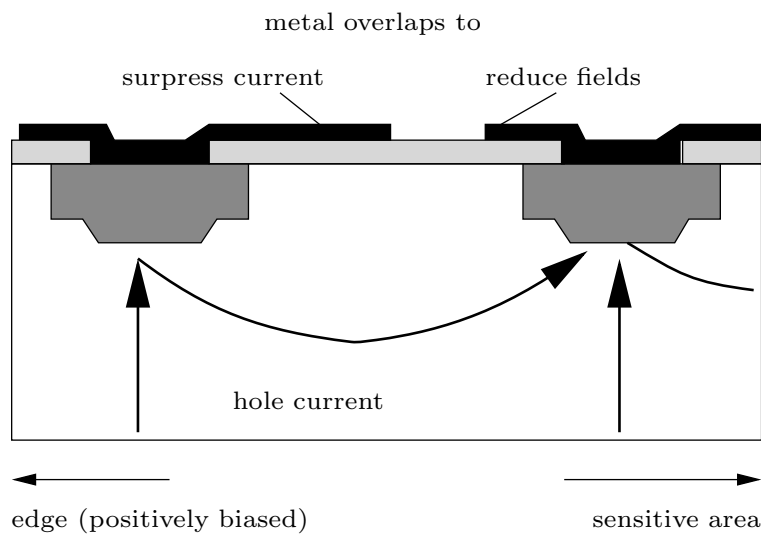


Figure 4.6.2.: Schematic cross section of a possible guard ring design with metal overlaps according to [107, 108]. Picture taken from [85].

That such a guard ring structure results not necessarily in a design which is sufficiently radiation hard for the AGIPD sensor can be seen in Figure 4.6.3 where the CCR current for a Sintef diode as function of voltage and different X-ray radiation doses after annealing at 80°C for 10 minutes is shown. The diode was manufactured on a material with a resistivity of 14 kΩ·cm and a thickness of 500 μm resulting in a full depletion voltage of 48 V. The area of the diode was 5 mm × 5 mm and the guard ring structure was 1.4 mm wide and consists of a CCR as well as 12 floating rings with inwardly directed field plates. The breakdown voltage before irradiation was ~ 900 V and decreases with irradiation to values of ~ 230 V at 100 MGy which is still more than four times the full depletion voltage but not tolerable for the AGIPD. The guard-ring structures of other vendors also do not guarantee to satisfy the specifications of the AGIPD sensor with respect to the breakdown voltage after the irradiation, and hence the optimization of this structure was needed.

Due to the large number of parameter the approaches for the optimization of guard-ring structures which one can find in the literature are quite different. They range from analytical formulas for multiple floating rings [109, 110] over TCAD based optimization methodologies

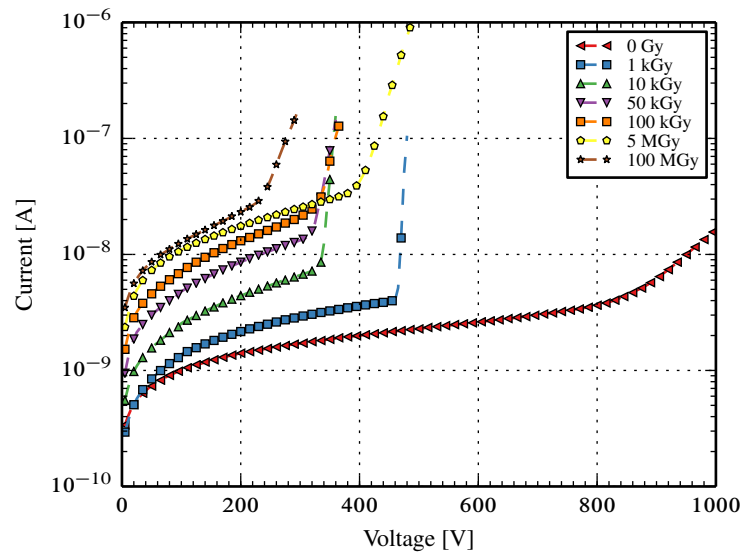


Figure 4.6.3.: CCR current of a Sintef diode after annealing at 80°C for 10 minutes for different X-ray radiation doses.

[111–113] for the optimum spacing between the rings and the ring width up to "trial and error" [114]. The analytical formulas can not be used in the presence of oxide charges. The TCAD based optimization methodologies were used for floating rings without metal overhang. As will be shown in the next section a *p-n* junction without metal overhang can break down below 20 V for oxide charges of $3 \cdot 10^{12} \text{ cm}^{-2}$ which would result in at least 50 floating rings for the AGIPD. Therefore a metal overhang is needed. The breakdown voltage of a *p-n* junction with metal overhang depends on the junction depth, oxide thickness and length of the overhang. Hence, our strategy starts with the investigation of the degradation of the breakdown voltage of a structure without guard ring under irradiation which will allow us to choose an optimal oxide thickness and the junction depth.

4.6.2. Zero guard ring

Introduction and influence of impact ionization models

The effect of a metal overhang on a *p-n* junction is in principle known since the experimental studies of the surface field on gate-controlled diodes by Grove et al. [115] and studies of Conti and Conti [116] who showed that the breakdown can happen not only at the junction but also at the edge of the metal overhang. Since then, a number of related studies were published [94, 117–121] but none of these works with a parameter space that is technologically relevant for the AGIPD sensor or high X-ray radiation dose. Consequently, in order to be able to choose the

optimal oxide thickness and the junction depth, the following simulations have been performed.

The zero guard-ring structure which was used in the simulations is shown in Figure 4.6.4. On the pixel side it consisted of half a pixel and the CCR. At the opposite side there was an n^+ -implant (channel stopper) near the scribe line. The gap between pixel and CCR was $20\ \mu\text{m}$. A metal overhang of $5\ \mu\text{m}$ was used for the pixel and the pixel side of the CCR. Because both pixel and CCR were grounded the breakdown always happens on the scribe-line side of the CCR. The implant window width of the CCR was $20\ \mu\text{m}$ and that of the n^+ -implant $10\ \mu\text{m}$. For the bulk resistivity $5\ \text{k}\Omega\cdot\text{cm}$ was used. The backside consists out of an Al layer and the n^+ -implant for which the doping profile from Figure 4.3.8 was used. The overall structure has a width of $600\ \mu\text{m}$ and thickness of $500\ \mu\text{m}$. The simulation has been performed in 2D with symmetric boundary conditions at the pixel edge. This corresponds to a strip with the width of a pixel surrounded by the CCR and scribe lines on both sides. The parameters which were varied were the junction depth d_j , oxide thickness t_{ox} and the length of the right metal overhang l_{mo} of the CCR. In principle a simpler structure would be sufficient for this study but the simulated structure is easier to extend to a full guard-ring structure.

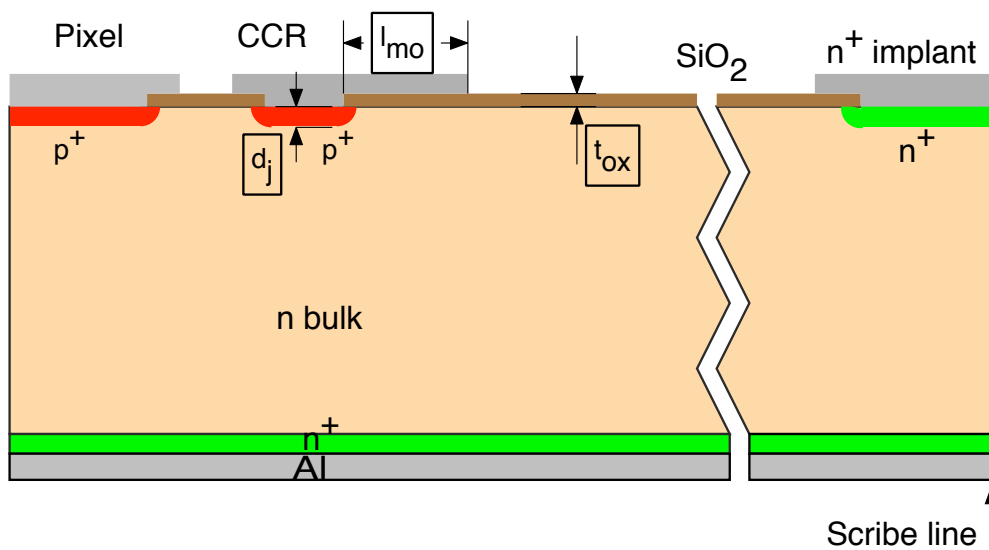


Figure 4.6.4.: The zero guard-ring structure for the breakdown analysis of the CCR as function of junction depth d_j , oxide thickness t_{ox} and the length of the right metal overhang l_{mo} of the CCR.

As discussed in Section 2.2.5.3 breakdown of a junction due to avalanche generation starts

if either of the ionization integrals I_n or I_p equals one. Since these breakdown criteria do not depend on current densities, a breakdown analysis can be performed by computing only the Poisson equation and ionization integrals under the assumption of constant quasi-Fermi levels in the depletion region. Although this approach is often used, it is expected that due to the considerable simplifications that are necessary to compute the integrals, the results will be inaccurate. To avoid this it is required to calculate the $I-V$ (current-voltage) curve of the CCR. An example for different oxide charges is shown in Figure 4.6.5. The increase of the leakage current with oxide charge is due to the surface current which is taken for the different oxide charges according Table 4.4.1. For the calculation of the breakdown voltage V_{bd} as criterion the quantity

$$K = \frac{dI}{dV} \frac{V}{I} \quad (4.6.1)$$

[122] with $K_{bd} = 10$ was used, and its value for the different oxide charges is indicated as a vertical line in Figure 4.6.5. The strong decrease of V_{bd} with increasing oxide charges is clearly seen. The value $K = 1$ corresponds to an ohmic resistor, and $K \gg 1$ to avalanche breakdown. The results obtained are slightly sensitive to the exact choice of the value for $K_{bd} \geq 3$ with increasing oxide charge. For the highest oxide charge of $3 \cdot 10^{12} \text{ cm}^{-2}$ the relative deviation between V_{bd} extracted with $K_{bd} = 10$ and $K_{bd} = 3$ is about 15 %.

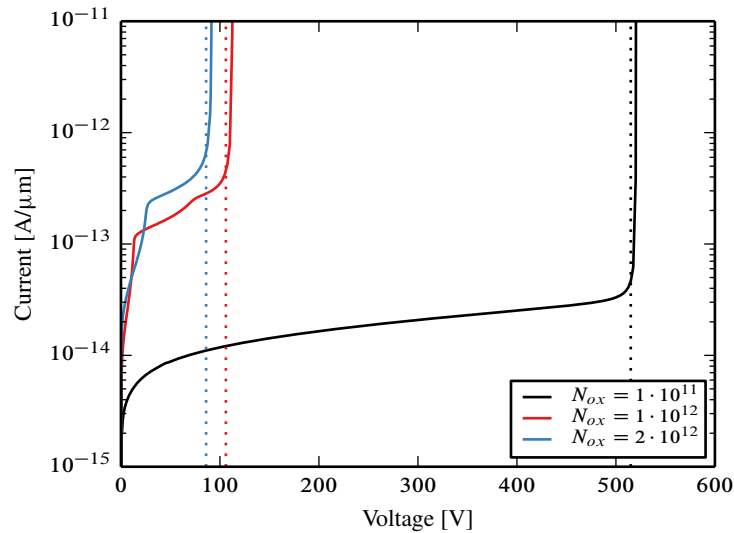


Figure 4.6.5.: $I-V$ curve of the CCR for a junction depth of $1.2 \mu\text{m}$, oxide thickness 300 nm , metal overhang of $5 \mu\text{m}$ and different oxide charges. The increase of the leakage current with oxide charge below breakdown is due to the surface current. The vertical lines represents the breakdown voltage according to equation 4.6.1 with $K_{bd} = 10$.

The $I-V$ curve and hence the V_{bd} depend on the impact ionization and transport model which is used in the simulation. As stated in Section 4.4 the optimization of the sensor was done using the van Overstraeten–de Man impact ionization model together with the drift-diffusion for the transport. These models are the standard models in Synopsys TCAD and commonly used in sensor simulations. The question arises whether these models are sufficiently reliable in the case of high oxide charges causing a high concentration of electrons in the accumulation layer. A simple estimation of the electron density at the interface [123] indicates that it is in the order of 10^{18} to 10^{19} cm^{-3} for oxide charges between $1 \cdot 10^{12}$ and $3 \cdot 10^{12} \text{ cm}^{-2}$. Such a high electron density at the interface results in an inversion layer at the edge of the p^+ -implant in the unbiased case as shown in Figure 4.6.6(a). Applying a reverse bias a large gradient of the local electrical field component parallel to the current flow can be reached in a small region as can be seen in Figure 4.6.6(b). A model like the one from van Overstraeten–deMan which uses the local electric field for the calculation of the impact ionization rates can be expected to overestimate these rates under such circumstances. The reason is that the carriers first have to gain an energy on their path through the device which is larger than the threshold energy for ionization before impact ionization can take place. The ionization rate at a specific place, thus, will depend, qualitatively spoken, not only on the local field, but also upon the field distribution in that vicinity [93]. In Synopsys TCAD there are also two "pseudolocal" field models implemented, the Okuto–Crowell and the Lackner model. For a detailed discussion on these models see [27]. These models were also used for comparison.

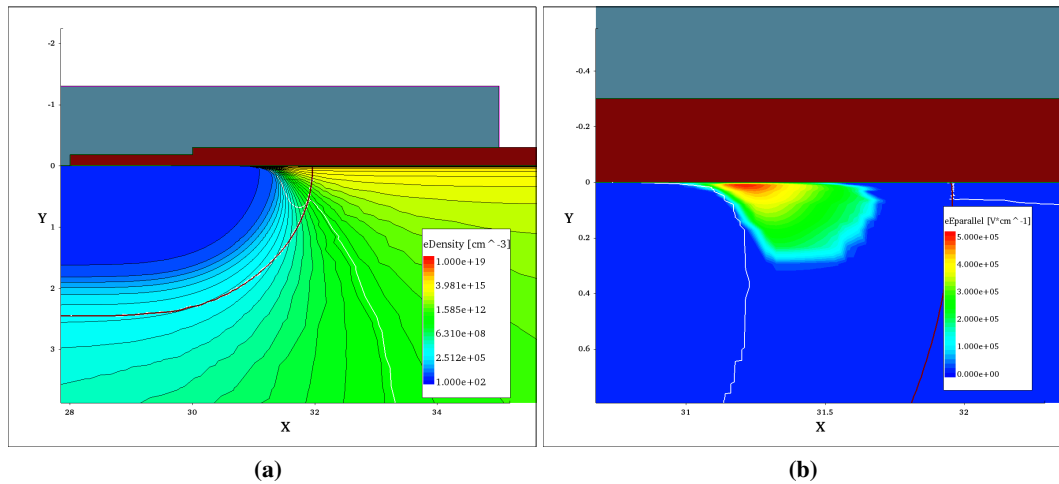


Figure 4.6.6.: (a) Electron density at 0 V showing an inversion layer in the p^+ -implant. (b) Electric field parallel to the electron current at 10 V. The brown line indicates the metallurgical junction and the white line the depletion boundary.

To indicate the difference between the impact ionization models the $I-V$ curves for the above geometry with $N_{ox} = 1 \cdot 10^{12}$ and $3 \cdot 10^{12} \text{ cm}^{-2}$ are shown in Figure 4.6.7 together with

a simulation where the avalanche generation was switched "off". In Table 4.6.1 the extracted breakdown voltages V_{bd} for the criteria (4.6.1) with $K_{bd} = 10$ and for the impact ionization integral equals one, V_{bdI} , are summarized. For the case $N_{ox} = 1 \cdot 10^{12} \text{ cm}^{-2}$ the difference in the breakdown voltage for the different models is relatively small. The relative deviation of V_{bd} for the Okuto–Crowell and the Lackner model to the van Overstraeten–deMan model is less than 5 %. In addition the agreement between V_{bd} and V_{bdI} is good.

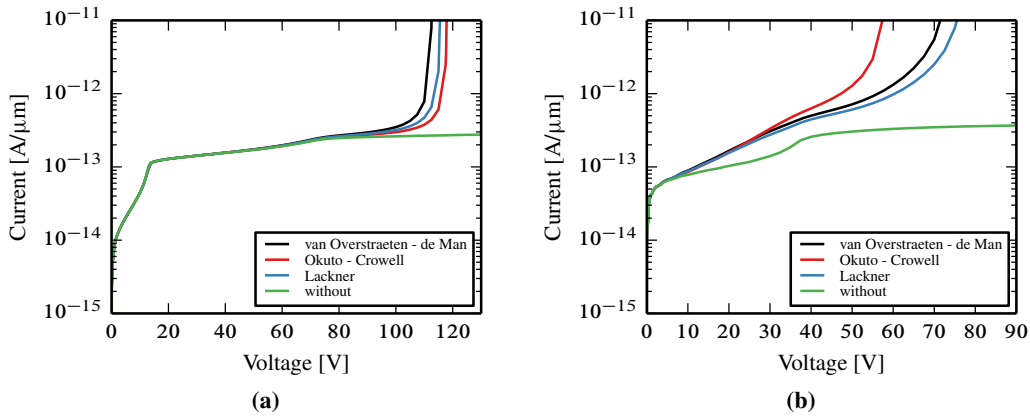


Figure 4.6.7.: I – V curve of the CCR using different impact ionization models and the geometry as in Figure 4.6.5. (a) $N_{ox} = 1 \cdot 10^{12} \text{ cm}^{-2}$ and $d_j = 1.2 \mu\text{m}$ (b) $N_{ox} = 3 \cdot 10^{12} \text{ cm}^{-2}$ and $d_j = 2.4 \mu\text{m}$

For the case of $N_{ox} = 3 \cdot 10^{12} \text{ cm}^{-2}$ the situation is more complex. The V_{bd} for the van Overstraeten–deMan and Lackner model is still in good agreement, whereas the value for the Okuto–Crowell model gives a value 20 % less than the value for the van Overstraeten–deMan model. In principle this behavior is expected because for electric fields higher than about $3 \cdot 10^5 \text{ V/cm}$ the ionization rate for electrons in the Okuto–Crowell model is larger than in the van Overstraeten–deMan model [27, p. 100]. Also the comparison between the values of V_{bd} and V_{bdI} shows a large difference. Comparing the I – V curves with avalanche switched "on" to the curve with avalanche switched "off" it can be seen that around 10 V some multiplication starts to occur. For better visualization in Figure 4.6.8 the multiplication factor, defined by $M = I/I_0$ with I_0 the current without avalanche and I the current for the van Overstraeten–deMan model is shown as function of voltage. At a voltage of around 10 V, an increase of M can be seen which reaches a value of $M = 2$ at approximately 25 V. A further increase of the voltage does not start immediately the avalanche, $M \rightarrow \infty$, but instead first a stabilization of M occurs before it again starts to rise and values of $M = 3$ at 56 V and of $M = 10$ at 66 V are reached. Using in this situation the impact ionization integral as breakdown criterion would lead to wrong conclusions.

In principle one could think to use a hydrodynamic/energy balance transport model including a full nonlocal description of impact ionization which is often used to take hot carrier effects

Model	$N_{ox} = 1 \cdot 10^{12} \text{ cm}^{-2}$		$N_{ox} = 3 \cdot 10^{12} \text{ cm}^{-2}$	
	V_{bd}	V_{bdI}	V_{bd}	V_{bdI}
van Overstraeten–de Man	106 V	99 V	66 V	23 V
Okuto–Crowell	111 V	108 V	52 V	22 V
Lackner	109 V	103 V	69 V	23 V

Table 4.6.1.: Breakdown voltages of the I – V curve from Figure 4.6.7. V_{bd} is the value extracted with (4.6.1) with $K_{bd} = 10$ and V_{bdI} the value using the ionization integral.

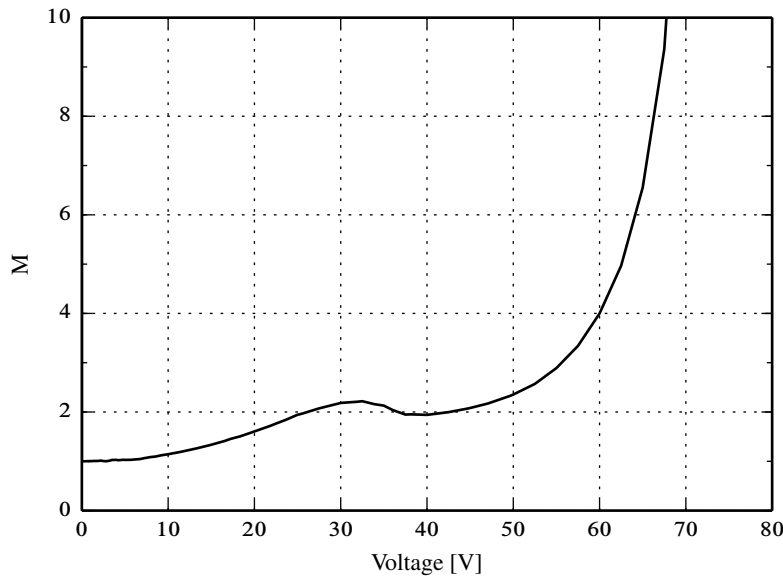


Figure 4.6.8.: Multiplication factor as function of voltage for the van Overstraeten–deMan model and $N_{ox} = 3 \cdot 10^{12} \text{ cm}^{-2}$.

in MOS devices into account. Such a simulation was also performed resulting in a 48 % higher breakdown voltage for the $N_{ox} = 3 \cdot 10^{12} \text{ cm}^{-2}$ case. But here one has to be careful. The hydrodynamic transport model in Synopsys TCAD is based on Stratton’s approach [124] for solving the Boltzmann transport equation in the relaxation time approximation. In this approach the assumption of a heated Maxwellian distribution is made which is only valid for carrier densities above 10^{16} cm^{-3} . Because for our sensor the bulk doping is much lower this assumption is not justified.

A further point is that the parameter for the impact ionization models are derived from bulk device measurements. Slotboom et al. [125] investigated the surface impact ionization in silicon devices and found from measurements on CCDs and MOS transistor that the electron multiplication near the Si-SiO₂ interface is reduced compared to the bulk. The electron mean

free path is $l_{surf} = 0.64 \times l_{bulk}$. In [126] it is shown with Monte Carlo simulations that there are no or only minor differences between surface and bulk impact ionization. The point is that there is no physical effect which is different in the surface and bulk impact ionization, but if one uses a local field model as done in [125] for the interpretation of the measurements one has to use different models. Including this surface model into the simulation for the case of $N_{ox} = 3 \cdot 10^{12} \text{ cm}^{-2}$ increases the breakdown voltage to similar results as obtained from the hydrodynamic simulation.

In summary: Due to the fact that a Monte Carlo simulation for the structure shown are not possible and detailed measurements to calibrate the parameter are not available using the van Overstraeten–deMan together with the drift-diffusion model and the breakdown criterion (4.6.1) seems to be reasonable. As a result the breakdown voltage could be underestimated.

Simulation results

In Figure 4.6.9 the breakdown voltage vs. oxide-charge density is plotted for the 1.2 μm (a) and 2.4 μm (b) deep junction for metal overhangs of 0, 5 and 10 μm , and oxide thicknesses of 200, 300, 500 and 1000 nm. As expected, in all these cases the breakdown voltage decreases with increasing oxide-charge density, but there are important differences. In case of the 2.4 μm deep junction for the different oxide thicknesses and without metal overhang the breakdown voltage decrease from values around 500 V for $N_{ox} = 1 \cdot 10^{11} \text{ cm}^{-2}$ to values of 20 V for $N_{ox} = 3 \cdot 10^{12} \text{ cm}^{-2}$. Actually, for $N_{ox} = 1 \cdot 10^{11} \text{ cm}^{-2}$ the breakdown voltage is slightly increasing from 485 V for 200 nm to 505 V for 1000 nm oxide thickness. This increase can be attributed to some edge effects due to the fact that the metal was terminated at the implant window edge and not shifted inwards. Compared to the 1.2 μm deep junction these V_{bd} values are 40 % higher due to the smaller curvature at the edge.

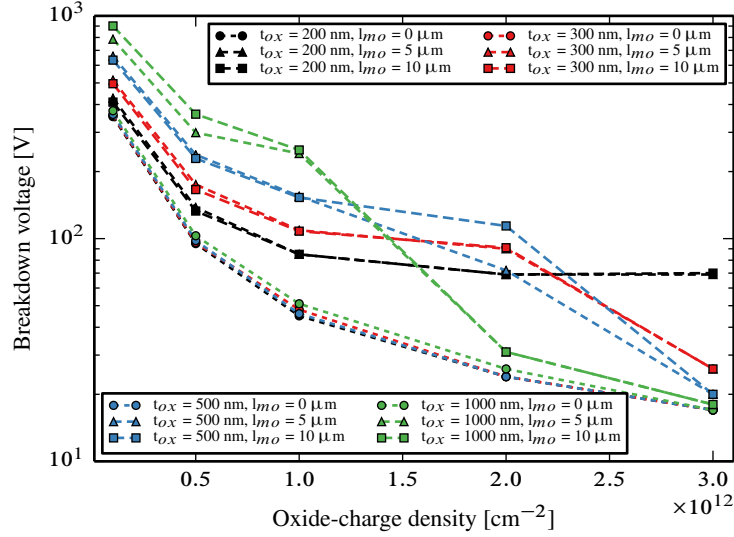
For an oxide thickness of 200 nm the breakdown voltage without metal overhang is slightly higher than with an overhang of 5 or 10 μm . Such a reduction of V_{bd} is due to the field crowding at the edge of the metal overhang which is similar to the cylindrical part of a planar junction. In a first approximation the oxide thickness plays a role similar to the junction depth [127] given by

$$d'_j = \frac{\epsilon_{Si}}{\epsilon_{SiO_2}} t_{ox}, \quad (4.6.2)$$

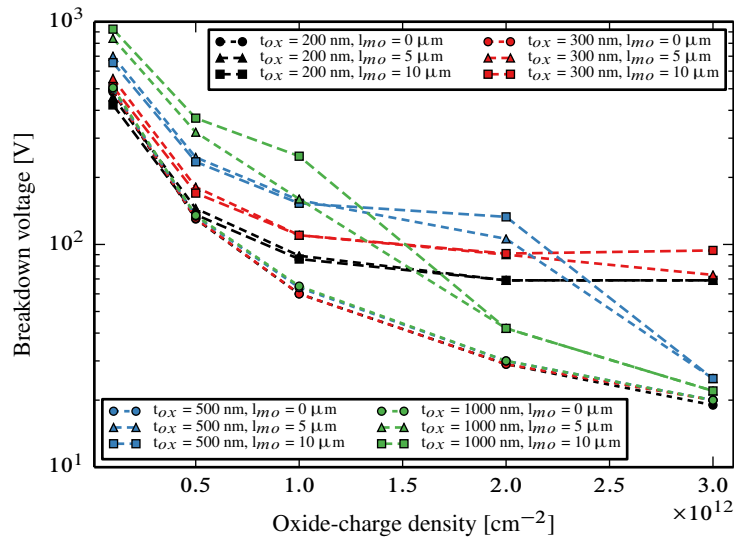
where d'_j is the equivalent junction depth, indicating that a too thin oxide can result in an edge breakdown at the overhang with V_{bd} which is lower than that of the p - n junction⁵. For the thicker oxides and also for the 200 nm oxide in the case of $N_{ox} \geq 5 \cdot 10^{11} \text{ cm}^{-2}$ the breakdown voltage with metal overhang is always higher than without.

For a 1000 nm thick oxide with $l_{mo} = 10 \mu\text{m}$ and $N_{ox} = 1 \cdot 10^{11} \text{ cm}^{-2}$ a V_{bd} of 920 V can be reached which reduces to a value of 20 V at $N_{ox} = 3 \cdot 10^{12} \text{ cm}^{-2}$ indicating that the effect

⁵An ideal field-plate structure requires the use of a dielectric layer that is very thin near the p - n junction and thickens outward from the metallurgical junction region [128].



(a)



(b)

Figure 4.6.9.: Breakdown voltage for 0 GR (CCR only) as function of N_{ox} for different metal overhangs and oxide thicknesses. (a) the 1.2 μm deep junction (b) the 2.4 μm deep junction

of the overhang is lost. A similar reduction is found for the 500 nm thick oxide, whereas the 200 nm and 300 nm oxide for $N_{ox} = 3 \cdot 10^{12} \text{ cm}^{-2}$ shows breakdown voltages higher than for the case without metal overhang. This indicates that with a fine scan in oxide thickness one should find an optimum oxide thickness.

In Figure 4.6.10 the breakdown voltage vs. oxide thickness for N_{ox} between $1 \cdot 10^{12}$ and $3 \cdot 10^{12} \text{ cm}^{-2}$ and $l_{mo} = 5, 10 \mu\text{m}$ for the 2.4 μm deep junction is shown. From this plot it can be seen that with increasing oxide-charge density the optimum value of the oxide thickness decreases. In addition, the range of oxide thicknesses over which a overhang of 10 μm results in a higher breakdown voltage compared to the 5 μm also decreases with increasing oxide charge. For example at $N_{ox} = 2 \cdot 10^{12} \text{ cm}^{-2}$ for $t_{ox} \approx 400 \text{ nm}$ to $t_{ox} \approx 700 \text{ nm}$ the breakdown voltage for $l_{mo} = 10 \mu\text{m}$ is higher than for $l_{mo} = 5 \mu\text{m}$ with a maximum at around 600 nm where the breakdown voltage is roughly 75 % higher. At $N_{ox} = 3 \cdot 10^{12} \text{ cm}^{-2}$ this range is only 40 nm and the maxima of V_{bd} are at 280 nm with a value of 80 V for $l_{mo} = 5 \mu\text{m}$ and at 300 nm

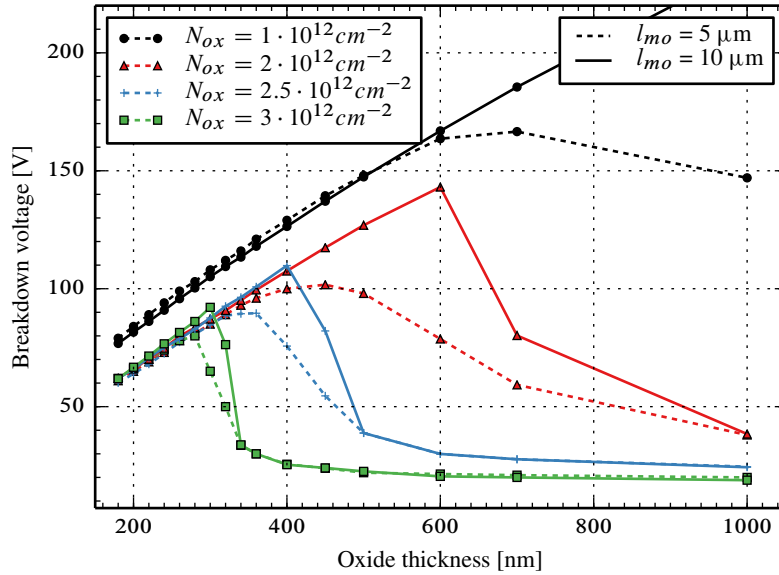


Figure 4.6.10.: Breakdown voltage for 0 GR (CCR only) as function of the oxide thickness for different oxide-charge densities N_{ox} and metal overhangs l_{mo} for the 2.4 μm deep junction.

with a value of 92 V for $l_{mo} = 10 \mu\text{m}$. Keeping in mind that, as discussed in Section 4.6.1, the overhang should be small, $l_{mo} = 5 \mu\text{m}$ was chosen for the guard rings.

The effect of the junction depth is shown in Figure 4.6.11 for $l_{mo} = 5 \mu\text{m}$. The effective metal overhang, which is the difference between the metal overhang and the lateral extension of the junction, is 4 μm for $d_j = 1.2 \mu\text{m}$ and 3 μm for $d_j = 2.4 \mu\text{m}$. The plot 4.6.11(a) shows the breakdown voltage vs. oxide thickness. The optimum oxide thickness for $d_j = 1.2 \mu\text{m}$ decreases to 230 nm compared to 280 nm for $d_j = 2.4 \mu\text{m}$ in the case of $N_{ox} = 3 \cdot 10^{12} \text{ cm}^{-2}$.

The plot 4.6.11(b) shows the breakdown voltage minus the flatband voltage shift

$$\Delta V_{fb} = \frac{qN_{ox}t_{ox}}{\epsilon_0\epsilon_{SiO_2}} \quad (4.6.3)$$

due to the oxide-charge density. A negative value for the breakdown voltage minus the flatband voltage shift indicates that at breakdown part of the silicon surface under the metal is in accumulation and the maximal field where the breakdown occurs is located at the junction. For a positive value the silicon surface under the metal is in depletion. In this case field maxima occur at the junction and at the edge of the metal overhang. At both locations the breakdown can occur and in the optimal case the breakdown occur at both locations simultaneously. This means that the breakdown conditions, which are different for the junction and the edge of the metal overhang, are reached simultaneously.

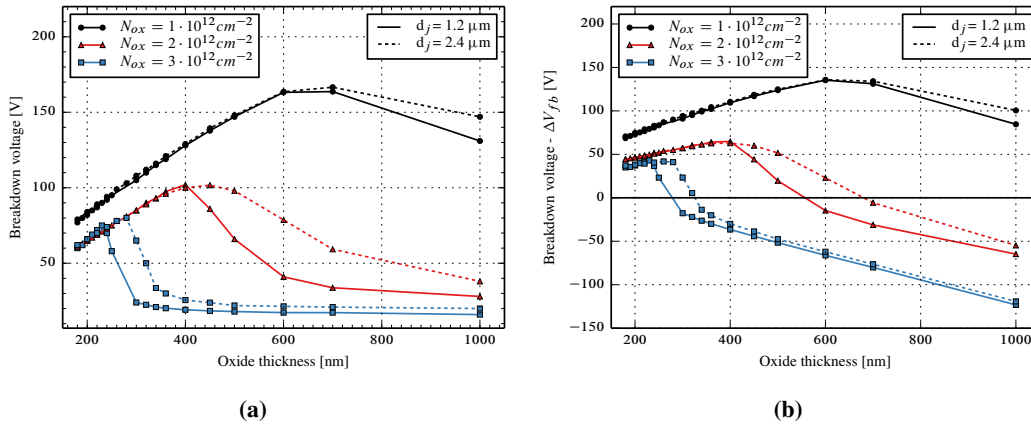


Figure 4.6.11.: (a) Breakdown voltage for 0 GR (CCR only) as function of the oxide thickness for different values of N_{ox} , an Al overhang of 5 μm , and junction depths d_j of 1.2 μm (solid) and 2.4 μm (dashed). (b) Breakdown voltage minus flatband voltage shift.

The breakdown voltage as function of oxide thickness can be now understood by taking for example the case of $N_{ox} = 2 \cdot 10^{12} \text{ cm}^{-2}$ with $d_j = 1.2 \mu\text{m}$. For an oxide thickness of 200 nm the breakdown voltage is 65 V and if the flatband voltage shift is subtracted 50 V. The potential at 60 V is shown in Figure 4.6.12(a) and the electric field at the Si-SiO₂ interface in Figure 4.6.13. As can be seen at this voltage the surface under the metal is depleted and the breakdown occurs at the edge of the metal overhang where the critical field is reached earlier than at the junction. Increasing the oxide thickness reduces the field crowding at the edge of the overhang and increases the field at the junction resulting in a higher breakdown voltage. At 400 nm the maximum breakdown voltage of 100 V is reached. From the potential shown Figure 4.6.12(b) and the electric field in Figure 4.6.13 it is difficult to judge whether the breakdown occurs simultaneously at the junction and the edge of the metal overhang because

4. Optimization of the AGIPD sensor

the critical fields are different at these locations. But theoretically it should be simultaneous, because as can be seen from Figure 4.6.11 the breakdown voltage is approximately maximal. Further increasing the oxide thickness to 600 nm reduces the breakdown voltage to 40 V which is smaller than the other breakdown values. If the flatband voltage shift is subtracted from the breakdown voltage the result is negative. From the potential shown Figure 4.6.12(c) it can be seen that only a part of the silicon region under the metal is depleted and from the electric field it can be seen that the breakdown occurs at the junction.

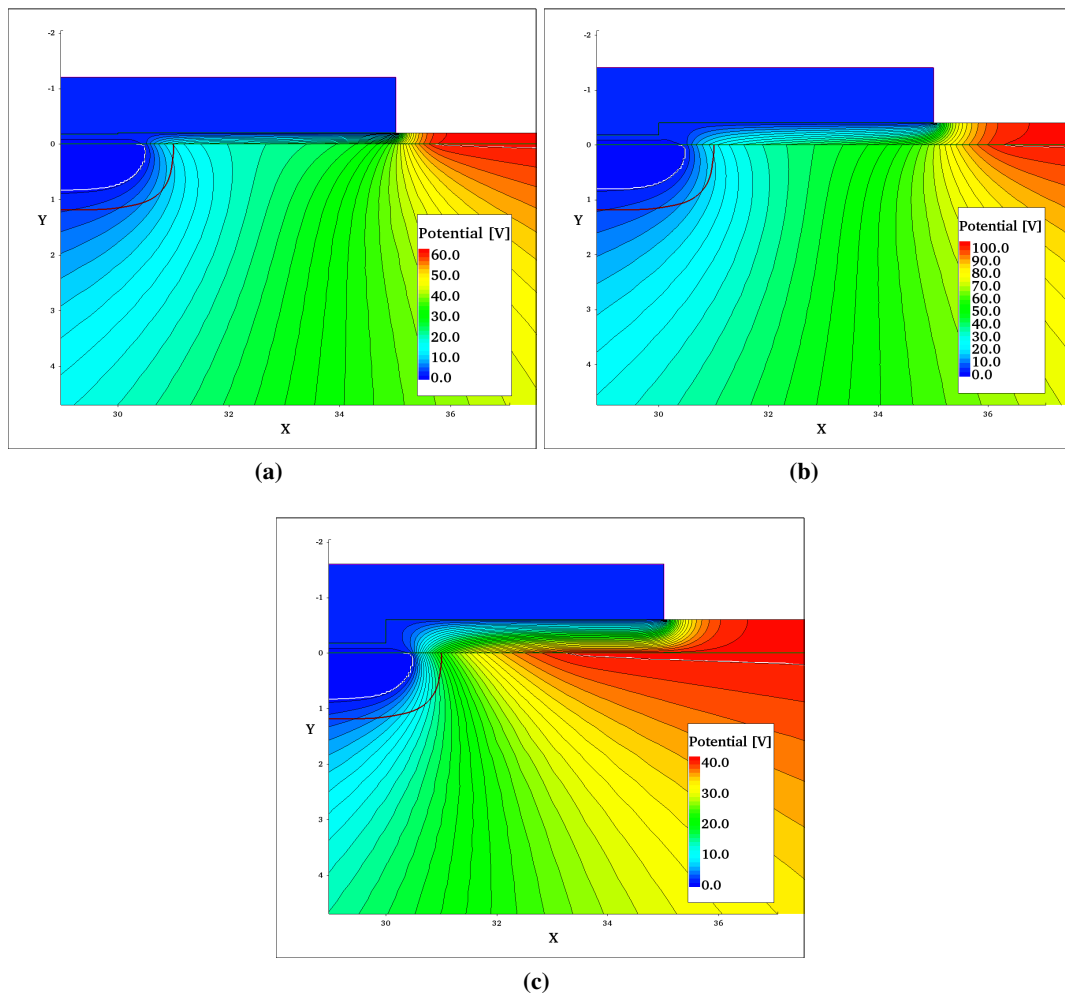


Figure 4.6.12.: Electrostatic potential at breakdown for $N_{ox} = 2 \cdot 10^{12} \text{ cm}^{-2}$ and $d_j = 1.2 \mu\text{m}$. (a) $t_{ox} = 200 \text{ nm}$, $V = 60 \text{ V}$ (b) $t_{ox} = 400 \text{ nm}$, $V = 100 \text{ V}$ (c) $t_{ox} = 600 \text{ nm}$, $V = 40 \text{ V}$

One problem in the design of a guard ring structure for a large range of oxide-charge densities can be seen in Figure 4.6.14 where the potential at the Si-SiO₂ interface at a bias of 100 V as function of position measured from the edge of the implant window for oxide-charge densities

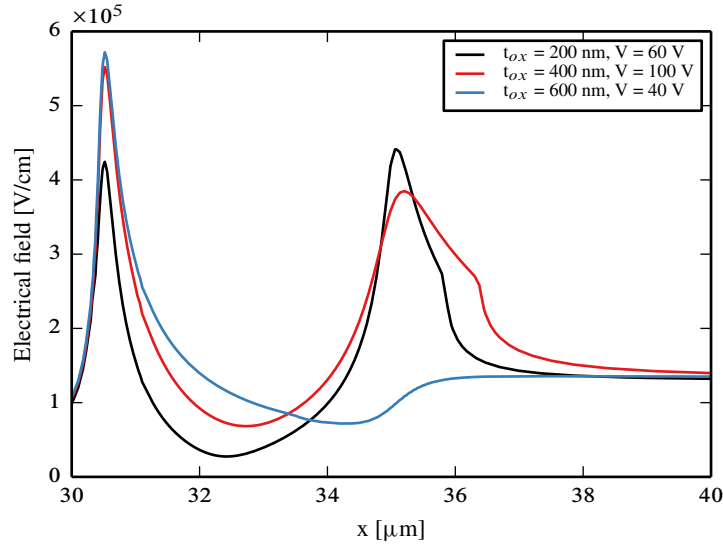


Figure 4.6.13.: Electric field at the Si-SiO₂ interface vs. position for $N_{ox} = 2 \cdot 10^{12} \text{ cm}^{-2}$ and $d_j = 1.2 \text{ }\mu\text{m}$.

from $1 \cdot 10^{10}$ to $1 \cdot 10^{12}$ is shown. For $N_{ox} = 1 \cdot 10^{10} \text{ cm}^{-2}$ the electron density at the Si-SiO₂ interface is $3 \cdot 10^{14} \text{ cm}^{-3}$ and the potential at the interface reaches the value of the applied bias at $x = 138 \text{ }\mu\text{m}$. Consequently the depletion region at the interface is $\approx 138 \text{ }\mu\text{m}$ wide. For $N_{ox} = 1 \cdot 10^{12} \text{ cm}^{-2}$ the electron density at the interface is $2.3 \cdot 10^{18} \text{ cm}^{-3}$ and the depletion width is reduced to $8 \text{ }\mu\text{m}$. Optimizing the guard ring structure for the highest oxide charge requires therefore a very narrow spacing of the rings. At low oxide-charge density the inner rings will be in punch-through conditions and thus contribute little to the overall voltage drop. As will be discussed in the next section without special care the depletion region can in this case reach the cut edge.

The necessity to reduce the oxide thickness in order to achieve a high breakdown voltage at high oxide charges, has the danger of increasing the electric field in the oxide, in particular at the metal overhang. For example for the 250 nm thick oxide with a junction depth of $d_j = 2.4 \text{ }\mu\text{m}$ and $N_{ox} = 3 \cdot 10^{12} \text{ cm}^{-2}$ at 80 V, which is close to the breakdown voltage, the mean electric field strength at the edge of the overhang in the oxide is around 2.3 MV/cm. Such a high electric field raises the question of the long-term reliability of the sensor as the dose at which the oxide-charge density begins to saturate, depending on the irradiation scenario is achieved relatively fast compared to the planned 3 years of operation. The dielectric breakdown strength of thermally grown SiO₂ is around 8-10 MV/cm [129] but due to the statistical nature of oxide breakdown a wide variability of breakdown distributions are typically found. Even if the applied fields are less than the dielectric breakdown strength, the question is whether this stress together with

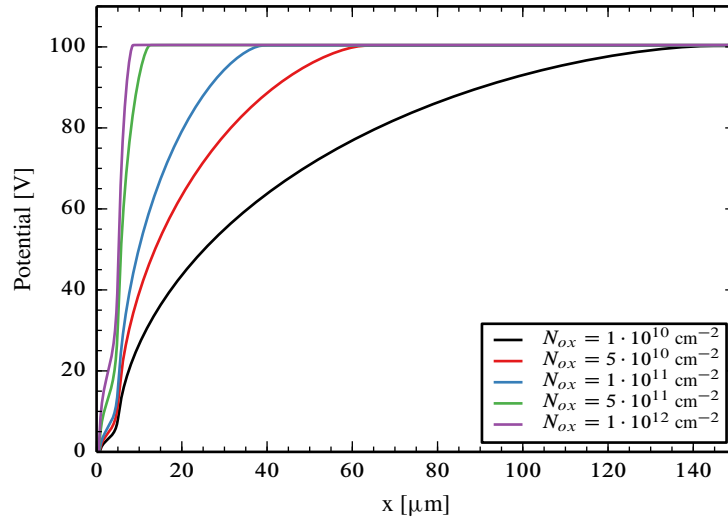


Figure 4.6.14.: Potential distribution at the Si-SiO₂ interface as function of position for a reverse voltage of 100 V. The position is measured from the edge of the implantation window. The oxide thickness is 300 nm and the junction depth 1.2 μm.

the radiation induced defects lead to an earlier time-dependent dielectric breakdown (TDDB). As shown in [130] no big changes of the average oxide breakdown properties have been found on AC-coupled detectors with 200 nm coupling oxide and doses up to 170 kGy(Si) gamma irradiation. However, an increase of low field breakdowns was observed⁶. Measurements by Fleetwood et al. [131] after a dose of 200 kGy(SiO₂) of 10 keV X-rays on thin oxide (7 nm) also show no significant changes. He pointed out that radiation induced defects in SiO₂ tend to be point defects, while the defects contributing to dielectric breakdown tend to be extended clusters of defects that are physically linked to a conducting path and that the passage of high currents through an oxide will lead to the annealing of some radiation damage due to the capture of electrons at the positive charge centers. In addition, there are two aspects which will result in a lower electric field: 1.) The simulations were done without a passivation layer which reduces the field crowding at the edge of the metal overhang and increases the breakdown voltage. 2.) The simulations assumed a uniform oxide charge distribution along the interface, but due to the field direction in the oxide below the metal overhang radiation induced holes will tend to drift in the direction of the metal resulting in a lower positive charge at the interface. Taking this into account it can be assumed that if the oxide quality is good the radiation induced defects should not result in an oxide breakdown at voltages below the breakdown voltage of the simulation presented.

⁶Low field breakdowns are normally due to pinholes, voids, particles and scratches.

Summary and conclusions

Simulations of zero guard-ring structures have been done for different metal overhangs, oxide thicknesses and junction depths as function of oxide-charge densities. For oxide-charges densities up to $N_{ox} = 1 \cdot 10^{12} \text{ cm}^{-2}$ simulations with the drift-diffusion model and with different impact ionization models give similar results and only a small dependence on the breakdown criteria. For higher oxide-charge densities the breakdown voltage depends on the criterion. In this case to reach a high breakdown voltage a metal overhang and a reduction of the oxide thickness is required. For a junction depth of 2.4 μm and 5 μm metal overhang the optimum oxide thickness is 280 nm. These results and the simulations of the pixel in Section 4.7 lead to the choice of a 250 nm oxide with 2.4 μm p^+ -implant as compromise between technological feasibility and high V_{bd} for the further optimization. Although high electric fields occur in the oxide below the Al overhang, we are of the opinion that they should not result in a reduced breakdown voltage.

4.6.3. Optimization of the guard-ring structure

Introduction and optimized design

From Figure 4.6.11 one can extract a $V_{bd} \approx 70 \text{ V}$ for $t_{ox} = 250 \text{ nm}$ with $d_j = 2.4 \mu\text{m}$ and $N_{ox} = 3 \cdot 10^{12} \text{ cm}^{-2}$. Because the breakdown voltage of a guard-ring structure with n_{fr} floating rings can not be larger than $(n_{fr} + 1) \times V_{bd}^1$, with V_{bd}^1 the breakdown voltage of one $p^+ - n$ junction, one can estimate that a least $n_{fr} = 14$ rings are needed to reach a breakdown voltage of about 1000 V. This is the case for the straight sections of the guard rings, whereas at the corners of the guard rings the corners increase the electrical field and reduce the breakdown voltage. To take this into account an additional ring, so $n_{fr} = 15$, was used. The layout of the sensor region simulated for the guard-ring optimization is shown in Figure 4.6.15. The difference to the structure used for the zero guard ring simulations is the introduction of the 15 floating rings and that the width is 1.2 mm measured from the mid of the gap between pixel and CCR to the scribe line. From the layout one sees that more than 60 geometrical parameters are required to describe this layout which makes a systematical variation of all these parameters impractical. To reduce the number of independent parameters some parameters were fixed and some additional dependences between the parameters were introduced. So, Al overhangs towards the n^+ implant were fixed for all guard rings to 5 μm . The widths of the $p^+ - n$ junctions were assumed to be the same for all guard rings. For the gaps between the guard rings it was assumed that they increase by a constant value or following some geometric progression from GR1 to GR15. The same was done for the Al overhangs towards the pixel of the guard rings. With this assumption 2D simulations in Cartesian coordinates for the optimization of the straight sections of the guard rings have been performed until the voltage differences between adjacent guard rings for bias voltages close to breakdown were approximately the same for the saturation value of the oxide-charge density of $N_{ox} = 3 \cdot 10^{12} \text{ cm}^{-2}$. Finally, simulations for the corners of the guard-ring structure were performed in cylindrical coordinates, in order to check that V_{bd}

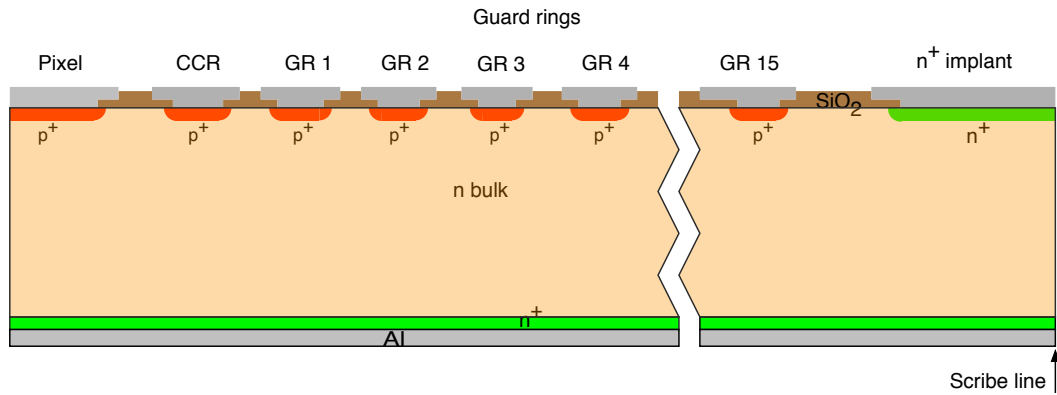


Figure 4.6.15.: Layout of the sensor region simulated for the guard-ring optimization.

does not decrease significantly at the corners. Cylindrical symmetry around the center of the circle defining the outer pixel corner has been assumed. The optimized design parameters for the guard-ring structure are given in Table 4.6.2. In Table 4.6.3 the results of the 2D simulations in Cartesian (2D (x, y)) and cylindrical (2D (r, z)) coordinates for the breakdown voltage as function of oxide-charge density and bulk resistivity for the optimized guard-ring design are given. They show that in the simulation the AGIPD specifications for the breakdown voltage can be met over the entire dose range.

Discussion of the simulation results

In Figure 4.6.16(a) the CCR current for the straight sections of the guard ring scaled to the full AGIPD sensor, which has a circumference of $2 \cdot (10.52 + 2.56)$ cm, is shown. As can be seen this design met the sensor specifications for the CCR current at 500 V and 20°C for the entire dose range. The current for $N_{ox} = 3 \cdot 10^{12} \text{ cm}^{-2}$ at 500 V is $\approx 1 \cdot 10^{-6} \mu\text{A}$ and increasing to a value of $\approx 3 \cdot 10^{-6} \mu\text{A}$ at 1000 V which is well within the specifications.

From the CCR current for $N_{ox} = 2 \cdot 10^{12} \text{ cm}^{-2}$ it can be seen, as stated in Table 4.6.3, that the breakdown voltage is slightly lower than for $N_{ox} = 3 \cdot 10^{12} \text{ cm}^{-2}$. The reason is that it is possible to optimize the spacings between the rings only for one oxide-charge density and this was done here for $N_{ox} = 3 \cdot 10^{12} \text{ cm}^{-2}$. Because the differences of breakdown voltage of one ring for different oxide-charge densities with $N_{ox} \geq 2 \cdot 10^{12} \text{ cm}^{-2}$ and $t_{ox} = 250 \text{ nm}$ are very small, as one can see from Figure 4.6.11, small difference in the punch-through voltage of the rings for $N_{ox} \geq 2 \cdot 10^{12} \text{ cm}^{-2}$ can result in a slightly lower breakdown voltage than for $N_{ox} = 3 \cdot 10^{12} \text{ cm}^{-2}$.

The Figure 4.6.16(b) shows the CCR current of the corners which is roughly two orders lower than that of the straight sections and contributes substantially to the total CCR current only if the

Parameter	Value
<i>Technological parameters</i>	
Oxide thickness	250 nm
Junction depth	2.4 μm
<i>Guard rings</i>	
Gap between pixel- and CCR p^+ implants	20 μm
Width of the p^+n junction of the CCR	90 μm
Al overhang of the CCR	5 μm
Gap between CCR and GR 1	12 μm
Widths of the p^+n junctions of the GRs	25 μm
Al overhangs towards pixels for GRs 1-15	2, 3, 4, ..., 16 μm
Al overhangs towards n^+ implant for GRs 1-15	5 μm
Gaps between GRs 1-2, 2-3, ..., 14-15	13.5, 15, 16.5, ..., 33 μm
Distance GR 15 to n^+ scribe-line implant	50 μm
Width of n^+ scribe-line implant	340 μm
Al overhang of n^+ scribe-line implant	15 μm

Table 4.6.2.: Optimized design parameters for the guard-ring structure of the AGIPD sensor.

guard ring is breaking down at the corner as shown here at 910 V for $N_{ox} \geq 2 \cdot 10^{12} \text{ cm}^{-2}$.

The difficulties in determining the optimal spacing between the implants of the guard rings for high breakdown voltage at the straight sections as well as at the corners of the guard-rings, can be seen in Figure 4.6.17, which shows the simulated guard-ring potential vs. bias voltage in Cartesian (left) and cylindrical coordinates (right) for $N_{ox} = 3 \cdot 10^{12} \text{ cm}^{-2}$ and a bulk resistivity of 5 $\text{k}\Omega\cdot\text{cm}$. Comparing the potential of the individual rings for the Cartesian with the cylindrical case shows that the punch-trough voltage of the rings is lower in the Cartesian case and they are therefore at a lower potential with increasing voltage as in the cylindrical case. For the Cartesian case the voltage differences between adjacent guard rings are similar at high voltages as shown

$N_{ox} [\text{cm}^{-2}]$	3 $\text{k}\Omega\cdot\text{cm}$		5 $\text{k}\Omega\cdot\text{cm}$		8 $\text{k}\Omega\cdot\text{cm}$	
	2D (x,y)	2D (r,z)	2D (x,y)	2D (r,z)	2D (x,y)	2D (r,z)
$1 \cdot 10^{12}$	> 1100 V	1060 V	> 1100 V	> 1100 V	> 1100 V	> 1100 V
$2 \cdot 10^{12}$	1000 V	830 V	1080 V	910 V	950 V	950 V
$3 \cdot 10^{12}$	1010 V	840 V	> 1100 V	910 V	1000 V	960 V

Table 4.6.3.: Results of the 2D simulations in Cartesian and cylindrical coordinates of the breakdown voltage as function of the surface density of oxide charges and bulk resistivity for the optimized guard-ring design.

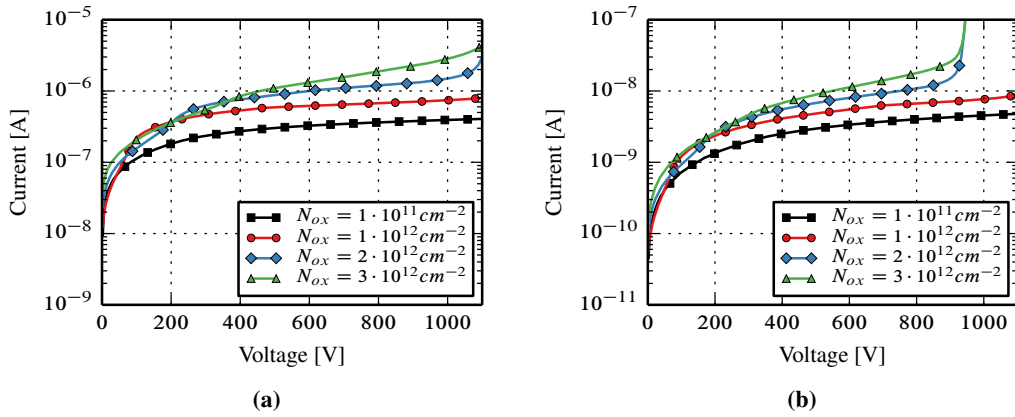


Figure 4.6.16.: CCR current of the guard ring structure for different oxide-charge densities and a resistivity of $5 \text{ k}\Omega\cdot\text{cm}$. (a) CCR current for the straight section of the guard ring from the (x,y) simulation scaled to the full AGIPD sensor. (b) CCR current of the corners from the (r,z) simulation.

in Figure 4.6.18 where the potential at 0.01 nm below the interface vs. position at a reverse voltage of 880 V is displayed. The contributions of the individual guard rings to the overall voltage drop are similar, and a high breakdown voltage with values above 1100 V is achieved. In Figure 4.6.18 it can also be seen that in cylindrical coordinates the voltage drop between the inner guard rings is higher than between the outer ones which results in a reduced breakdown voltage of 910 V .

In the optimized guard-ring structure the gap between CCR and GR1 is $12 \mu\text{m}$ and the spacing between the rings is increased by $1.5 \mu\text{m}$ per ring. Reducing the gap between CCR and GR1 is not possible without violating the design rules if one wants to maintain the metal overhang of $5 \mu\text{m}$ for the CCR. Using an increase for the spacing of $1.0 \mu\text{m}$ per ring results in an increase of the breakdown voltage at the corners to 1044 V for $N_{ox} = 3 \cdot 10^{12} \text{ cm}^{-2}$, but at the same time a decrease at the straight section to 748 V .

The implant width of the guard rings in the optimized design is $25 \mu\text{m}$. Trying to reduce this width to save space results in a decrease of the breakdown voltage at the corner as well at the straight sections if the other parameter are kept the same. The simulation results in Table 4.6.4 indicate that a reduction of the implant width, e. g. to $10 \mu\text{m}$, decreases the breakdown voltage at the corners from 910 V to 655 V . To meet the AGIPD specifications, additional guard rings would be required, which makes up most of the saved space.

The design concept of the guard-ring structure is that for the highest oxide-charge density the voltage drop of the individual rings is similar at breakdown. This requires a narrow spacing between the rings. The consequence for low oxide charges, as also shown in Figure 4.6.18 for $N_{ox} = 1 \cdot 10^{11} \text{ cm}^{-2}$, is that due to the low punch-through voltage the contribution of the inner

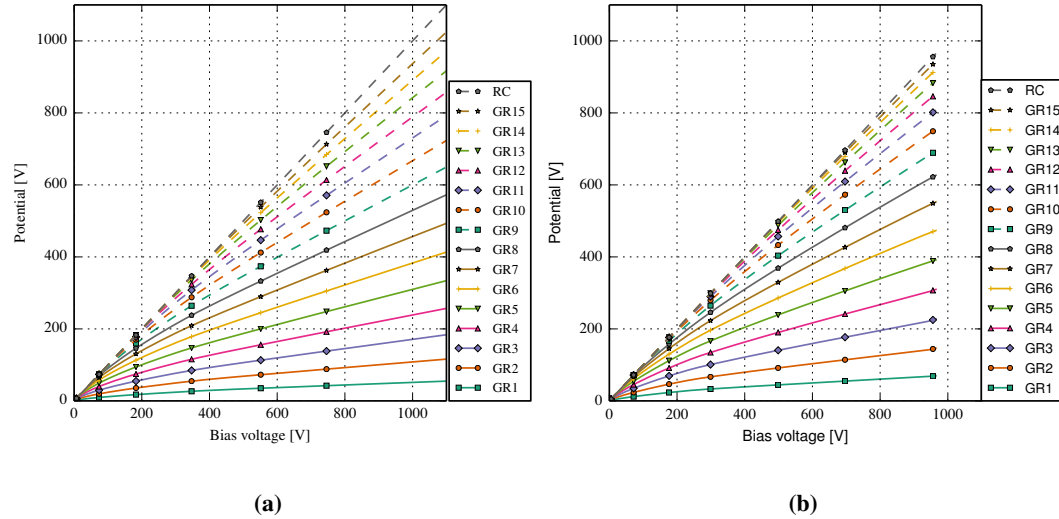


Figure 4.6.17.: Simulated potential of the 15 guard rings (GR) vs. bias voltage for $N_{ox} = 3 \cdot 10^{12} \text{ cm}^{-2}$ and a resistivity of $5 \text{ k}\Omega\cdot\text{cm}$. The voltage is applied at the rear contact (RC). (a) Simulation of the straight section of the guard rings in Cartesian coordinates. (b) Simulation of the corners in cylindrical coordinates.

guard ring to the overall voltage drop is less than that of the last rings. In the given example the voltage drop at GR1 is $\approx 25 \text{ V}$ whereas the voltage drop between GR15 and the backside potential is $\approx 130 \text{ V}$. The fact that GR15 is not on the backside potential has the consequence that the depletion region of the bulk extends much beyond GR15 and there is the risk that the depletion region reaches the cut edge leading to a high leakage current. To prevent these additional rings with an increased spacing could be used⁷ or as in our design a $340 \mu\text{m}$ wide n^+ scribe-line implant (channel stopper) with a metal overhang of $15 \mu\text{m}$.

To determine the range of bulk resistivity for which this design is working, simulations for different bulk resistivity and $N_{ox} = 5 \cdot 10^{10} \text{ cm}^{-2}$ have been performed. In the right Figure 4.6.19 the minimal distances of the depletion boundary to the cut edge as function of resistivity for different voltages is shown. For a resistivity of $10 \text{ k}\Omega\cdot\text{cm}$ the depletion boundary at 880 V is only a few micrometer from the cut edge. To be safe, the maximum resistivity was specified as $8 \text{ k}\Omega\cdot\text{cm}$ where the minimal distance of the depletion boundary is $50 \mu\text{m}$. For oxides with an initial oxide-charge density of $1 \cdot 10^{10} \text{ cm}^{-2}$ simulations for $8 \text{ k}\Omega\cdot\text{cm}$ gives a minimal distance of $25 \mu\text{m}$ at 880 V . Such a distance should probably be safe, but it depends on the damage inflicted during sawing (chip-outs, etc.). In this case, or also if the effective oxide charge is negative due to humidity effects or additional treatments which reduce the effective positive

⁷These additional rings should be designed without an outward metal overhang to ensure that the rings are on the same potential as the oxide. At the end this would require a full redesign of the guard-ring structure.

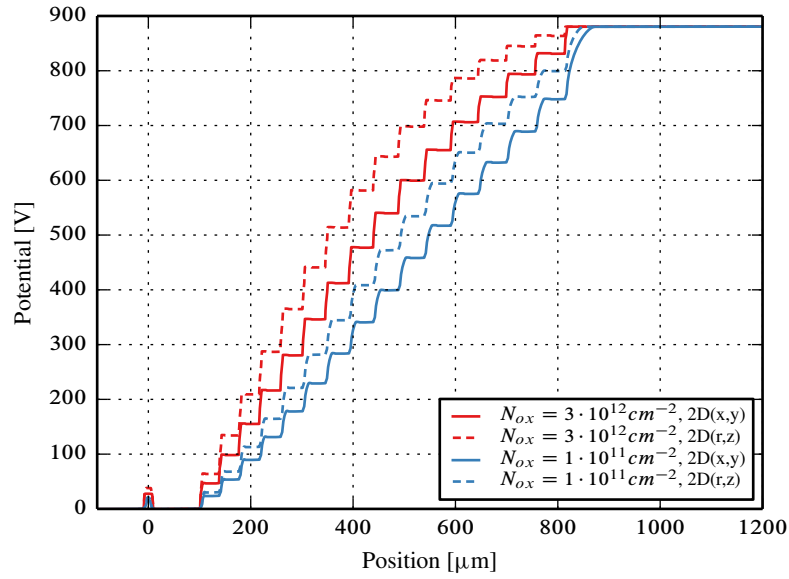


Figure 4.6.18.: Potentials $y = 0.01$ nm below the interface vs. position at a reverse voltage of 880 V.

charges in the dielectrics the maximum voltage has to be reduce until enough positive oxide charges are generated by irradiation.

It is clear that the guard-ring structure disturbs the potential distribution in the region of the last pixel resulting in an effectively wider pixel and in a higher noise. To reduce this effect the width of the p^+n junction of the CCR was chosen as $90 \mu\text{m}$ which results in a CCR which is half a pixel. In addition, this wide CCR increases the radius at the corners leading to a higher breakdown voltage. In Figure 4.6.20 the streamlines of the electric field are shown at 550 V for $N_{ox} = 1 \cdot 10^{11} \text{ cm}^{-2}$ and $N_{ox} = 1 \cdot 10^{12} \text{ cm}^{-2}$. To determine the effective pixel size the x-coordinate at the backside of the sensor of the last streamline which is ending at the pixel can be extracted. It can be seen that for $N_{ox} = 1 \cdot 10^{11} \text{ cm}^{-2}$ the effective pixel size is about $22 \mu\text{m}$

implant width [μm]	2D (x,y)	2D (r,z)
10	925 V	655 V
15	1000 V	765 V
20	1040 V	850 V
25	> 1100 V	910 V

Table 4.6.4.: Results of the 2D simulations in Cartesian and cylindrical coordinates of the breakdown voltage for different implant widths while keeping the other parameters the same. The oxide-charge density is $3 \cdot 10^{12} \text{ cm}^{-2}$ and the bulk resistivity $5 \text{ k}\Omega\cdot\text{cm}$.

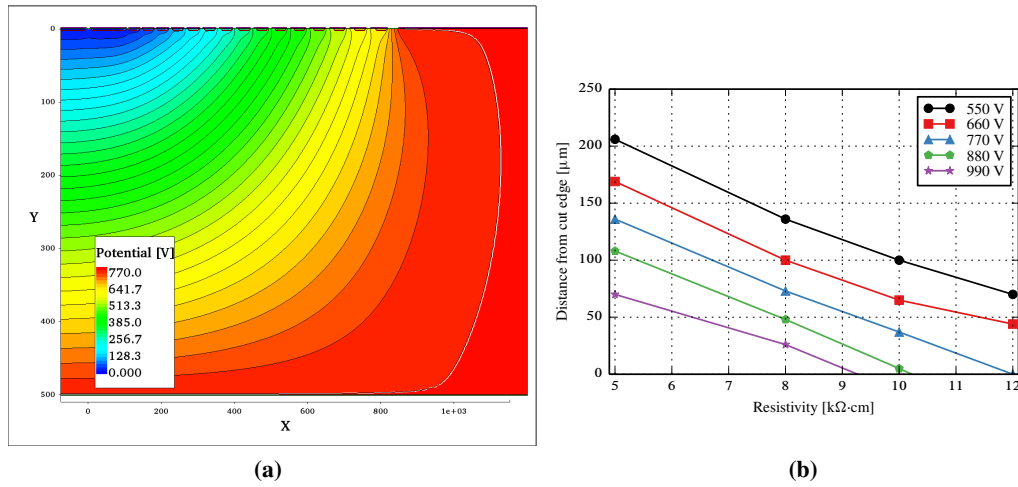
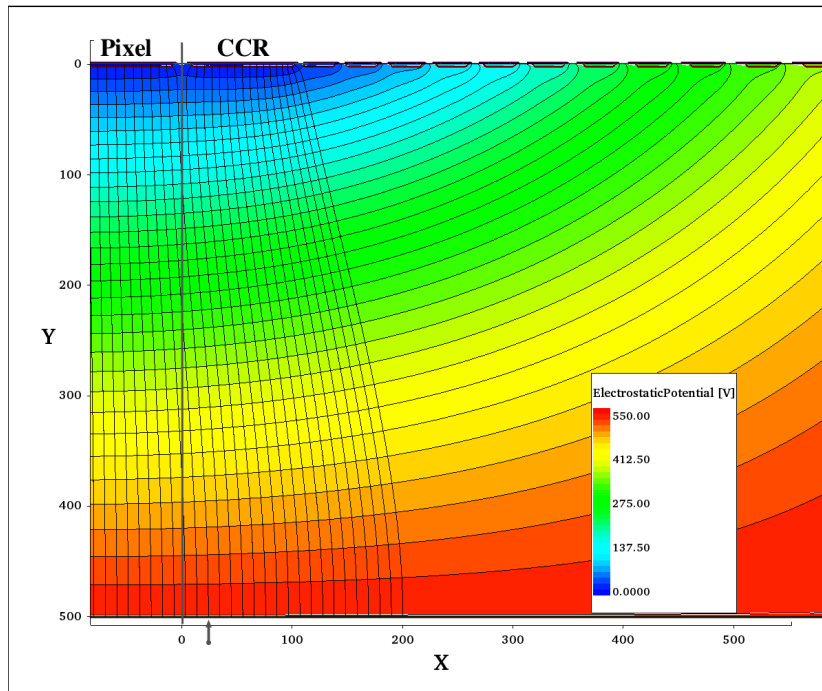


Figure 4.6.19.: (a) Potential at 770 V for $N_{ox} = 5 \cdot 10^{10} \text{ cm}^{-2}$ and $8 \text{ k}\Omega\cdot\text{cm}$. The white line indicates the depletion boundary. (b) Minimal distance of the depletion boundary to the cut edge as function of resistivity for different voltages for $N_{ox} = 5 \cdot 10^{10} \text{ cm}^{-2}$.

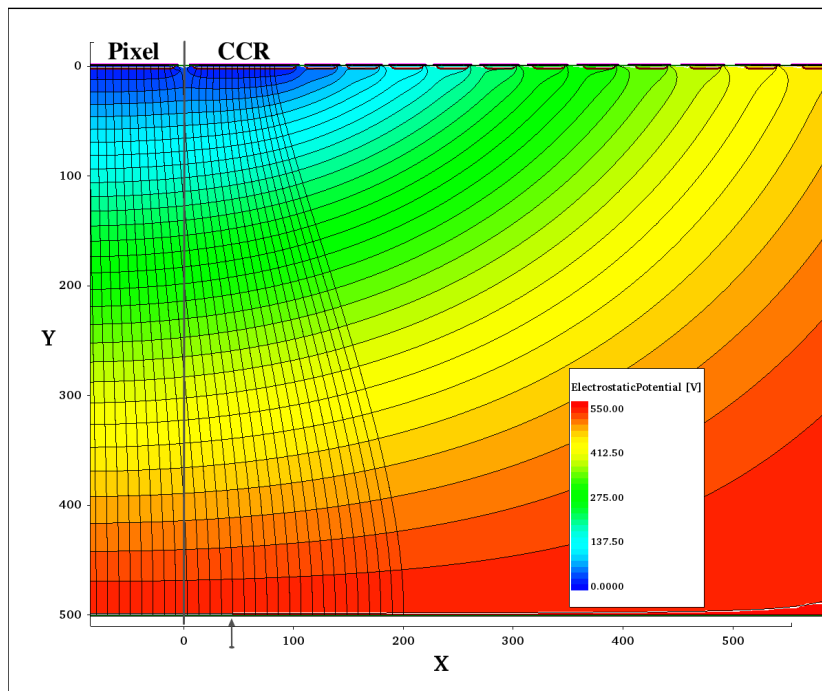
larger than normal and increasing to a value of $47 \text{ }\mu\text{m}$ at $N_{ox} = 3 \cdot 10^{12} \text{ cm}^{-2}$.

4.6.4. Summary and conclusions

The simulation shown that the optimized guard-ring structure meets the AGIPD specification with respect to breakdown voltage and leakage current over the full dose range. Problems can arise for non-irradiated sensors with low oxide-charge densities or operation in a humid atmosphere if the bulk resistivity is too high. In this case a lower operational voltage would be required. Because the AGIPD detector will be operated in vacuum this problem should not appear.



(a)



(b)

Figure 4.6.20.: Streamlines of the electric field at 550 V showing the increase of the effective pixel size. (a) $N_{ox} = 1 \cdot 10^{11} \text{ cm}^{-2}$ (b) $N_{ox} = 3 \cdot 10^{12} \text{ cm}^{-2}$. To limit the computational time only streamlines in the interval $x \in [-100 \mu\text{m}, 200 \mu\text{m}]$ and starting at $y = 500 \mu\text{m}$ where calculated.

4.7. Pixel optimization

4.7.1. Introduction

The design of the pixel requires finding the geometrical and process parameters in such a way that the specifications of the sensor can be met in terms of the breakdown voltage, leakage current and interpixel capacitance. Even if the influence of some of these parameter is in principle obvious, an optimization can be done only with TCAD simulations. But here numerical issues occur, since a squared pixel is inherently a 3D problem. The reason is that due to the large pixel size and the fine mesh at the interface, which is required to describe accurately the surface damage, the computer resources needed for the optimization are too large. For example for a pixel with a gap of 20 μm the area of the Si-SiO₂ interface outside of the implant is around 7600 μm^2 . Covering this with a grid of 100 nm \times 100 nm would results in $7.6 \cdot 10^5$ grid points only for the top layer. Because for oxide-charge densities of $3 \cdot 10^{12} \text{ cm}^{-2}$ the electron density at the interface reaches values of 10^{19} cm^{-3} resulting in a Debye length of $\approx 1.5 \text{ nm}$ a grid with 100 nm mesh size will not resolve sufficiently accurate the y-dependent (lateral) variation of the accumulation layer as function of reverse bias or of a periodic AC voltage required for capacitance simulations. Consequently, one has to rely on 2D simulations to identify the dependencies of the results on the geometrical and process parameters. The 2D simulation results for the dark current and interpixel capacitance can be scaled to 3D values which will not give the correct voltage dependence, but enough information for limiting cases and enables one to reduce the parameter space. Finally, a check of the breakdown voltage and dark current as function of voltage by a 3D simulation was done where only 1/4 pixel was simulated with symmetric boundary conditions.

4.7.2. 2D-Simulation results

Geometric model and current scaling

The geometric model used in the 2D device simulation is shown in Figure 4.5.1(a). As seen from the top view shown in the Figure 4.7.1(a) it is a cut from the middle of one pixel with a size of 200 μm and the sensor thickness 500 μm to the middle of the direct-neighbor pixel resulting in a strip geometry in 2D with an extension in the third dimension of 1 μm . For the $I-V$ simulation both strips were grounded and the reverse bias was applied on the backside. To scale the current from 2D to 3D in the non-irradiated case where the bulk current is dominating the sum of the current of both strips was multiplied with a factor of 200 to obtain the correct pixel volume as shown in the Figure 4.7.1(b). In the irradiated case the surface current dominates and the sum of the current of both strips was multiplied with a factor of 400 which gives approximately the correct area of the SiO₂ as indicated in the Figure 4.7.1(c). Thereby the brown areas at the corners of the pixel were counted twice resulting in an relative error of less than 11 % for a gap of $\leq 40 \mu\text{m}$ as long as an additional rounding of the implant at the corner is not taken into

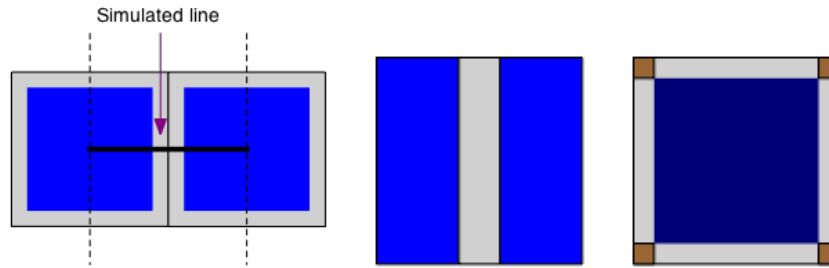


Figure 4.7.1.: (a) Top view of simulated area (b) Scaling in the non-irradiated case (c) Scaling in the irradiated case

account. The gap and metal overhang were varied in the range given in Table 4.7.1 and the oxide thickness between 200 nm and 1000 nm.

gap [μm]	20	30	40
overhang [μm]	0, 2.5, 5	5, 10	0, 2.5, 5, 10

Table 4.7.1.: Simulated gap and metal overhang values

Oxide-thickness dependence

The dependence of the breakdown voltage on the oxide thickness is similar to the case of the zero guard ring structure and can be seen from the current vs. voltage plot shown in Figure 4.7.2. The simulation was done for a gap of 20 μm , metal overhang of 5 μm , junction depth of 1.2 μm and oxide-charge density of $3 \cdot 10^{12} \text{ cm}^{-2}$. The breakdown voltage decreases with increasing oxide thickness to a value which is given by the junction breakdown. Only oxides with $t_{ox} < 300 \text{ nm}$ show no breakdown in this configuration and therefore the further simulations were restricted to oxide thicknesses of $\leq 300 \text{ nm}$. Increasing the gap to values larger than 20 μm while keeping the metal overhang and the oxide thickness will result in a higher electric field at the implant edges and leads to lower breakdown voltages compared to the 20 μm gap case.

Electron-accumulation layer

One important point is the formation of the electron-accumulation layer and its dependence on the geometry, boundary conditions and voltage. Following the discussion in [24] for a non-irradiated sensor with an oxide-charge density of e.g. $1 \cdot 10^{11} \text{ cm}^{-2}$ without any applied reverse-bias, an electron-accumulation layer will be present at the Si-SiO₂ interface in the gap region to compensate the positive oxide charge. Applying a reverse-bias on the backside of the sensor makes the space-charge region grown from the strips, both in depth and laterally. The increase of the voltage across the oxide in the gap region is accompanied by a decrease in charge

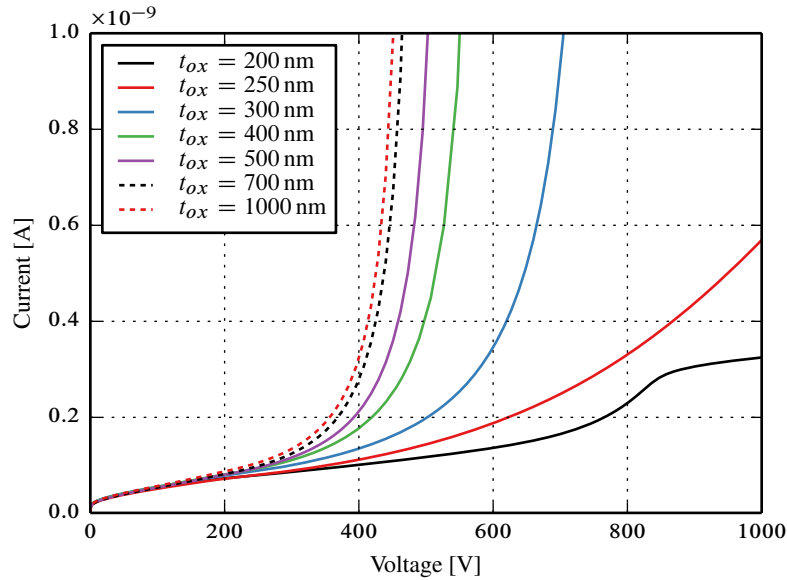


Figure 4.7.2.: Current vs. voltage for different oxide thicknesses. The used parameter are a gap of $20\ \mu\text{m}$, a metal overhang of $5\ \mu\text{m}$, a junction depth of $1.2\ \mu\text{m}$ and an oxide-charge density of $N_{ox} = 3 \cdot 10^{12}\ \text{cm}^{-2}$.

density of the electron-accumulation layer. The question is, and this depends strongly on the gap, boundary condition and oxide charge, whether the space-charge regions of the two strips merge in the depth of the n -bulk with increasing reverse bias before or after the flatband condition at the interface are reached. In the first case the merging of the space-charge regions forms a barrier for the electrons caught near the surface and the reduction of the electron layer is slowed down drastically. Its potential changes only slowly with the backside potential resulting in an accumulation layer even for higher voltages. In the second case the electron layer will disappear completely before such a situation arises and with reverse-bias voltage above flatband conditions the space-charge region in the gap region will grow from the Si-SiO₂ interface into the sensor volume.

For an irradiated sensor with Neumann boundary conditions the gap has to be small to reach a high breakdown voltage and an electron-accumulation layer will be always present. An example is shown in Figure 4.7.3(a) where the electron density at 500 V for a gap of $20\ \mu\text{m}$ and an oxide-charge density of $N_{ox} = 2.1 \cdot 10^{12}\ \text{cm}^{-2}$ corresponding to an X-ray dose of 1 MGy is plotted. The white line in the plot indicates the depletion boundary. The electron layer covers most of the interface of the gap even below the metal overhang which is $5\ \mu\text{m}$. The maximum depth of the electron layer is around $1.5\ \mu\text{m}$ and is reached in the middle of the gap. To both sides along the symmetry axis in the middle of the gap the electron density is increased compared to the rest of the depleted bulk due to a current flowing from the accumulation layer to the rear

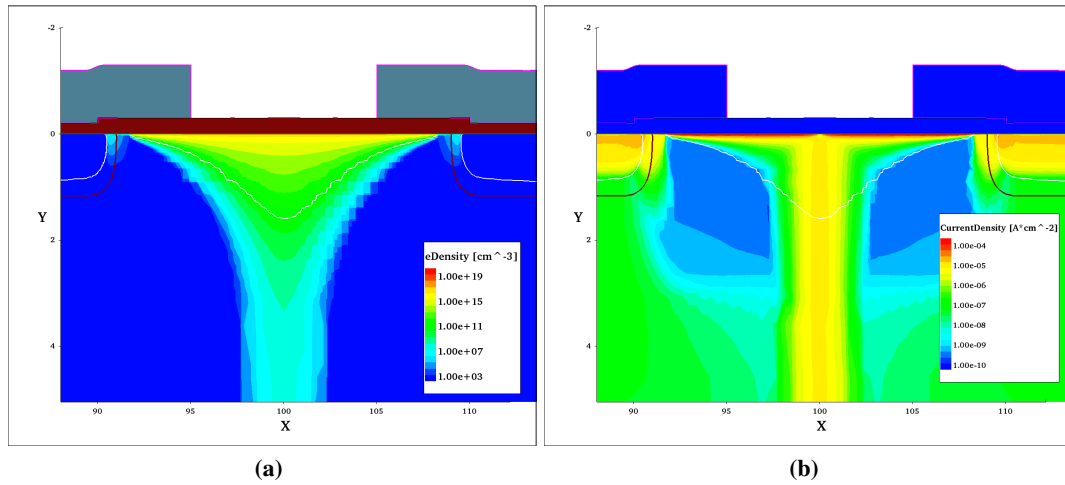


Figure 4.7.3.: Electron density (a) and current density (b) at 500 V for a gap of 20 μm and oxide-charge density $N_{ox} = 2.1 \cdot 10^{12} \text{ cm}^{-2}$ corresponding to an X-ray dose of 1 MGy.

contact as shown in Figure 4.7.3(b). This current flow arises from the condition for a stationary state of the accumulation layer. The current flowing out of the accumulation layer has to be equal to the current flowing into and generated within the accumulation layer. This condition also determines the potential of the accumulation layer. From the cut of the electrostatic potential at $x = 96, 98$ and $100 \mu\text{m}$ (midgap) shown in Figure 4.7.4(a) it can be seen that there is a barrier which traps the electrons at the interface and that in the gap center at around $4 \mu\text{m}$ the potential has a saddle point and the electric field is zero. The current will flow over this saddle point where the barrier is smallest as shown in the band diagram in Figure 4.7.4(b). The current is due to thermionic emission of electrons which leads to an exponential $I-V$ characteristics [16]. Because the surface current is generated in the depleted area at the Si-SiO₂ interface the holes will directly move to the p^+ -implant whereas most of the electrons will enter the electron-accumulation layer. Consequently, in the stationary state essentially all electrons generated by surface generation will leave the accumulation layer via the saddle point and reach the backplane.

The voltage and dose dependence of the width of the electron-accumulation layer is presented in Figure 4.7.5(a). They were obtained from the electron density 10 nm below the Si-SiO₂ interface using as condition a value of the electron density equal to the bulk doping. The left axis shows the difference between the gap width and the accumulation layer width, since the surface current is proportional to this difference, and the right axis shows the accumulation layer width. The simulations were done for a gap of 20 μm , oxide thickness of 300 nm, junction depth of 1.2 μm and metal overhangs of 2.5 and 5 μm . As can be seen, in the non-irradiated case a small, only weak voltage dependent accumulation layer is present even at high voltages. In the case of $N_{ox} = 1.3 \cdot 10^{12} \text{ cm}^{-2}$ corresponding to an X-ray dose of 100 kGy and $N_{ox} = 2.1 \cdot 10^{12} \text{ cm}^{-2}$

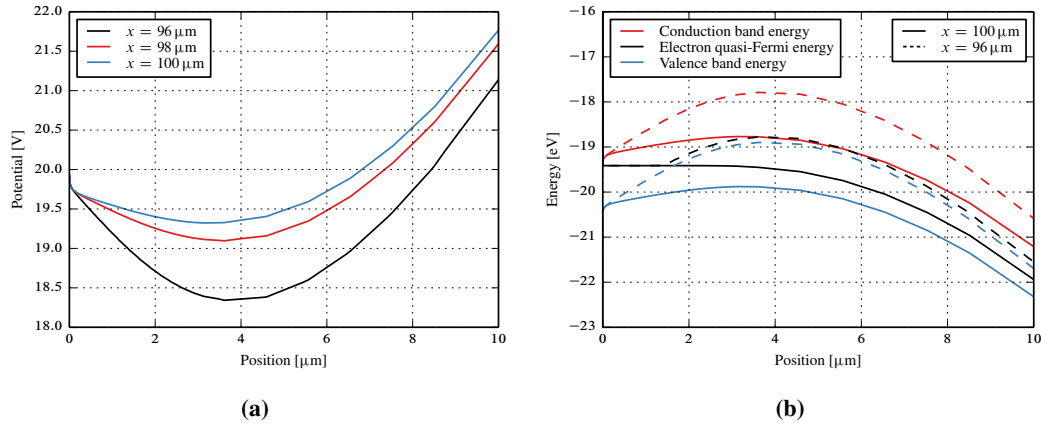


Figure 4.7.4.: Cuts of the electrostatic potential (a) and the band diagram (b) at 500 V for a gap of $20 \mu\text{m}$ and oxide-charge density $N_{ox} = 2.1 \cdot 10^{12} \text{ cm}^{-2}$ corresponding to an X-ray dose of 1 MGy.

corresponding to an X-ray dose of 1 MGy at low voltages practically the entire region between the junctions is covered by the accumulation layer and for high voltages the region under the metal overhang depletes without a significant depletion of the gap region which is not covered by metal. The current vs. voltage dependence in Figure 4.7.5(b) indicates the correlation of the depleted surface and current. Because for sufficient high oxide-charge densities only the region under the metal is depleted the metal overhang should be small to minimize the leakage current. The results for $N_{ox} = 2.8 \cdot 10^{12} \text{ cm}^{-2}$ corresponding to an X-ray dose of 10 MGy are similar up to 900 V for both metal overhangs and the currents shows a breakdown.

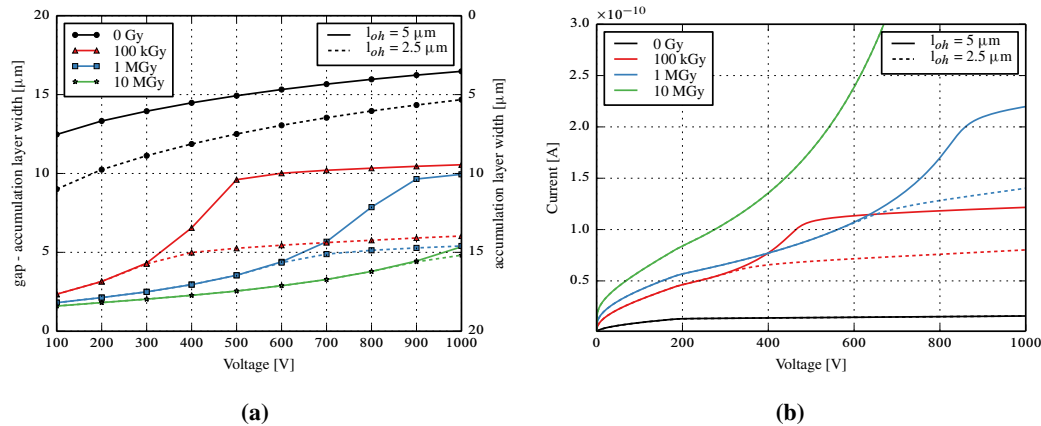


Figure 4.7.5.: Accumulation layer width (a) and current (b) as function of voltage for a gap of $20 \mu\text{m}$, junction depth of $1.2 \mu\text{m}$ and metal overhangs of 2.5 and $5 \mu\text{m}$.

Gap- and junction-depth dependence

For the design of the pixel one has to take into account that the distance between the implants along the diagonal is

$$d = \sqrt{2} \cdot (2 \cdot r + \text{gap}) - 2 \cdot r \quad (4.7.1)$$

where r is the radius of the implant at the corner. For a gap of 20 μm and a radius of 10 μm the distance is 36.6 μm and for a radius of 5 μm the distance is 32.4 μm . A 2D simulation with these distances as gap will result in a too high breakdown voltage for the pixel, since in 3D the electric field is enhanced due to the curvature of the implant at the corner. This enhancement is evident, because for the spherical region at the corner the field lines approach a point in 3D while they approach a line in 2D for the cylindrical junction at the edges. Therefore with a 2D simulation it is difficult to estimate up to which gap no breakdown should occur, but certainly not below 40 μm . That this can be achieved only with the deeper junction can be seen from Figure 4.7.6 which shows $I-V$ simulations for gaps of 20, 30 and 40 μm , oxide thickness of 300 nm, metal overhang 5 μm and at 10 MGy. For the junction depth of 1.2 μm and a gap of 40 μm the breakdown voltage is below 300 V. A decrease of the oxide thickness to 250 nm will not increase the breakdown voltage sufficiently for a sensor which can be operated safely at high voltages. The $I-V$ curves for the junction depth of 2.4 μm do not show a breakdown up to

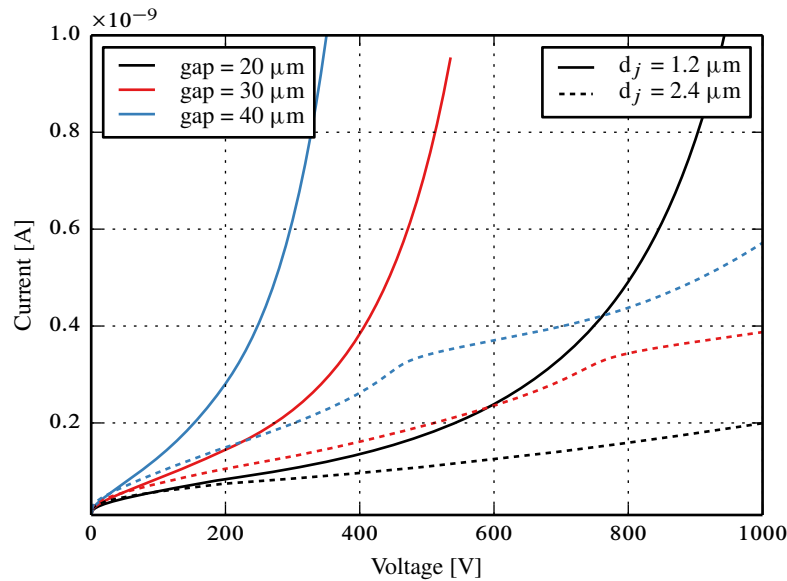


Figure 4.7.6.: Single pixel current as function of voltage for different gaps, junctions depth, oxide thickness of 300 nm, metal overhang 5 μm and at 10 MGy.

1000 V. Consequently, the deeper junction should be used for the sensor. The comparison of the $I-V$ curves for different gaps indicates that the region under the metal overhang depletes at a

lower voltage for a larger gap which is due to the higher electric fields in this case. Because the distance between the implants along the diagonal is larger than the gap to the nearest neighbor this behavior prevents a scaling of the 2D results to 3D for a square pixel.

Interpixel capacitance

As mentioned in the introduction a 3D simulations of the interpixel capacitance for irradiated pixels is not possible. To have at least an estimation, the 2D simulation results were scaled to 3D values. As will be shown in the next section the electron-accumulation layer has a different voltage dependence in 2D and 3D whereupon at a given voltage the accumulation layer width in 2D is greater or equal to the one in 3D between direct neighbor pixels. This will mean that the 2D scaled results will be an upper limit. For the scaling of the 2D simulated interstrip capacitances $C_{int,si}^s$, analytical expressions for the interstrip capacitance $C_{int,th}^s$ [132] and for the interpixel capacitance $C_{int,th}^p$ [133], which both neglect the metal overhang, were used and the assumption that the 3D simulated interpixel capacitance $C_{int,si}^p$ is given by

$$C_{int,si}^p = \frac{C_{int,si}^s}{C_{int,th}^s} \times C_{int,th}^p \quad (4.7.2)$$

was made.

According to [133] the total pixel capacitance can be divided into three different contributions (see Figure 4.7.7): Each pixel has a pixel-to-substrate capacitance C_0 . Each of the four nearest neighbor pixel is capacitively coupled to the center pixel by C_1 , and all diagonal neighbor pixel by C_2 . When all adjacent pixels are virtually grounded at the input of the charge-sensitive amplifiers the total pixel capacitance is given by $C_P = C_0 + 4C_1 + 4C_2$. For the calculation of the capacitances normalized to the one-dimensional plate capacitance C_{1d} , with the normalized width $\lambda = L/W$, and the normalized separation $s = S/W$ the following expressions have been used:

$$\frac{C_0}{C_{1d}} = (1.15)^{1/\lambda} + \frac{2.3}{\lambda} \left[1 - e^{-(s/\sqrt{\lambda})} \right] \quad (4.7.3)$$

$$\frac{C_1}{C_{1d}} = \frac{0.23}{s + 0.18} \left(\frac{1}{\lambda} \right)^{0.75} - 0.07 \left(\frac{1}{\lambda} \right) \quad (4.7.4)$$

$$\frac{C_2}{C_{1d}} = (0.1)^\lambda \left[1 - 1.15 \left(\frac{7}{s + 3} - 1 \right) s \right] \quad (4.7.5)$$

Using this expression the interpixel capacitance is given by

$$C_{int,si}^p = 4C_1 + 4C_2. \quad (4.7.6)$$

The interstrip capacitance is much more complex and will not be presented. The value which

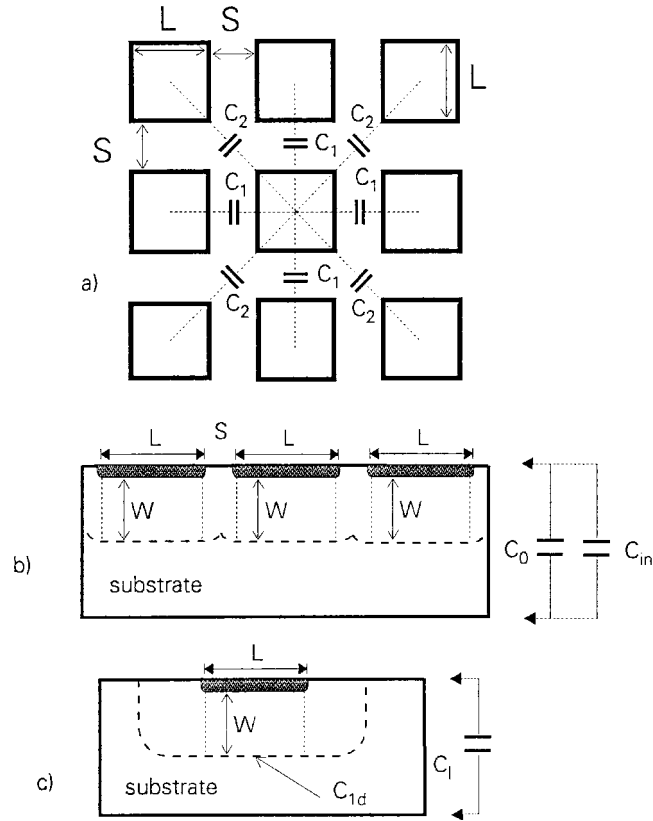


Figure 4.7.7.: (a) Pixel diode array and (b) depletion region of the diode. Diode side L , space between diodes S , depletion region W , pixel-to-substrate capacitance C_0 ; capacitance between adjacent pixels C_1 ; capacitance between diagonal pixels C_2 ; plate capacitance C_{1d} ; and the input capacitance of the preamplifier C_{in} . Picture taken from [133].

was used for a gap of $20 \mu\text{m}$ is $C_{int,th}^s = 0.88 \text{ pF/cm}$ [132].

Simulation results of the interpixel capacitance as function of voltage are shown in Figure 4.7.8. As parameters a gap of $20 \mu\text{m}$, an oxide thickness of 250 nm , a metal overhang of $5 \mu\text{m}$ and a $2.4 \mu\text{m}$ deep junction were used. The capacitance was calculated at 100 kHz , but because no interface traps were include no frequency dependence will occur. The voltage dependence of the interpixel capacitance for the higher oxide charges is due to the electron-accumulation layer. For the non-irradiated case the interpixel capacitance is 98 fF at 500 V increasing to 120 fF for $N_{ox} = 1 \cdot 10^{12} \text{ cm}^{-2}$. In this case the region under the metal is depleted which is not the case for $N_{ox} = 3 \cdot 10^{12} \text{ cm}^{-2}$ resulting in an interpixel capacitance of 310 fF . Even if the correct voltage dependence of the interpixel capacitance can not be calculated in 2D, the results, which are upper limits, shows that with the above parameters the specifications will be met.

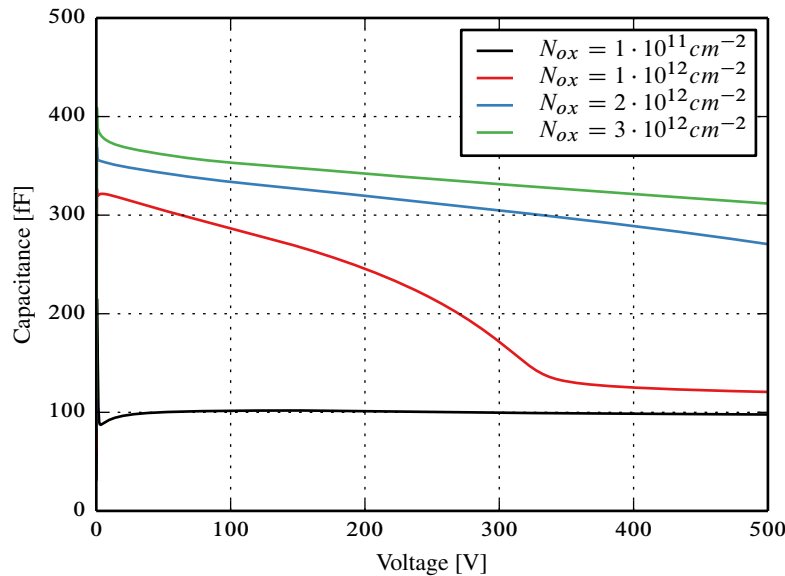


Figure 4.7.8.: Interpixel capacitance as function of voltage for a gap of 20 μm , oxide thickness of 250 nm, metal overhang of 5 μm and junction depth of the 2.4 μm .

4.7.3. 3D-Simulation results

The 2D simulation results show that with a gap of 20 μm , a metal overhang of 5 μm , an oxide thickness of 250 nm, and a 2.4 μm deep junction the sensor specifications can be met. To check this, 3D simulations were performed for a 1/4 of a pixel as shown in Figure 4.7.9. At the corner a radius of the implant of 10 μm and radius of 12 μm for the metal was used. At the lateral edges of the pixel reflecting Neumann boundary condition were employed. This means that effectively the simulated geometry consist out of a 1/4 of pixel together with its mirror images from the reflection along the edges and the center of the diagonal to the next direct neighbor.

The simulated I - V curves in 3D and 2D for different oxide charges are shown in Figure 4.7.10 where all results are scaled to a full pixel. First the important results is that even for $N_{ox} = 3 \cdot 10^{12} \text{ cm}^{-2}$ the simulations do not show a breakdown up to 1000 V and the currents are within the sensor specifications. The 3D curves shows some small wiggles which are due to the mesh size at the interface and could only be avoided using a finer mesh but which is limited by the computational resources. As can be seen by a comparison of the 3D and the 2D results for the different oxide-charge densities the voltage dependence of the current is different. For $N_{ox} \leq 2 \cdot 10^{12} \text{ cm}^{-2}$ the calculated currents for low and high voltage are similar, but not in the intermediated voltage range. Similar to the 2D case in 3D essentially only the region under the metal depletes which can be seen by the fast increase of the current and the subsequent saturation for increasing voltages. But this happens in 3D at a lower voltage than in 2D. This is

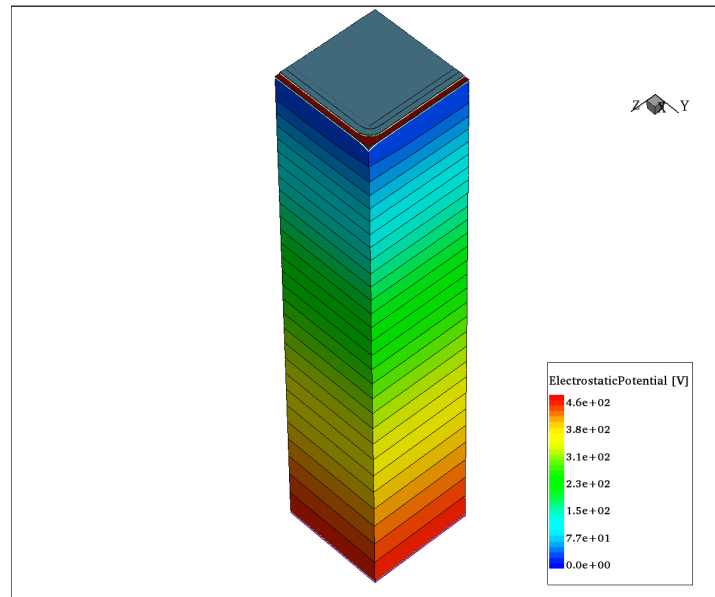


Figure 4.7.9.: Pixel used for 3D simulation. Shown is the electrostatic potential at 460 V for $N_{ox} = 1 \cdot 10^{12} \text{ cm}^{-2}$.

due to the corners of the pixel which cannot be taken correctly into account in 2D simulations.

The electrostatic potential distribution shown in Figure 4.7.11a for $N_{ox} = 1 \cdot 10^{12} \text{ cm}^{-2}$ and a reverse bias of 460 V indicates that a saddle point is located in the middle between pixels along the diagonal. Along the edge a few micrometer below the interface the electrostatic potential is reduced forming a barrier for the electrons in the accumulation layer. From the current density plot (see Figure 4.7.11b) it can be seen that the thermionic emission current flows only at the corner. Therefore in the stationary state the electrons generated by the surface generation somewhere at the depleted interface and entering the accumulation layer can leave it only by a current flowing over the saddle point at the corner. A behavior not reproducible in 2D.

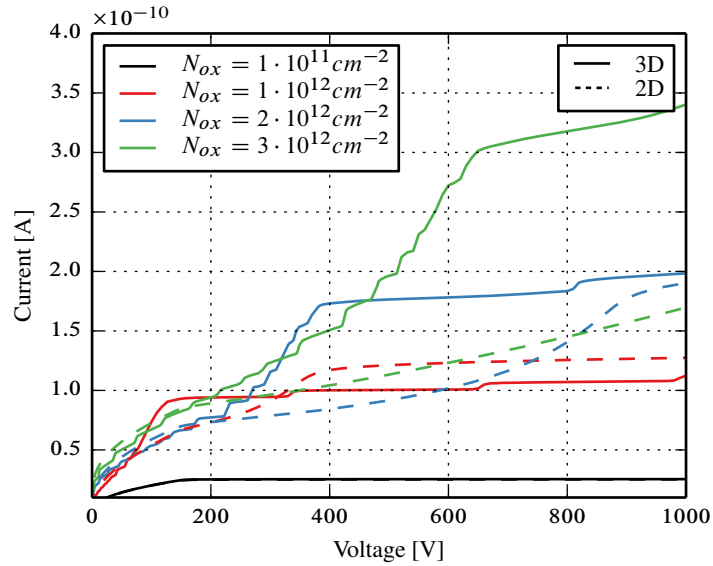


Figure 4.7.10.: Current as function of voltage simulated in 3D and 2D for different oxide-charge densities with a gap of 20 μm , an oxide thickness of 250 nm, a metal overhang of 5 μm and a junction depth of the 2.4 μm .

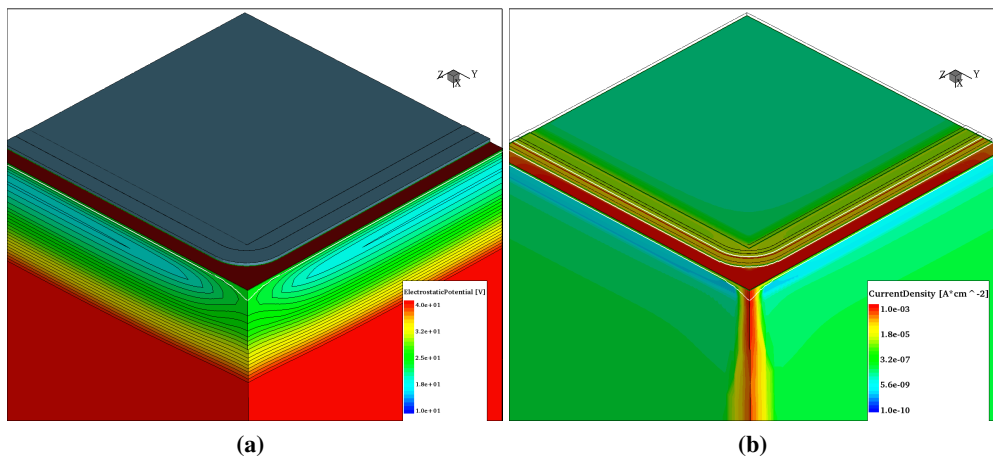


Figure 4.7.11.: Electrostatic potential (a) and current density (b) for $N_{ox} = 1 \cdot 10^{12} \text{ cm}^{-2}$ and a reverse voltage of 460 V. In the plot of the current density the Al layer and the oxide are removed.

4.8. AGIPD-sensor layout

Based on the TCAD simulations the following design of the AGIPD sensor was built. Figure 4.8.1 shows the drawing of one AGIPD sensor. The overall dimensions of the sensor after cutting are $107.6 \text{ mm} \times 28.0 \text{ mm}$. Each sensor consists of 2×8 fields of 64×64 pixels each. Each field is bump-bonded (4096 pixels plus 64 to the CCR) to a separate AGIPD-readout ASIC.

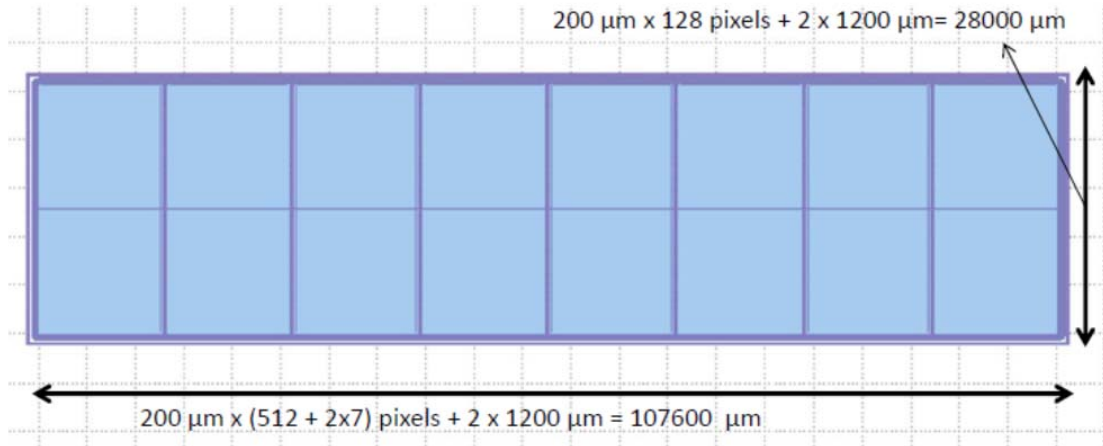


Figure 4.8.1.: Overall layout and dimensions of a sensor. The 2 rows of 8 fields correspond to the 16 readout ASICs bump-bonded to the sensor. The sensor dimensions after cutting are $107600 \mu\text{m} \times 28000 \mu\text{m}$.

The standard pixel dimensions are $200 \mu\text{m} \times 200 \mu\text{m}$. Figure 4.8.2 shows the layout of the standard pixel with the following parameters:

- Gap between p^+ -implantations: $20 \mu\text{m}$
- Metal overhang: $5 \mu\text{m}$
- Radius of p^+ -implantation at pixel corner: $10 \mu\text{m}$
- Radius of metal layer at pixel corner: $12 \mu\text{m}$

The squares are the vias to connect the p^+ -implant through the SiO_2 to the metal layer. The octagons centered at (100,30) are the opening through the passivation layer, the UBM (under-bump-metal) and the indium layer, respectively. In order to avoid inactive regions at the interfaces between readout ASICs and maintain the $200 \mu\text{m}$ pixel pitch some pixel have to be rotated around the centre of the sensor and the pixels to the right and to the left to the 7 vertical inter-ASIC boundaries have dimensions of $400 \mu\text{m} \times 200 \mu\text{m}$.

Figure 4.8.3 shows the layout of the guard-ring structure at the left lower corner of the sensor. The parameters are given in Table 4.6.2. The distance from the middle between the last pixel and the CCR to the cut-edge is $1200 \mu\text{m}$. The figure in the bottom shows the guard-ring structure at

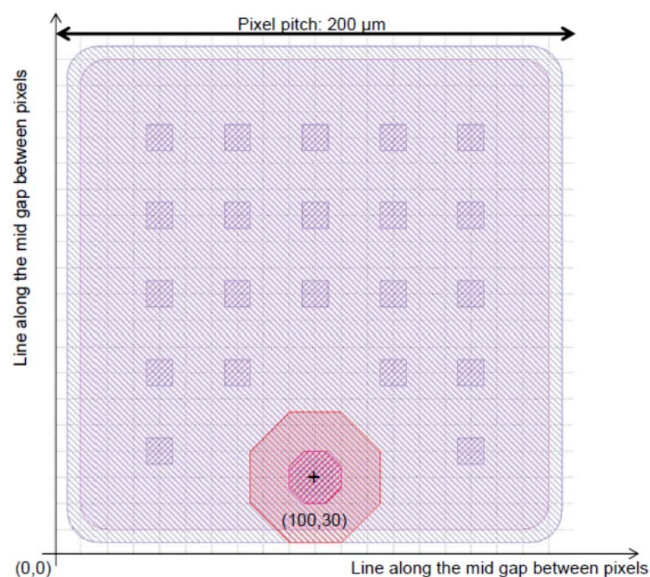


Figure 4.8.2.: Layout and parameters of a standard pixel of $200\ \mu\text{m} \times 200\ \mu\text{m}$.

the left, middle and right lower corners of the sensor. Through rotation the corresponding upper part of the sensor is obtained.

The geometrical parameter of the guard-ring structure and the pixel are optimized for a oxide thickness of $250\ \text{nm}$ and a junction depth of $2.4\ \mu\text{m}$. The simulated sensor dark current, CCR dark current and interpixel capacitance at $500\ \text{V}$ are given in Table 4.8.1. The sensor dark current is calculated from the 3D pixel simulations and the interpixel capacitance from the 2D simulations.

Dose [MGy]	Sensor dark current [μA]	CCR dark current [μA]	C_{int} [fF]
0.01	7.4	0.6	120
1	12.7	0.9	270
10	14.4	1.2	312

Table 4.8.1.: Simulated performance at $500\ \text{V}$.

4. Optimization of the AGIPD sensor

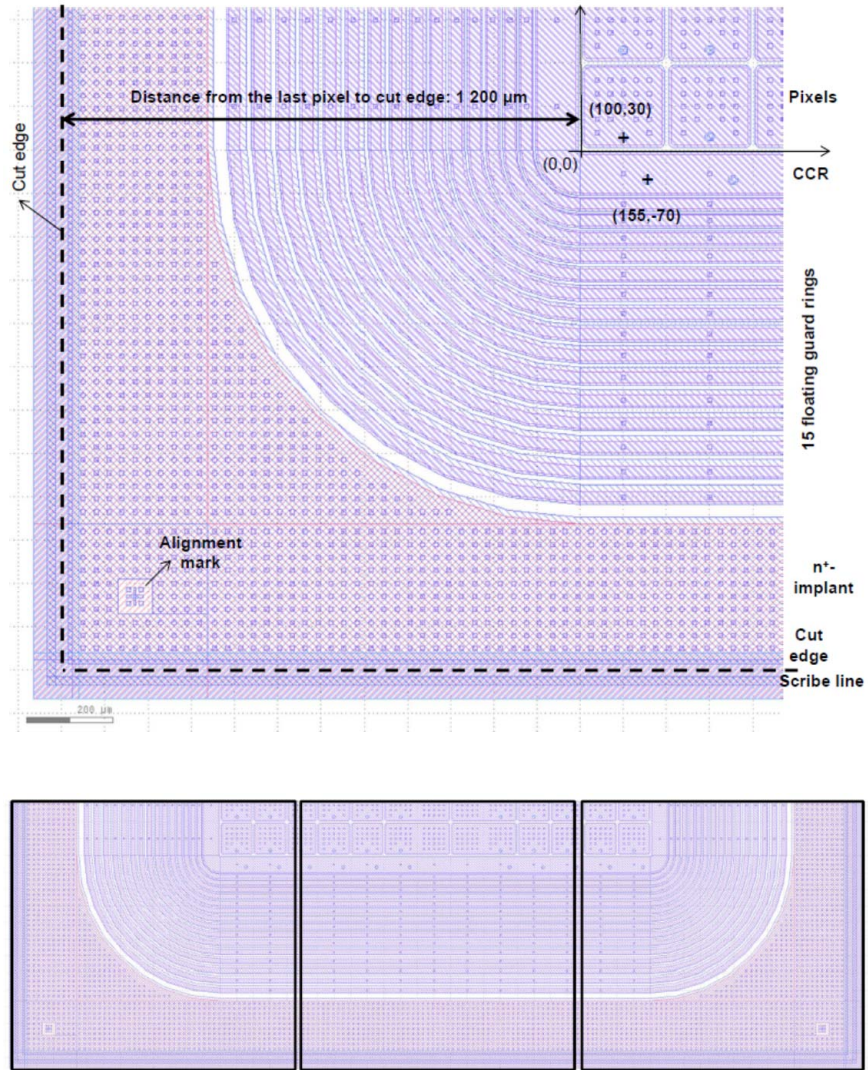


Figure 4.8.3.: Top: Layout of the left lower corner of the sensor. Bottom: Layout of the left, middle and right lower side.

4.9. Summary

The requirements of the AGIPD sensor are challenging for the design of a $p^+ - n$ pixel sensor. Especially the required high breakdown voltage in combination with the surface damage and vacuum operation requires a special design. It was shown that this requires the usage of a deeper implant than usual, a thinner oxide and a metal overhang. In addition the pixel gap has to be small to further reduce the electrical field at the implant edges and to reduce the surface current. The pixel and the guard-ring structure was optimized so that the sensor specification are met over the full dose range.

5. Measurement results of optimized AGIPD test structures

After negotiations with various vendors SINTEF [72] has been selected for the production of the AGIPD sensors. SINTEF was willing to modify their standard process so that our requirements can be fulfilled with respect to the oxide thickness and junction depth. The order comprises 72 working sensors to be delivered in two batches of 36 sensors each. The first batch was delivered in February 2013. One wafer (WAFER04) with two bad AGIPD sensors on it, but with working test structures, was chosen to verify the optimization of the sensor for the X-ray radiation hardness. To show that this optimization was successful this chapter is organized as follows: First an overview of the design of the test structures and the AGIPD sensor processing is given. Then the electrical characteristics of the non-irradiated test structures and some details on the X-ray radiation is presented followed by the measurements after irradiation and the comparison to the prediction of the simulation. Even if the AGIPD sensor is designed for the operation in vacuum also tests under humid conditions have been performed and will be shown at the end of this chapter.

5.1. AGIPD sensor processing and overview on the test structures

The AGIPD sensors was processed on 6 inch wafers with two full size sensors on one wafer. The placement of the sensors and the test structures for quality-control on the wafer is shown in Figure 5.1.1. From the dimensions of the AGIPD sensor in principle three sensors could be placed on one wafer, but due to the automatic handling of the wafer a larger safety region at the periphery of the wafer is required which allows only the placement of two sensors on each wafer. The geometrical parameters of the sensors are the ones given in Section 4.8. In addition to the two AGIPD sensors the following test sensors and test structures were placed on the wafer:

64 × 64 Single sensor: These sensors consist of 64 × 64 pixel which will be bump-bonded to a single AGIPD read-out chip to test the gain switching of the ASIC and the overall functionality. In total 10 of these sensors were placed on the wafer with two of them having a different pixel layout compared to the proposed design.

16 × 16 Single sensor: These sensors are designed for the test with older AGIPD chips (AGIPD-02/03/04 with 64 × 64 pixel).

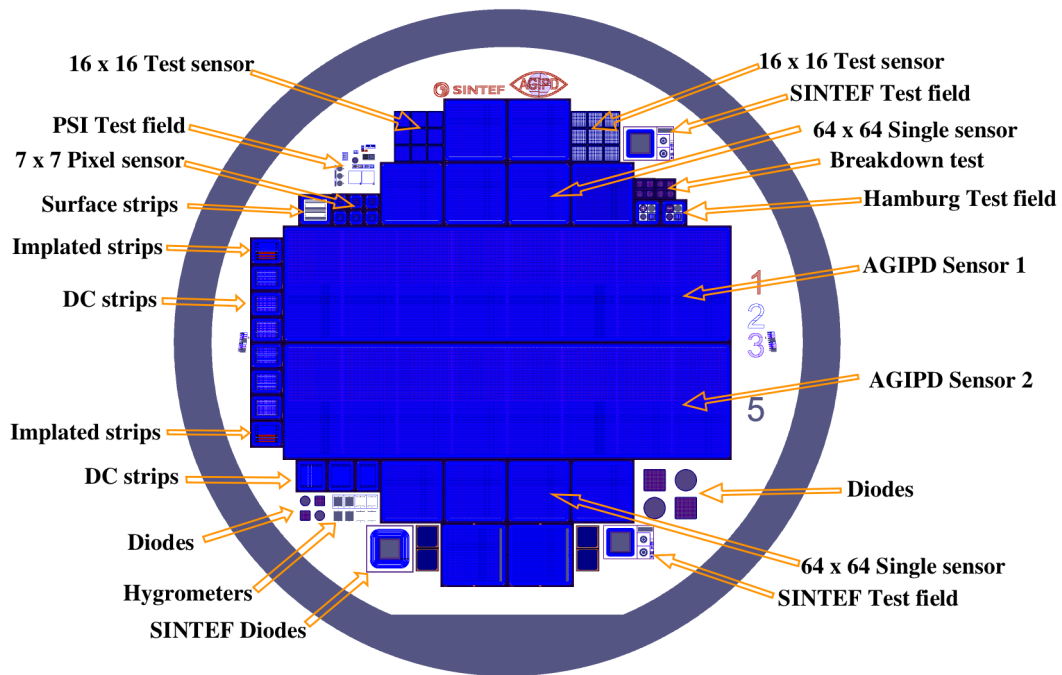


Figure 5.1.1.: Layout of the AGIPD wafer.

7 × 7 Single sensor: This sensor (see Figure 5.1.2) is designed to test the X-ray radiation hardness of the pixel and guard-ring structure used in the AGIPD sensor. To allow tests without the need for the bump-bonding to a special chip, the pixels are connected to the direct neighbor pixels via 10 μm wide metal lines. The connections have been done in two different ways. In the first design all pixel are connected together forming a net. This allows the measurement of the $C/I-V$ of all pixel with one probe needle. To measure the interpixel capacitance and resistance in the second design the central pixel is surrounded by three rings. In addition, the 7 × 7 single sensors have different openings of the passivation of the guard rings. In the first design only the CCR is fully opened. In the second the CCR and all guard-rings are opened and in the third design the CCR is fully opened and every guard ring has four openings of 20 μm × 150 μm. In total 6 of these sensors are on the wafer.

SINTEF Test field: The main structures on this test field (see Figure 5.1.3(a)) are a squared pad diode, a rectangular MOS-capacitor (MOS-C) and two circular Gate-Controlled Diodes (GCD). The pad diode has an implant window of 5 mm × 5 mm and no metal overhang. The pad is surrounded by a 1.4 mm wide guard-ring structure consisting of a CCR and 12 floating rings. The distance between pad and CCR is 50 μm. The gate area of the MOS-C is 3.5 mm × 1.0 mm. The diameter of the diode of the GCDs is 400 μm and the gates have a length of 100 μm and 220 μm, respectively and overlap the diode by 10 μm.

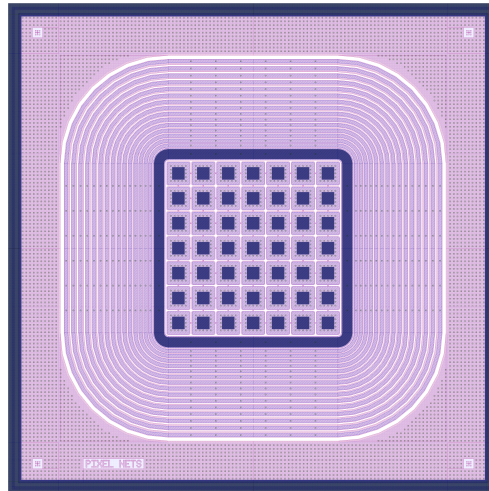


Figure 5.1.2.: Layout of the 7×7 test sensor with all pixels interconnected and for the guard-ring structure only the CCR is opened.

A second circular ring diode is surrounding the central diode of the GCDs with an inner radius of $540 \mu\text{m}$ and $660 \mu\text{m}$, respectively, and an implant width of $100 \mu\text{m}$.

Hamburg Test field: This test field (see Figure 5.1.3(b)) consists of a pad diode, MOS-C, GCD and p-MOSFET surrounded by the guard-ring structure used for the sensors. The pad diode has a square shape with an implant window of $1.5 \text{ mm} \times 1.5 \text{ mm}$ and a metal overhang of $10 \mu\text{m}$. The pad diode is surrounded by a p^+ -implanted ring spaced $30 \mu\text{m}$ away of the pad implant and connected to the CCR of the guard-ring structure. The MOS-C is circular with a diameter of 1.5 mm . A metal ring surrounds the gate at a distance of $20 \mu\text{m}$ and connected to the CCR of the surrounding guard-ring structure. The GCD has a finger-like structure with 6 vertical and 1 horizontal gates surrounded by a diode. The width of the 7 fingers is $100 \mu\text{m}$ each and the length for the 6 vertical and 1 horizontal finger are $1000 \mu\text{m}$ and $1100 \mu\text{m}$, respectively. The gate area is $7.1 \cdot 10^{-3} \text{ cm}^{-2}$. The p-MOSFET is circular. The p^+ -implant of the source has a radius of $250 \mu\text{m}$ and the gate has also a width of $250 \mu\text{m}$. In a second test field the p-MOSFET is replaced by circular GCD and the squared pad diode by circular pad diode.

PSI Test field: The main structures of this test field are a circular MOS-C and a GCD. In addition, test structures for oxide-breakdown and sheet-resistance measurements are implemented.

DC coupled strips: These structures consist of strips with $200 \mu\text{m}$ pitch and different gaps and metal overhangs. $C/I-V$ measurements can be performed in order to obtain the leakage current, interstrip capacitance and breakdown voltage. Due to the 2-D geometry a better comparison between measurements and TCAD simulations can be achieved.

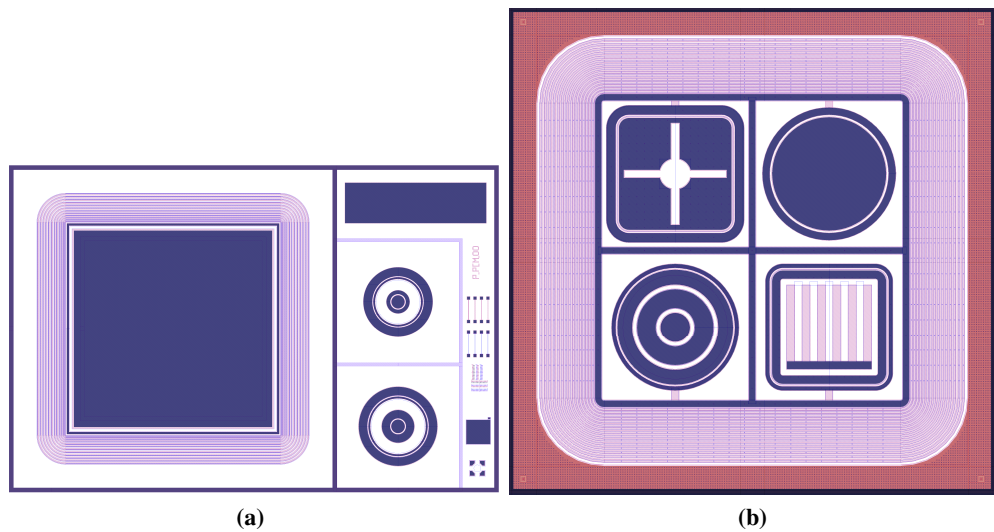


Figure 5.1.3.: (a) SINTEF test field (b) Hamburg test field

Implanted strips: With $I-V$ measurements on this structure the resistivity of the p^+ and n^+ implant can be determined.

Surface strips: The structure consists of several aluminum strips. There are two opening through the passivation layer at the two ends of each aluminum strip. $I-V$ measurements on this structure can be made to determine the resistivity of the metal layer.

Diodes: Square and circular diodes with different areas are placed on the wafer to measure the capacitance and current as function of voltage.

Hygrometers: The structure consists of two groups of finger-like aluminum strips deposited on top of a SiO_2 insulating layer. $I-V$ measurements on this structure can be made to determine the surface resistivity as function of humidity.

The design of the guard-ring structure of the AGIPD sensors make use of an n^+ -scribe-line implant. Therefore the processing of the sensors requires five instead of typically four masks. These mask are:

NDIFF For the n^+ -scribe-line implant of the guard-rings structure.

PDIFF For the p^+ -implants.

PCONT For the formation of the VIAS to contact the implant to the metal.

PMET For the metallization.

PPASS For the opening of the passivation to contact to the metal.

The subsequent bump-bonding of the sensor to the ASICs requires two additional masks for the indium and under-bump metallization (UBM).

The starting material for the first batch of the AGIPD sensors was high-purity, high-resistivity silicon from TOPSIL [134]. The crystal orientation is $\langle 100 \rangle$ and the bulk resistivity between 7.4 and 8.6 $\text{k}\Omega\cdot\text{cm}$. Lifetime measurements done by TOPSIL using the photo conductive decay method result in values of 10.2 ms for the minority carrier lifetime indicating the high purity of the silicon. To show the complexity involved in the fabrication of the AGIPD sensors in the following an outline of the process is given which does not include any confidential informations.

1. Oxidation a SiO_2 layer of 750 nm
2. Photolithography front side, mask NDIFF
3. POCL_3 deposition
4. Phosphorus drive-in and oxidation
5. Strip oxide
6. Oxidation to 200 nm
7. Strip backside oxide
8. Photolithography front side, mask PDIFF
9. Boron implantation (dose $5 \cdot 10^{15} \text{cm}^{-2}$, energy 70 keV) photoresist masking
10. Implant anneal (temperature 1025°C , time 4 h) in N_2 , oxidation (to 100 nm on backside)
11. Backside phosphorus implantation
12. Implant anneal, getter, oxide anneal
13. Photolithography front side, mask PCONT
14. Open contact holes on front side and back side
15. Back and front side metallization
16. Photolithography front side, mask PMET
17. Sinter in forming gas to reduce interface traps
18. Passivation by PECVD deposition ($0.5 \mu\text{m SiO}_2$, $0.25 \mu\text{m SiN}$)
19. Photolithography front side, mask PPASS
20. Open passivation openings (RIE etch)
21. Final bake

To check the doping profile and junction depth of the p^+ -implant, a spreading resistance measurement by SOLECON [135] on behalf of SINTEF was performed. The spreading resistance measurement determines a resistivity-depth profile in silicon. Using values of carrier mobility, a majority carrier concentration-depth profile can be calculated. To determine the dopant profile from this measurement the space-charge redistribution under the bevel used for the spreading resistance profile has to be taken into account using a Poisson solver. To get a first impression of the doping profile the majority-carrier concentration-depth profile is sufficient and the measurement results obtained on a higher doped ($\approx 10^{15} \text{cm}^{-3}$) wafer than used for the AGIPD sensors together with the doping profile used for the simulations are shown in Figure 5.1.4. The results indicate that the required junction depth was achieved and the profile is

in reasonable agreement with the simulations. The differences between the measures and the simulated profiles mainly comes from the fact that not all high temperature steps, including gas mixtures and gas flows, which can lead to a dopant redistribution were simulated because these steps are company secrets.

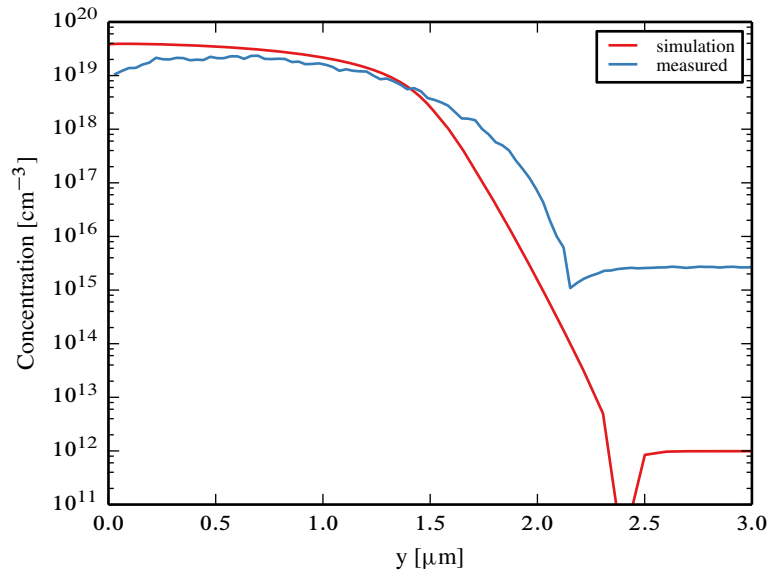


Figure 5.1.4.: Profile obtained by spreading resistance measurement and doping profile used in simulations. For the measurement a higher doped wafer than for the AGIPD sensors was used. This leads to the difference in the concentration in the bulk. The spreading resistance measurement was performed by SOLECON.

For the quality control SINTEF performed $I-V$ measurements of the CCR current of the sensors with pixels left floating. By this the CCR current includes also the contribution of the pixels and is therefore higher than measured with pixels grounded. The results are shown in Figure 5.1.5. As can be seen, there is a large variation in the breakdown behavior for the different $I-V$ curves making it difficult to define the V_{bd} and to assess the yield. To quantify the yield 3 categories were defined with equation 4.6.1 as breakdown criterion using $K_{bd} = 10$. The first category is defined as $V_{bd} > 900\text{ V} \ \& \ I(900\text{ V}) < 200\text{ nA}$, which is the specifications given in Table 4.1.1. The second is $V_{bd} < 900\text{ V} \ \& \ I(900\text{ V}) < 200\text{ nA}$ and the third is $V_{bd} < 900\text{ V} \ \& \ I(900\text{ V}) > 200\text{ nA}$. The results are presented in Table 5.1.1 showing that 67.5% of the sensors fulfill the specifications. In addition, the values for less restrictive requirements, using 500 V instead of 900 V for V_{bd} , are given resulting in 80% good sensors.

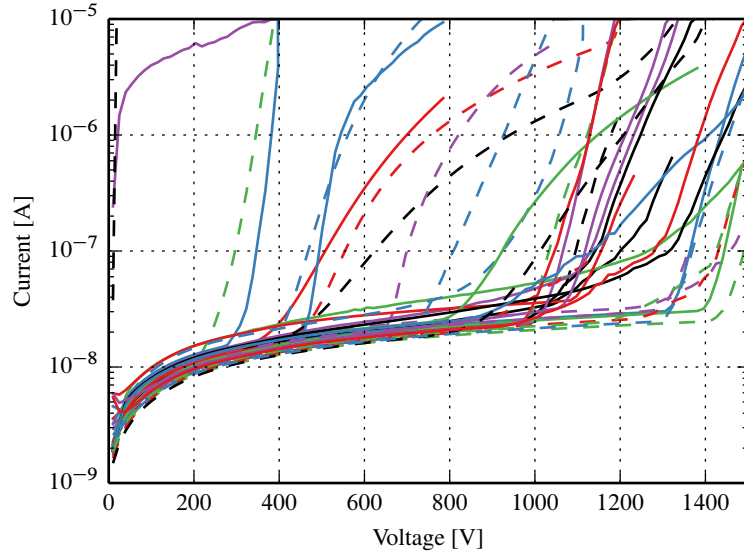


Figure 5.1.5.: I - V measurements of the CCR current of the sensors with pixels floating for the first batch. The measurements were performed by SINTEF.

900 V			
Category	Criteria	No. of sensors	
1	$V_{bd} > 900 V$ & $I(900 V) < 200$ nA	27 (67.5%)	
2	$V_{bd} < 900 V$ & $I(900 V) < 200$ nA	2 (5%)	
3	$V_{bd} < 900 V$ & $I(900 V) > 200$ nA	11 (27.5%)	
500 V			
1	$V_{bd} > 500 V$ & $I(500 V) < 200$ nA	32 (80%)	
2	$V_{bd} < 500 V$ & $I(500 V) < 200$ nA	2 (5%)	
3	$V_{bd} < 500 V$ & $I(500 V) > 200$ nA	6 (15%)	

Table 5.1.1.: Yield for the first batch.

5.2. Electrical characteristics of the non-irradiated test structures

A number of important parameter like the bulk resistivity, oxide-charge density and surface-current density have been determined before irradiation. In addition, the currents of the pixels and CCR have been determined and the breakdown voltage of the CCR has been checked. For this $C/G-V$ and $I-V$ measurements have been performed. The used set-ups typically consist of a cold chuck, a Keithley 6517A multi meter, a Keithley 6485 pico-ammeter, a Keithley 6487 power supply, an Agilent 4980A LCR meter, a temperature-control system and the possibility to reduce the humidity on top of the device under test with a dry-air flow.

For the determination of the bulk resistivity and of the doping profile the $C-V$ at 1 kHz of a SINTEF pad diode was measured with the CCR grounded. As for an uniformly doped bulk a plot of $1/C^2$ versus reverse voltage V is linear with a slope determined by the doping concentration N_d in Figure 5.2.1(a) the result of the $C-V$ measurement is shown as $1/C^2-V$. Since the measurement result of the capacitance above depletion was ≈ 5.7 pF whereas for the given device thickness of 500 μm and an area of $5.05 \text{ mm} \times 5.05 \text{ mm}$ a value of ≈ 5.4 pF is expected a constant stray capacitance of 0.275 pF was subtracted from the measurement.

From a linear fit of $1/C^2$ in the range between 30 V and 80 V a doping concentration of $5.3 \cdot 10^{11} \text{ cm}^{-3}$ was extracted which corresponds to a bulk resistivity of $7.8 \text{ k}\Omega\cdot\text{cm}$. This value is inside the resistivity range of the starting material showing that the process did not change considerably the resistivity. But one has to mention that this value is close to the limit of the specification for the AGIPD sensors. The full depletion voltage, V_{fd} , which is determined by the kink in the $1/C^2-V$ curve is 95 V.

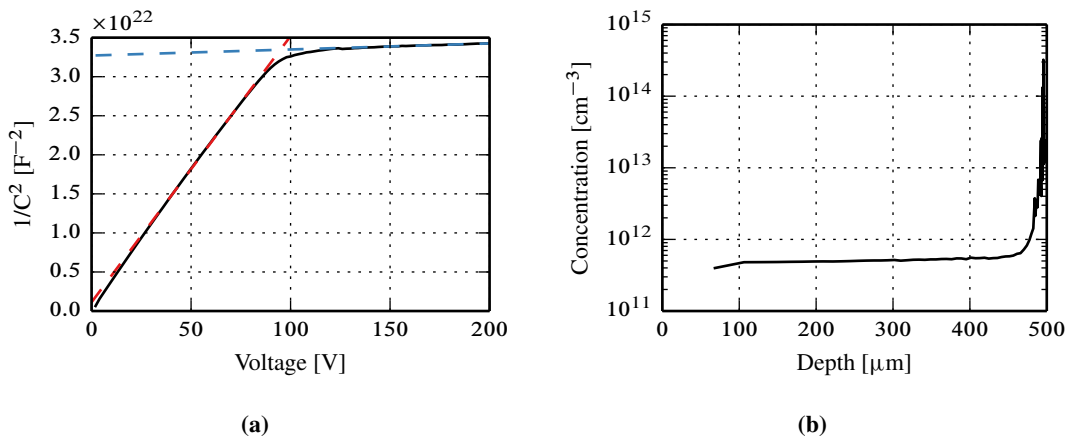


Figure 5.2.1.: (a) $1/C^2-V$ at 1 kHz for a SINTEF pad diode (b) Doping profile

Under the assumption of the depletion approximation and ignoring edge effects the doping

profile can be calculated using [67]

$$x_d = \frac{\epsilon_0 \epsilon_{Si} A}{C} \quad (5.2.1)$$

for the depletion width and

$$N_d(x_d) = \frac{2}{q \epsilon_0 \epsilon_{Si} A^2 d (1/C^2) / dV} \quad (5.2.2)$$

for the doping concentration. The result is shown in Figure 5.2.1(b). The concentration shows an increase from $4.8 \cdot 10^{11} \text{ cm}^{-3}$ at a depth of $100 \text{ }\mu\text{m}$ to a value of $5.8 \cdot 10^{11} \text{ cm}^{-3}$ at a depth of $450 \text{ }\mu\text{m}$. This gives a longitudinal doping non-uniformity of $\approx 20 \%$. But one has to mention that here also edge effects of the capacitance are relevant which were not included in this simple analysis. What can not be measured, but which is important for the AGIPD, is the transverse doping non-uniformity over a full sensor.

Figure 5.2.2 shows the $I-V$ measurement of the SINTEF pad diode at $T = 20^\circ\text{C}$ up to 1000 V . The curve of the $I-V$ shows first a decrease of the current with increasing voltage and then an increase of the current which is not simply $\propto \sqrt{V}$ and without any sign of saturation above full depletion. Because this behavior was also observed on other diodes this is an indication that due to the high minority carrier lifetime beside the generation current in the space region also contributions of surface generation and diffusion currents are important. In general for a

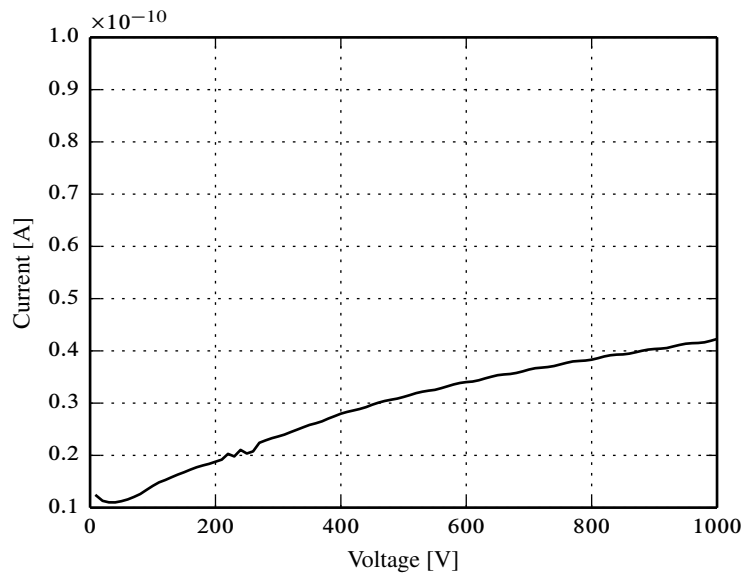


Figure 5.2.2.: $I-V$ measurement of the SINTEF pad diode at $T = 20^\circ\text{C}$ up to 1000 V

reverse-biased p^+-n junction in steady-state conditions the current is given by [67]

$$I = \frac{qn_iWA}{\tau_g} + qn_i s_g A_s + qn_i^2 FA \frac{D_p}{N_d L_p} \quad (5.2.3)$$

where A is the diode area; A_s is the surface area of the space-charge region (scr); W is the scr width; τ_g is the generation lifetime in the scr; s_g , is the surface generation velocity in the scr; L_p , is the diffusion length which is equal to $(D_p \tau_r)^{1/2}$ with the recombination lifetime τ_r and F is a correction factor that depends on the sample geometry and is a complicated function of the active layer thickness, the diffusion lengths, doping densities and possible interface recombination velocity at the $n-n^+$ side.

From this equation it can be seen, that if one neglects the surface current and the diffusion current it is only possible to estimate from the $I-V$ a lower limit of the generation lifetime. At 100 V, which is slightly above full depletion, the current is 14 pA resulting in a $\tau_g = 0.87$ s. Compared to previously measured samples from other vendors, where τ_g was in the order of a few ms, this is a very long lifetime indicating the high purity of the silicon bulk. This value is reasonable, because according to [67] $\tau_g \approx (50 - 100)\tau_r$ and τ_r was before processing $\tau_r = 10$ ms. Beside the advantage of a low bulk current this long generation lifetime has some impact on the measurements and simulations. Typical ramping speeds of $C-V$ and $I-V$ measurements can be too high for the often made assumption of a steady-state in the analysis¹. In the simulations the long generation lifetime also leads to numerical problems resulting in a bad convergence.

For the determination of the oxide-charge density the MOS-C of the Hamburg test field was used. The $C-V$ for different frequencies is shown in Figure 5.2.3(a). The $C-V$ curves are similar to the one of an ideal MOS-C [136] and show no frequency dependent shift meaning that the interface-trap density must be very low. From the 1 kHz curve in strong accumulation an oxide thickness of 245 nm can be determined. Assuming an uniformly doped bulk with $N_d = 5.3 \cdot 10^{11} \text{ cm}^{-3}$ as measured from the pad diode (this assumption is reasonable because due to the Debye length limitation the doping can not be measured close to the interface) the flatband capacitance is given by

$$C_{FB} = \left(\frac{1}{C_{ox}} + \sqrt{\frac{k_B T}{q^2 \epsilon_0 \epsilon_s i N_d}} \right)^{-1} A_g, \quad (5.2.4)$$

with A_g the gate area resulting in $C_{FB} = 29.3$ pF. From the $C-V$ dependence a flatband voltage of $V_{FB} = -0.39$ V can be extracted. Considering that the metal-semiconductor work-function difference $\Phi_{MS} = -0.42$ V and using the equation

$$V_{FB} = \Phi_{MS} - \frac{qN_{ox}}{C_{ox}} \quad (5.2.5)$$

¹Actually to reproduce the behavior of the $I-V$ below full depletion in 1D a transient simulation is needed.

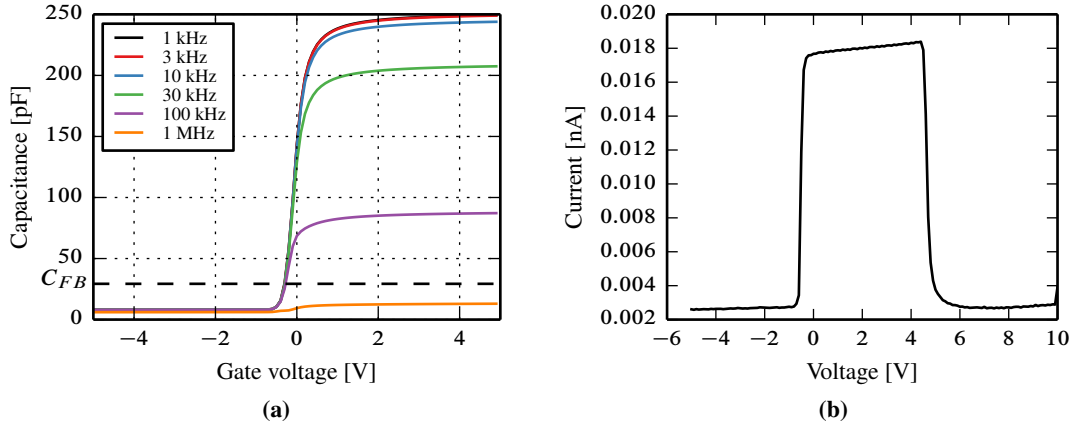


Figure 5.2.3.: (a) $C-V$ of non-irradiated MOS-C from the Hamburg test field (b) $I-V$ of the finger GCD from the Hamburg test field with the diode biased at 5 V.

for N_{ox} results in a value of $N_{ox} = -2 \cdot 10^9 \text{ cm}^{-2}$. Given the uncertainties in the calculation of the doping concentration and that the other MOS-C on the wafer shows a similar behavior one can conclude that the effective oxide-charge density is close to zero, probably even negative. In previously investigated samples from SINTEF with an oxide thickness of 750 nm, only positive oxide-charge densities had been observed [14]. The difference is probably related to changes in the production process which attempted to minimize the oxide-charge density before X-ray irradiation.

For the determination of the surface-current density the finger GCD of the Hamburg test field was used. In Figure 5.2.3(b) the $I-V$ measurement with the diode biased at 5 V is shown. The measurement results were scaled to $T = 20^\circ\text{C}$ using the formula [14]

$$I_{surf}(T) = I_{surf} \cdot \left(\frac{T}{T_{meas}} \right)^2 \cdot \exp \left[\frac{0.605eV}{k_B} \cdot \left(\frac{1}{T_{meas}} - \frac{1}{T} \right) \right]. \quad (5.2.6)$$

From the difference of the current in inversion and depletion a surface-current density of $J_{surf} = 2.2 \text{ nA/cm}^2$ was determined. A value which is 4 times lower than measured on previously investigated samples from SINTEF. The corresponding surface generation velocity is 2.25 cm/s.

Measurements of the $I-V$ of the pixels and CCR of the 3 interconnected 7×7 single sensors at $T = 20^\circ\text{C}$ under dry-air flow before and after cutting of the wafer are shown in Figure 5.2.4. The results of the pixels are scaled to one pixel and the current of the CCR is scaled to the full AGIPD sensor. The current of the pixel saturates at a value of 0.42 pA after full depletion and do not show a change due to cutting. For the CCR current after cutting a slightly higher current with a value of 20 nA at 500 V appears and a soft breakdown at around 800 V can be observed,

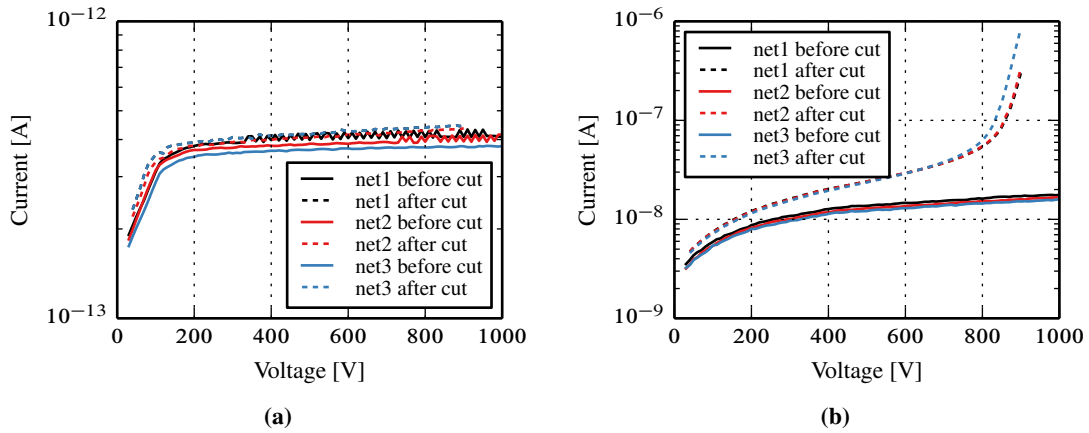


Figure 5.2.4.: I - V measurements of the interconnected 7×7 single sensors before and after cutting. (a) Current per pixel (b) CCR current scaled to the full AGIPD sensor

which is not present before cutting. Due to the fact that the oxide-charge density is low and the resistivity is close to the limit of the specifications the assumption can be made that the soft breakdown is a result of the bulk depletion into the cut edge as shown in the previous chapter. If this is correct after increasing the oxide-charge density the soft breakdown should disappear. To demonstrate this, low dose irradiations up to 800 Gy (SiO_2) of DC coupled strip structures, which have the same guard-ring structure as the 7×7 single sensors, were performed with a PHYWE X-ray tube using a tungsten target. The results of the I - V measurements under dry conditions of the CCR current before and after low dose irradiation are presented in Figure 5.2.5. The measurements after irradiation were done without an annealing. As can be seen the current increases with dose due to the increase of the interface traps and the soft breakdown at around 800 V in the non-irradiated case disappears at a dose of ≈ 200 Gy.

To prevent the soft breakdown of the AGIPD sensors the question arises, whether one performs an additional low dose irradiation before or after bump bonding. After bump bonding the sensors have to be calibrated, which is done with X-rays and it is expected that a sufficient dose will be reached. An irradiation before bump bonding has to be performed on the wafer level and the dose must be so that after the different temperatures steps, which are required for the bump bonding, the positive oxide charge is still high enough to prevent the soft breakdown. An additional test on a DC coupled strip structure and a MOS-C consisting of an irradiation to 200 Gy and then an annealing sequence with 10 minutes at 80°C , 24 hours at 60°C and 250 seconds at 200°C shows no soft breakdown in the I - V of the CCR and an oxide-charge density of $\approx 5 \cdot 10^{10} \text{ cm}^{-2}$.

To summarize: The measurements on test structures of the first batch show that the bulk resistivity is at the limits of the specifications, the bulk current and the surface current are low and that the oxide-charge density is unexpectedly low or even negative. Since the designed guard-

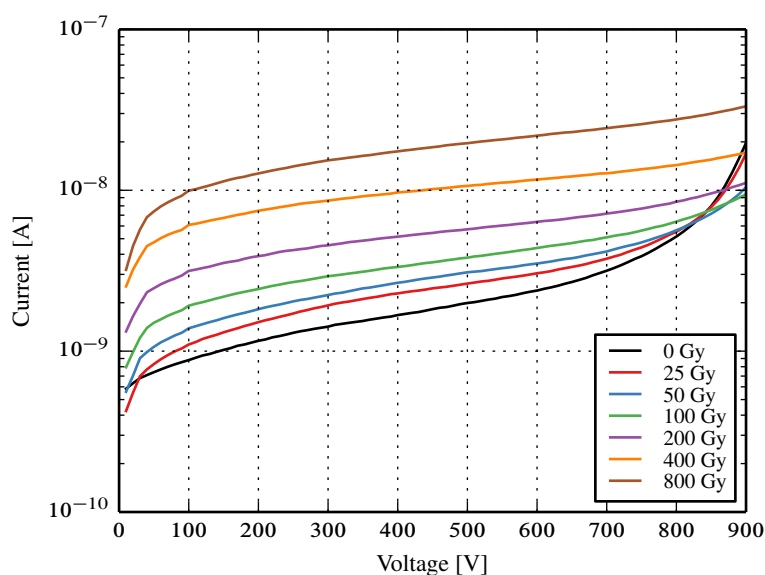


Figure 5.2.5.: I - V measurements of the CCR current before and after low dose irradiation.

ring structure requires a certain amount of positive oxide charges to prevent a soft breakdown one has to consider a low dose preirradiation before bump bonding or during the calibration to increase the oxide-charge density.

5.3. High dose X-ray irradiation at PETRA III

The high dose X-ray irradiations have been performed during two beamtimes at the beamline P11 of PETRA III (DESY-Hamburg). For the irradiations a set-up has been used which is discussed in [14] and shown in Figure 5.3.1(a) as used at the P11. The set-up consists of an adjustable Ta collimator, which is used to precisely define the region of irradiation on the sensor, and a sample holder, which is connected to a liquid cooling system. The test sensors and test fields planned to be irradiated were glued onto a special designed ceramic and wire-bonded to the 5 biasing lines of the substrate. The ceramic substrates were mounted into the sample holder during irradiation. The picture in Figure 5.3.1(b) was taken from a camera during irradiation showing collimator and the sample on the ceramic. The white spot left to the sample indicates the beam reaction with the ceramic.

The beamline P11 at PETRA III provides a monoenergetic X-ray beam from an undulator. During the first beamtime a X-ray energy of 12 keV has been used for the irradiation and during the second beamtime 8 keV were used to get a higher dose rate. Using a CMOS camera (pco.edge 5.5) with a resolution of 2560×2160 pixel, each with a pitch of $6.5 \mu\text{m}$ and readout speed of 100 frames per second an image of the direct beam was taken (see Figure 5.3.2(a)) and

5. Measurement results of optimized AGIPD test structures

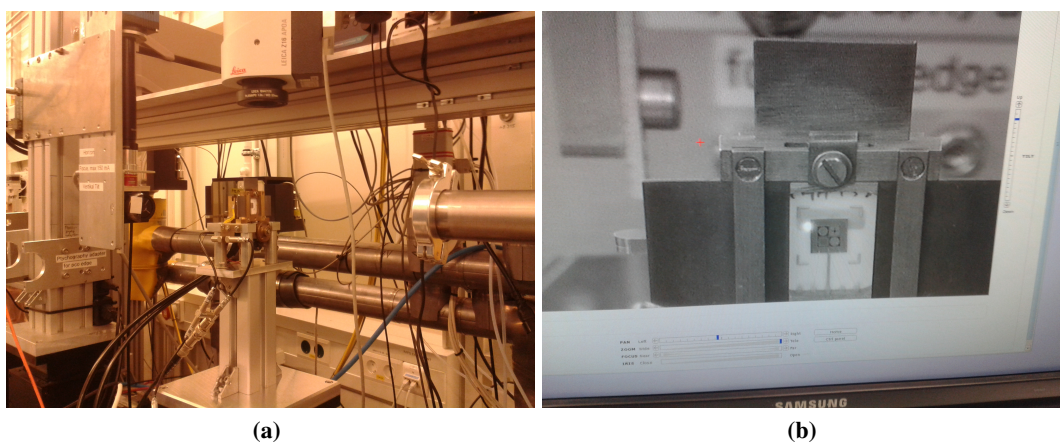


Figure 5.3.1.: (a) X-ray radiation stand at P11 (b) Picture showing the collimator and the sample on the ceramic during irradiation.

horizontal and vertical cut through the beam center were made (see Figure 5.3.2(b)). The size of the beam spot from the image is approximately $1.2 \text{ mm} \times 1.4 \text{ mm}$.

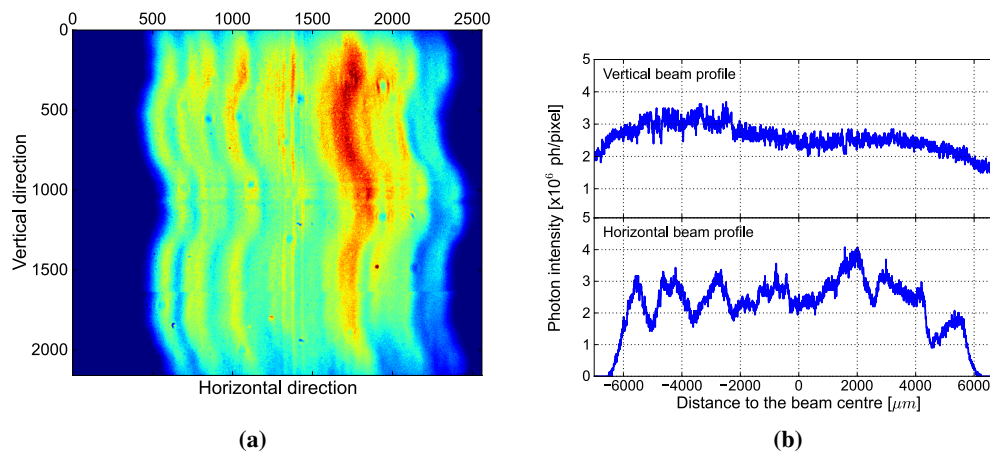


Figure 5.3.2.: (a) Image of the direct beam at the beamline P11 of PETRA III (b) Horizontal and vertical beam profiles along the cuts through the beam centre.

The photon intensity was calibrated with a silicon photodiode. The area of the photodiode is $1.0 \text{ cm} \times 1.0 \text{ cm}$, which is large enough to cover the entire beam. The photo-current from the $300 \mu\text{m}$ thick photodiode for 8 keV X-rays was 3.5 mA, which corresponds to a photon intensity

of $1 \cdot 10^{13}$ photons/s obtained from a direct conversion using

$$I_{X-ray} = \frac{3.6 \text{ eV } I_{diode}}{q E_{X-ray} \left(1 - e^{-\frac{T_{Si}}{L_{X-ray}}} \right)} \quad (5.3.1)$$

where I_{diode} is the photo-current, q the elementary charge, E_{X-ray} the energy of the X-rays, T_{Si} the thickness of the photodiode and L_{X-ray} the X-ray attenuation length for the energy E_{X-ray} . Thus, the average dose rate in SiO_2 within the beam spot was 26 kGy/s for irradiation with 8 keV X-rays. The irradiation with 12 keV X-rays were done with a dose rate between 0.42 and 7.1 kGy/s.

As the size of the test sensors and test fields are larger than the beam spot, irradiations by scanning the entire beam were needed in order to obtain an uniform irradiation. In this work, "square waveform"-shape irradiation path has been taken: The carrier stage of the sample holder was moved along the horizontal direction with a constant speed V_x from one end to the other; the stage was then moved vertically by a small step of Z_{step} at the end and then move back horizontally. The accumulated dose is proportional to the dose rate integrated over the entire beam area, and divided by the moving speed V_x and the vertical step Z_{step} . Details of dose calculation are documented in [14]. In this work, a constant speed V_x of 1.0 mm/s during scans was used. The vertical step of Z_{step} was changed to obtain the different doses.

The test sensor and test field were irradiated without bias voltage applied with 12 keV X-rays to accumulated doses of 10 kGy, 100 kGy and 1 MGy. With 8 keV X-rays the irradiation was done to 10 MGy for test sensors and test fields and up to 100 MGy for the corner of the guarding of a test sensor without scanning of the beam. During irradiation, the cooling temperature was set to $T = 15^\circ\text{C}$.

5.4. Measurement results after irradiation

5.4.1. Dose dependence of damage-related parameters from the test structures

The test structures investigated were a circular MOS-C and the GCD with a finger structure from the Hamburg test field. During the irradiations, no voltages were applied to the electrodes of the MOS-C or the GCD. The first $C/G-V$ and $I-V$ measurements were performed within 1 hour after each irradiation and additional annealing was done in order to obtain reproducible results and to compare the results to previous studies.

Figure 5.4.1 shows the results of the $C-V$ measurements at 1 and 10 kHz for the MOS-C before irradiation, and after irradiation to 0.01, 0.1, 1 and 10 MGy before and after annealing for 10 minutes at 80°C . Here only data are presented for which the voltage was ramped from positive values (accumulation) to negative values (inversion). As already observed in [75], the irradiated MOS-Cs show hysteresis effects, which however, are not discussed further here.

5. Measurement results of optimized AGIPD test structures

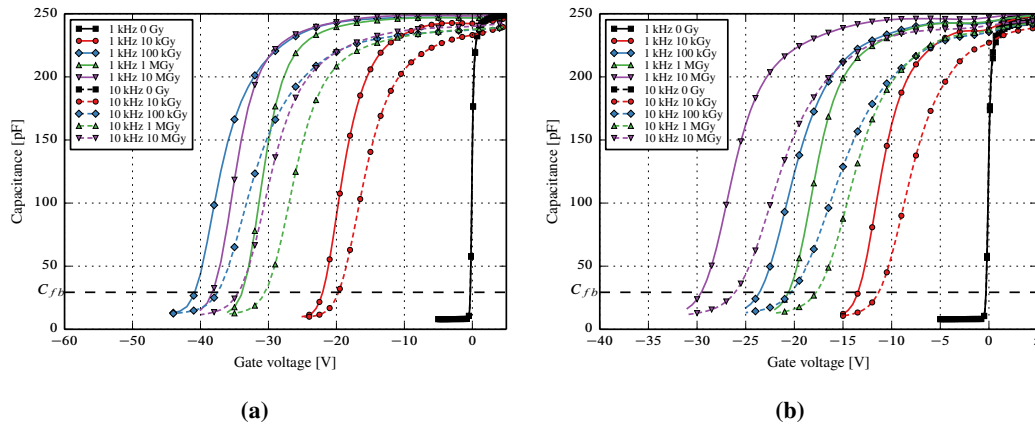


Figure 5.4.1.: $C-V$ curves for a non-irradiated and an irradiated MOS-C produced together with the AGIPD sensors (a) before and (b) after annealing for 10 minutes at 80°C . The value of the flatband capacitance, C_{fb} , is indicated by a horizontal line. Due to problems during the irradiation, the 10 MGy value may be somewhat lower.

The $C-V$ curves for the irradiated MOS-C show large shifts to negative voltages, a stretching of the transition from accumulation to inversion, and a strong dependence on frequency, as expected for radiation-induced positive oxide charges and interface traps. To extract the oxide-charge density, N_{ox} , as function of dose, and to compare the results to previous measurements [14], the flatband-voltage shift of the 1 kHz curves was used. The maximal flatband-voltage shift of 41 V corresponding to $N_{ox} = 3.6 \cdot 10^{12} \text{ cm}^{-2}$ has been found before annealing at 100 kGy. However after annealing the 10 MGy curve shows the maximal flatband-voltage shift. This may be related to the different dose rates used for the irradiations. In table 5.4.1 the values of N_{ox} for the different dose values, directly after irradiation and after annealing for 10 minutes at 80°C , are given. The values agree with the previous measurements on SINTEF samples with 750 nm oxide, which showed that a saturation value of $2 - 4 \cdot 10^{12} \text{ cm}^{-2}$ is reached for a dose of about 100 kGy.

The $I-V$ measurement of the GCD before and after annealing for 10 minutes at 80°C are presented in Figure 5.4.2. The measurements are scaled using equation 5.2.6 to 20°C . The maximum surface current is reached at 1 MGy before and after annealing. Before annealing the surface-current density is $2.7 \mu\text{A}/\text{cm}^2$ and after annealing about $1.5 \mu\text{A}/\text{cm}^2$. All extracted values for J_{surf} are also given in table 5.4.1.

To summarize: Apart from a small negative oxide-charge density before irradiation, the values of the oxide-charge and surface-current densities before and after X-ray irradiation determined from the test structures produced by SINTEF on the same wafers as the AGIPD sensors are similar to the ones from the test samples from the standard SINTEF process, which we obtained in autumn 2012. The values are somewhat different from the ones shown in table 4.4.1, which

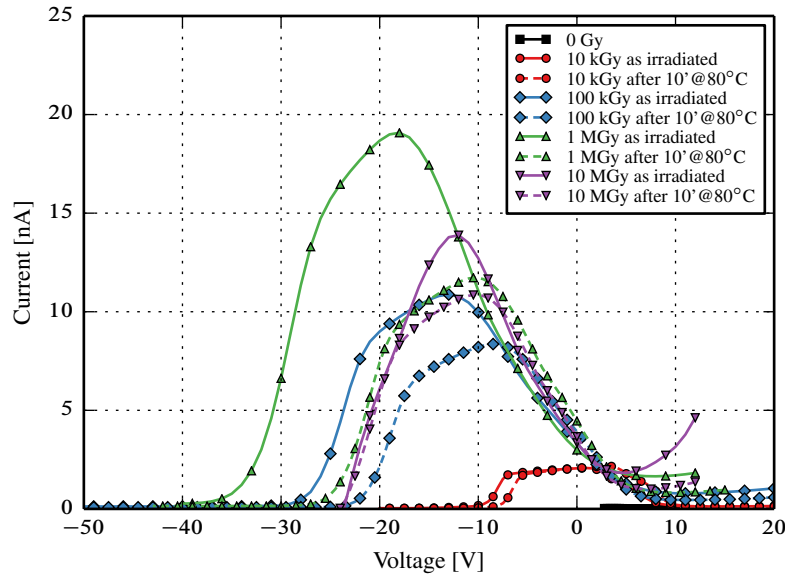


Figure 5.4.2.: $I-V$ of the GCD scaled to 20°C measured before and after annealing for 10 minutes at 80°C .

were used for the sensor optimization. The latter have been determined until spring 2012 from test structures from three other vendors [14]. The observed difference do not invalidate the optimization of the AGIPD-sensor design. However, they result in some differences between the results of the simulations and the measurements.

Dose [MGy]	As irradiated		After 10 min. @ 80°C	
	N_{ox} [cm^{-2}]	J_{surf} [$\mu\text{A}/\text{cm}^2$]	N_{ox} [cm^{-2}]	J_{surf} [$\mu\text{A}/\text{cm}^2$]
0.01	$1.8 \cdot 10^{12}$	0.3	$1.2 \cdot 10^{12}$	0.3
0.1	$3.6 \cdot 10^{12}$	1.5	$2.1 \cdot 10^{12}$	1.2
1	$3.0 \cdot 10^{12}$	2.7	$1.8 \cdot 10^{12}$	1.6
10	$3.4 \cdot 10^{12}$	1.9	$2.6 \cdot 10^{12}$	1.5

Table 5.4.1.: Dependence on X-ray dose of the oxide-charge density N_{ox} and the surface-current density J_{surf} at 20°C from test structures produced together with the AGIPD sensors.

5.4.2. Dose dependence of the electrical characteristics of test sensors

An important part of this work is the evaluation of the performance of the pixel and of the guard-ring structure. For this investigation the different 7×7 pixel sensors were irradiated. The

5. Measurement results of optimized AGIPD test structures

irradiations were carried out in different ways: In the first the sensor was irradiated uniformly; in the second, using a 1 mm thick Ta absorber, only half of the sensor was irradiated, in order to produce a highly non-uniform irradiation; in the third only the corner of the guard-ring structure was irradiated.

The Figure 5.4.3(a) shows as function of voltage the measured CCR currents, scaled to the full size of the AGIPD sensor, for the non-irradiated and the uniformly irradiated sensor at 20°C in a dry (relative humidity below 5 %) atmosphere. The measurements have been done within one hour after the irradiation, and in addition, after annealing for 10 minutes at 80°C. The maximum voltage of 900 V is due to limitations of the cold chuck of the probe station.

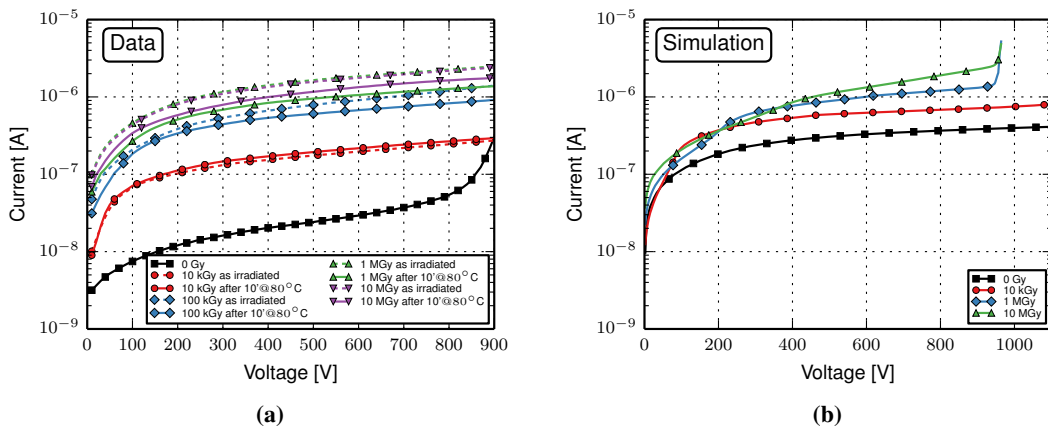


Figure 5.4.3.: (a) CCR current of the 7×7 test sensor measured at 20°C and scaled to the full AGIPD sensor for different dose values before and after annealing. (b) Simulations of the CCR current scaled to the full AGIPD sensor for the different dose values, with the values of N_{ox} and J_{surf} used for the optimization and given in Zable 4.4.1.

For the irradiated sensors no breakdown up to 900 V is observed. The current increases with dose and saturates around 1 MGy, compatible with the surface-current densities shown in table 5.4.1. The maximal current measured at 20°C and 900 V after annealing for 10 minutes at 80°C is about 2 μA. The value at -20°C is 40 nA. This annealing reduces the currents by about a factor 2. All values are well within the specifications given in table 4.1.1. We note here, that a sensor not optimized for X-ray radiation hardness with 12 guard rings produced by SINTEF after irradiation to 100 kGy has a breakdown voltage of about 300 V [137], which demonstrates that the optimization has been necessary and successful.

The Figure 5.4.3(b) shows for comparison the predictions from the simulations for the CCR currents presented in the chapter 4 with the parameters given in Table 4.4.1. For the predictions of the full-size sensor, the CCR currents from the 2D simulation in Cartesian coordinates were scaled to the length of the straight sections of the AGIPD guard ring and the currents from the 2D simulation in cylindrical coordinates added. The breakdown at 910 V for oxide-charge densities

above 10^{12} cm^{-2} is due to the breakdown at the corners of the CCR. No such breakdown is observed in the measurements, showing that the assumptions made in the simulations have been conservative. We note, that for the irradiated sensor the predicted and measured currents agree. For the non-irradiated sensor, the apparent disagreement is due to the assumed generation lifetime of 1 ms in the simulation, whereas as shown above for this device the lifetime is much longer.

The Figure 5.4.4(a) shows the currents per pixel measured at 20°C in a dry atmosphere for the non-irradiated and the uniformly-irradiated sensor. No breakdown is observed up to a voltage of 900 V. After annealing for 10 minutes at 80°C the maximal current per pixel is below 0.2 nA at 20°C and below 3 pA at -20°C . These values are well within the specifications shown in Table 4.1.1. The Figure 5.4.4(b) shows the predictions of the 3D simulations for comparison. Again, the values from the simulations and the measurements for the irradiated sensors are similar.

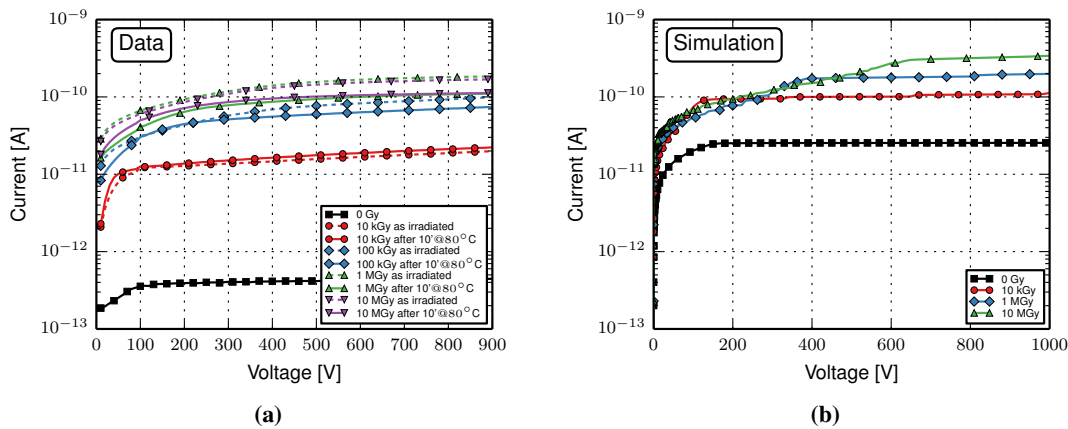


Figure 5.4.4.: (a) Current at $T=20^\circ\text{C}$ per pixel of the 7×7 test sensor for different dose values before and after annealing. (b) 3D simulations of the current at $T=20^\circ\text{C}$ per pixel for the different dose values with the values of N_{ox} and J_{surf} used for the optimization and given in Table 4.4.1.

To verify that the AGPID sensor also works if the irradiation is non-uniform, half of a sensor was irradiated up to a dose of 1 MGy whereas the other half was shielded by a 1 mm Ta absorber. The results for the CCR current for dose values up to 1 MGy, shown in Figure 5.4.5, are as expected from the sum of the currents from a half-size irradiated and a half-size non-irradiated sensor.

To achieve an even higher non-uniform irradiation only the corner region of the guard-ring structure was irradiated to 100 MGy. Also under this circumstances no breakdown up to 900 V was observed.

Finally, the inter-pixel capacitance C_{int} as function of dose has been measured. It is found, that C_{int} has some dependence on frequency, which however is less than 30 % at 500 V, and will

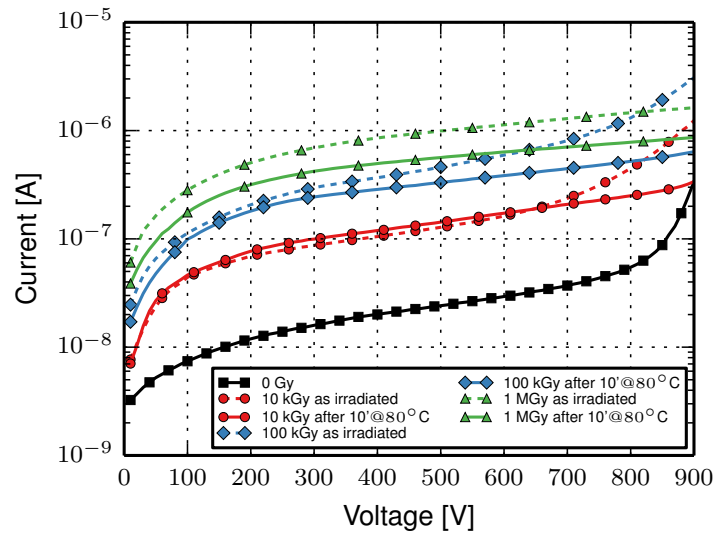


Figure 5.4.5.: CCR current of the half-size irradiation 7×7 test sensor scaled to the full AGIPD sensor for different dose values before and after annealing.

not be further discussed here. In figure 5.4.6, C_{int} at 1 MHz after annealing for the uniformly and half-irradiated sensor, together with the results before irradiation, are presented. Before irradiation a value of 102 fF at 500 V is obtained, compared to the prediction of 98 fF. At a voltage of 500 V the maximum value of C_{int} of 130 fF, reached at 10 kGy, is well within the specifications.

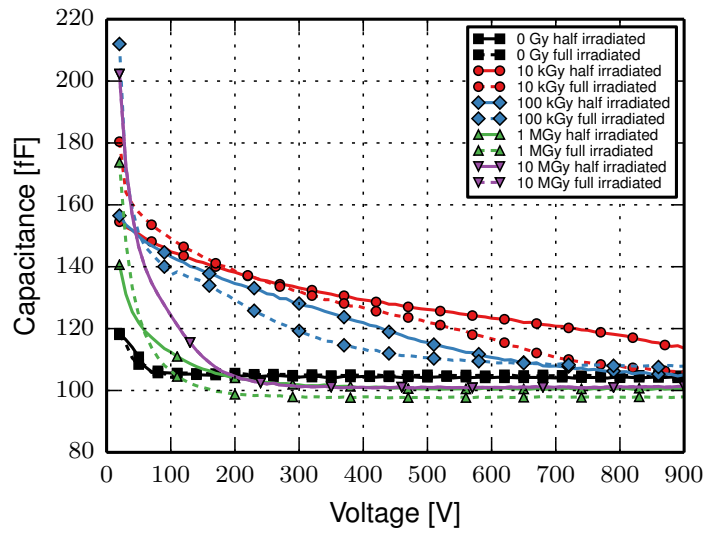


Figure 5.4.6.: Inter-pixel capacitance C_{int} at 1 MHz for the uniformly and half irradiated sensors after annealing for 10 minutes at 80°C.

5.5. Humidity related effects

Even though the AGIPD sensor is designed for operation in vacuum, testing and calibration of the sensor will be also done in ambient atmosphere without humidity control. In addition, it is planned to build single modules which will operate in ambient atmosphere, but these modules do not necessarily require the high voltage operations as the AGIPD detector. Nevertheless stable operation of the sensor under these circumstances is important. Therefore also $I-V$ measurements of the CCR current under humid conditions have been performed. In Figure 5.5.1 the CCR currents in dry and humid conditions are shown before and after irradiations. The currents are scaled to the full AGIPD sensor and a temperature of 20°C. As can be seen under

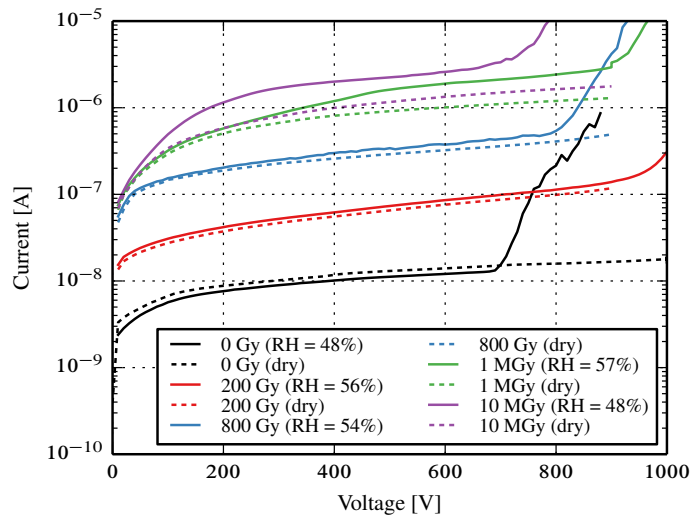


Figure 5.5.1.: CCR current of the test sensor scaled to 20°C and to the full AGIPD sensor for different dose values measured in dry and humid conditions.

humid conditions typically the current is slightly increased and a breakdown occurs. Even if the breakdown voltage is high enough to operate the sensor at 500 V this is contrary to the measurements under dry conditions. Such instabilities are not uncommon and are typically related to passivation and design issues².

For the passivation of the sensor SINTEF uses a PECVD deposition of a 0.5 μm thick layer of SiO_2 and a 0.25 μm thick layer of SiN . Figure 5.5.2 shows a cross section of the sensor in the region between GR1 and GR2. It is seen that the passivation, where the brown area is the SiO_2 and the other one the SiN , covers only parts of the aluminum. Both, the SiO_2 and the SiN , are not perfect isolators but have a finite conductivity. For PECVD at 300°C deposited SiN the

²For different breakdown voltages under dry and humid conditions see [138]. In the ALICE detector double-side modules supplied by SINTEF show high current with humidity and have to be switch off if $\text{RH} > 15\%$ [139].

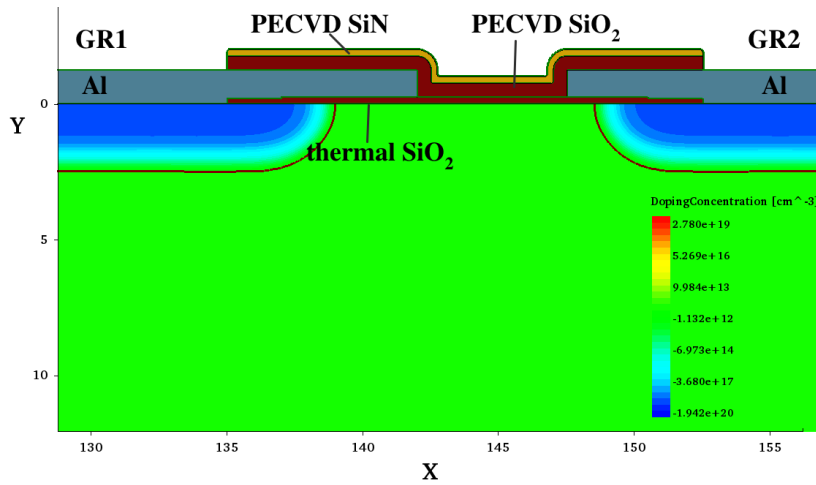


Figure 5.5.2.: Cross section of the sensor in the region between GR1 and GR2. The different layers in the middle between the metals are from bottom to top: 0.25 μm thermal SiO_2 (brown) and the passivation consisting of 0.5 μm SiO_2 (brown) and 0.25 μm SiN (ocher)

surface resistivity is about $10^{13} \Omega/\text{sq}$ and the bulk resistivity $10^{15} \Omega \cdot \text{cm}$ [36]. Values which are at least one order of magnitude lower than that for SiO_2 . For the bulk resistivity the reason that SiO_2 has a higher resistivity than SiN is a result of the greater bandgap and lower trap density compared to SiO_2 . Due to this conductivity, even under dry conditions, a small current will flow in and on the surface of the insulators.

The observed results can now be explained by at least two ways. The first one is based on the adsorption of ions from the surrounding air and the second on the surface conductivity. The amount of available ions and the surface conductivity are both influenced by humidity. In the first case the ions are attracted from the surrounding air and tend to neutralize the surface charge induced by the electrical field which is mainly due to the potential difference of the neighboring rings. This will result more or less in an accumulation of charges at the corners of the SiN in the gap between the rings and will change the effective oxide charge at the Si-SiO₂ interface. If these changes are too large on the different guard rings the potential difference between adjacent rings can be too large and a breakdown can occur even for the irradiated sensors.

In the second case under humid conditions always a water film, which is a few monolayer thick, will be present on top of the passivation which reduces the surface conductivity. Simulations show that a current flowing on top of the passivation from one ring to the next ring can considerably change the potential distribution of the different guard rings. In order to simulate this effect a 10 nm thick intrinsic polysilicon layer was deposited on top of the passivation and turned around the corner of the SiN to contact with the Al. The resistivity was changed by adjusting the mobilities of the carriers. An example of the potentials of the straight section of the 15 guard rings vs. bias voltage for $N_{ox} = 3 \cdot 10^{12} \text{ cm}^{-2}$ in the case without passivation (dry conditions) and with passivation and polysilicon layer is shown in Figure 5.5.3(a) and Figure 5.5.3(b),

respectively. The difference of this two cases is especially obvious for the inner guard rings were

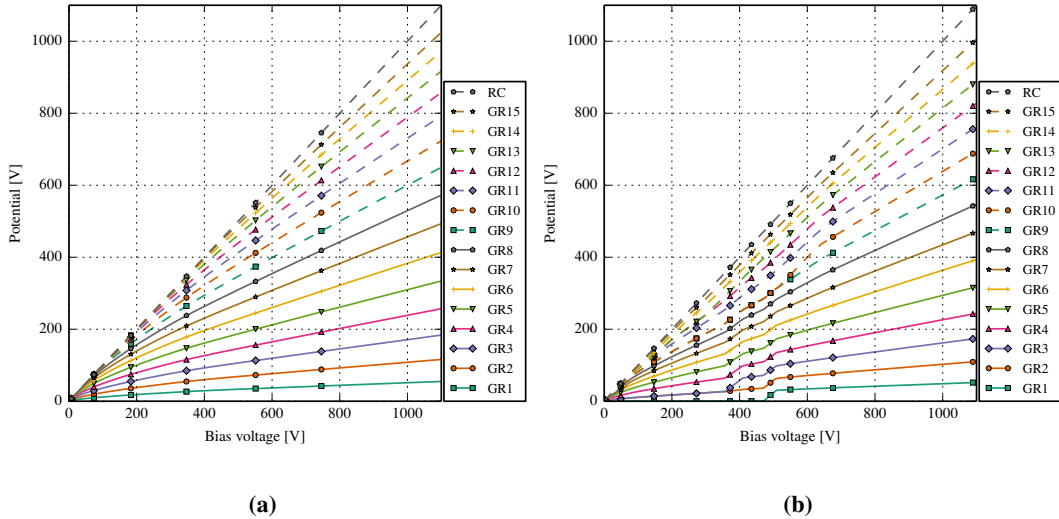


Figure 5.5.3.: Simulated potential of the 15 guard rings (GR) vs. bias voltage for $N_{ox} = 3 \cdot 10^{12} \text{ cm}^{-2}$ for the straight section. The voltage is applied at the rear contact (RC). (a) Without passivation layer (dry conditions) (b) With passivation and 10 nm polysilicon layer on top.

the punch-through between the rings in both cases is quite different. For example, GR1 is up to 500 V on ground potential in the case with passivation and polysilicon layer, whereas in the dry case the potential of GR1 is at low reverse bias at a higher potential. Such a behavior can lead to instabilities.

To figure out the detailed reason for the difference between the measurements in dry and humid conditions further investigations are needed. For example measurements of the potentials of the guard rings and inspection with an IR camera to locate hot spots. If the main reason is the surface current one could try to replace the SiN with SiO₂ which has a higher resistivity.

5.6. Summary

The AGIPD sensor fabricated by SINTEF and optimized for high operating voltage at high X- ray doses in an atmosphere of a relative humidity below 5%, meets all specifications for the entire dose range for both uniform as well as for non-uniform irradiation. The reason for a soft breakdown for the non-irradiated sensor around 800 V is understood and does not present a problem. The measured current-voltage characteristics and the values for the inter-pixel capacitance as function of X-ray dose are quite similar to the predictions from the simulations. The breakdown voltage for the radiation-optimized design is significantly higher than for the standard design, and thus the optimization is considered a success.

6. Charge losses and boundary conditions in segmented $p^+ - n$ silicon sensors

As shown in the previous chapters in a segmented silicon sensor the electrical field in the gap region beneath the Si-SiO₂ interface is sensitive to charges in the SiO₂, in additional passivation layers and on the outer surface due to environmental conditions. The electrical field can be disturbed in such a way that for example charges injected by laser light are incompletely collected.

In [99] charge losses in segmented $p^+ - n$ silicon sensors at the Si-SiO₂ interface have been studied using a multi-channel time-resolved current measurement setup (multi-TCT). The electron-hole pairs were produced by a focused (rms 3 μm) sub-nanosecond laser light with a wavelength of 660 nm, with an absorption length at room temperature of approximately 3.5 μm . The charge signals induced in the readout strips and the rear electrode as a function of the position of the light spot are described by a model which allows a quantitative determination of the charge losses and of the widths of the electron-accumulation and hole-inversion layers close to the Si-SiO₂ interface. Depending on the applied bias voltage, biasing history and environmental conditions, like humidity, incomplete electron or hole collection and different widths of the accumulation layers were observed. In addition, the results depend on the time after biasing the sensor, with time constants which can be as long as days.

This chapter summarizes the results of [99] and several figures are taken from there. The measurements have been performed by T. Poehlsen [15]. The TCAD simulations which allowed to understand and interpret the data have been performed by the author. Their complexity significantly surpasses previous simulation of silicon sensors.

6.1. Sensor under investigation

The sensor which has been investigated is a DC-coupled $p^+ - n$ strip sensor produced by Hamamatsu [71]. The relevant parameters of the sensors are listed in Table 6.1.1 and a cross-section is shown in Figure 6.1.1. The sensor is covered by a passivation layer with openings at the two ends of each strip for bonding. The sensor was investigated as produced, and after irradiation with 12 keV photons to 1 MGy (SiO₂) followed by annealing for 60 minutes at 80°C. The corresponding values for oxide charge density, N_{ox} , integrated interface trap density, N_{it} , and surface current density, I_{surf} , shown in Table 6.1.2 have been derived from measurements on

6. Charge losses and boundary conditions in segmented p^+n silicon sensors

Parameter	Value
coupling	DC
pitch	50 μm
depletion voltage	$\sim 155 \text{ V}$
doping concentration	$\sim 10^{12} \text{ cm}^{-3}$
single strip capacitance	$\sim 1.4 \text{ pF}$
rear side capacitance	$\sim 12 \text{ pF}$
gap between p^+ implants	39 μm
width p^+ implant window	11 μm
depth p^+ implant	unknown
aluminum overhang	2 μm
number of strips	128
strip length	7.956 mm
sensor thickness	450 μm
thickness SiO_2	700 nm
passivation layer	unknown
crystal orientation	$\langle 111 \rangle$

Table 6.1.1.: Parameters of the Hamamatsu sensor.

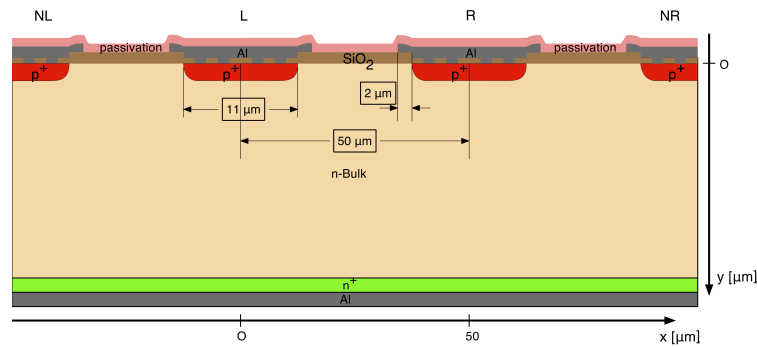


Figure 6.1.1.: Schematic layout of the strip region of the DC-coupled Hamamatsu p^+n sensor, and definition of the x and y coordinates. The drawing is not to scale.

MOS capacitors and gate-controlled diodes from Hamamatsu [14] and scaled to the measurement conditions of the sensor.

X-ray dose	0 Gy	1 MGy (60 min. at 80°C)
N_{ox}	$1.3 \cdot 10^{11}/\text{cm}^2$	$1.4 \cdot 10^{12}/\text{cm}^2$
N_{it}	$0.87 \cdot 10^{10}/\text{cm}^2$	$1.6 \cdot 10^{12}/\text{cm}^2$
I_{surf}	$9.8 \text{ nA}/\text{cm}^2$	$2.2 \text{ }\mu\text{A}/\text{cm}^2$

Table 6.1.2.: Oxide charge density, N_{ox} , interface trap density integrated over the Si-band gap, N_{it} , and surface current density, I_{surf} , obtained from measurements on test structures, a MOS capacitor and a gate-controlled diode, produced by Hamamatsu. The values for a temperature of 22.9°C before and after X-ray irradiation to 1 MGy and annealing for 60 minutes at 80°C are presented. The actual measurements were taken at 21.8°C and, for the irradiated structures after annealing for 10 minutes at 80°C, and then scaled (scale factor ~ 0.7) to above values, which correspond to the measurement conditions of the sensor investigated.

6.2. Electrostatic potential and weighting potential

In this section 2-D simulations using SYNOPSIS TCAD [88] are presented. They illustrate the distribution of the field and potential in the region of the strips and the Si-SiO₂ interface, and are used to calculate the weighting potentials [140–143], which are required to estimate the expected signals, i.e. the charges induced in the readout strips and the rear electrode, as a function of the position of the injected light.

The simulated electric potential in a strip sensor close to the Si-SiO₂ interface between the strip implants depends on the oxide charge density, the density of charged interface states, the current distribution in the sensor and the boundary conditions. The boundary conditions take into account the effect of charges laying outside of the simulated region. Usually in a sensor simulation Neumann boundary conditions (zero electric field component normal to the surface) are applied at the outer surface of the SiO₂ or the passivation layer (if simulated) because they are imposed in a natural way by the finite element solvers. The Neumann boundary conditions are a good approximation for a dry and clean environment [101]. As shown in [123] for a sensor kept under bias the steady-state condition is that, due to the small surface conductivity, the outer surface will assume the same potential as the neighboring metal strips. This condition corresponds to Dirichlet boundary conditions and can be realized in the simulation by depositing a thin (10 nm) Al layer on top of the passivation and defining this as a contact with 0 V applied (assuming the strips are on ground). Because the Al layer on top of the passivation layer works as a gate this is also known as gate boundary conditions [101].

In Figure 6.2.1 the electric potential for the Hamamatsu sensor with the strips at 0 V and the rear contact at 200 V for Neumann and Dirichlet boundary conditions are shown where a positive oxide charge density of $2 \cdot 10^{12} \text{ cm}^{-2}$ and a surface current density of $8 \text{ }\mu\text{A}/\text{cm}^2$ are

assumed. That there is little difference in electrical field inside the silicon is due to the high oxide charge density used in the simulation.

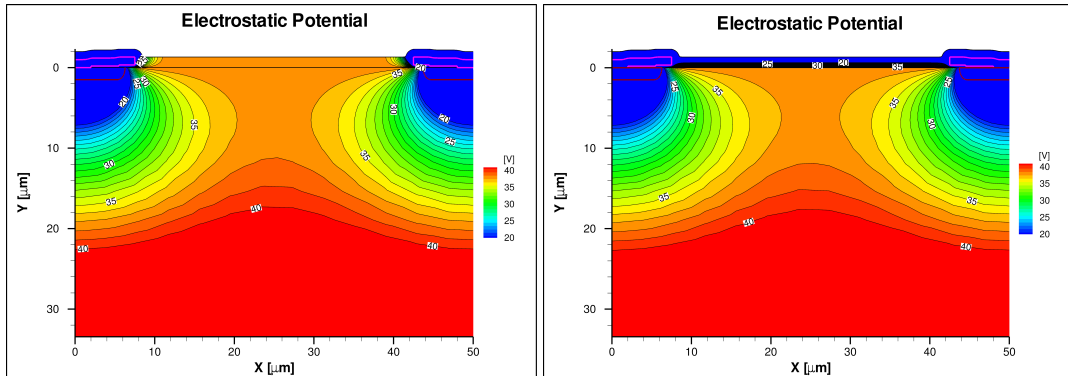


Figure 6.2.1.: Electric potential for the Hamamatsu strip sensor calculated using SYNOPSIS TCAD. Neumann boundary conditions (left) and Dirichlet boundary conditions (right) on the SiO_2 surface, a positive oxide charge density of $2 \cdot 10^{12} \text{ cm}^{-2}$ and a surface current density of $8 \mu\text{A}/\text{cm}^2$ are assumed. The bias voltage, applied to the rear contact is 200 V. The sensor has a pitch of $50 \mu\text{m}$ and a thickness of $450 \mu\text{m}$. Only the region $35 \mu\text{m}$ from the strip surface is shown. The colour scale covers only the range between 20 and 40 V, and the distance between the equipotential lines is 1 V.

In Figure 6.2.2 the electron density for the same simulation is presented. The high electron density of several 10^{18} cm^{-3} shows that an accumulation layer with a width in x direction of about $35 \mu\text{m}$ has formed below the Si-SiO₂ interface. The dark current is mainly due to the surface generation current from the depleted Si-SiO₂ interface. The holes generated at the interface drift to the p^+ strips. The electrons first diffuse over the saddle point of the potential at $x = 25 \mu\text{m}$ and $y \approx 6 \mu\text{m}$ and then drift along the field lines to the rear contact, as can be seen from the increased electron density at the symmetry plane between the strips for larger y values. Between the readout strips, approximately $6 \mu\text{m}$ below the Si-SiO₂ interface, the potential has a saddle point and the electric field points from the accumulation layer into the sensor. Thus, electrons produced close to the accumulation layer may not reach the rear contact during the integration time of the measurement.

The impact of different boundary conditions can be seen in Figure 6.2.3 where the width of the accumulation layer simulated 10 nm below the Si-SiO₂ interface is plotted as function of the oxide-charge density for a bias of 200 V. In the case of Neumann boundary conditions already at an oxide-charge density as low as $3 \cdot 10^{10} \text{ cm}^{-2}$ a $10 \mu\text{m}$ wide accumulation layer is present, whereas in the case of Dirichlet boundary conditions the accumulation layer is absent up to an oxide-charge density of $4 \cdot 10^{11} \text{ cm}^{-2}$ which then strongly increases reaching the same width as in the case of Neumann boundary conditions at approximately $2 \cdot 10^{12} \text{ cm}^{-2}$. The details depends on the gap width, oxide thickness and oxide-charge density. For a discussion see [24, 85]. It should be noted that, given the uncertainties on the boundary conditions, the

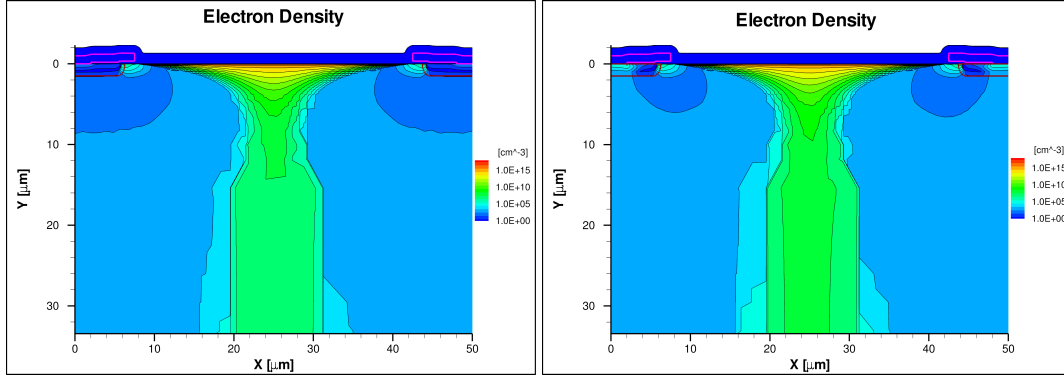


Figure 6.2.2.: Free electron density for the Hamamatsu strip sensor. The conditions for the simulations are the same as for Figure 6.2.1.

simulations presented only serve as an illustration.

In a sensor the induced current in the electrode j of a moving point charge q is according to the Shockley-Ramo theorem [140, 141] given by

$$\frac{dQ_j}{dt} = I_j = q\vec{v} \cdot \nabla\phi_{w,j}, \quad (6.2.1)$$

where \vec{v} is the instantaneous velocity of the charge carrier and $\phi_{w,j}$ the weighting potential of the electrode j . To calculate the charge Q_j induced on the electrode j by a charge q moving in the time interval $[t_1, t_2]$ from position \vec{x}_1 to \vec{x}_2 the expression (6.2.1) has to be integrated over the time interval resulting in:

$$Q_j = \int_{t_1}^{t_2} I_j(t) dt = \int_{t_1}^{t_2} q\vec{v}(t) \cdot \nabla\phi_{w,j} dt = q \int_{\vec{x}_1}^{\vec{x}_2} \nabla\phi_{w,j} d\vec{x} = q (\phi_{w,j}(\vec{x}_2) - \phi_{w,j}(\vec{x}_1)) \quad (6.2.2)$$

The dimensionless weighting potential is a measure of the coupling of a the test charge to the read-out electrode. There is the question of how to calculate this weighting potential. According to Ramo's definition, all electrodes must be kept at 0 V while the electrode under consideration is raised to 1 V. As shown in 1964 by Gunn [142] and later using a different approach by Hamel and Julien [143] this definition is not always correct. If in addition to the electrodes regions with movable charges are present the correct formula for the weighting field is:

$$\phi_{w,j}(\vec{x}) = \left. \frac{\partial\phi(\vec{x})}{\partial V_j} \right|_{V_{op}} \quad (6.2.3)$$

Accumulation layer or polarizable insulators are examples for such regions. Thus, the weighting potential of electrode j is given by the gradient of the electric potential $\phi(\vec{x})$ with respect to

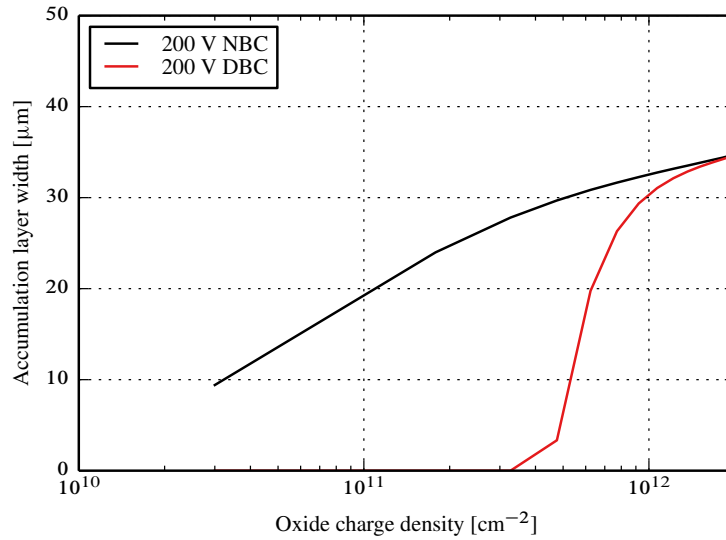


Figure 6.2.3.: Accumulation layer width as function of oxide charge density for a bias of 200 V in the case of Neumann boundary conditions (NBC) and of Dirichlet boundary conditions (DBC).

the voltage on electrode j while the potentials on all other electrodes are maintained at their operating values.

Figure 6.2.4 shows the weighting potential for strip L (centred at $x = 0$), $\phi_{w,L}$, for the above mentioned simulations of the Hamamatsu strip sensor. Both the two-dimensional distributions, as well as its x dependence for y values of 0.01, 1, 2 and 3 μm below the Si-SiO₂ interface are shown. $\phi_{w,L}$ is obtained from the difference of the potential calculated with strip L at 1 V and all other strips at 0 V minus the potential with all strips at 0 V. In both cases the backplane is biased to 200 V. In this way the effects of the mobile charge carriers in the accumulation layer are properly taken into account. One consequence is that $\phi_{w,L}$ is constant over the accumulation layer. It should also be noted that, as expected, the weighting potential is hardly affected by the boundary conditions on the sensor surface. A similar simulation has been done for the weighting potential of the rear contact.

Using TCAD for a detailed simulation of a TCT setup is time consuming and complicated. Therefore based on the simulation of the weighting potential and assumption for the spot size of the laser a model was developed in order to estimate the collected charge by the individual strips and by the rear contact as function of the position x of the laser beam. Fitting of the model to the measurements allows the determination of charge losses. For the details see [99].

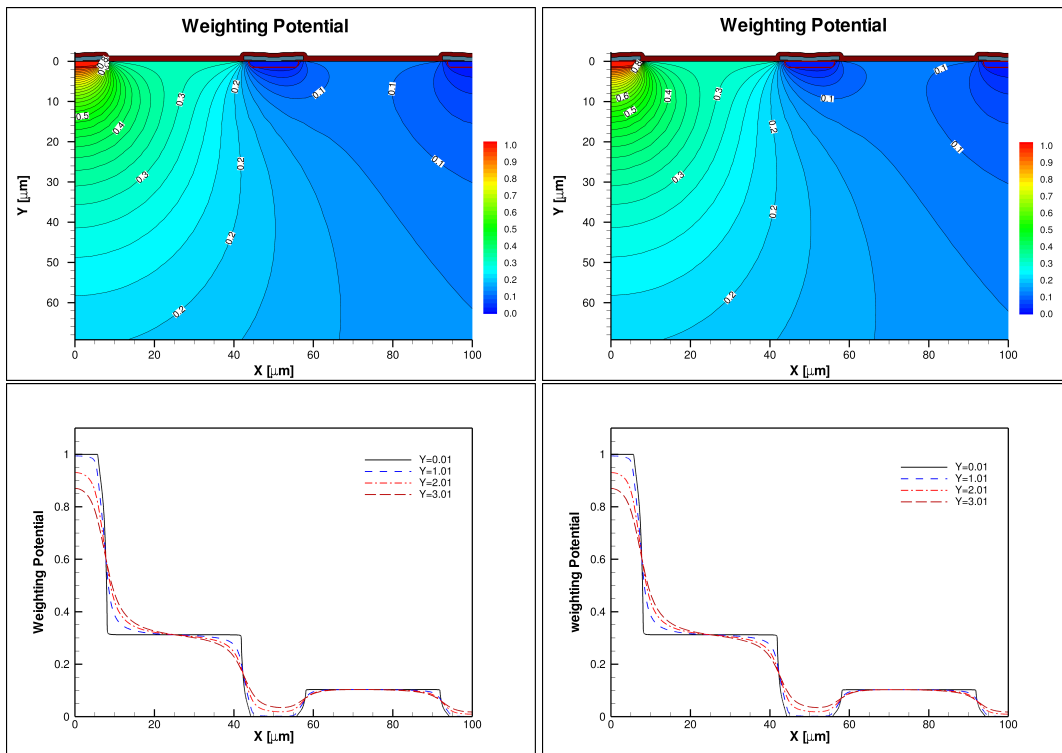


Figure 6.2.4.: Weighting potential for strip L for the Hamamatsu strip sensor. The top row shows the two-dimensional distributions, the bottom row the one-dimensional distributions 0.01, 1.0, 2.0 and 3.0 μm below the Si-SiO₂ interface. The parameters for the simulations are the same as for Figure 6.2.1.

6.3. Summary of measurements and discussion of the results

In this section the measurements results are summarized and an attempt is made to qualitatively interpret the results and discuss their relevance for the operation of p^+n sensors.

The measurements were performed at room temperature and at a bias voltage of 200 V under the following environmental conditions:

- "humid": sensor biased to 200 V in a humid atmosphere (relative humidity > 60 %),
- "dried at 0 V": sensor stored at 0 V for a long time, then put into a dry atmosphere for > 60 minutes (relative humidity < 5 %), and then biased to 200 V for the measurements,
- "dried at 500 V": sensor kept for a few hours at 500 V in a humid atmosphere (relative humidity > 60 %), then dried for > 60 minutes and afterwards biased in the dry atmosphere to 200 V for the measurements.

For the non-irradiated strip sensor the most relevant observed results are

- Electron losses when ramping up the voltage in a dry atmosphere ("dried at 0 V - 0 Gy"),
- Hole losses when ramping down the voltage in a dry atmosphere ("dried at 500 V - 0 Gy"),
- No or little charge losses in a humid atmosphere ("humid - 0 Gy"), and
- The time to reach the steady state after a voltage change is about an hour in a humid and \sim 100 hours in a dry atmosphere as shown in Figure 6.3.1.

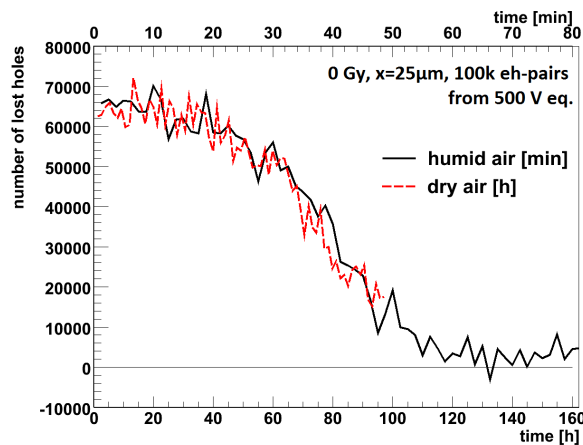


Figure 6.3.1.: Number of holes lost for light pulses generating \sim 100 000 eh -pairs as a function of the time after the voltage applied to the non-irradiated sensor has been reduced from 500 V in steady-state conditions, to 200 V . The upper scale of the horizontal axis (in minutes) refers to the situation "humid", the lower one (in hours) to "dry". Taken from [99].

First the cause of the charge losses and their dependence on time and humidity are discussed. The explanations are supported by detailed two-dimensional simulations of the sensor assuming different boundary conditions on the surface of the passivation and different values of $q \cdot N_{ox}^{eff} = q \cdot (N_{ox} + N_{it}^{don} - N_{it}^{acc})$, the effective charge density at or close to the Si-SiO₂ interface. q is the elementary charge, N_{ox} the density of positive oxide charges, and N_{it}^{don} and N_{it}^{acc} the density of filled donor and acceptor states at the interface, integrated over the silicon band gap.

The observations are explained in the following way: For the initial conditions the assumption is made that the sensor is in steady-state conditions at 0 V with zero charge density on its surface. When the sensor is biased, parts of the p^+ implants will be depleted, resulting in negative charges at the p^+n junctions of the strips. These negative charges are balanced by the positive charges of the depleted n bulk and of the n^+ implant of the rear contact, if the sensor is biased above depletion. These charges produce an electric field at the Si-SiO₂ interface and at the sensor surface. If surface charges on top of the passivation do not move, the electric field at the surface will have a longitudinal component which points to the p^+ implants and a transverse component at the Si-SiO₂ interface which points into the SiO₂¹. This is seen in the top left plot of Figure 6.3.2, which shows for a sensor biased to 200 V a TCAD simulation of the longitudinal surface field for a density $N_{ox}^{eff} = 10^{11} \text{ cm}^{-2}$ and zero surface-charge density. This longitudinal surface field, which reaches values of 100 kV/cm in the simulation, will cause the redistribution of surface charges until a uniform surface potential is reached. This is the steady-state condition for a given applied voltage. As the effective surface conductivity increases with increasing humidity, the steady state will be reached in a shorter time for humid than for dry conditions. The left plot of Figure 6.3.3 shows the simulated surface charge distribution for $N_{ox}^{eff} = 10^{11} \text{ cm}^{-2}$, the p^+ implants at 0 V, and the rear contact at 200 V, which approximately represents the steady-state condition. The potential on the surface is also set to 0 V. In principle the potential on the surface should have been set to a voltage so that the integrated charge on the surface is zero. We however did not manage to perform such a simulation. A crude estimation indicates that the surface potential is between 1/3 to 1/2 of the potential of the accumulation layer.

If the sensor is in steady-state conditions under bias and the voltage is ramped down, the field direction will be opposite to the situation discussed above: The transverse component of the electric field will point into the Si and the longitudinal component of the surface field will point away from the p^+ implants. This can be seen at the bottom left plot of Figure 6.3.2, which shows the simulated longitudinal field distribution for the sensor initially in steady-state conditions at 500 V and then biased to 200 V in a dry atmosphere, i.e. assuming the surface charge distribution from the steady-state simulation at 500 V. We note, that the maximum value of the simulated surface field is only 25 kV/cm, significantly smaller than the value for the case discussed above. The wiggles in the curves are an artifact of the simulation: The surface charge distribution at

¹In the simulation this is realized by defining a boundary at $y = -100 \text{ } \mu\text{m}$ where Neumann boundary conditions are applied. On the surface of the passivation layer, fixed charges, in this case zero, are put. For the simulation "dried at 500 V" the surface-charge distribution obtained for the steady-state conditions at 500 V is used.

6. Charge losses and boundary conditions in segmented $p^+ - n$ silicon sensors

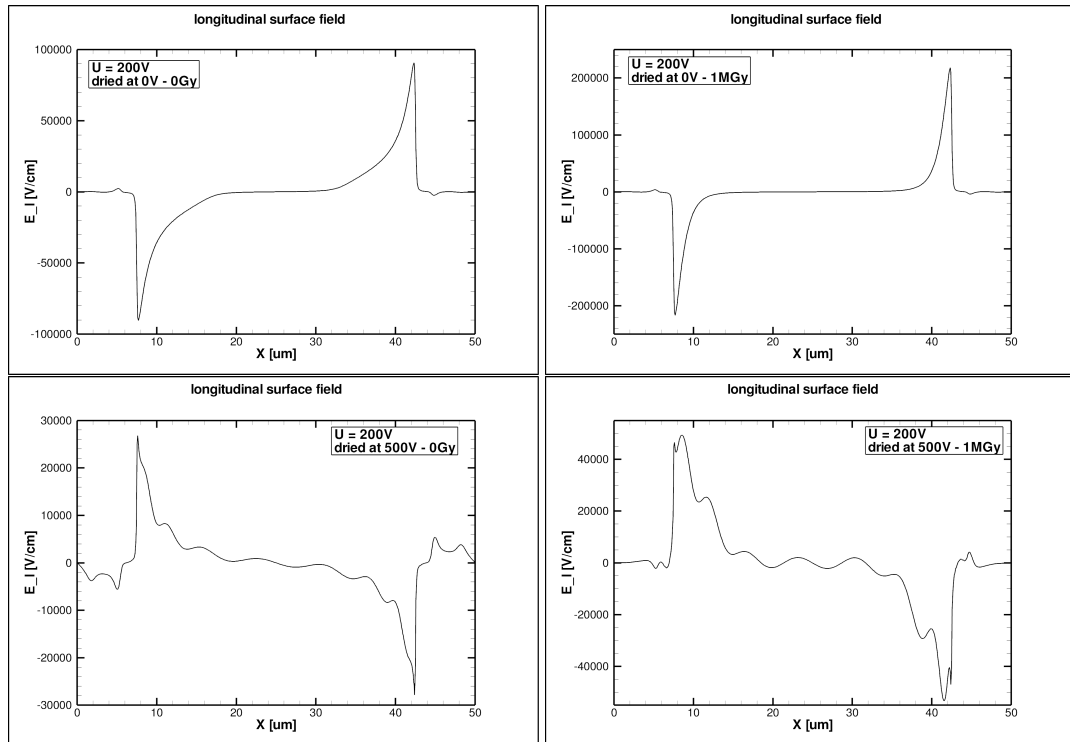


Figure 6.3.2.: Simulated longitudinal component of the surface field for the sensor biased to 200 V under dry conditions. Left: Non-irradiated sensor ($N_{int}^{eff} = 10^{11} \text{ cm}^{-2}$); right: Irradiated sensor ($N_{int}^{eff} = 10^{12} \text{ cm}^{-2}$); top: Steady-state conditions at 0 V, and bottom at 500 V. The strips are centred at $x = 0$ and $50 \text{ } \mu\text{m}$.

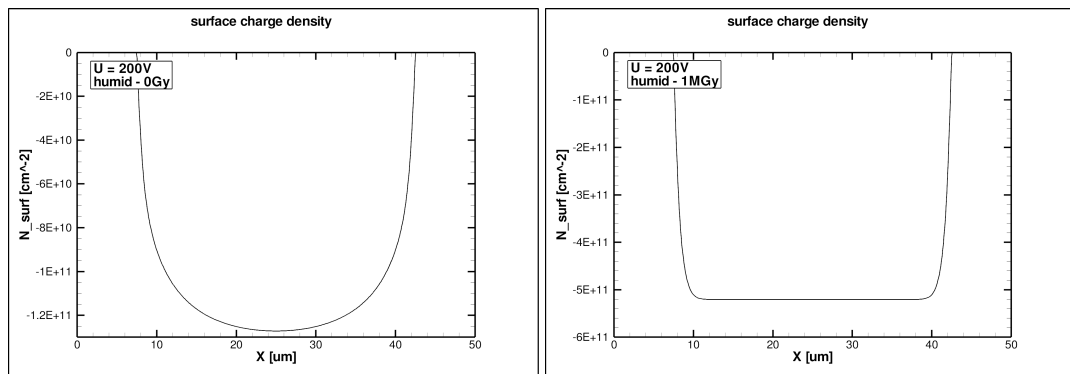


Figure 6.3.3.: Simulated distribution of the charge-carrier density on the surface of the sensor biased to 200 V for steady-state conditions. Left: Non-irradiated sensor ($N_{ox}^{eff} = 10^{11} \text{ cm}^{-2}$); right: Irradiated sensor ($N_{ox}^{eff} = 10^{12} \text{ cm}^{-2}$).

500 V has been parameterized by the sum of 10 Gaussians. It should be stressed that, given the assumptions made in the simulations, the results should be understood as qualitative only.

For completeness also on the right sides of Figures 6.3.2 and 6.3.3 the simulated surface fields and surface-charge distributions for a density $N_{ox}^{eff} = 10^{12} \text{ cm}^{-2}$ are shown, which corresponds to a sensor with X-ray radiation damage. It should be noted that qualitatively the results are similar to the non-irradiated situation. However, both the surface fields and the surface-charge densities are significantly higher than for the non-irradiated sensor.

The dependence of the surface sheet resistance, R_{\square} , on humidity, and the impact on the performance of MOS structures, are well documented [136, 144, 145]. Under the simplified assumption that the sheet resistance is independent of the electric field, the time dependence of the distribution of the surface charge on the way to the steady state scales with R_{\square} . This scaling is observed in the measurements shown in Figure 6.3.1. The ratio of the time constants of ~ 120 is compatible with values from the literature. A crude estimation of the surface resistivity, following the approach presented in [146], gives values for R_{\square} of the order of $10^{17} \Omega$ for the humid, and approximately a factor 120 higher for the dry conditions. Similar values for R_{\square} are reported in [136, 146].

It should be mentioned that the time it takes to reach the steady state on the surface of the sensor does not depend on the distance between the injected light and the end of the strips where the openings in the passivation are located. This agrees with the expectation that the steady state on the sensor surface is reached by a local redistribution of the surface charges, and not by charges moving from or to the bond pads.

Next the reasons for the different type of charge losses for the different measurement conditions with the help of TCAD simulations are explained. Figures 6.3.4 and 6.3.5 show simulated distributions of the electric potential and of the electron and hole densities in the sensor close to the Si-SiO₂ interface for different measurement conditions. The discussion starts with the situation of significant electron losses, which are observed for the condition "dried at 0 V - 0 Gy". At the beginning the assumption is made that the sensor is in steady-state conditions at 0 V with zero charge density on its surface. If the sensor is biased to 200 V in the condition "dried at 0 V - 0 Gy" the surface-charge density remains zero, and an electron-accumulation layer forms below the Si-SiO₂ interface as seen by the high electron density visible in the middle left plot of Figure 6.3.5 and the top plot of Figure 6.3.6: The electron density reaches a maximum value of $\sim 3 \cdot 10^{16} \text{ cm}^{-3}$ at the interface for a depth of $\sim 5 \text{ nm}$ in y . The white lines in Figures 6.3.4 and 6.3.5 indicate the electron density of $\sim 10^{12} \text{ cm}^{-2}$, which corresponds to the n doping of the sensor. Inspection of the corresponding potential distribution (middle left plot of Figure 6.3.4) shows, that the potential has a saddle point $\sim 5 \mu\text{m}$ below the Si-SiO₂ interface, and that the electric field points from the interface into the sensor. Thus holes produced close to the interface will drift in a short time along the field lines to the readout strips where they are collected. Hole losses due to recombination in the accumulation layer are estimated to be negligible. However, a fraction of the electrons produced close to the accumulation will reach the accumulation layer and, like those produced in this layer, will spread over the layer with

6. Charge losses and boundary conditions in segmented p^+n silicon sensors

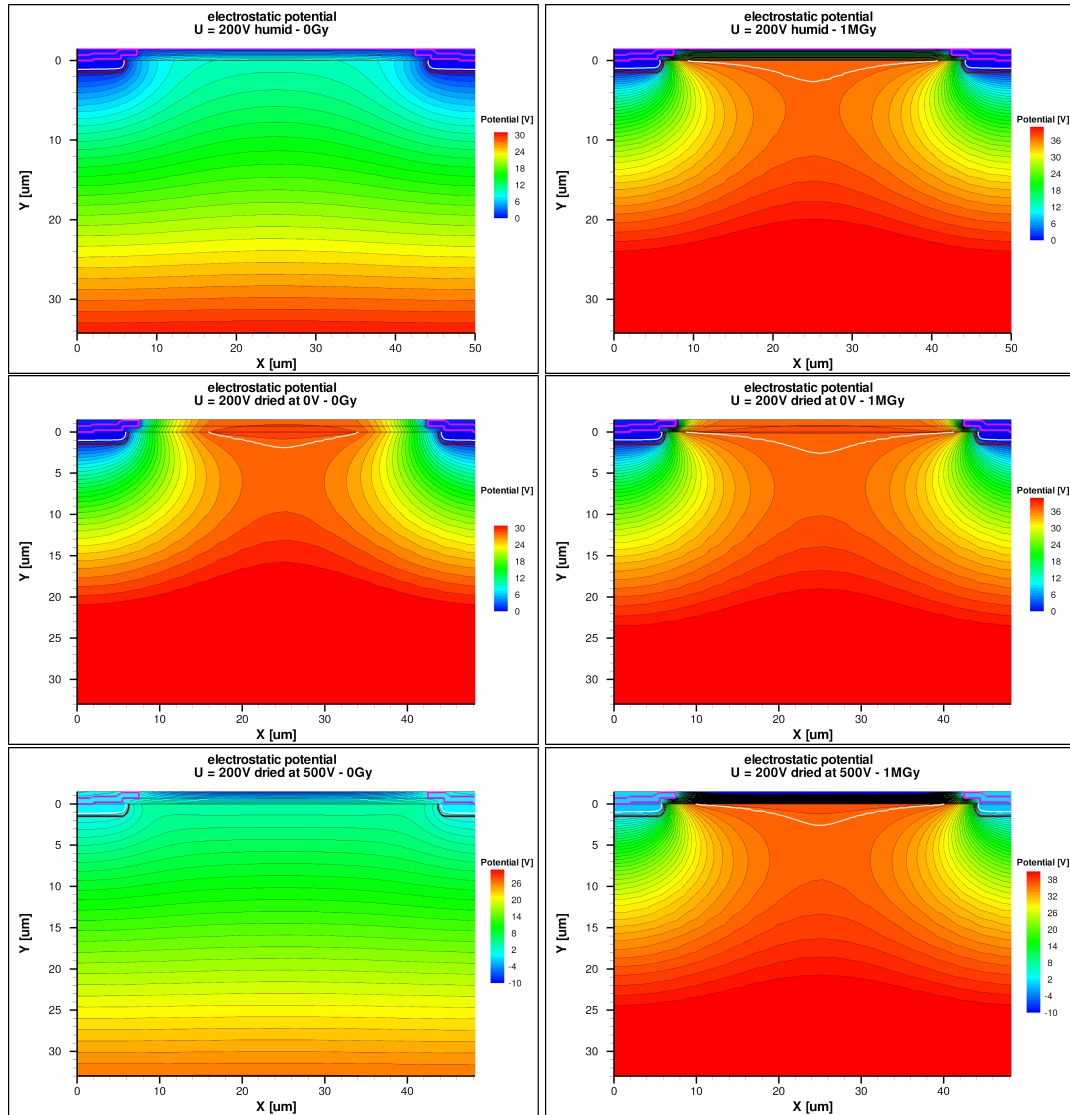


Figure 6.3.4.: Simulated potential distribution for the sensor biased to 200 V: Non-irradiated (left - $N_{ox}^{eff} = 10^{11} \text{ cm}^{-2}$) and irradiated to 1 MGy (right - $N_{ox}^{eff} = 10^{12} \text{ cm}^{-2}$) for the conditions "humid" (top), "dried at 0 V (middle)" and "dried at 500 V (bottom)".

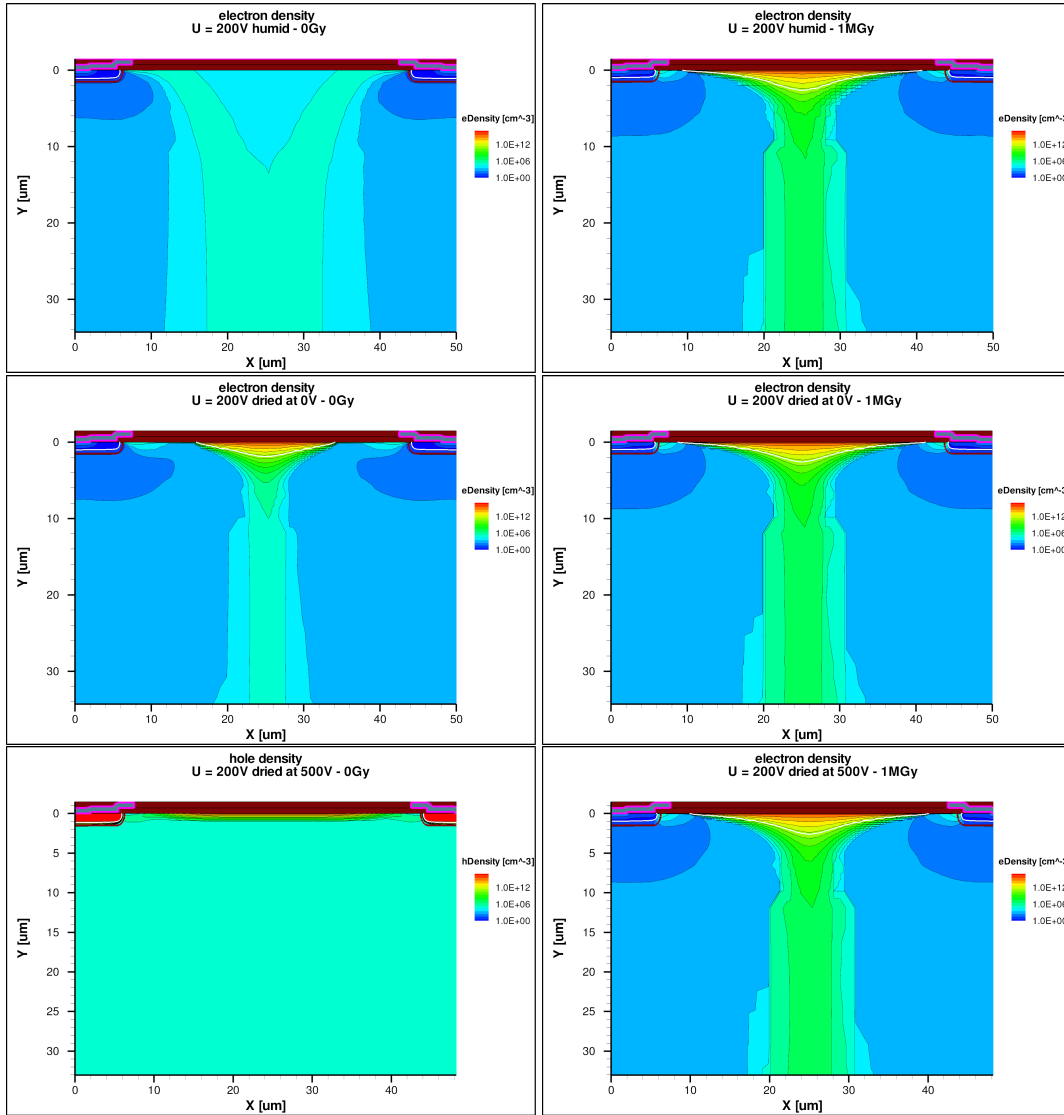


Figure 6.3.5.: Simulated electron and hole densities close to the Si-SiO₂ interface for the sensor biased to 200 V: Non-irradiated (left - $N_{ox}^{eff} = 10^{11} \text{ cm}^{-2}$) and irradiated to 1 MGy (right - $N_{ox}^{eff} = 10^{12} \text{ cm}^{-2}$) for the conditions "humid" (top), "dried at 0 V (middle)" and "dried at 500 V (bottom)". Except for the bottom left plot, which shows the holes density, only the electron densities are shown.

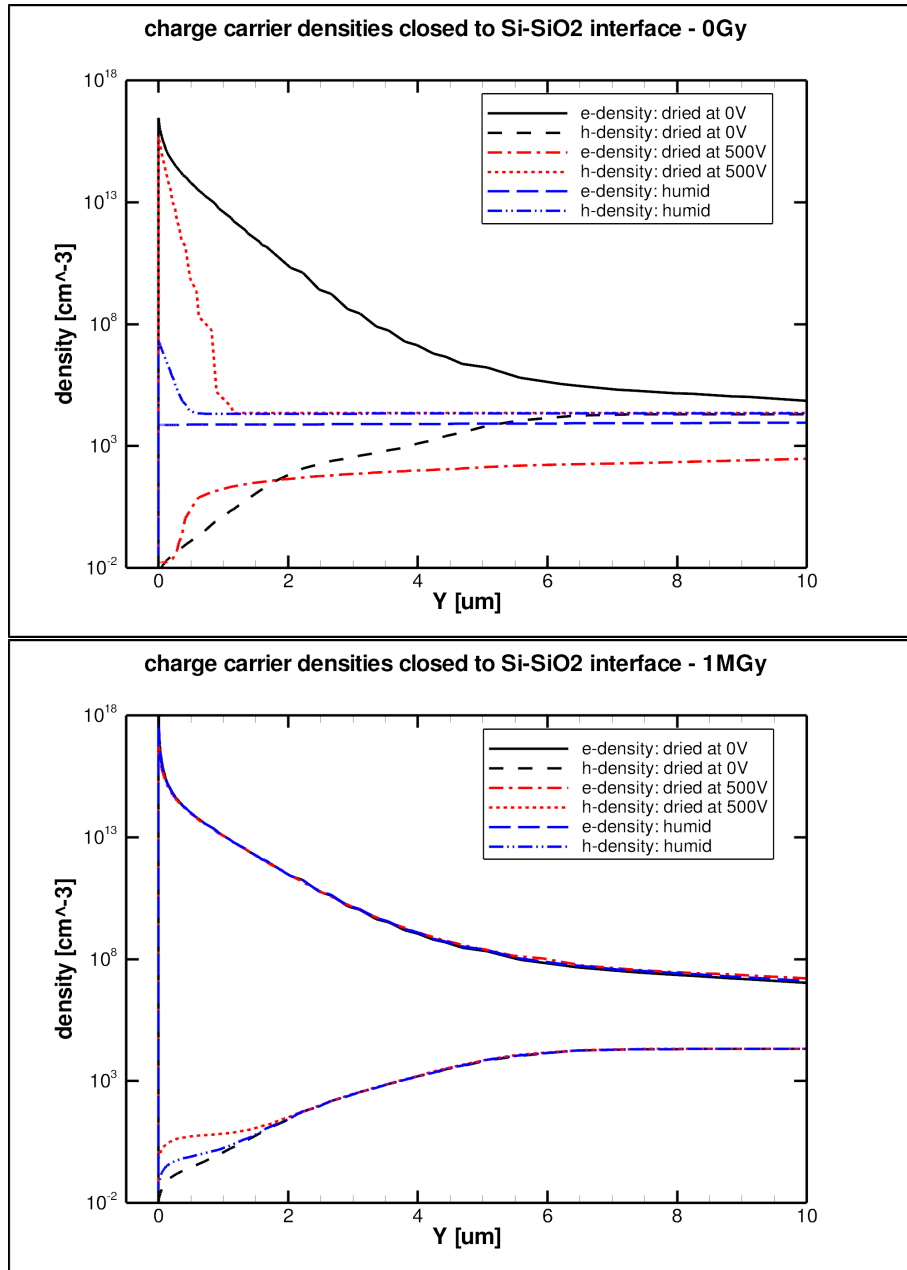


Figure 6.3.6.: Simulated charge carrier densities close to the Si-SiO₂ interface in the symmetry plane between the strips for the sensor biased to 200 V and different measurement conditions. Left for $N_{ox}^{eff} = 10^{11} \text{ cm}^{-2}$, corresponding to a non-irradiated sensor, and right for $N_{ox}^{eff} = 10^{12} \text{ cm}^{-2}$, corresponding to a sensor irradiated to dose of 1 MGy. A high electron density at the interface ($y = 0$) is evidence for an electron-accumulation layer, a high hole density for an inversion layer.

a time constant given by the dielectric relaxation time $\tau_R = \epsilon_{Si}/(q \cdot \mu_e \cdot n)$. ϵ_{Si} denotes the dielectric constant of silicon, μ_e the electron mobility and n the position dependent electron density. For $n = 10^{15} \text{ cm}^{-3}$ the value is $\tau_R = 5 \text{ ps}$ [136], which is short compared to the charge collection time of a few nanoseconds. These electrons are "lost", as they do not induce a significant signal within the integration time of the measurements. As they spread at least over the entire length of the accumulation layer along the sensor strips, the resulting increase in electron density and change of the local electric field will be quite small. A study of the impact of the number of electrons "lost" on the charge collection, and the time required to return to the pre-light injection state, is the topic of [15]. It should be noted that Figure 6.3.5 shows that, the depth of the electron-accumulation layer have its maximum in the symmetry plane between the readout strips and decrease towards the readout strips.

Next the situation of hole losses which occur for the condition "dried at 500 V - 0 Gy" is discussed. In this case the negative charges on the surface overcompensate the positive charges at the interface, and a hole inversion layer forms below the Si-SiO₂ interface. This can be seen in the bottom left of Figure 6.3.5 and in Figure 6.3.6 as a high density of holes at the interface. The value found for the maximum hole density is $\sim 4 \cdot 10^{15} \text{ cm}^{-3}$. It should be noted that the depth of the inversion layer is much smaller than for the accumulation layer and essentially independent of position x . The potential distribution presented in the bottom left plot of Figure 6.3.4 shows that the electric field distribution resembles the situation of a pad sensor: The electric field in the sensor points towards the Si-SiO₂ interface and the transverse field component is small. This explains the large value of the hole diffusion term σ_{diff} observed for this condition in [99].

Finally the situation of no or little losses, which is observed for the condition "humid - 0 Gy" is discussed. In this case the potential on the surface of the sensor is uniform, the redistributed surface charges compensate the positive interface charges of density N_{ox}^{eff} , and neither an electron-accumulation nor a hole-inversion layer forms at the Si-SiO₂ interface. As shown in Figure 6.3.6 top, both electron and hole densities are below $\sim 10^8 \text{ cm}^{-3}$ at the Si-SiO₂ interface. From the corresponding potential distribution shown on the top left plot of Figure 6.3.4 one can conclude, that the electric field close to the Si-SiO₂ interface is weak and points to the interface. Nevertheless, most holes generated in this region will diffuse until they reach a region of higher field and then drift to a readout strip.

The results of the simulations for the irradiated sensor for the three measurement conditions are shown on the right sides of Figures 6.3.4, Figure 6.3.5 and the bottom of Figure 6.3.6. Given the high positive charge density at the interface of $N_{ox}^{eff} = 10^{12} \text{ cm}^{-2}$ electron-accumulation layers are present under all three conditions. Given that the charge densities change by 20 orders of magnitudes, the curves for the electron densities appear indistinguishable on top of each other. Nevertheless, the values at $y = 0$ are quite different: $2.5 \cdot 10^{18}$, $6 \cdot 10^{17}$ and $8 \cdot 10^{16} \text{ cm}^{-3}$ for "dried at 0 V - 1 MGy" "humid - 1 MGy" and "dried at 500 V - 1 MGy", respectively. Qualitatively this dependence is expected from the differences in surface-charge distributions and also fits the measured numbers of the electrons and holes collected as presented in [99]: Electron losses $\sim 90\%$ for "dried at 0 V - 1 MGy" and $\sim 30\%$ for "humid - 1 MGy". For the

situation "dried at 500 V - 1 MGy", different to the expectation from the simulation, no or only minor electron or hole losses are observed. Given all the uncertainties in the assumptions made in the simulations, one should not be worried by this difference. It should be noted, that by changing the value of N_{ox}^{eff} in the simulation, the accumulation layer also changes.

6.4. Summary

Using dedicated TCAD simulations the observed losses of electrons (holes) close to the Si-SiO₂ interface can be qualitatively understood by the formation of an electron-accumulation (hole-inversion) layer at the interface and by the distribution of the electric field in the sensor close to the interface. Both are influenced by the distribution of charges on the surface of the sensor and by the density of charged states in the region of the Si-SiO₂ interface. The latter is a strong function of X-ray radiation damage. After changing the sensor voltage it takes some time until the steady-state conditions of the surface-charge distribution are reached. The time constant, which can be as long as several days, depends on the humidity.

7. Summary and conclusions

Due to its high intensity and high repetition rate the European XFEL is a challenging environment for $p^+ - n$ pixel sensors. The sensors have to withstand X-ray doses of up to 1 GGy for 3 years of operation at a high bias voltage required to limit the charge-collection time to below 100 ns, the approximate integration time of the AGIPD readout, and to avoid too large a spread of the charges during their drift through the sensor. The X-ray damage, the high bias voltage and the demand of vacuum operation of the AGIPD detector require a specially optimized sensor.

The X-ray irradiation results in an increase of the oxide-charge density, N_{ox} , and the formation of traps at the Si-SiO₂ interface, which cause an increase of the surface-current density, J_{surf} . In measurements on MOS Capacitors and Gate-Controlled Diodes from four different vendors it was found that for irradiation without applied bias voltage the oxide-charge density N_{ox} increases up to doses of 1 to 10 MGy and then saturates. Typical values after annealing at 80°C for 10 minutes are: $N_{ox} = 10^{12} \text{ cm}^{-2}$ at 10 kGy, $2 \cdot 10^{12} \text{ cm}^{-2}$ at 1 MGy, and $3 \cdot 10^{12} \text{ cm}^{-2}$ at 1 GGy. The values for the different samples differ by approximately a factor two. The values of J_{surf} too, show an increase up to dose values between 1 and 10 MGy. For higher values the measured J_{surf} values decrease, which is not yet understood. Typical values after annealing at 80°C for 10 minutes are: $J_{surf} = 0.3 \text{ } \mu\text{A}/\text{cm}^2$ at 1 kGy, and 2 to 6 $\mu\text{A}/\text{cm}^2$ for the maximal values. Again, the values differ significantly for the different technologies.

Using these radiation-damage parameter in TCAD simulations the pixel and the guard-ring structure were optimized so that the sensor specifications, especially a breakdown voltage of more than 900 V, are met over the full dose range. To achieve this a deeper implant (2.4 μm) than usual is required, an oxide thickness of 250 nm and metal overhangs. It is shown that the gap between the pixels should be small and a value of 20 μm is chosen. The guard-ring structure consists of a current collection ring, CCR, 15 floating guard rings, GR, and an n^+ scribe line implant. The total width of the guard-ring structure is 1.2 mm.

Irradiation of test structures shows that the AGIPD sensor fabricated by SINTEF and optimized for high operating voltage at high X-ray doses in an atmosphere of a relative humidity below 5%, meets all specifications for the entire dose range for both uniform as well as for non-uniform irradiation. Non-irradiated sensors show a soft breakdown at around 800 V. The reason is understood, does not present a problem and can be cured by irradiating the sensor with an X-ray dose of $\approx 200 \text{ Gy}$. The measured current-voltage characteristics and the values for the inter-pixel capacitance as function of X-ray dose are quite similar to the predictions from the simulations. The breakdown voltage for the radiation-optimized design is significantly higher than for the standard design, and thus the optimization is considered a success.

7. Summary and conclusions

A more accurate comparison between measurements and simulation requires an accurate determination of the interface-trap distribution in the bandgap and the cross sections of electrons and holes. It is shown that this is a complicated task for high-ohmic silicon which has yet to be solved.

Using detailed TCAD simulations it has been shown that charge losses in $p^+ - n$ silicon sensors at the Si-SiO₂ interface can be qualitatively understood on the basis of boundary conditions on the surface of the sensor and oxide charges which cause the formation of an electron-accumulation (hole-inversion) layer and change the distribution of the electric field in the sensor close to the interface.

Bibliography

- [1] P. Emma, et al., First lasing and operation of an Ångstrom-wavelength free-electron laser, *Nature Photonics* **4**(9) 641–647. 2010.
- [2] J. M. J. Madey, Stimulated Emission of Bremsstrahlung in a Periodic Magnetic Field, *Journal of Applied Physics* **42**(5) 1906. 1971.
- [3] P. Schmüser, M. Dohlus, J. Rossbach, C. Behrens, *Free-Electron Lasers in the Ultraviolet and X-Ray Regime: Physical Principles, Experimental Results, Technical Realization*, Springer, 2014.
- [4] H. N. Chapman, Coherent imaging with x-ray free-electron lasers, in: M. Angst, T. Brückel, D. Richter, R. Zorn (Eds.), *Scattering Methods for Condensed Matter Research: Towards Novel Applications at Future Sources*, Forschungszentrum Jülich, 2012.
- [5] M. Altarelli, et al., *The European X-Ray Free-Electron Laser*, Technical design report, DESY, Hamburg, Germany, 2006.
- [6] Sacla, URL: <http://xfel.riken.jp/eng/index.html>.
- [7] AGIPD, URL: http://photon-science.desy.de/research/technical_groups/detectors/projects/agipd/index_eng.html.
- [8] B. Henrich, et al., The adaptive gain integrating pixel detector AGIPD a detector for the European XFEL, *Nucl. Instr. and Meth. A* **633**, **Supplement 1** S11 – S14. 2011.
- [9] A. Mancuso, *CONCEPTUAL DESIGN REPORT Scientific Instrument SPB*, Technical Report TR-2011-007, 2012.
- [10] A. Madsen, *CONCEPTUAL DESIGN REPORT Scientific Instrument MID*, Technical Report TR-2011-008, 2012.
- [11] H. Graafsma, Requirements for and development of 2 dimensional X-ray detectors for the european X-ray Free Electron Laser in Hamburg, *Journal of Instrumentation* **4**(12) P12011. 2009.
- [12] M. M. Seibert, et al., Single mimivirus particles intercepted and imaged with an X-ray laser, *Nature* **469**(7332) 78–81. 2012.

- [13] J. Becker, Signal development in silicon sensors used for radiation detection, Ph.D. thesis, Universität Hamburg, Hamburg, 2010. DESY-THESIS-2010-033.
- [14] J. Zhang, X-ray Radiation Damage Studies and Design of a Silicon Pixel Sensor for Science at the XFEL, Ph.D. thesis, Universität Hamburg, Hamburg, 2013. DESY-THESIS-2013-018.
- [15] T. Poehlsen, Charge Losses in Silicon Sensors and Electric-Field Studies at the Si–SiO₂ Interface, Ph.D. thesis, Universität Hamburg, Hamburg, 2013. DESY-THESIS-2013-025.
- [16] S. M. Sze, K. K. Ng, Physics of semiconductor devices, John Wiley & Sons Sons, 2007.
- [17] S. M. Sze, M.-K. Lee, Semiconductor Devices: Physics and Technology, John Wiley & Sons, 2012.
- [18] H. C. de Graaff, F. M. Klaassen, Compact Transistor Modelling for Circuit Design, Springer, 1990.
- [19] B. El-Kareh, Silicon Devices and Process Integration: Deep Submicron and Nano-Scale Technologies, Springer, 2009.
- [20] E. H. Nicollian, J. R. Brews, MOS (Metal Oxide Semiconductor) Physics and Technology, John Wiley & Sons, 2009.
- [21] N. Arora, Mosfet Modeling for VLSI Simulation, World Scientific, 2009.
- [22] M. Balkanski, R. F. Wallis, Semiconductor physics and applications, Oxford University Press, 2000.
- [23] M. Grundmann, The Physics of Semiconductors: An Introduction Including Nanophysics and Applications, Springer, 2010.
- [24] G. Lutz, Semiconductor Radiation Detectors, Springer, 2009.
- [25] C. Leroy, P.-G. Rancoita, Silicon Solid State Devices and Radiation Detection, World Scientific, 2012.
- [26] A. B. Sproul, M. A. Green, Intrinsic carrier concentration and minority-carrier mobility of silicon from 77 to 300 k, *Journal of Applied Physics* **73**(3) 1214–1225. 1993.
- [27] A. Schenk, Advanced Physical Models for Silicon Device Simulation, Springer, 1998.
- [28] A. Schenk, U. Krumbein, Coupled defect-level recombination: Theory and application to anomalous diode characteristics, *Journal of Applied Physics* **78** 3185. 1995.
- [29] D. Fitzgerald, A. Grove, Surface recombination in semiconductors, *Surface Science* **9**(2) 347–369. 1968.

- [30] A. G. Chynoweth, Ionization rates for electrons and holes in silicon, *Phys. Rev.* **109**(5) 1537–1540. 1958.
- [31] M. J. Berger, et al., Xcom, URL: <http://physics.nist.gov/xcom>.
- [32] G. W. Fraser, A. F. Abbey, A. Holland, K. McCarthy, A. Owens, A. Wells, The X-ray energy response of silicon Part A. Theory, *Nucl. Instr. and Meth. A* **350**(1) 368–378. 1994.
- [33] F. Scholze, H. Rabus, G. Ulm, Mean energy required to produce an electron-hole pair in silicon for photons of energies between 50 and 1500 eV, *Journal of Applied Physics* **84**(5) 2926. 1998.
- [34] D. Schroder, Effective lifetimes in high quality silicon devices, *Solid-State Electronics* **27**(3) 247–251. 1984.
- [35] R. S. Nakhmanson, Theory of Mis Capacitance, *Solid-State Electronics* **19**(9) 745–758. 1976.
- [36] S. Wolf, R. N. Tauber, *Silicon Processing for the VLSI Era Volume 1*, Lattice Press, 1986.
- [37] G. Barbottin and A. Vapaille, *Instabilities in Silicon Device Volume 1*, North-Holland, 1986.
- [38] W. Warren, J. Kanicki, F. C. Rong, E. H. Poindexter, Paramagnetic Point Defects in Amorphous Silicon Dioxide and Amorphous Silicon Nitride Thin Films I., *Journal of The Electrochemical Society* **139**(3) 880–889. 1992.
- [39] P. M. Lenahan, J. F. Conley Jr, What can electron paramagnetic resonance tell us about the Si/SiO₂ system?, *Journal of Vacuum Science & Technology B* **16**(4) 2134–2153. 1998.
- [40] G. Barbottin, A. Vapaille, *New Insulators Devices and Radiation Effects, Volume 3*, Elsevier, 1999.
- [41] D. M. Fleetwood, S. T. Pantelides, R. D. Schrimpf, *Defects in Microelectronic Materials and Devices*, CRC, 2009.
- [42] W. Warren, M. Shaneyfelt, D. M. Fleetwood, J. Schwank, P. Winokur, R. Devine, Microscopic nature of border traps in MOS oxides, *IEEE Transactions on Nuclear Science* **41**(6) 1817–1827. 1994.
- [43] F. J. Grunthaner, P. J. Grunthaner, J. Maserjian, Radiation-induced defects in SiO₂ as determined with XPS, *IEEE Transactions on Nuclear Science* **29**(6) 1462–1466. 1982.

- [44] E. H. Poindexter, P. J. Caplan, B. E. Deal, R. R. Razouk, Interface states and electron spin resonance centers in thermally oxidized (111) and (100) silicon wafers, *Journal of Applied Physics* **52**(2) 879–884. 1981.
- [45] T. P. Ma and Paul V. Dressendorfer (Ed.), *Ionizing Radiation Effects in MOS Devices and Circuits*, John Wiley & Sons, New York, 1989.
- [46] M. L. Reed, J. D. Plummer, Chemistry of Si-SiO₂ interface trap annealing, *Journal of Applied Physics* **63**(12) 5776. 1988.
- [47] A. Stesmans, Passivation of Pb₀ and Pb₁ interface defects in thermal (100) Si/SiO₂ with molecular hydrogen, *Applied Physics Letters* **68**(15) 2076. 1996.
- [48] B. E. Deal, Standardized terminology for oxide charges associated with thermally oxidized silicon, *IEEE Transactions on Electron Devices* **27**(3) 606–608. 1980.
- [49] D. Fleetwood, Border Traps in Mos Devices, *IEEE Transactions on Nuclear Science* **39**(2) 269–271. 1992.
- [50] B. E. Deal, A. S. Grove, General Relationship for the Thermal Oxidation of Silicon, *Journal of Applied Physics* **36**(12) 3770. 1965.
- [51] O. V. Aleksandrov, A. I. Dus, A model of formation of fixed charge in thermal silicon dioxide, *Semiconductors* **45**(4) 467–473. 2011.
- [52] D. M. Fleetwood, Fast and slow border traps in MOS devices, *IEEE Transactions on Nuclear Science* **43**(3) 779–786. 1996.
- [53] T. R. Oldham, *Ionizing Radiation Effects in MOS Oxides*, World Scientific, 1999.
- [54] J.-L. Leray, Total dose effects: Modeling for present and future, in: *IEEE NSREC Short Course*, 1998.
- [55] J. Schwank, Total dose effects in mos devices, in: *IEEE NSREC Short Course*, 2002.
- [56] T. Oldham, F. McLean, Total ionizing dose effects in MOS oxides and devices, *IEEE Transactions on Nuclear Science* **50**(3) 483–499. 2003.
- [57] H. Barnaby, Total-Ionizing-Dose Effects in Modern CMOS Technologies, *IEEE Transactions on Nuclear Science* **53**(6) 3103–3121. 2006.
- [58] J. Schwank, M. Shaneyfelt, D. Fleetwood, J. Felix, P. Dodd, P. Paillet, V. Ferlet-Cavrois, Radiation Effects in MOS Oxides, *IEEE Transactions on Nuclear Science* **55**(4) 1833–1853. 2008.

- [59] A. Lelis, H. Boesch Jr, T. Oldham, F. McLean, Reversibility of trapped hole annealing, *IEEE Transactions on Nuclear Science* **35**(6) 1186–1191. 1988.
- [60] A. Lelis, T. Oldham, H. Boesch, F. McLean, The Nature of the Trapped Hole Annealing Process, *IEEE Transactions on Nuclear Science* **36**(6) 1808–1815. 1989.
- [61] T. Grasser, B. Kaczer, W. Goes, H. Reisinger, T. Aichinger, P. Hehenberger, P. Wagner, F. Schanovsky, J. Franco, M. T. Luque, The paradigm shift in understanding the bias temperature instability: from reaction–diffusion to switching oxide traps, *IEEE Transactions on Electron Devices* **58**(11) 3652–3666. 2011.
- [62] A. Holmes-Siedle, L. Adams, *Handbook of radiation effects*, Oxford University Press, 2002.
- [63] R. Graves, C. Cirba, R. D. Schrimpf, R. Milanowski, A. Michez, D. M. Fleetwood, S. Witczak, F. Saigne, Modeling low-dose-rate effects in irradiated bipolar-base oxides, *IEEE Transactions on Nuclear Science* **45**(6) 2352–2360. 1998.
- [64] S. N. Rashkeev, C. Cirba, D. M. Fleetwood, R. D. Schrimpf, S. Witczak, A. Michez, S. T. Pantelides, Physical model for enhanced interface-trap formation at low dose rates, *IEEE Transactions on Nuclear Science* **49**(6) 2650–2655. 2002.
- [65] R. F. Pierret, The gate-controlled diode s_0 measurement and steady-state lateral current flow in deeply depleted MOS structures, *Solid-State Electronics* **17**(12) 1257–1269. 1974.
- [66] R. F. Pierret, R. J. Grossman, Depleted surface recombination velocity s_0 measurements using, *Solid-State Electronics* **20**(4) 373–379. 1977.
- [67] D. K. Schroder, *Semiconductor material and device characterization*, Wiley-IEEE Press, 2006.
- [68] G. W. Hughes, Interface-state effects in irradiated MOS structures, *Journal of Applied Physics* **48**(12) 5357. 1977.
- [69] Canberra industries inc., URL: <http://www.canberra.com>.
- [70] Cis forschungsinstitut für mikrosensorik und photovoltaik gmbh, URL: <http://www.cismst.org>.
- [71] Hamamatsu photonics, URL: <http://www.hamamatsu.com>.
- [72] SINTEF ICT, URL: <http://www.sintef.no>.
- [73] J. G. Simmons, J. G. Taylor, Theory of non-steady-state interfacial thermal currents in MOS devices, and the direct determination of interfacial trap parameters, *Solid-State Electronics* **17** 125–130. 1974.

- [74] H. A. Mar, J. G. Simmons, Surface-Generation Statistics and Associated Thermal Currents in Metal-Oxide-Semiconductor Structures, *Phys. Rev. B* **11**(2) 775–783. 1975.
- [75] J. Zhang, I. Pintilie, E. Fretwurst, R. Klanner, H. Perrey, J. Schwandt, Study of radiation damage induced by 12 keV X-rays in MOS structures built on high-resistivity *n*-type silicon, *Journal of Synchrotron Radiation* **19**(3) 340–346. 2012.
- [76] G. Potdevin, U. Trunk, H. Graafsma, HORUS, an HPAD X-ray detector simulation program, *Journal of Instrumentation* **4**(09) P09010–P09010. 2009.
- [77] G. Potdevin, U. Trunk, H. Graafsma, Performance simulation of a detector for 4th generation photon sources: The AGIPD, *Nucl. Instr. and Meth. A* **607**(1) 51–54. 2009.
- [78] G. Potdevin, H. Graafsma, Analysis of the expected AGIPD detector performance parameters for the European X-ray free electron laser, *Nucl. Instr. and Meth. A* **659**(1) 229–236. 2011.
- [79] J. Becker, H. Graafsma, Advantages of a logarithmic sampling scheme for XPCS experiments at the European XFEL using the AGIPD detector, *Journal of Instrumentation* **7**(04) P04012–P04012. 2012.
- [80] T. Hoshino, M. Kikuchi, D. Murakami, Y. Harada, K. Mitamura, K. Ito, Y. Tanaka, S. Sasaki, M. Takata, H. Jinnai, A. Takahara, X-ray photon correlation spectroscopy using a fast pixel array detector with a grid mask resolution enhancer, *Journal of Synchrotron Radiation* **19**(6) 988–993. 2012.
- [81] C. Gallrapp, A. L. Rosa, A. Macchiolo, R. Nisius, H. Pernegger, R. Richter, P. Weigell, Performance of novel silicon *n*-in-*p* planar pixel sensors, *Nucl. Instr. and Meth. A* **679**(0) 29–35. 2012.
- [82] R. Arora, W. Mosch, *High Voltage and Electrical Insulation Engineering*, Wiley-IEEE Press, 2011.
- [83] J. Becker, D. Greiffenberg, U. Trunk, X. Shi, R. Dinapoli, A. Mozzanica, B. Henrich, B. Schmitt, H. Graafsma, The single photon sensitivity of the Adaptive Gain Integrating Pixel Detector, *Nucl. Instr. and Meth. A* **694**(C) 82–90. 2012.
- [84] R. Klanner, J. Becker, E. Fretwurst, I. Pintilie, T. Pöhlsen, J. Schwandt, J. Zhang, Challenges for silicon pixel sensors at the European XFEL, *Nucl. Instr. and Meth. A* **730**(C) 2–7. 2013.
- [85] L. Rossi, P. Fischer, T. Rohe, N. Wermes, *Pixel Detectors: From Fundamentals to Applications*, Springer, 2006.

- [86] D. Greiffenberg, J. Becker, L. Bianco, R. Dinapoli, P. Goettlicher, H. Graafsma, H. Hirse-
mann, S. Jack, R. Klanner, A. Klyuev, H. Krüger, S. Lange, A. Marras, A. Mozzanica,
S. Rah, B. Schmitt, J. Schwandt, I. Sheviakov, X. Shi, U. Trunk, J. Zhang, M. Zimmer,
Optimization of the noise performance of the AGIPD prototype chips, *Journal of
Instrumentation* **8**(10) P10022–P10022. 2013.
- [87] J. Lindhard, M. Scharff, H. Schiott, Range concepts and heavy ion ranges, *Kgl. Danske
Videnskab Selskab Mat-fys Medd* **33**(14) 42pp. 1963.
- [88] Synopsys TCAD, URL: <http://www.synopsys.com/>.
- [89] S. Tian, Predictive Monte Carlo ion implantation simulator from sub-keV to above 10
MeV, *Journal of Applied Physics* **93**(10) 5893. 2003.
- [90] M. Posselt, B. Schmidt, C. S. Murthy, T. Feudel, K. Suzuki, Modeling of damage
accumulation during ion implantation into single crystalline silicon, *Journal of The
Electrochemical Society* **144**(4) 1495–1504. 1997.
- [91] S. Furukawa, H. Matsumura, H. Ishiwara, Theoretical considerations on lateral spread of
implanted ions, *Jap. J. Appl. Phys* **11**(2) 134–142. 1972.
- [92] P. Pichler, *Intrinsic Point Defects, Impurities, and Their Diffusion in Silicon*, Springer,
2004.
- [93] S. Selberherr, *Analysis and Simulation of Semiconductor Devices*, Springer, 1984.
- [94] G. Beck, A. Carter, J. Carter, N. Greenwood, A. Lucas, D. Munday, T. Pritchard, D. Robin-
son, C. Wilburn, K. Wyllie, The breakdown voltage of unguarded and field plate guarded
silicon detector diodes, *Solid-State Electronics* **45**(1) 183–191. 2001.
- [95] T. Ohsugi, Y. Iwata, H. Ohyama, T. Ohmoto, M. Yoshikawa, T. Handa, K. Kurino,
K. Fujita, H. Kitabayashi, N. Tamura, T. Hatakenaka, M. Maeohmichi, M. Takahata,
M. Nakao, H. Iwasaki, T. Kohriki, S. Terada, Y. Unno, R. Takashima, K. Yamamoto,
K. Yamamura, Micro-discharge noise and radiation damage of silicon microstrip sensors,
Nucl. Instr. and Meth. A **383**(1) 166–173. 1996.
- [96] H. Spieler, *Semiconductor detector systems*, Oxford University Press, 2005.
- [97] G. A. M. Hurkx, D. B. M. Klaassen, M. P. G. Knuvers, A new recombination model
for device simulation including tunneling, *IEEE Transactions on Electron Devices* **39**(2)
331–338. 1992.
- [98] J. Zhang, E. Fretwurst, R. Klanner, I. Pintilie, J. Schwandt, M. Turcato, Investigation
of X-ray induced radiation damage at the Si–SiO₂ interface of silicon sensors for the
European XFEL, *Journal of Instrumentation* **7**(12) C12012. 2012.

- [99] T. Poehlsen, E. Fretwurst, R. Klanner, S. Schuwalow, J. Schwandt, J. Zhang, Charge losses in segmented silicon sensors at the Si–SiO₂ interface, *Nucl. Instr. and Meth. A* **700** 22 – 39. 2013.
- [100] T. Poehlsen, J. Becker, E. Fretwurst, R. Klanner, J. Schwandt, J. Zhang, Study of the accumulation layer and charge losses at the Si–SiO₂ interface in p⁺n-silicon strip sensors, *Nucl. Instr. and Meth. A* **721** 26 – 34. 2013.
- [101] R. Richter, L. Andricek, T. Gebhart, D. Hauff, J. Kemmer, G. Lutz, R. Weiss, A. Rolf, Strip detector design for ATLAS and HERA-B using two-dimensional device simulation, *Nucl. Instr. and Meth. A* **377**(2) 412–421. 1996.
- [102] S. M. Sze, G. Gibbons, Effect of junction curvature on breakdown voltage in semiconductors, *Solid-State Electronics* **9**(9) 831–845. 1966.
- [103] Y. C. Kao, E. D. Woolley, High voltage planar p-n junctions, *Proceedings of the IEEE* **55**(8) 1409–1414. 1967.
- [104] M. S. Adler, V. A. K. Temple, A. Ferro, R. Rustay, Theory and breakdown voltage for planar devices with a single field limiting ring, *IEEE Transactions on Electron Devices* **24**(2) 107–113. 1977.
- [105] B. J. Baliga, Closed-form analytical solutions for the breakdown voltage of planar junctions terminated with a single floating field ring, *Solid-State Electronics* **33**(5) 485–488. 1990.
- [106] K. Brieger, W. Gerlach, J. Pelka, Blocking Capability of Planar Devices with Field Limiting Rings, *Solid-State Electronics* **26**(8) 739–745. 1983.
- [107] B. S. Avset, L. Evensen, The effect of metal field plates on multiguard structures with floating p⁺ guard rings, *Nucl. Instr. and Meth. A* **377**(2-3) 397–403. 1996.
- [108] A. Bischoff, N. Findeis, D. Hauff, P. Holl, J. Kemmer, P. Klein, P. Lechner, G. Lutz, R. Richter, L. Strüder, Breakdown protection and long-term stabilisation for Si-detectors, *Nucl. Instr. and Meth. A* **326**(1-2) 27–37. 1993.
- [109] V. Boisson, M. Le Helley, J. Chante, Analytical expression for the potential of guard rings of diodes operating in the punchthrough mode, *IEEE Transactions on Electron Devices* **32**(4) 838–840. 1985.
- [110] D.-G. Bae, S.-K. Chung, An analytical model for punch-through limited breakdown voltage of planar junction with multiple floating field limiting rings, *Solid-State Electronics* **44**(12) 2109–2116. 2000.

- [111] E. Stefanov, G. Charitat, L. Bailon, Design methodology and simulation tool for floating ring termination technique, *Solid-State Electronics* **42**(12) 2251–2257. 1998.
- [112] X. Cheng, J. Sin, J. Shen, Y. Huai, R. Li, A general design methodology for the optimal multiple-field-limiting-ring structure using device simulator, *IEEE Transactions on Electron Devices* **50**(11) 2273–2279. 2003.
- [113] N. El Baradai, C. Sanfilippo, R. Carta, F. Cappelluti, F. Bonani, An Improved Methodology for the CAD Optimization of Multiple Floating Field-Limiting Ring Terminations, *IEEE Transactions on Electron Devices* **58**(1) 266–270. 2011.
- [114] M. Da Rold, N. Bacchetta, D. Bisello, A. Paccagnella, G.-F. Dalla Betta, G. Verzellesi, O. Militaru, R. Wheadon, P. Fuochi, C. Bozzi, R. Dell’Orso, A. Messineo, G. Tonelli, P. G. Verdini, Study of breakdown effects in silicon multiguard structures, *IEEE Transactions on Nuclear Science* **46**(4) 1215–1223. 1999.
- [115] A. S. Grove, O. Leistiko, W. W. Hooper, Effect of surface fields on the breakdown voltage of planar silicon p-n junctions, *IEEE Transactions on Electron Devices* **14**(3) 157–162. 1967.
- [116] F. Conti, M. Conti, Surface breakdown in silicon planar diodes equipped with field plate, *Solid-State Electronics* **15**(1) 93–105. 1972.
- [117] A. Rusu, C. Bulucea, Deep-depletion breakdown voltage of silicon-dioxide/silicon MOS capacitors, *IEEE Transactions on Electron Devices* **26**(3) 201–205. 1979.
- [118] A. Rusu, O. Pietreanu, C. Bulucea, Reversible breakdown voltage collapse in silicon gate-controlled diodes, *Solid-State Electronics* **23**(5) 473–480. 1980.
- [119] K.-P. Brieger, W. Gerlach, N. A. Liontas, Numerische Untersuchung des Sperrverhaltens von planaren pn-Übergängen mit Feldplatten, *Electrical Engineering (Archiv für Elektrotechnik)* **69** 165–174. 1986.
- [120] K. Ranjan, A. I. Bhardwaj, S. Chatterji, A. K. Srivastava, R. K. Shivpuri, Analysis and optimal design of Si microstrip detector with overhanging metal electrode, *Semicond. Sci. Technol.* **16**(7) 635–639. 2001.
- [121] S. Chatterji, K. Ranjan, A. Bhardwaj, A. K. Srivastava, A. Kumar, M. K. Jha, R. K. Shivpuri, S. L. Khanna, Simulation Study of Irradiated Si Sensors Equipped With Metal-Overhang for Applications in LHC Environment, *IEEE Transactions on Nuclear Science* **51**(2) 298–312. 2004.
- [122] N. Bacchetta, D. Bisello, A. Candelori, M. Rold, M. Descovich, A. Kaminski, A. Messineo, F. Rizzo, G. Verzellesi, Improvement in breakdown characteristics with multiguard

- structures in microstrip silicon detectors for CMS, *Nucl. Instr. and Meth. A* **461** 204–206. 2001.
- [123] A. Longoni, M. Sampietro, L. Strüder, Instability of the behaviour of high resistivity silicon detectors due to the presence of oxide charges, *Nucl. Instr. and Meth. A* **288** 35. 1990.
- [124] R. Stratton, Diffusion of hot and cold electrons in semiconductor barriers, *Physical Review* **126**(6) 2002–2014. 1962.
- [125] J. W. Slotboom, G. Streutker, G. Davids, Surface impact ionization in silicon devices, in: *Electron Devices Meeting, 1987 International*, volume 33, 1987, pp. 494–497.
- [126] C. Jungemann, S. Yamaguchi, H. Goto, Is there experimental evidence for a difference between surface and bulk impact ionization in silicon?, in: *Electron Devices Meeting, 1996. IEDM '96., International*, 1996, pp. 383–386.
- [127] V. P. O’Neil, P. G. Alonas, Relation between oxide thickness and the breakdown voltage of a planar junction with field relief electrode, *IEEE Transactions on Electron Devices* **26**(7) 1098–1100. 1979.
- [128] K.-P. Brieger, E. Falck, W. Gerlach, The contour of an optimal field plate-an analytical approach, *IEEE Transactions on Electron Devices* **35**(5) 684–688. 1988.
- [129] C. M. Osburn, D. W. Ormond, Dielectric breakdown in silicon dioxide films on silicon I. Measurement and interpretation, *Journal of The Electrochemical Society* **119**(5) 591–597. 1972.
- [130] A. Paccagnell, A. Candelori, A. Milani, E. Formigoni, G. Ghidini, F. Pellizzer, D. Drera, P. Fuochi, M. Lavale, Breakdown properties of irradiated MOS capacitors, *IEEE Transactions on Nuclear Science* **43**(6) 2609–2616. 1996.
- [131] D. M. Fleetwood, P. S. Riewe, L. C. and Winokur, F. W. Sexton, Dielectric breakdown of thin oxides during ramped current-temperature stress, *IEEE Transactions on Nuclear Science* **47**(6) 2305–2310. 2000.
- [132] P. W. Cattaneo, Capacitances in micro-strip detectors: A conformal mapping approach, *Solid-State Electronics* **54**(3) 252–258. 2010.
- [133] A. Cerdeira, M. Estrada, Analytical expressions for the calculation of pixel detector capacitances, *IEEE Transactions on Nuclear Science* **44**(1) 63–66. 1997.
- [134] Topsil semiconductor materials, URL: <http://www.topsil.com>.
- [135] Solecon, URL: <http://www.solecon.com/>.

- [136] A. Grove, *Physics and Technology of Semiconductor Devices*, John Wiley & Sons, New York, NY, 1967.
- [137] J. Schwandt, E. Fretwurst, R. Klanner, I. Pintilie, J. Zhang, Study of high-dose X-ray radiation damage of silicon sensors, in: *Proceedings of SPIE*, volume 8777, 2013, p. 87770K.
- [138] F. Hartjes, Moisture sensitivity of AC-coupled silicon strip sensors, *Nucl. Instr. and Meth. A* **552**(1-2) 168–175. 2005.
- [139] G. Luparello, Performance of ALICE silicon tracker detector, in: *Vertex 2013*, 2013.
- [140] W. Shockley, Currents to conductors induced by a moving point charge, *Journal of Applied Physics* **9** 635–636. 1938.
- [141] S. Ramo, Currents induced by electron motion, *Proceedings of the I.R.E.* **27**(9) 584–585. 1939.
- [142] J. B. Gunn, A general expression for electrostatic induction and its application to semiconductor devices, *Solid-State Electronics* **7**(10) 739–742. 1964.
- [143] L.-A. Hamel, M. Julien, Generalized demonstration of ramo’s theorem with space charge and polarization generalized demonstration of ramo’s theorem with space charge and polarization effects, *Nucl. Instr. and Meth. A* **597** 207–211. 2008.
- [144] M. Atalla, A. Bray, R. Lindner, Stability of thermally oxidized silicon junctions in wet atmospheres, *Proceedings of the IEE - Part B: Electronic and Communication Engineering* **106**(17) 1130–1137. 1959.
- [145] W. Shockley, W. Hooper, H. Queisser, W. Schroen, Mobile electric charges on insulating oxides with application to oxide covered silicon pn junctions, *Surface Science* **2** 277–287. 1964.
- [146] P. A. Heimann, A sensitive method for measuring surface conductivity of insulators, *Journal of Applied Physics* **53**(1) 546. 1982.

A. Appendix

A.1. Simulated doping profiles

Dose [cm ⁻²]	Energy [keV]	Temperature [°C]	junction depth [μm]	lateral extension [μm]	peak concentration [cm ⁻³]
1 · 10 ¹⁵	70	975	1.16	0.99	1.8 · 10 ¹⁹
5 · 10 ¹⁵	70	975	1.48	1.29	5.3 · 10 ¹⁹
1 · 10 ¹⁶	70	975	1.76	1.43	8.5 · 10 ¹⁹
1 · 10 ¹⁵	150	975	1.46	1.07	1.7 · 10 ¹⁹
5 · 10 ¹⁵	150	975	1.72	1.22	5.8 · 10 ¹⁹
1 · 10 ¹⁶	150	975	1.98	1.61	9.5 · 10 ¹⁹
1 · 10 ¹⁵	200	975	1.61	1.12	1.3 · 10 ¹⁹
5 · 10 ¹⁵	200	975	1.82	1.32	5.4 · 10 ¹⁹
1 · 10 ¹⁶	200	975	2.06	1.54	9.8 · 10 ¹⁹
1 · 10 ¹⁵	70	1025	1.92	1.71	1.3 · 10 ¹⁹
5 · 10 ¹⁵	70	1025	2.4	1.95	3.9 · 10 ¹⁹
1 · 10 ¹⁶	70	1025	2.75	2.35	6.1 · 10 ¹⁹
1 · 10 ¹⁵	150	1025	2.16	1.7	1.3 · 10 ¹⁹
5 · 10 ¹⁵	150	1025	2.57	2.16	4.3 · 10 ¹⁹
1 · 10 ¹⁶	150	1025	2.91	2.4	6.9 · 10 ¹⁹
1 · 10 ¹⁵	200	1025	2.28	1.75	1.2 · 10 ¹⁹
5 · 10 ¹⁵	200	1025	2.6	2.1	4.2 · 10 ¹⁹
1 · 10 ¹⁶	200	1025	2.97	2.35	6.8 · 10 ¹⁹

Table A.1.1.: Simulated doping profiles. Drive-in time 4 hours.

List of Publications

First author

-
- 2014 *Design and First Tests of a Radiation-Hard Pixel Sensor for the European X-Ray Free-Electron Laser*,
IEEE Transactions on Nuclear Science Vol. 61 (4) 1894-1901
- 2013 *Study of high-dose X-ray radiation damage of silicon sensors*
Proceedings of SPIE, volume 8777, 2013, p. 87770K
- 2013 *Design of the AGIPD sensor for the European XFEL*
Journal of Instrumentation 8 C01015 (2013)
- 2013 *Design of the AGIPD sensor for the European XFEL*
Nucl. Instr. and Meth. A 737 252-254 (2013)
- 2012 *Optimization of the radiation hardness of silicon pixel sensors for high x-ray doses using TCAD simulations*,
Journal of Instrumentation 7 C01006 (2012)
-

Contributing author

-
- 2013 *Study of High-dose X-ray Radiation Damage of Silicon Sensors*
Nucl. Instr. and Meth. A 732 117-121 (2013)
- 2013 *Challenges for silicon pixel sensors at the European XFEL*
Nucl. Instr. and Meth. A 730 2-7 (2013)
- 2013 *Time dependence of charge losses at the Si-SiO₂ interface in p⁺-n-silicon strip sensors*
Nucl. Instr. and Meth. A 731 172-176 (2013)
- 2013 *Study of the accumulation layer and charge losses at the Si-SiO₂ interface p⁺-n-silicon strip sensors*
Nucl. Instr. and Meth. A 721 26-34 (2013)
- 2013 *Charge losses in segmented silicon sensors at the Si-SiO₂ interface*
Nucl. Instr. and Meth. A 700 22-39 (2013)
- 2013 *X-ray induced radiation damage in segmented p⁺-n silicon sensors*
Proceeding of Science (Vertex 2012), 019 (2013)
- 2012 *Investigation of X-ray induced radiation damage at the Si-SiO₂ interface of silicon sensors for the European XFEL*
Journal of Instrumentation 7 C12012 (2012)
- 2012 *Study of radiation damage induced by 12 keV X-rays in MOS structures built on high resistivity n-type silicon*
Journal of Synchrotron Radiation Vol.19 Issue 3 340-346 (2012)
-

Acknowledgements

First of all, I would like to thank Robert Klanner for giving me the opportunity of joining his group and for supervising this work. His critical view and his detailed and elaborate comments have been very helpful and have improved this work a lot.

I also would like to thank Eckhard Elsen, Erika Garutti and Heinz Graafsma for acting as members of my disputation committee and Georg Steinbrück for chairing the disputation.

Many thanks to Eckart Fretwurst for sharing his broad knowledge of silicon sensors with me and for proofreading of the thesis. Furthermore, I would like to thank Jiaguo Zhang and Ioannis Kopsalis for their contributions to the irradiations, measurements and discussions, and Thomas Pöhlens for the collaboration on the work on the charge losses.

I would like also to express my thanks to Michael Matysek for organizing the computational hardware for me and Frank Schlünzen for keeping the TCAD software update. Many thanks to Peter Buhmann and Wolfgang Gärtner for the continuous improvement and maintenance of the measurement infrastructure of the laboratory and for helping in the measurements. In addition, I would like to thank Thor-Erik Hansen from SINTEF, who was willing to change the standard process for us and Alke Meents and his team for the support during the irradiation at the beamline P11 of PETRA III.

I am most thankful to the colleagues of the AGIPD collaborations for their support of my work and many fruitful discussions.

Finally I want to thank my family for their support during all the years.

